le cnam

Conservatoire national des arts et métiers

ÉCOLE DOCTORALE SCIENCES DES MÉTIERS DE L'INGÉNIEUR

Laboratoire de Mécanique des Structures et des Systèmes Couplés

Thèse de doctorat

Présentée par : **Nicolas CORTES**

Soutenue le : **3 février 2026**

Discipline : **Génie Mécanique, Génie Civil**

Spécialité : **Mécanique des fluides**

APPORT DU COUPLAGE FLUIDE STRUCTURE HAUTE-FIDÉLITÉ POUR LA MODÉLISATION DES ÉOLIENNES DE NOUVELLE GÉNÉRATION

THÈSE DIRIGÉE PAR :

M. Xavier AMANDOLESE Professeur, Cnam

ET CO-ENCADRÉE PAR :

M. Jean-Lou PFISTER Ingénieur de Recherche, IFPEN

M. Jean-Sébastien SCHOTTÉ Ingénieur de Recherche, ONERA

M. Ronan BOISARD Ingénieur de Recherche, ONERA

M. Frédéric BLONDEL Ingénieur de Recherche, IFPEN

Jury

M. Grégory PINON	Professeur, Université Le Havre Normandie	Président
M. Jean-Camille CHASSAING	Professeur, Sorbonne Université	Rapporteur
M. Thomas ANDRIANNE	Professeur, Liège Université	Rapporteur
M. Xavier AMANDOLESE	Professeur, Cnam	Directeur de thèse
Mme. Sophie RAMANANARIVO	Professeure, École Polytechnique	Examinatrice
Mme. Caroline BRAUD	Chargée de recherche, École Centrale de Nantes	Examinatrice
M. Emmanuel BRANLARD	Professeur, University of Massachusetts Amherst	Examinateur
M. Nicolas ALFEREZ	MCF, Cnam	Examinateur

Parvenu à l'issue de mon doctorat en Sciences pour l'ingénieur spécialité Mécanique des fluides, et ayant ainsi pratiqué, dans ma quête du savoir, l'exercice d'une recherche scientifique exigeante, en cultivant la rigueur intellectuelle, la réflexivité éthique et dans le respect des principes de l'intégrité scientifique, je m'engage, pour ce qui dépendra de moi, dans la suite de ma carrière professionnelle quel qu'en soit le secteur ou le domaine d'activité, à maintenir une conduite intègre dans mon rapport au savoir, mes méthodes et mes résultats.

Remerciements

Je tiens avant tout à remercier les rapporteurs, Jean-Camille CHASSAING et Thomas ANDRIANNE, d'avoir pris le temps d'examiner aussi minutieusement mes travaux. Je remercie également l'ensemble des membres du jury d'avoir accepté d'évaluer mon travail de thèse. La pertinence des questions a donné lieu à de très intéressantes discussions. Merci à Grégory PINON d'en avoir assumé la présidence.

Je souhaite à présent remercier les personnes qui m'ont encadré durant ces années et qui m'ont offert une grande liberté d'action tout en restant disponibles lorsque j'en avais besoin. Merci Xavier de m'avoir aidé à prendre les décisions concernant les grandes directions de la thèse. Nos discussions m'ont toujours permis de garder une vision d'ensemble et un recul sur mes travaux. Grâce à toi, même lorsque le chemin devenait sinueux, le cap restait clair. J'ai également beaucoup apprécié garder un lien avec l'expérimental grâce à toi. Pouvoir aller au cœur d'une soufflerie avec toi pour tester ces vibrations induites par décrochage a été une expérience incroyable !
Jean-Lou, merci pour tous tes conseils avisés et tes réponses bienveillantes à toutes mes questions, les plus simples comme les plus alambiquées. Tu m'as également beaucoup appris, notamment sur les rotations qui m'ont plus d'une fois donné le tournis. Jean-Sébastien, je te remercie, savoir que ta porte était toujours ouverte m'a beaucoup aidé. Nos échanges m'ont permis de clarifier de nombreuses petites incompréhensions et de prendre des décisions assez rapides au quotidien. Merci Ronan pour m'avoir transmis ta vision de la CFD ainsi que toutes les bonnes pratiques. Fred, merci pour les discussions sur l'aérodynamique des éoliennes. Je souhaiterais également remercier Ivan et Christophe qui m'ont apporté une aide indispensable dans la prise en main de *Cassiopée* et *FastS*. Enfin, je remercie le GENCI d'avoir accepté d'héberger mes très gros calculs.

Au-delà du travail scientifique, je remercie tous ceux qui ont contribué à rendre mon quotidien agréable et épanouissant. J'adresse un grand merci à mes collègues de l'ONERA. Merci à Théo, Alain, Antoine et tous mes coéquipiers du Volley pour ces super matchs contre les autres entreprises. Merci à Maxime, Dimitri, Théo et Cédric qui m'ont fait découvrir la boxe. Merci à Charly, Federico, Adrien, Pierre-Emmanuel et Christophe pour ces séances de ping-pong riches en effets improbables et rebonds sur les murs. Marine merci de m'avoir accompagné à la danse. J'ai été heureux de partager le bureau avec toi, tu repérais tout ce qui était faux en un coup d'œil. Merci Roger d'avoir été mon maître de jonglage suite à l'apparition spontanée de balles de Tennis dans la salle de pause. J'adresse un autre grand merci à mes collègues de l'IFPEN pour toutes les passionnantes discussions qui ont animé la salle café. J'ai beaucoup apprécié partir en congrès avec vous, que ce soit à Florence ou à Nantes. Je remercie tous mes colloques de bureau, Caro, Enikő, Yewei et Erwan, pour tous les échanges que nous avons pu avoir dans ce bureau à la fenêtre diatherme. Merci à mes camarades doctorants, Nina, Eddy, Édouard, Paul, Mary et etc, pour toutes les sorties que nous avons pu faire.

Je ne peux conclure sans penser à mes amis qui m'ont permis de sortir la tête de la thèse lorsque j'en avais besoin. Merci Thibaut, Pierre et Stan pour ces vacances inoubliables et toutes ces sorties dans Paris. Merci à toute la Brigade du Fun pour ces accueils chaleureux sur Discord. Merci Édouard et Micky pour ces virées en Charente et en Provence. Enfin, je veux remercier ma famille pour ses encouragements et son soutien indéfectible. C'est en grande partie grâce à vous si je suis arrivé jusque là.

Résumé

Afin de réduire le coût de l'énergie éolienne, les rotors deviennent de plus en plus grands, avec des pales plus légères, plus élancées et donc plus flexibles. Cette évolution les rend plus sensibles aux instabilités aéroélastiques, en particulier à l'arrêt, lorsque des vents forts peuvent provenir de n'importe quelle direction. Les phénomènes aéroélastiques résultent de l'interaction entre les charges aérodynamiques et la déformation de la structure. Parmi les instabilités susceptibles d'apparaître sur une pale à l'arrêt, cette thèse se concentre sur les vibrations induites par "décrochage" (Stall Induced Vibrations, SIV), où un processus de décrochage dynamique non linéaire peut conduire à un transfert d'énergie défavorable du fluide vers la structure. Alors que les approches numériques couplant des codes de simulations "haute-fidélité" fluide et structure (CFD/CSM) sont courantes en aéronautique, elles demeurent rares dans le domaine éolien. L'objectif principal de cette thèse est donc de développer un outil de simulation CFD/CSM couplé et de l'utiliser, conjointement à des approches plus simples, pour étudier le comportement aéroélastique des grandes pales d'éoliennes à l'arrêt. Un environnement de simulation modulaire a ainsi été développé en Python afin de coupler des solveurs aérodynamiques et structurels de complexité croissante, d'un modèle sectionnel utilisant un chargement aérodynamique quasi-statique à un solveur "haute-fidélité" CFD/CSM. Chaque module incluant le couplage a été validée, et ce solveur modulaire a permis d'étudier les SIV de la pale de référence IEA15MW avec un niveau de précision croissant. Les simulations haute fidélité étant coûteuses, un modèle simplifié a été élaboré afin d'établir des cartes de stabilité et d'identifier les configurations critiques. Il s'agit d'un modèle sectionnel équivalent à deux degrés de liberté, développé sur la base de paramètres équivalents de masse, raideur, angle d'attaque moyen, corde et polaires aérodynamiques. Les résultats obtenus avec une formulation quasi-statique du chargement aérodynamique ou décrochage dynamique de l'ONERA, ont été comparées à une approche continue de type éléments finis. Cette comparaison a mis en évidence les atouts et limites des approches simplifiées pour les pales modernes, fortement vrillées et flexibles. Enfin, des simulations CFD/CSM haute fidélité ont été menées à l'aide d'un solveur URANS couplé à un modèle de poutre non linéaire. L'analyse statique a permis de décrire les cellules de décrochage pour différentes incidences et vitesses de vent. Des simulations réalisées en forçant harmoniquement le mouvement de la pale sur son premier mode de flexion ont ensuite permis d'étudier le déphasage entre mouvement et chargements aérodynamiques, paramètre clé de la stabilité dynamique du système. Enfin, des simulations de réponse à la rafale ont été réalisées afin d'évaluer l'influence des conditions de vent sur le comportement aéroélastique de la pale, tout en capturant plus finement les effets instationnaires et tridimensionnels de l'écoulement.

Mot-clés : Aéroélasticité, Éolienne, Vibrations induites par décrochage, Modèle sectionnel équivalent, Couplage haute-fidélité CFD/CSM

Abstract

To reduce the cost of wind energy, wind turbines are becoming increasingly large, with blades that are lighter, more slender and thus more flexible. This makes them more prone to aeroelastic instabilities, especially at standstill, where strong winds can strike from any direction. Aeroelastic phenomena result from the interaction between aerodynamic loads and structural deformation. Among the instabilities of concern for wind turbines at standstill, this work focuses on stall induced vibrations (SIV), where complex nonlinear dynamic stall process can lead to a fluid-structure energy transfer. While high-fidelity CFD/CSM approaches are widely used in aeronautics, their application to wind turbines remains rare. The objective of this thesis is therefore to develop a high fidelity coupled CFD/CSM framework and to use it, together with low-fidelity methods, to investigate the aeroelastic behavior of large wind turbine blades at standstill. A modular Python framework was thus developed to couple structural and aerodynamic solvers across different fidelity levels, from sectional models with either quasi-steady or unsteady nonlinear aerodynamics formulations, to high-fidelity CFD/CSM. Each step of the partitioned coupling was validated and this framework was used to investigate stall-induced vibrations (SIV) of the IEA15MW blade with progressively refined methods. Since high-fidelity simulations are too costly to cover wide ranges of wind conditions, simplified models were built to provide stability maps and guide the selection of critical cases. An equivalent two degrees of freedom section model of the IEA15MW full blade was developed, highlighting the identification procedure of the equivalent mass, stiffness, mean angle of attack, chord and polar. Its prediction, using quasistatic aerodynamics or ONERA dynamic stall model, were compared to a continuous finite-element blade approach under strip theory. This comparison highlighted both the potential and the limitations of such low-fidelity methods for modern twisted and flexible blades. High-fidelity CFD/CSM simulations were then carried out using an unsteady RANS solver coupled with a nonlinear blade model. Static aeroelastic analysis focused on the description of the stall cells under several conditions of incidence and wind speeds, while forced oscillations in the first flapwise mode allowed a detailed analysis of the phase lag in the motion induced aerodynamic loading that mainly impacts the dynamic stability. Finally, few aeroelastic responses to an imposed gust have been computed and discussed using the high-fidelity framework. It allowed a first estimation on the effect of the wind conditions (direction and speed) with a better computation of the 3D unsteady flow behavior.

Keywords : Aeroelasticity, wind turbine, Stall induced vibrations, equivalent section model, High-fidelity CFD/CSM coupling

Contents

List of Figures ix

List of Tables xvii

List of Acronyms and Symbols xxi

Introduction 1

1 Aeroelastic phenomenon on wind turbines at standstill 9
1.1 Coupled mode flutter . . . 10
1.1.1 Methods to evaluate the coupled mode flutter speed . . . 10
1.1.2 Coupled mode flutter on wind turbine blade . . . 11
1.1.3 Summary . . . 13
1.2 Vortex induced vibrations . . . 13
1.2.1 Vortex induced vibrations past a circular cylinder . . . 13
1.2.2 Vortex induced vibrations past 2D airfoils . . . 15
1.2.3 Vortex induced vibrations past wind turbine blades . . . 17
1.2.4 Summary . . . 20
1.3 Stall-induced vibrations . . . 20
1.3.1 Static stall . . . 21
1.3.2 Dynamic stall . . . 23
1.3.3 3D Stall . . . 33
1.3.4 Aeroelastic studies on SIV . . . 37
1.4 Conclusion . . . 43

2 Numerical methods for high-fidelity aeroelasticity simulations 45
2.1 General fluid structure coupling . . . 45
2.2 Fluid solver : FastS . . . 46
2.2.1 Numerical schemes . . . 46
2.2.2 Arbitrary Lagrangian Eulerian formulation . . . 48
2.2.3 Chimera method . . . 49
2.3 Mesh Deformation : Quantum . . . 49
2.4 Structural solver : Project Chrono . . . 50
2.4.1 Data entry of the beam model . . . 50
2.5 Spatial coupling between a fluid solver and structural solver . . . 51
2.5.1 Conservative vs Consistent approach . . . 52
2.5.2 Transfer methods . . . 53
2.6 Temporal coupling . . . 55
2.6.1 Static coupling . . . 55
2.6.2 Dynamic coupling . . . 55
2.7 Summary . . . 57

3 Implementation and validation of a modular python framework for coupled fluid-structure simulations 59
3.1 General organization of the framework . . . 60
3.2 Validation of the IEA15MW blade beam model . . . 61
3.3 Identification of the ONERA dynamic stall model parameters . . . 63
3.4 Validation of the dynamic stall modeling with CFD . . . 65
3.4.1 Methodology . . . 65
3.4.2 Results and discussion for fixed-wing cases . . . 67
3.4.3 Results and discussion for oscillating-wing cases . . . 69
3.4.4 Fully resolved flow field . . . 70
3.5 Implementation and Validation of the motion transfer . . . 71
3.5.1 Coupling with the sectional models . . . 71
3.5.2 Coupling with the CFD solver . . . 72
3.6 Implementation of the load transfer . . . 76
3.6.1 Orientation of the slices and integration . . . 76
3.6.2 Comparison between the CFD and the strip theory models . . . 77
3.6.3 Calculation of the generalized forces for the beam FEM model . . . 78
3.6.4 Precautions with the slices . . . 80
3.7 Comparison of the static aeroelastic coupling between the CFD and the strip theory models . . . 81
3.8 Restart of dynamic aeroelastic simulations . . . 83
3.9 Conclusion . . . 83

4 Study of stall-induced vibrations at standstill with low fidelity models 85
4.1 Development of an equivalent section model . . . 86
4.1.1 Step 1 : Equations of motion of a 2dof equivalent section model . . . 87
4.1.2 Step 2: Modal equations of the blade . . . 90
4.1.3 Step 3: Identification of the section model edgewise direction and equivalent chord . . . 94
4.1.4 Step 4: Identification of an equivalent polar . . . 96
4.1.5 Step 5: Identification of the flexion-torsion coupling stiffness and the angle of torsion . . . 97
4.1.6 Summary and implementation . . . 99
4.2 Effect of the dynamic stall model . . . 101
4.2.1 Stability map . . . 102
4.2.2 Stability analysis for a wind of fixed angle of incidence . . . 103
4.2.3 Stability analysis for a wind of fixed velocity . . . 104
4.2.4 Effect of the loops orientation . . . 105
4.3 Stability analysis using a finite element model of the blade . . . 106
4.3.1 Spanwise distribution of the fluid-structure energy transfer . . . 107
4.3.2 Stability analysis . . . 108
4.4 Discussions . . . 109
4.4.1 Equivalent dynamic stall . . . 109
4.4.2 The equilibrium modification . . . 110
4.4.3 Comparison with a simpler sectional model . . . 111
4.4.4 Sensitivity to a parameter of the ONERA model . . . 113
4.5 Conclusion . . . 114

5 Study of stall-induced vibrations at standstill with high fidelity models 115
5.1 Cases description . . . 116
5.1.1 The numerical setup . . . 116
5.1.2 Choice of the cases to simulate . . . 118
5.2 Study of the aeroelastic static equilibriums . . . 119
5.2.1 Analysis of the $\phi_0 = 17°$ and $U_0 = 40$m/s case . . . 119
5.2.2 Effect of the wind angle of incidence ϕ_0 . . . 123
5.2.3 Effect of the wind speed U_0 . . . 126
5.3 Study of the dynamic behavior of the aerodynamic loads induced by an imposed harmonic motion of the blade . . . 128
5.3.1 Description of the imposed motions . . . 128
5.3.2 Analysis of the $\phi_0 = 17°$ and $U_0 = 40$m/s case . . . 130
5.3.3 Effect of the incidence ϕ_0 . . . 137
5.3.4 Effect of the wind speed U_0 . . . 139
5.4 Study of the aeroelastic dynamic behavior of the blade in stall conditions with a high-fidelity aeroelastic unsteady coupling . . . 140
5.4.1 Description of the wind gust used to perturbed the blade . . . 140
5.4.2 Analysis of the $\phi_0 = 17°$ and $U_0 = 40$m/s case . . . 142
5.4.3 Effect of the incidence ϕ_0 . . . 143
5.4.4 Effect of the wind speed U_0 . . . 145
5.5 Conclusion . . . 148

Conclusion and perspectives 149

List of communications 155

Appendix 157

A Presentation of the IEA15MW 159
A.1 General description . . . 159
A.2 The polars of the IEA15MW . . . 161
A.2.1 2D polars . . . 162
A.2.2 Construction of 3D aeroelastic polars . . . 165

B Calculation of the A, B and C matrix of the equivalent polar equation 167

C Calculation of the aerodynamic damping and stiffness 169
C.1 Aerodynamic stiffness . . . 169
C.2 Aerodynamic damping . . . 170
C.2.1 Alternative calculation . . . 170
C.2.2 Link with the phase shift . . . 171
C.3 Application to the blade of the IEA15MW . . . 171

D Calculation of the phase shift with the blade velocity 173

Bibliography 175

Résumé du mémoire 187

List of Figures

1 Global cumulative installed capacity (in gigawatts) for wind energy and estimated LCOE for the U.S. interior region in cents per kilowatt-hour from 1980 to 2017 [137] 1
2 Wind turbine blade innovation comparing a modern commercial blade (top) and a commercial blade from the mid-1980s (bottom) scaled to the same length [137] . . 2
3 Scheme of the grand challenges in the sciences of wind energy. (Image credit: Besiki Kazaishvili, National Renewable Energy Laboratory – NREL.) [138] 3
4 Schematic representation showing the wind direction likely to trigger aeroelastic instabilities. The range of direction depends on the airfoil. The size of the arrow gives an idea of the critical velocity. Small arrow means low critical velocity. 4

1.1 Scheme of the unstable mode 10
1.2 Different technical frameworks for flutter analysis and prediction: analytical methods, CFD-based methods, and ROM-based methods. [6] 10
1.3 Experimental setup [19] 12
1.4 Dimensionless spectral map of the response versus the dimensionless wind speed based on the accelerometer data [19]. The horizontal lines correspond to the first three flapwise natural frequencies, and the first torsional natural frequency (the continuous line). 12
1.5 Vortex shedding during large amplitude VIV [1] 13
1.6 Regimes of fluid flow across smooth circular cylinder [18] 14
1.7 Vortex-induced vibrations of a spring supported damped circular cylinder [18] . . . 15
1.8 Dimensionless amplitude of the crossflow oscillations A^* versus the reduced velocity for angles of attack in the range 55° to 135° [12] 16
1.9 Instantaneous isosurface for the vortex criterion Q coloured by velocity magnitude. The initial blade geometry is shown in grey. The inflow speed is 50m/s at 90° pitch with no inclination. [40] 17
1.10 18
1.11 Wake visualization by iso-surfaces of Q-criterion. Includes both pure CFD simulations (stiff) and FSI ones (flex) [71] 18
1.12 19
1.13 Scheme of a static polar 21
1.14 Flow about an airfoil section at increasing angles of attack showing the progressive forward movement of flow separation and the onset of stall [80] 22
1.15 Scheme of the boundary layer separation 22
1.16 Comparison of lift static polars between leading edge stall and trailing edge stall . 23
1.17 Dynamic stall events on a NACA0012 airfoil around 15° with an amplitude of 10° and a reduced frequency $k = 0.15$ at $Re = 2.5 \cdot 10^6$ [23] 23
1.18 Instantaneous contours of entropy at the mid-span showing overall process of dynamic stall during a ramp motion from 8° up to 30° with a pitch rate of 2.8° by U_0/c second. (Re = 1e6) [13] 25
1.19 Phase averaged normalized vorticity fields and surface pressure coefficients illustrating various stages of the dynamic stall mechanism, $\alpha = 0° + 30° \sin(\omega t)$, $k = 0.074$, $Re = 2.5e5$ [99]. 25
1.20 Spatio-temporal (x–α) contours of span-averaged wall skinfriction coefficient on the airfoil suction surface [13]. 26

1.21 Contours of spanwise-averaged skin friction coefficient $< C_f >$ on the suction side of the four airfoils through the constant pitch-rate motion. [122] 27
1.22 The temporal change of suction-side surface pressure presented for selected test cases of the reduced frequency series. Black solid lines mark the start and end of the piching motion; black dotted lines specify the passage of the static stall angle. [75] 28
1.23 Influence of the reduced frequency $k = \frac{\pi fc}{U_0}$ on the lift and moment coefficient; Experiments on a NACA63421 section model in harmonic pitching motion of mean angle of attack 12° and mean amplitude 8°, for $Re = 10^6$ and $I_{tu} = 1.1\%$. [3] . . . 28
1.24 Influence of the turbulence intensity on the lift and moment coefficients; Experiments on a NACA63421 section model in harmonic pitching motion of mean angle of attack 12° and mean amplitude 8°, for $Re = 10^6$ and reduced frequency $k = \frac{\pi fc}{U_0} = 0.183$. [3] 29
1.25 Scheme for the ONERA model. a is negative on the scheme. 30
1.26 Definition of Δc_l [37] 31
1.27 Effect of the parameters a_0 and a_2 on the lift dynamic stall loop. [39] 32
1.28 Effect of the parameters r_0 and r_2 on the lift dynamic stall loop. [39] 32
1.29 Effect of the parameter E_2 on the lift dynamic stall loop. [39] 32
1.30 Stall-cell flow pattern observed in the suction side of a NACA0015 wing model with aspect ratio AR=4 at the angle of attack 16° and Reynolds number $4.04 \cdot 10^5$; oil flow visualization; the mean flow is coming from to bottom. [36] 33
1.31 The CFD obtained SC structure. Q = 1 iso-surface. Interpreted vortex core lines with vorticity direction are also shown.[92] 34
1.32 Evolution of the instantaneous 3D flow structure of the pitching AR=4 wing using isosurfaces of normalized stagnation density at different instants of the pitching cycle [61] 35
1.33 Front view of instantaneous 3D flow structure evolution of the AR=16 wing using isosurfaces of normalized stagnation density [61] 36
1.34 Front view of instantaneous 3D flow structure evolution of the AR=8 wing using isosurfaces of normalized stagnation density [62] 36
1.35 Typical section with one degree of freedom in torsion 37
1.36 Dynamic stall loop of a NACA0012 forced to oscillate in pitch around 15° with an amplitude of 10° and a reduced frequency $k = 0.15$ at $Re = 2.5 \cdot 10^6$ [23]. 38
1.37 A typical blade section with one degree of freedom x(t) in the direction of vibration θ relative to the rotor plane [64] 39
1.38 Evolution of the aerodynamic damping of the FFA-W3-211 airfoil with the incidence ϕ_0 and the direction of vibration θ for stall-induced vibrations in linear translation. 40
1.39 Schematic representation showing the wind direction likely to trigger aeroelastic instabilities. The range of direction depends on the airfoil. The size of the arrow gives an idea of the critical velocity. Small arrow means low critical velocity. 43

2.1 Scheme of the partitioned coupling 46
2.2 Illustration of the chimera method. The interpolated cells are in blue and the masked cells are in red. [96] 49
2.3 The corotational kinematic description [49] 50
2.4 Cutting Lines and Pressure Force Orientation during Force Read-Out in EllipSys3D [68] 53
2.5 Wing structure modeled as a simple beam finite element [22] 54

2.6 Loose coupling schemes [68] . . . 56
2.7 Strong coupling scheme [68] . . . 56

3.1 UML diagram of the aeroelastic python framework . . . 60
3.2 Evolution of the natural frequencies with the number of nodes . . . 62
3.3 Natural frequencies of the IEA15MW blade obtained as part of the IEA Task 47 . 62
3.4 Comparison of the tip displacements with Loubeyres et al. [87]. (The axes are the ones of Loubeyres et al. [87]) . . . 63
3.5 Comparison between the experimental results of Fuglsang et al. [51] with the results obtained with the ONERA dynamic stall model using the set of parameter reported in Table 3.1. Unsteady lift, drag and moment coefficient of the FFA-W3-241 airfoil forced to oscillate in pitch with an amplitude of two degrees, for different mean angles of attack, at a reduced frequency $k = \frac{\omega c}{2U_0} = 0.093$. . . . 64
3.6 Convergence of time step for the dynamic stall loop of reduced frequency $k = 0.183$ and turbulence intensity 4%. . . . 66
3.7 Steady lift coefficient (left) and moment coefficient about the quarter chord (right) results. FastS-full is obtained with a full integration of the stress over the airfoil while FastS-exp is calculated using the same integration method as the experiment [3]. . . . 67
3.8 Mean pressure coefficient comparison between simulation (FastS-exp, FastS-full) and experiment (exp) for three angles of attack. . . . 68
3.9 Static and dynamic lift coefficients (top) and moment coefficients (bottom) for three reduced frequencies; comparison of numerical predictions (FastS-exp and Onera dynamic stall model) with experiments reported in [3]. The lift loops turn clockwise while the moment loops turn counter-clockwise. The letters indicate specific states used in the following figures. . . . 69
3.10 Snapshots of the vorticity field for the reduced frequency $k_3 = 0.183$ at three angles of attack during the upstroke (a, b, c) and the downstroke (d, e, f), for the NACA63421 airfoil. . . . 70
3.11 Scheme of the different frames: global frame $\mathcal{R}$ (black), section frame $\mathcal{R}_s$ (red) and section wind frame $\mathcal{R}_{sw}$ (blue). . . . 71
3.12 Scheme of the displacement transfer method . . . 73
3.13 Scheme of the attribution of the mesh point to a curvilinear abscissa. The blue line is centerline of the beam while the grey dots are the skin fluid mesh points projected in the YZ plane. . . . 74
3.14 Deformation of the skin mesh . . . 75
3.15 Scheme of the slices. The red frames are the local section frame $\mathcal{R}_s$. . . . 76
3.16 Comparison between the loads obtained with CFD and the loads obtained with the strip theory ($U_0 = 40m/s$ and $\alpha_0 = 3°$). The two set of polars is explained in Appendix A. . . . 77
3.17 Illustration of the hypothesis of linear evolution of the loads within the beam elements 78
3.18 Shape functions . . . 79
3.19 Scheme explaining the production of an unwanted moment. The black line is the beam. The dotted blue line is the exact geometry of the blade while the solid blue line is the discretized geometry. The slice is represented in grey. . . . 81
3.20 Evolution of the tip position in Y over the coupling iterations for the beam/CFD simulation and simulations with the strip theory assumption. . . . 82

3.21 Deformation of the blade for $\phi_0 = 3°$ and $U_0 = 40$m/s calculated with CFD and the strip theory assumption. The solid line represents the initial configuration. 82

4.1 Scheme of a 2dof section 87
4.2 Scheme indicating the coordinate system of the blade 90
4.3 Comparison of the different terms of the aerodynamic dampings 94
4.4 Equivalent polars of the IEA15MW before the translation by $\alpha^{2D}_{\text{twist}}$. The polar at 75% of radius is added for comparison. 97
4.5 Equivalent polar in moment of the IEA15MW before the translation by $\alpha^{2D}_{\text{twist}}$. The polar at 75% of radius is added for comparison. 99
4.6 Flowchart of the equivalent section model development. 100
4.7 Stability map of the equivalent section model using quasi-steady aerodynamics and a linearized modal blade model with the 7 first modes using quasi-steady aerodynamics. The colored areas are unstable. 101
4.8 Stability map of the equivalent section using quasi-steady aerodynamics or the ONERA dynamic stall model. The colored areas are unstable. 103
4.9 Eigenvalues for $\phi_0 = 22°$ with increasing reduced velocity from 0.75m/s to 70m/s ($\mathcal{U}_R$ from 0.1 to 9.26) 104
4.10 Eigenvalues for $\mathcal{U}_R = 5.31$ ($U_0 = 40$m/s) with increasing incidence from 10° to 25° 105
4.11 Evolution of the load coefficient in flapwise direction in function of (a) the effective angle of attack and (b) the flapwise coordinate. The imposed motion is a sinusoid translation along the flapwise direction. The wind speed is 40m/s ($\mathcal{U}_R = 5.3$). . . . 106
4.12 Impact of the dynamic stall loops on the sectional power along the blade for forced flapwise motion at $U_0 = 50m/s$ and $\phi_0 = 19°$ 107
4.13 $\phi_0 - U_0$ map comparing the stability of the sectional model and the FEM blade model. Both models are coupled with the ONERA dynamic stall model using parameters reported in Table 3.1 108
4.14 Comparison of the generalized force between the equivalent section and the blade model for forced flapwise motion at $U_0 = 50m/s$ and $\phi_0 = 19°$ 110
4.15 Comparison of the equilibrium between the equivalent section model and the blade model at $\phi_0 = 17°$. ($\mathcal{U}_R = 9.25$ approximately correspond to $U_0 = 70m/s$) 111
4.16 Comparison of the equivalent section model with a 75% section model; Stability maps using either quasi-steady aerodynamics or the ONERA dynamic stall model. The colored areas are unstable. 112
4.17 Comparison between the stability map of the beam and the equivalent section with and without the torsion. 113
4.18 Effect of the modification of parameter r_{0_l} on the dynamic stall loops and on the stability map. 113

5.1 Close-blade mesh of the IEA15MW blade 116
5.2 Scheme of the background mesh on the XY plan (not at scale). The black dot represents the pitch axis and the circle is the mesh of the blade. $c_{\text{ref}} = 3$ m. 117
5.3 $\phi_0 - U_0$ stability map of the blade model coupled with the ONERA dynamic stall model. 119
5.4 Deformation of the blade for $\phi_0 = 17°$ and $U_0 = 40$m/s; comparison of high-fidelity FEM-CFD results with predictions using aerodynamic strip theory. 120

5.5 Load coefficients on the blade for $\phi_0 = 17°$ and $U_0 = 40$m/s (The forces have been nondimensionalized using the factor $\frac{1}{2}\rho c_{\text{eq}} U_0^2$ and the moments using $\frac{1}{2}\rho c_{\text{eq}}^2 U_0^2$). The shaded area corresponds to airfoils close to cylinder and where the loads are not well captured. 121
5.6 Pressure coefficient and streamlines of friction on the suction side of the blade . . . 122
5.7 Criterion Q equal to 50 colored by the velocity in Z. 122
5.8 Comparison of the load coefficient in the Y axis for different angles of incidence ϕ_0 at $U_0 = 40$m/s. The forces have been nondimensionalized using the factor $\frac{1}{2}\rho c_{\text{eq}} U_0^2$. 123
5.9 Coefficient of pressure on the skin suction side with streamline of friction for several angle of incidence ϕ_0 at $U_0 = 40$m/s 124
5.10 Comparison of the size and amplitude of the stall cells for different angle of incidence ϕ_0 at $U_0 = 40$m/s. The solid lines indicate the mean value. 125
5.11 Comparison of the load coefficients in the Y axis for $U_0 = 40$m/s and 50m/s. The forces have been nondimensionalized using the factor $\frac{1}{2}\rho c_{\text{eq}} U_0^2$. 126
5.12 Coefficient of pressure on the skin suction side with streamline of friction for two wind speed at $\phi_0 = 17°$ 126
5.13 Deformation in torsion due to the wind speed U_0. 127
5.14 Comparison of the size and amplitude of the stall cells for for two wind speeds at $\phi_0 = 17°$. The solid lines indicate the mean value. 127
5.15 Illustration of the 1st flexion mode in flapwise around the aeroelastic equilibrium state (grey solid line) at $U_0 = 40\,\text{m/s}$ and $\phi_0 = 17°$. The dashed line represents the initial configuration of the blade. The blade is projected on the three plans. 129
5.16 Modal coordinate of the imposed motion 129
5.17 Load coefficients on the blade for $\phi_0 = 17°$ and $U_0 = 40$m/s. The solid lines are the mean loads while the dashed lines indicate the minimal and maximal values. The forces have been nondimensionalized using the factor $\frac{1}{2}\rho c_{\text{eq}} U_0^2$ and the moments using $\frac{1}{2}\rho c_{\text{eq}}^2 U_0^2$. Figure 5.5 is reported in grey. 130
5.18 Phase shift between the sectional forces on Y and the flapwise velocity for the $\phi_0 = 17°$ and $U_0 = 40$m/s case. The red areas represents the areas of negative aerodynamic damping. The shape of F_Y is reported in dotted line. 132
5.19 Pressure coefficient on the suction side along with streamline of friction for a wind angle of incidence $\phi_0 = 17°$ at $U_0 = 40$m/s over one period of flapwise oscillation. Some schemes indicate the motion of the blade. 133
5.20 Dynamic stall loops as a function of the effective angle of attack between two stall cells (a) and within a stall cell (b) for a reduced frequency $k = 0.094$. All the loops are clockwise. The static polars in black are explained in the Appendix A. 134
5.21 Amplitude and phase delay (with the flapwise velocity) of the motion-induced pressure for the blade section located at 80% of the span. 134
5.22 Variations of the pressure coefficient around its mean value induced by the imposed motion, for the two sections at 0.80 span (outside a stall cell) and at 0.82 span (within a stall cell). The solid lines are the mean loads while the dashed lines indicate the minimal and maximal values. 136
5.23 Phase shift of the pressure coefficient for the two sections at 0.80 span (outside a stall cell) and at 0.82 span (within a stall cell) span. The phase shift resulting from the integration of the pressure is added for comparison. 136
5.24 Phase shift between the sectional forces on Y and the flapwise velocity for the different wind angle of incidence ϕ_0 at $U_0 = 40$m/s. 137

5.25 Aerodynamic damping and stiffness as well as the aeroelastic pulsation calculated from the forced motion simulations for various angle of incidence at $U_0 = 40\,\mathrm{m/s}$ and reduced frequency $k = 0.094$. 138
5.26 Phase shift between the force in Y and the flapwise velocity, for two wind speeds $U_0 = 40m/s$ and $50m/s$ (i.e. different reduced velocity $\mathcal{U}_R = 5.3$ and 6.61) at $\phi_0 = 17°$. 139
5.27 Aerodynamic damping and stiffness as well as the aeroelastic pulsation calculated from the forced motion simulations for two wind speeds $U_0 = 40m/s$ and $50m/s$ (i.e. two different reduced velocity $\mathcal{U}_R = 5.3$ and 6.61) at $\phi_0 = 17°$. 140
5.28 Evolution of V_{gust} with time 141
5.29 Tip displacements in X (left) and Y (right) as a function of the time; Unsteady aeroelastic simulation for $\phi_0 = 17°$ and $U_0 = 40$m/s. The grey area gives the duration of the gust. 142
5.30 Tip displacements in X (left) and Y (right) as a function of the time; Unsteady aeroelastic simulation for $U_0 = 40$m/s, $\phi_0 = 17°$ and 18°. The grey area gives the duration of the gust. 143
5.31 Damping and frequency over time of the tip position history for two wind angles of incidence ($U_0 = 40$m/s). The dotted lines correspond to the frequencies of the (a) edgewise and (b) flapwise mode. 143
5.32 Damping and frequency towards the Y direction in function of the angle of incidence ϕ_0 at $U_0 = 40$m/s. The dotted lines correspond to the flapwise mode. 144
5.33 Tip displacement history for two wind speeds, $U_0 = 40m/s$ and $50m/s$ (i.e. reduced velocity $\mathcal{U}_R = 5.3$ and 6.61) at $\phi_0 = 17°$. The grey area gives the duration of the gust. 145
5.34 Damping and frequency over time of the tip position history for two wind speeds, $U_0 = 40m/s$ and $50m/s$ at $\phi_0 = 17°$ 146
5.35 Damping and frequency towards the Y direction in function of the wind speed U_0 at $\phi_0 = 17°$. The dotted lines correspond to the flapwise mode. 147

A.1 The IEA Wind 15-MW reference wind turbine [53] 159
A.2 View from the suction side (top) and trailing edge (bottom) of the offshore wind turbine blade [53] 160
A.3 Blade planform spanwise quantities [53] 160
A.4 Blade beam structural properties [53] 161
A.5 DTU FFA-W3 airfoil family used in the IEA Wind 15-MW blade design [53] 161
A.6 Static polars of the FFA-W3-211 (span>0.77) at $Re = 10^7$ for IEA and Bidadi, at $Re = 5 \cdot 10^6$ for FastS2D 162
A.7 Static polars of the FFA-W3-241 (span=0.64) at $Re = 10^7$ for IEA and Bidadi, at $Re = 5 \cdot 10^6$ for FastS2D 162
A.8 Static polars of the FFA-W3-270 (span=0.54) at $Re = 10^7$ for IEA and Bidadi, at $Re = 5 \cdot 10^6$ for FastS2D 163
A.9 Static polars of the FFA-W3-301 (span=0.44) at $Re = 10^7$ for IEA and Bidadi, at $Re = 5 \cdot 10^6$ for FastS2D 163
A.10 Static polars of the FFA-W3-330 (span=0.33) at $Re = 10^7$ for IEA and Bidadi, at $Re = 5 \cdot 10^6$ for FastS2D 163
A.11 Static polars of the FFA-W3-360 (span=0.25) at $Re = 10^7$ for IEA and Bidadi, at $Re = 5 \cdot 10^6$ for FastS2D 164
A.12 Static polars of the FFA-W3-500 (span=0.15) at $Re = 10^7$ for IEA and Bidadi, at $Re = 5 \cdot 10^6$ for FastS2D 164

A.13 Static polars along Y taking into account the 3D flow for three span coordinate. For AEL_moy, a mean over 5% of the blade is used to reduce the impact of the stall cells 165

C.1 Evolution of (a) the aerodynamic damping and (b) stiffness as well as (c) the aeroelastic pulsation during the forced motion simulations for various angle of incidence at $U_0 = 40\,\mathrm{m/s}$ and reduced frequency $k = 0.094$. 171
C.2 Evolution of (a) the aerodynamic damping and (b) stiffness as well as (c) the aeroelastic pulsation during the forced motion simulations for two wind speeds $U_0 = 40m/s$ and $50m/s$ (i.e. two different reduced velocity $\mathcal{U}_R = 5.3$ and 6.61) at $\phi_0 = 17°$. 172

D.1 Force coefficient C_Y and velocity V_Y with time at span=0.80 for the configuration with a wind speed of 40m/s and an angle of incidence of 17°. 173
D.2 Force coefficient $C_Y - \overline{C_Y}$ before and after being filtered with time at span=0.80 for the configuration with a wind speed of 40m/s and an angle of incidence of 17°. . . 174
D.3 Cross correlation of the filtered force coefficient C_Y with the velocity V_Y. 174
R.1 Schéma d'un mode instable issu du flottement 188
R.2 189
R.3 Représentation schématique montrant la direction du vent susceptible de déclencher des instabilités aéroélastiques. L'épaisseur de la flèche donne une idée de la vitesse critique. 192
R.4 Schéma du couplage partitionné 193
R.5 Diagramme UML du framework python 194
R.6 Déformation du maillage de peau 196
R.7 Schéma des coupes. Les repères rouges sont les repères locaux des sections $\mathcal{R}_s$. . . 196
R.8 Schéma de la section équivalente 198
R.9 Cartes de stabilité de la section équivalente et du modèle modal linéarisé de pale (avec les 7 premiers modes) utilisant une aérodynamique quasi-stationnaire. Les zones colorées sont instables. 198
R.10 Évolution des coefficients de forces en fonction de (a) l'angle d'attaque effectif et (b) de la coordonnée *flapwise*. 199
R.11 Carte de stabilité $\phi_0 - U_0$ comparant le modèle de section equivalente et le modèle élément finis. 200
R.12 Coefficient de pression et lignes de friction sur l'extrado de la pale 201
R.13 Iso-surface de critère Q de valeur 50 colorisée par la vitesse selon Z 202
R.14 Déphasage entre les forces sectionnelles selon Y et la vitesse pour le cas $\phi_0 = 17°$ et $U_0 = 40\mathrm{m/s}$. Les zones rouges représentent les zones d'amortissement aérodynamique négatif. F_Y est représentée par une ligne pointillée. 203
R.15 Coefficient de pression à l'extrado et ligne de courant pour un angle d'incidence $\phi_0 = 17°$ et $U_0 = 40\mathrm{m/s}$ sur une période d'oscillation. 203
R.16 Déplacements du bout de pale selon X (à gauche) et selon Y (à droite) en fonction du temps pour $U_0 = 40\mathrm{m/s}$, $\phi_0 = 17°$ et 18°. La zone grise indique la durée de la rafale. 204
R.17 Déplacement du bout de pale pour deux vitesses de vent, $U_0 = 40m/s$ et $50m/s$ (c'est-à-dire une vitesse réduite $\mathcal{U}_R = 5,3$ et 6,61) à $\phi_0 = 17°$. La zone grise indique la durée de la rafale. 205

List of Tables

1.1 Table of the critical velocity for three aeroelastic instabilities 44

3.1 Parameters used in the ONERA model (set for the FFA-W3-241 airfoil) 64
3.2 Parameters used in the ONERA model (set for the NACA 63421 airfoil) 67

4.1 Dimensionless parameters of the 2D section 89
4.2 Parameters of the equivalent section 100

5.1 Repartition of the mesh 117
5.2 Computation cost for one iteration 118
5.3 List of the simulations 119

List of Acronyms and Symbols

Acronyms

ALE	Arbitrary Lagrangian Eulerian
AoA	Angle of attack
AR	Aspect ratio
AV	Arch vortex
BEMT	Blade element momentum theory
BET	Blade element theory
CFD	Computational fluid dynamics
CFL	Courant–Friedrichs–Lewy
CGNS	CFD General Notation System
CPU	central processing unit
CSM	Computational structural mechanics
CSS	Conventional serial staggered
DES	Detached eddy simulation
dofs	Degrees of freedom
DSV	Dynamic stall vortex
FEM	Finite element method
FSI	Fluid-structure interaction
GSS	Generalized serial staggered
IDW	Inverse distance weighting (interpolation)
IEA	International Energy Agency
LCO	Limit cycle oscillations
LCOE	Levelized cost of energy
LES	Large eddy simulation
LEV	Leading edge vortex
LSB	Laminar separation bubble
PIV	Particle image velocimetry
RANS	Reynolds-averaged Navier–Stokes

RBF	Radial basis function
RV	Ring vortex
SC	Stall cell
SIV	Stall induced vibrations
SL	Separation line
TEL	Trailing edge line
TS	Turbulent separation
TSV	Turbulent separation vortex
TV	Tip vortex
UML	Unified modeling language
URANS	Unsteady Reynolds-averaged Navier–Stokes
VIV	Vortex induced vibrations
VL	Vortex legs
ZDES	Zonal detached eddy simulation

Symbols

α_{edgewise}	Angle of the springs
α_{eff}	Effective angle of attack
α_{eff}^{2D}	Effective angle of attack of the section
α_0	Angle of attack of reference
L_{blade}	Blade length
$\mathbf{R}$	Rotation matrix
$\boldsymbol{\phi}$	Structural mode
c	Chord
c_{eq}	Equivalent chord
C_D	Drag coefficient
C_L	Lift coefficient
C_M	Moment coefficient
d_x	Damping of the edgewise mode
d_y	Damping of the flapwise mode
x	Degree of freedom in the edgewise direction

y	Degree of freedom in the flapwise direction
α_{torsion}	Degree of freedom in torsion
ρ	Density
d_G	Distance between the elastic center and the mass center
e	Distance between the aerodynamic center and the elastic center
D	Drag
q	Dynamic pressure
x_{ce}	Position of the elastic center
t	Global time
b	Half chord
ϕ	Effective incidence
ϕ_0	Incidence of the wind
L	Lift
m	Mass
m_{eq}	Equivalent mass
$\mathcal{M}$	Mass ratio
$\mathcal{M}_\alpha$	Torsional mass ratio
S_α	Mass unbalance
I	Moment of inertia
M	Moment
α	Pitch
y	Plunge
p	Pressure
ω	Pulsation
$\mathcal{U}_R$	Reduced velocity
$\mathbf{R}$	Resolvant
k_x	Edgewise stiffness
k_y	Flapwise stiffness
k_α	Stiffness in pitch
k_y	Stiffness in plunge

$k_{\alpha x}$	Coupled stiffness between the torsion and the edgewise flexion
$k_{\alpha y}$	Coupled stiffness between the torsion and the flapwise flexion
$k_{\alpha_{\text{torsion}}}$	Torsional stiffness
$\alpha_{\text{twist}}^{2D}$	Twist angle of the section
U_{eff}	Effective airspeed
$U_{\text{eff}_{\text{2D}}}$	Effective airspeed of the section
U_0	Wind speed

Introduction

To face climate change, it is necessary to transition from fossil fuels to less carbonated sources of energy. With solar energy, wind energy is a promising substitute to help us reduce our carbon emissions. In its report "Futurs énergétiques 2050" [118], the France electricity transmission system operator (RTE) produces scenarios allowing France to become carbon neutral in 2050. Each scenario is based on a drastic reduction in fossil fuels compensated in part by the increase of renewable energy including onshore and offshore wind energy. For example, in scenarios which do not rely on nuclear energy but only on renewable energies, the installed power of onshore wind turbines needs to pass from 18GW to 74GW in 2050, representing a multiplication by 4. Moreover, 60GW of offshore wind turbines need to be installed. To meet this growing demand, technological improvements are required to continue decreasing the cost of wind energy.

History of wind energy

Wind power has been used since the navigation of sailing vessels. It was then harvested with windmills centuries ago to grind grain and pump water. It is only in the early 20th that wind power has been applied to electricity production with the birth of aerodynamic science [137]. Since then, the production of wind energy has continuously grown (Figure 1). Today, wind energy constitutes 8% of the total electricity production in the world in 2024 [100]. The majority of wind-generated electricity takes place in China and USA. The cost of wind energy has also decreased significantly since the 1970s. Currently, the levelized cost of energy (LCOE) of land-based wind energy is about 40$/MWh while the LCOE of offshore wind energy is around 112$/MWh [130].

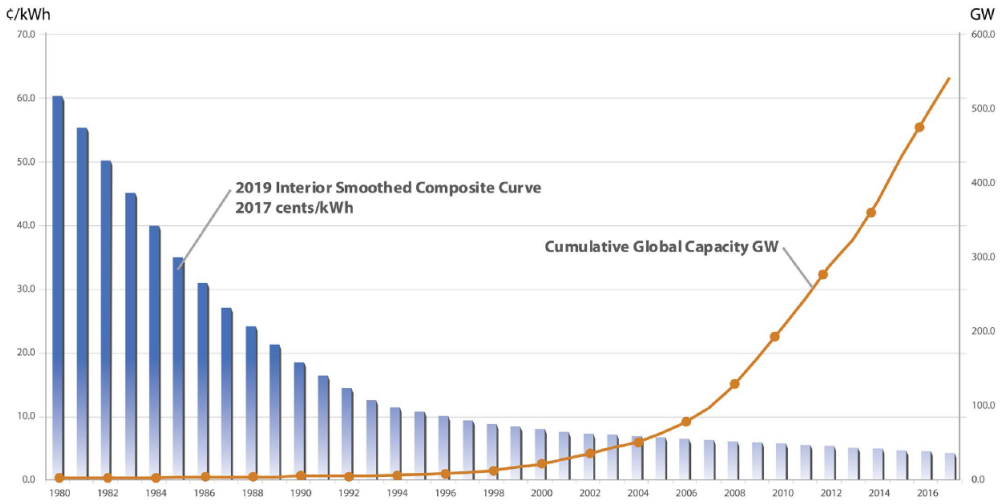

Figure 1: Global cumulative installed capacity (in gigawatts) for wind energy and estimated LCOE for the U.S. interior region in cents per kilowatt-hour from 1980 to 2017 [137]

This reduction in cost is due to three fundamental drivers: increased hub height, rotor diameter and power rating [137]. These improvements can be explained by the formula of the wind turbine power:

$$P = \frac{1}{2}\rho C_p A U_0^3 \tag{1}$$

where P is the instantaneous power produced, ρ is the air density, C_p is the power coefficient, A is the swept area of the rotor and U_0 is the wind speed.

Due to the atmospheric boundary layer, the wind speed increases with height. Thus, placing the rotor at a higher position allows us to obtain a higher free-stream velocity U_0. Even a slight augmentation of the wind speed passing through the rotor can have a great effect due to the cubic exponent. The second driver is to increase the swept area A by using longer blades. The power rises proportionally to the square of the blade length. The last improvement is the use of variable rotor speed to operate at maximum C_p for a wide range of conditions. Together, it leads to wind turbines with higher power rating. Less machines are necessary to get the same amount of energy [137]. In reality, these fundamental drivers imply a lot of technological innovations. For example, a current blade is compared to a 1980s blade in Figure 2. Increasing the length of the blade has been made possible by the introduction of composite materials, which have made the blade lighter. The modern ones are 90% lighter than a 1980s blade scaled at the same length. Higher tip speeds and high-lift airfoils have also led to better efficiency.

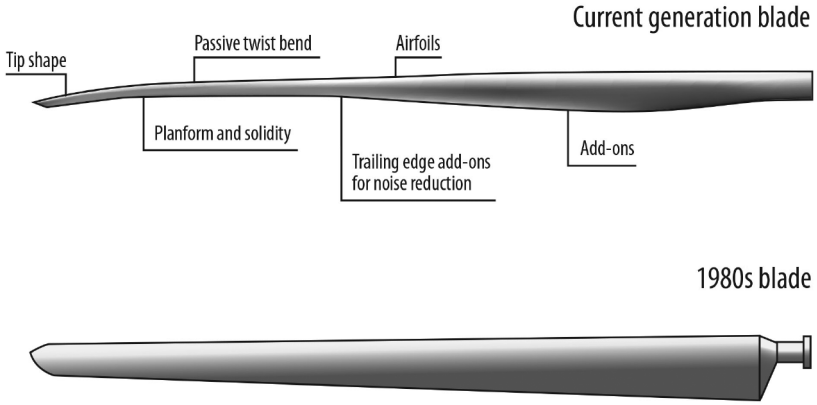

Figure 2: Wind turbine blade innovation comparing a modern commercial blade (top) and a commercial blade from the mid-1980s (bottom) scaled to the same length [137]

Challenges in the sciences of wind energy

In order to further improve wind turbine technology, research needs to fill several understanding gaps. The topic areas concerned are: Inflow and design criteria, Control and co-design, Aerodynamics and aeroelasticity, Wakes, Offshore wind technology, Manufacturing and materials, and High-fidelity modeling. They are summarized in Figure 3. For the sake of brevity, only a few areas are presented here, the reader is invited to read the article of Veers et al. [138] for additional information.

The size of offshore wind turbines is becoming so large that the machines extend beyond the atmospheric surface layer (i.e. the closest layer to the ground where the turbulence is produced), that constitutes about 10% of the total atmospheric boundary layer height. The inflow conditions are therefore very different from those experienced by smaller wind turbines. Moreover, the turbulence within the atmospheric surface layer is not fully understood yet. The inflow turbulence model imposed during the design phase is then simplified in order to envelop the worst conditions, which involves conservatism. After that, within large power plants, each turbine generates a wake that can affect the downwind turbines. The wakes generation, evolution and coupling with the atmospheric boundary layer are complex processes that make the wakes modeling difficult. It

also depends on the inflow and topography. Better wake models are needed to design efficient wind farms. Concerning materials, future requirements lie in recyclability. Recyclable alternative materials including thermoplastics and more exotic resin formulations that still meet structural constraints are needed. Progress in inspection and structural health monitoring is also required for better program maintenance.

Due to increasingly flexible blades, many of the design assumptions can also be questioned. Softer blades bring the new designs closer to the stability limits dictated by aeroelastic phenomena. Passing these boundaries can generate a high level of vibrations, decreasing the life time of the turbines or even leading to failures. That's why, the tower and blades flexibility are now being a part of design constraints. However, complex phenomena triggered by flow separation can not be described by low and mid fidelity models [138]. More knowledge about the aeroelastic behavior of wind turbines is thus needed to go beyond these constraints. The present thesis positions within this field of research.

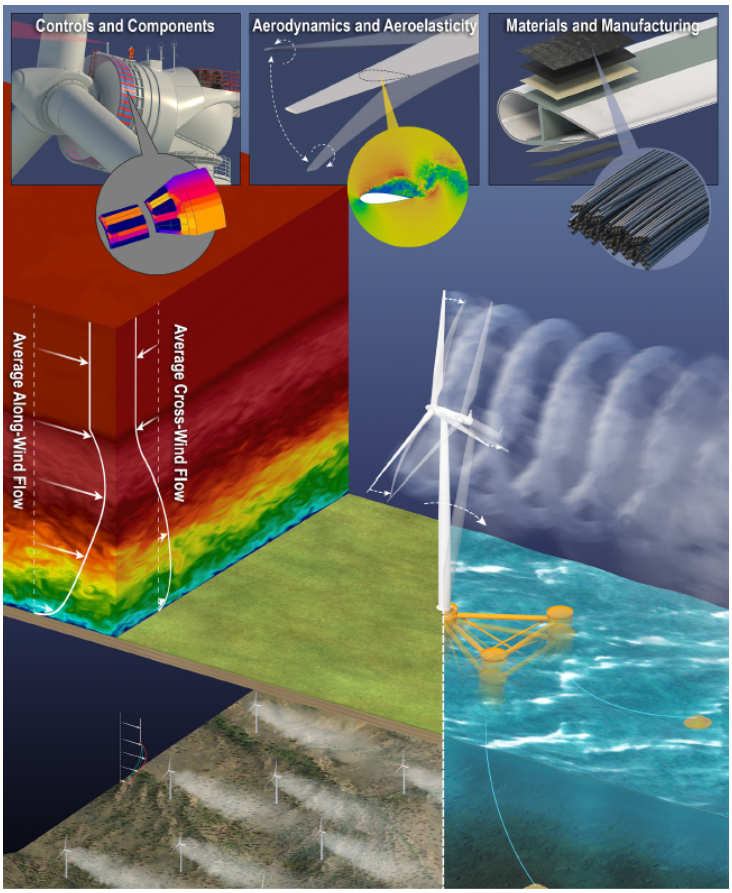

Figure 3: Scheme of the grand challenges in the sciences of wind energy. (Image credit: Besiki Kazaishvili, National Renewable Energy Laboratory – NREL.) [138]

Focus on aeroelasticity

Aeroelastic phenomena are defined by the interaction between the deformation of the structure and the fluid flow. When the structure moves, it modifies the fluid flow. Thus, the aerodynamic forces applied to the structure change and impact the structure motion. Dynamic instabilities may happen when this coupling produces a transfer of energy from the flow to the structure. As raised by Hansen [64] and Veers et al. [138], one of the most risky and problematic conditions for industry,

is when wind turbines are at standstill with a strong wind that can come from any direction. Such conditions can arise during the installation of the wind turbines, during maintenance or in the event of a failure of the control system when the rotors are stopped in strong wind conditions. The aerodynamic angles of attack can then be far away from normal operation, putting the blade in a stall state. These cases of parked position are the subject of Design Load Cases (DLC) 6 of the certification IEC 61400-1. In this DLC, the ultimate load analysis is based on site specific 50 year return wind speed. Pryor and Barthelmie [112] have estimated the 50 year return wind speed over the world. For example with typhoon conditions, the reference wind speed used for the DLC is fixed at 57 m/s.

In this standstill configuration, several aeroelastic mechanisms may theoretically affect a wind turbine blade, see Figure 4.

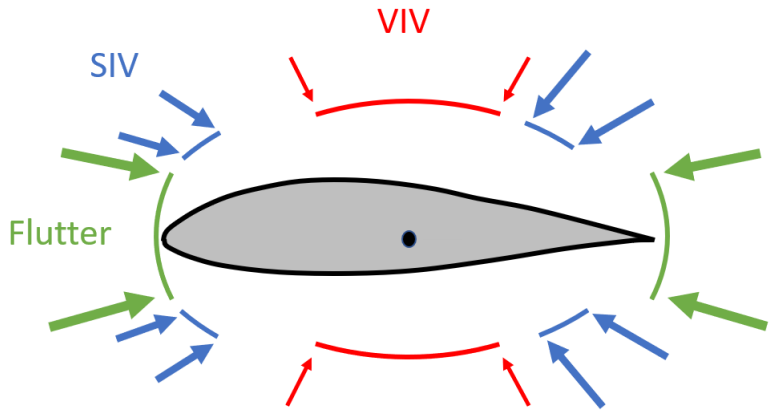

Figure 4: Schematic representation showing the wind direction likely to trigger aeroelastic instabilities. The range of direction depends on the airfoil. The size of the arrow gives an idea of the critical velocity. Small arrow means low critical velocity.

Vortex-Induced Vibrations (VIV) can occur when the wind flow past the blades creates vortices that shed and periodically interact with the blades [18]. Karman vortex wake generates an oscillatory force transverse to the mean flow direction. It thus mainly concerns high angle of attack wind direction (close to 90°) and velocities for which the vortex shedding frequency is close to the first edgewise mode of the blade. As a consequence of a non-linear coupling between the vortex-induced fluid force and the blade's motion, vibration of significant self-limited amplitude can be observed in a range of velocity where the wake frequency is controlled by the motion, a phenomenon referred to as lock-in. For lightweigh and low damped blade, VIV can cause increased stresses on the blades, leading to fatigue damage. Horcas et al. [71] investigated the vortex induced vibrations on an isolated blade of the IEA10MW using a high fidelity software coupling the Computational Fluid Dynamics (CFD) solver *EllipSys3D* with a Timoshenko beam of the solver *HAWC2*. They have simulated the aeroelastic response of the blade for many pitch and inclination angles. They have found two areas where VIV can arise. Putting the blade in these conditions, they described in detail the flow behavior, the effect of elasticity on the vortex shedding as well as the induced edgewise vibrations. However, the evolution of the VIV with wind speed is not investigated. And it could be interesting to see how the VIV evolves with a blade of a 15MW wind turbine.

Another phenomenon is coupled mode flutter. When the flow is attached, two or more structural modes can couple through the fluid and lead to an unstable aeroelastic mode. Boersma et al. [19] conducted a wind tunnel experiment on a 5MW wind turbine blade scale model and found, after normalization, a flutter speed of 230m/s. It is higher than the tip speed in operation and far

above the wind speed experienced by a wind turbine in a standstill position.

The last one is Stall Induced Vibrations (SIV). When the wind angle of attack is close or beyond the static stall region a dynamic stall process can occur. The flow around the blade then separates and reattaches partially or completely during each cycle of oscillation, generating non-linear dynamic loops in lift and drag [79]. This unsteady aerodynamic loading can be responsible for a positive energy transfer from the flow to the structure leading to vibrations and potentially damaging loads on the turbine. In this context, several studies have examined these instabilities on wind turbines. Wang et al. [141] simulated a full 10MW wind turbine in slow idling operation with yaw. The model was constituted of aeroelastic beam elements coupled with the ONERA dynamic stall model. It allowed to perform temporal simulations and eigenvalue analysis on the coupled system. Strong edgewise vibrations observed in the temporal simulations were supported by the eigenvalue analysis where edgewise modes were unstable over all azimuth angles. Flapwise modes were also unstable but only for a limited range of azimuth angles around 0°. However, simulations based on dynamic stall model are not capable of capturing the 3D behavior of the flow that may be important in the onset of the instability. Skrzypiński et al. [127] examined the possibility of SIV and VIV on an extruded airfoil using Unsteady Reynolds-Averaged Navier–Stokes Simulations (URANS). The airfoil was placed in an uniform flow at 24° angle of attack, which corresponds to the most unstable angle, regarding SIV, given by a pseudo-static analysis. The airfoil was forced to oscillate back and forth along the chord direction. It appears that when the frequency of oscillations is close to the frequency of the vortex shedding, the power of the aerodynamic loads is positive, indicating possible VIV. By decreasing the oscillating frequency, the power first drops and then becomes positive once again, indicating possible SIV. The cut-in wind speed necessary to trigger SIV was however very high for this setup. Moreover, it was only extruded airfoil simulations with imposed harmonic motions and further investigations may be necessary.

To summarize, the aeroelastic studies on wind turbines at standstill can be categorized using three criteria : the instability under study (VIV, flutter or/and SIV), the complexity of the structural model (section, blade or rotor) and the level of fidelity of the flow modelling (dynamic stall model, 2D CFD or 3D CFD). Vortex-induced vibrations on a blade and rotor have already been under focus with high-fidelity CFD/CSM coupling (CSM : Computational structural mechanics). Coupled mode flutter at standstill concerns wind speeds far above realistic conditions. Stall-induced vibrations have been investigated on full wind turbines with dynamic stall models and using section model approach coupled with URANS flow solvers. However, the literature lacks of studies focusing on blade's stall-induced vibrations using high fidelity coupling between a CFD model and a continuous beam model.

Objective of the thesis

The objective of this thesis is thus to implement and use a high-fidelity coupled CFD/CSM approach in order to investigate stall-induced vibrations on a large 15MW wind turbine blade at standstill. To this end, analysis with simplified approaches will be performed and confronted to the high-fidelity approach in order to understand the most important features of the SIV.

This work has been carried out between the ONERA (40%), the IFP Energies Nouvelles (40%) and the CNAM (20%).

Organization of the manuscript

In a **1st chapter**, a literature review about the aeroelastic instabilities that may arise on wind turbines is given. The emphasis is put on three main instabilities: coupled-mode flutter, vortex induced vibrations (VIV) and stall induced vibrations (SIV). It has permitted to identify the lack of studies focusing on blade's stall induced vibrations using high fidelity coupling and defined the objectives of the thesis. As the fluid-structure energy transfer in SIV strongly depends on the dynamic stall process, a large part of the review is also devoted to the static and dynamic stall of airfoils. 3D static stall signature, that could affect blade SIV is also reported. The review ends with a presentation of previous studies about SIV on wind turbines.

Chapter 2 introduces the methods necessary to conduct high-fidelity aeroelastic simulations. The CFD solver *FastS* and the structural solver *Project Chrono* used in this thesis are presented with their numerical methods. The software *Quantum* used to deform the fluid mesh is also introduced. Then, a small review on existing numerical methods to couple a fluid solver with a structural solver is provided. It is composed of transfer methods to pass the motion of the structure from the solid solver to the fluid mesh and transfer methods to extract the loads acting on the structure from the CFD solver. Finally, the temporal coupling methods to conduct dynamic simulations are presented.

The aim of **Chapter 3** is to detail the transfer methods that have been built in the present work in a modular Python framework that allows to switch easily between several levels of fluid-structure solver, from sectional model, using either a quasi-steady or nonlinear unsteady aerodynamic formulation, to high fidelity CFD/CSM. Each step of the aeroelastic partitioned coupling is also validated.

Using this modular framework, the stall induced vibrations of the IEA15MW blade, presented in Appendix A, are investigated with increasing fidelity methods. Low-fidelity methods are quick and easier to analyze and understand, it allows to explore a wide range of conditions and test the effect of many aspects of the system. Whereas higher fidelity methods provide more details in the physical behavior, but, being more costly less cases can be explored. **Chapter 4** presents an equivalent 2-dof (flapwise and edgewise) section model of the IEA15MW full blade, highlighting the identification procedure of the equivalent mass, stiffness, mean angle of attack, chord and polar. The effect of the ONERA dynamic stall model on the aeroelastic behavior is investigated by comparing it to a quasi-steady aerodynamic formulation. The equivalent section model is also compared to a continuous approach for which the blade, modeled by a finite element model using corotated Euler-Bernoulli beam elements, is coupled, under the strip theory assumption, to the ONERA dynamic stall model. A discussion regarding the strengths and weaknesses of both those low-fidelity approaches is also provided. Moreover, this study is used to choose the conditions of the few high-fidelity simulations that have been performed.

In **Chapter 5**, the benefit of using a high-fidelity CFD solver, here an URANS model, for aeroelastic studies of a wind turbine blade in stall regime, is highlighted. The present investigation is progressive. First, the focus is on the aeroelastic static equilibrium. Stall cells have been observed and described in detail. Then, the blade is forced to oscillate in its first flapwise mode, around equilibrium states, at different reduced velocities for which this mode is supposed to be stable or unstable according to low-fidelity results reported in Chapter 4. Emphasis has been put on the identification of the phase delay in the motion induced aerodynamic loading that mainly impacts the dynamic stability. Finally, few aeroelastic responses to an imposed gust have been computed and discussed using the high-fidelity *FastS-Chrono* framework. It allows a first estimation on the effect of the wind conditions (direction and speed) with a better computation of the 3D unsteady flow behavior.

A chapter **conclusion and perspectives** summarizes the work and major results and provides recommendations for further studies.

Chapter 1

Aeroelastic phenomenon on wind turbines at standstill

This chapter constitutes a state of the art on dynamic aeroelastic instabilities that may affect a wind turbine blade at standstill. This review focuses on three main aeroelastic phenomena that must be studied for the certification of wind turbines, namely coupled mode flutter, vortex induced vibrations (VIV) and stall-induced vibrations (SIV). The IEC 61400-1 certification contains design load cases (DLC) for wind turbine in parked position. The DLC 6.1 consists a verification of the ultimate loads under a wind of 50 year return period associated with a yaw misalignment of up to 15°. In addition to the present literature review, complementary information can be found in the reviews of Hansen [64] and Holierhoek [69], in particular concerning aeroelastic mechanisms that could affect wind turbines in operation.

Contents

1.1 Coupled mode flutter 10
1.1.1 Methods to evaluate the coupled mode flutter speed 10
1.1.2 Coupled mode flutter on wind turbine blade 11
1.1.3 Summary 13
1.2 Vortex induced vibrations 13
1.2.1 Vortex induced vibrations past a circular cylinder 13
1.2.2 Vortex induced vibrations past 2D airfoils 15
1.2.3 Vortex induced vibrations past wind turbine blades 17
1.2.4 Summary 20
1.3 Stall-induced vibrations 20
1.3.1 Static stall 21
1.3.2 Dynamic stall 23
1.3.2.1 Dynamic stall process in 2D 24
1.3.2.2 Dynamic stall models 29
1.3.3 3D Stall 33
1.3.3.1 3D Static stall : the stall cells 33
1.3.3.2 Dynamic stall on finite wings 35
1.3.4 Aeroelastic studies on SIV 37
1.3.4.1 Stall flutter 37
1.3.4.2 Flapwise/Edgewise instability 39
1.4 Conclusion 43

1.1 Coupled mode flutter

Coupled mode flutter is a severe aeroelastic instability that can cause structural rupture. It is characterized by the coupling of two or more structural modes through the flow. It was first observed on aircraft wings during the first world war and mainly concerns bending-torsion coupling. As its onset does not rely on any flow separation, it can be observed on wing or blade at low angle of attack. Theory of flutter based upon linear unsteady aerodynamic formulations has been successfully developed to predict the critical conditions for the generic case of a two degrees of freedom "pitch–plunge" oscillating wing (Sears and Sparks [121], Theodorsen [134]). For example, there is no risk of flutter if the center of mass is upstream of the elastic center, but for the IEA15MW, the center of mass is downstream of the elastic center. Since those early works the physical explanation of bending-torsion flutter has also been highlighted (see for example Bisplinghoff and Ashley [17], Fung [52]). It is now well understood that a combined aeroelastic mode (combining phase shifted bending and torsion) can transfer energy from the flow to the structure. An illustration is proposed in Figure 1.1. Most of the time, the pitch angle directs the lift force in the same direction as the velocity, making the power from the fluid to the structure positive.

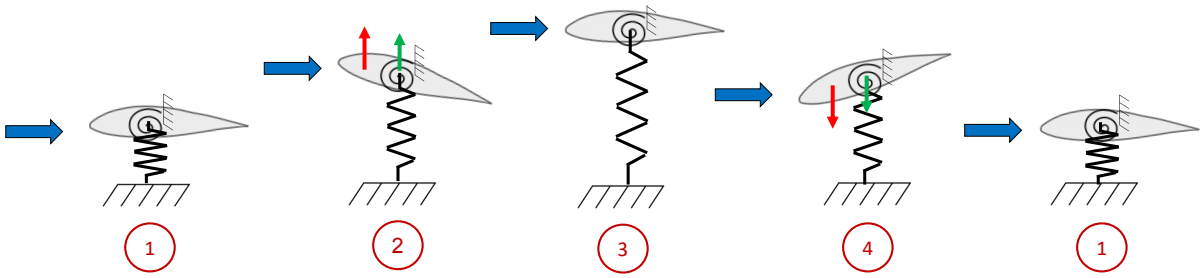

Figure 1.1: Scheme of the unstable mode

1.1.1 Methods to evaluate the coupled mode flutter speed

For more complex geometry, like wings, airplanes or wind turbines, the section model is not enough. To evaluate the critical speed of the coupled mode flutter, Antimirova et al. [6] have presented a large panel of methods, which are reported in Figure 1.2.

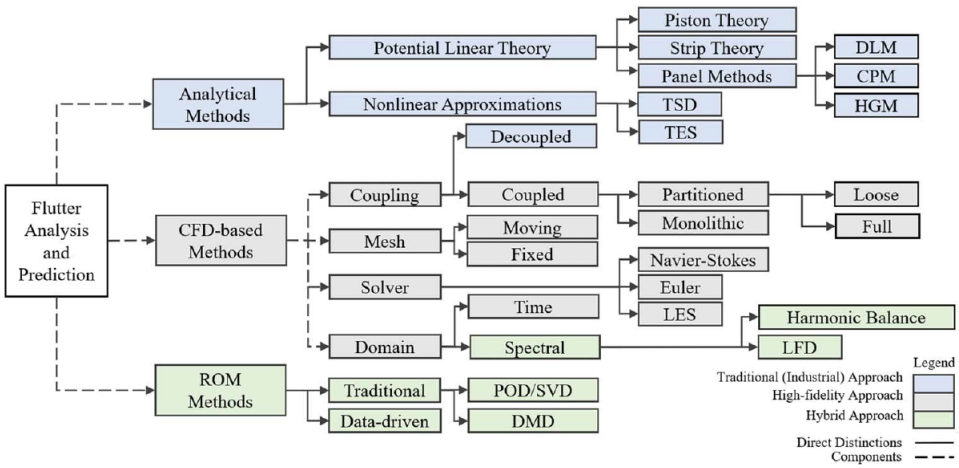

Figure 1.2: Different technical frameworks for flutter analysis and prediction: analytical methods, CFD-based methods, and ROM-based methods. [6]

Traditional methods based on potential linear theory are widely used in industry for their computational speed. They can describe efficiently and accurately coupled mode flutter for a large panel of flight conditions, especially in subsonic conditions. For a wind turbine, this methods are adapted. The CFD-based methods are costly and only used to investigate flutter when additional more complex phenomena are at stake. For example, it can be flow separation, compressibility effect in transonic or multi-bodies configurations. The Reduced Order Model (ROM) based methods aim at keeping some level of accuracy of the CFD while being computationally efficient by describing the main behavior of the full system through a finite number of modes. It is an ongoing research field.

1.1.2 Coupled mode flutter on wind turbine blade

In this section, numerical and experimental studies focusing on blades or even full wind turbines are presented to evaluate the risk of coupled-mode flutter. In operation, the flow is attached and as the blade rotates, the wind speed experienced by the blade is higher. These conditions suggest that the risk of coupled-mode flutter is higher in operation. That's why, most of the studies deal with wind turbine in operation. Nevertheless, the question of the risk of coupled mode flutter in our case of standstill condition can be raised.

To evaluate the flutter of a MW-sized blade in operation, Lobitz [86] used the finite element software NASTRAN with CBEAM elements coupled with the unsteady aerodynamic Theodorsen's model. Compared to steady aerodynamics, Theodorsen's model takes into account the relative speed induced by the displacement of the airfoil as well as the time delay between the movements and the aerodynamic loads. However, the movements have to be small and the flow has to be attached. Lobitz [86] found a flutter speed of approximately twice the operational speed. Pourazarm et al. [111] realized a parametric study of coupled-mode flutter for MW-size wind turbine blades to investigate the impact of natural frequencies and the mass offset. They also used the model of Theodorsen for the aerodynamic part but they proceeded with a modal analysis using the Galerkin method for the structural part. They concluded that if the flapwise natural frequency and the torsional natural frequency are getting closer due to design constraints, the flutter speed will decrease. It can be noticed that the reduction of the torsion frequency has much impact in comparison to the increase of the flapwise frequency. The ratio between these two natural frequencies is a major design parameter. Moreover, a proportional reduction of the flapwise and torsion frequency also leads to a lower flutter speed. Griffith and Chetan [58] compared the flutter characteristics of a series of four 100m blades of decreasing mass (SNL-100-0i). It was observed that as the mass is reduced, the flutter speed decreases due to the reduction in stiffness associated with the mass reduction. Moreover, they noted a major edgewise contribution in the flutter mode as the mass is reduced. This trend needs to be under concern because the edgewise aerodynamic damping is low. All these studies in operation suggest that even in operation the risk of coupled mode flutter is limited as it is above the operation speed.

However, it may be rushed to conclude that the risk of coupled mode flutter at standstill is low because it does not occur in operation. The air velocity is lower but the flow is very different between a standstill blade and a rotating one. Boersma et al. [19] conducted experiments on a standstill 30:1 scale NREL 5MW wind turbine blade placed in a wind tunnel. The experimental setup is shown in Figure 1.3. Some accelerometers and cameras allow them to track the frequency of the flapwise and torsional vibrations. As the wind speed increases, the first flapwise mode is excited by the turbulence. Then, it is the second flapwise mode. At a critical wind speed, the first torsional mode and the second flapwise mode coalesce (Figure 1.4) and a coupled-mode flutter occurs. This dimensionless wind speed corresponds to a wind speed of around 230 m/s for the

real size blade. It is well above the wind speed that will encounter a wind turbine in a standstill position.

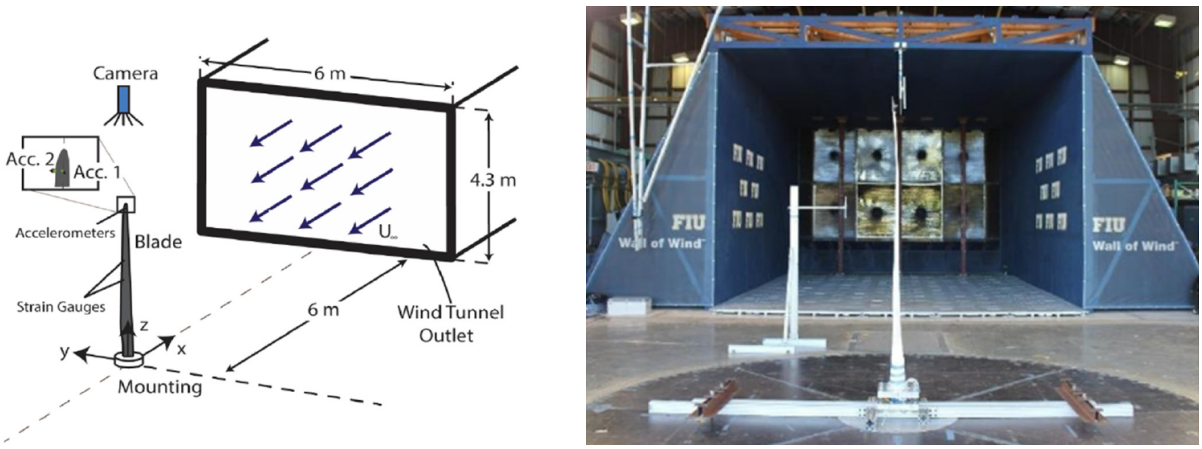

Figure 1.3: Experimental setup [19]

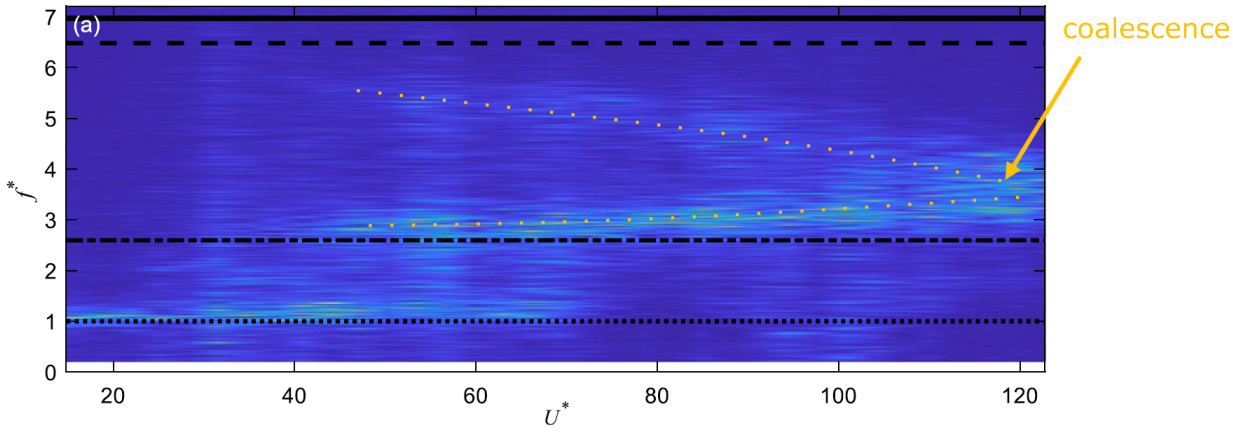

Figure 1.4: Dimensionless spectral map of the response versus the dimensionless wind speed based on the accelerometer data [19]. The horizontal lines correspond to the first three flapwise natural frequencies, and the first torsional natural frequency (the continuous line).

Effect of the up-scalling The flutter speed of the 5MW wind turbine blade of Boersma et al. [19] is very high and no wind can reach a speed of 230m/s. However, wind turbine blades are becoming larger and more flexible, the evolution of the flutter speed with the size of the blades needs to be investigated. In operation, the increase of size does not appear to directly impact the flutter margin. Kelley and Paquette [74] observed that the flutter speed decreases with increasing blade length, but the rated rotor speed also reduces at the same pace. As a consequence, the flutter margin remains unchanged. However, at standstill, the evolution of design, which makes the blade lighter and more flexible, reduces and brings closer the flapwise natural frequency and the torsional natural frequency. As a consequence, the flutter velocity decreases. Quantifying this decrease of flutter speed for large wind turbine blade is necessary but as the flow is attached at standstill, low and mid fidelity methods are appropriate and high-fidelity is not required.

1.1.3 Summary

Even if the wind turbines are becoming larger, it is probable that the critical flutter speed at standstill stays very high. Moreover, the methods to estimate the flutter speed in this subsonic condition are well known. Therefore, we chose not to investigate the coupled mode flutter at standstill with high-fidelity and focus on another aeroelastic phenomena.

1.2 Vortex induced vibrations

The present section deals with Vortex induced vibrations (VIV). It is an aeroelastic instability that affects bluff bodies that has first been studied by civil engineers for chimneys. As a bluff body, the tower is prone to VIV, but at very high angles of attack, the blades also act as bluff bodies that can experience VIV. This instability is triggered by the establishment of vortex shedding that generate periodic forces on the structure. If the frequency of the loads is close to a natural frequency of the structure, the flow can couple with the structure through a lock-in process that produces self-limited vibrations. An illustration of VIV is given in Figure 1.5.

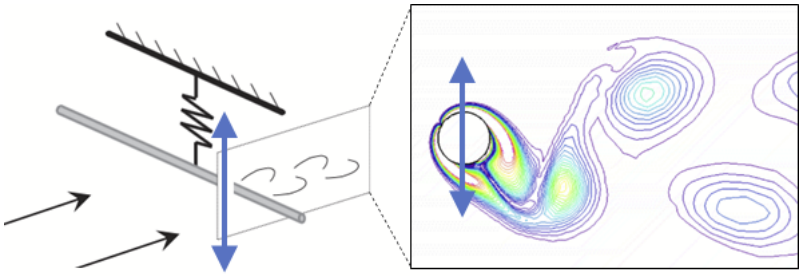

Figure 1.5: Vortex shedding during large amplitude VIV [1]

VIV is a complex phenomenon that is progressively explained in the following sections. First, the widely studied case of a circular cylinder is presented in order to introduce the main concepts of VIV. Then, the effect of the geometry is highlighted by replacing the circular cylinder by airfoils, wind turbine blades and a full rotor.

1.2.1 Vortex induced vibrations past a circular cylinder

Before describing the interaction between vortex shedding and an elastic cylinder, the conditions of appearance of the Von Kármán vortex street and its frequency need to be appreciate.

Kármán vortex street

Vortex shedding appears as an instability of the stationary flow around a bluff-body, that leads to an oscillatory regime where vortices are shed alternately from each side of the body. This phenomenon has been extensively studied especially in the case of circular cylinders (see the different regimes in Figure 1.6). The appearance of the vortex shedding depends on the Reynolds number. When the Reynolds is less than 5, the flow stays attached on all the cylinder. By increasing Reynolds, a pair of fixed vortices appears. And for a Reynolds between 40 and 150, a laminar vortex street takes place. By further increasing Reynolds, the vortex street becomes turbulent until $Re = 3 \cdot 10^5$ where it disorganized for a narrow range of Reynolds. For Reynolds greater than $3.5 \cdot 10^5$, a turbulent vortex street can be observed.

The Reynolds number experienced by a wind turbine blade can be estimated from its chord and the wind speed, $Re = \frac{cU_0}{\nu}$. The chord of the IEA15MW varies around 3m. Taking a wind speed of 20m/s, the Reynolds number is about $4 \cdot 10^6$. Thus, wind turbine blades are more likely to encounter a turbulent vortex street.

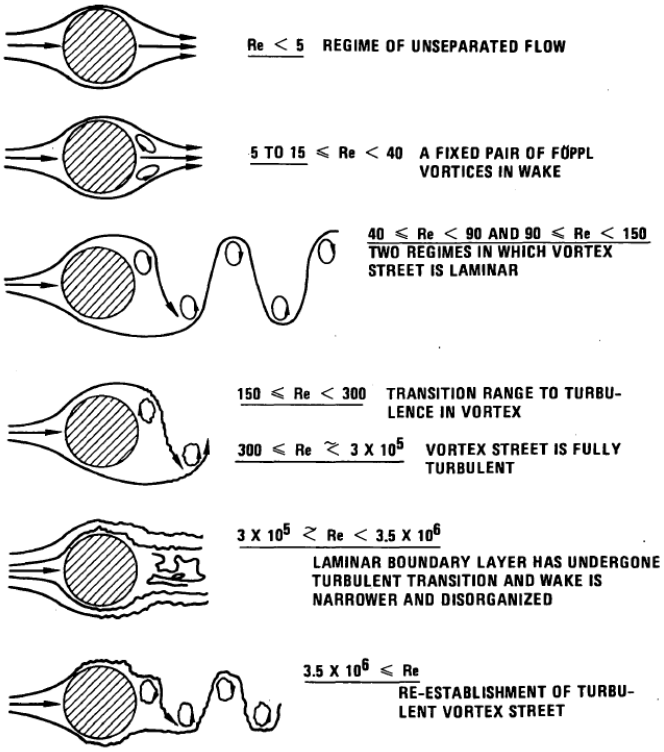

Figure 1.6: Regimes of fluid flow across smooth circular cylinder [18]

It has been observed experimentally that, for a given shape and Reynolds number, the dimensionless frequency of the vortex shedding is constant. This useful dimensionless number has been named the Strouhal number:

$$St = \frac{Df_s}{U_0}$$

where U_0 is the flow velocity and D a characteristic distance. The Strouhal number of various shapes at many Reynolds numbers has been documented when the bluff body is aligned with the wind. The Strouhal number of airfoils will be presented in a next section.

Elastically mounted body

This vortex shedding induces instationary forces on the body. If the body is elastic, the vortex emissions and the oscillations of the structure can interact. Figure 1.7 shows the evolution of the frequency of vortex shedding f_s (up) and the amplitude of the movement of the cylinder A_y (down) with the fluid velocity. At first glance, this phenomenon looks like resonance but there is more. When the frequency of the vortex-shedding is close to a modal frequency of the structure, the frequency of the vortex emission synchronizes with the structural frequency. This phenomenon is referred to as lock-in. The amplitude of oscillation is high during lock-in and low outside.

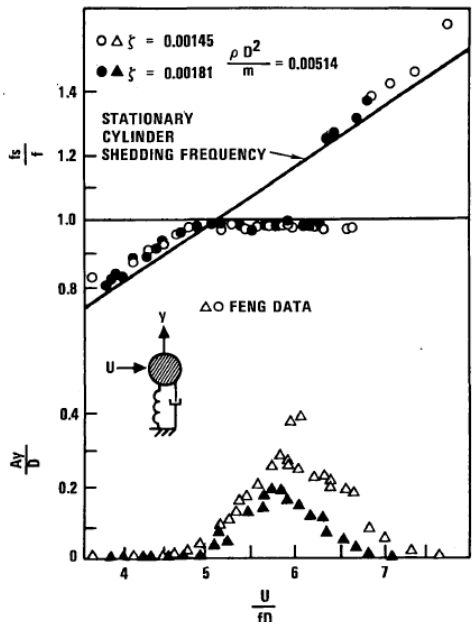

Figure 1.7: Vortex-induced vibrations of a spring supported damped circular cylinder [18]

Both the amplitude of oscillation and range of VIV lock-in strongly depend on the mass ratio μ (defined as the structure to fluid mass ratio) and damping factor ζ. A combined parameter, the Scruton number $S_c \propto \zeta\mu$, is generally used to quantify the mass-damping ratio of structure. Low Scruton generates strong VIV.

Vortex induced vibrations can be modeled with analytical models like the one of De Langre [35] using a Von Der Poll oscillator coupled to the dynamic equation of the structure.

1.2.2 Vortex induced vibrations past 2D airfoils

This section focuses on the effect of the modification of the geometry from a cylinder to an airfoil on the VIV.

Kármán vortex street past 2D airfoils

Some studies have been conducted on wind turbine airfoil sections at high Reynolds numbers ($Re = 1e6$). Pellegrino and Meskell [103] detailed the variation of the Strouhal number of the NREL S809 airfoil with the angle of attack. The results are obtained with CFD simulations of a fixed wing. The minimum St is about 0.13 at 90° of incidence and it increases when the angle of attack is getting away from 90°, it reaches around 0.19 at 50° and 130°. For the same Reynolds number, the Strouhal of a cylinder is between 0.2 and 0.4 depending on the surface roughness [18]. This means that an airfoil shape induces vortex shedding at a frequency lower than that of a cylinder. The mean and fluctuations of the aerodynamic coefficients of vortex shedding for a wide range of angle of attack has also been explored by Pellegrino and Meskell [103]. The maximum of the first harmonic of the lift has been obtained for an angle of attack of 130°. At such high angles of attack, the wake shape of the blade section is similar to that of a cylinder.

Elastically mounted airfoils

A vortex street can form in the wake of an airfoil for a range of angle of attack around 90°. To identify the level of vibrations induced by the VIV as well as the range of reduced velocity and angles of attack of the lock-in, studies on airfoil mounted on springs have been conducted numerically and experimentally. Skrzypiński et al. [125] have mounted the DU96-W-180 airfoil on springs and studied the VIV a 90° angle of attack. A range of dimensionless structural periods for potential lock-in has been identified by varying the wind velocity and looking at the amplitude of the oscillations. VIV occurred for reduced velocity $\mathcal{U}_R = \frac{U_0}{fc}$ around 6 and 9, where U_0 is the wind speed, c is the chord and f is the frequency of the structure. The maximum observed amplitude at 90° was 0.9 chord at a reduced velocity of 7.7, which corresponds to the inverse of the Strouhal numbers ($St = 0.13$) obtained by Pellegrino and Meskell [103]. By definition, $\mathcal{U}_R = 1/St$ means that the vortex shedding frequency matches the natural frequency of the structure. The study of Skrzypiński et al. [125] did not explore other angles of attack but experiments of VIV on airfoils among a range of angles of attack have been conducted by Benner et al. [12]. Using a water tunnel at $600 < Re < 13300$ which corresponds to a reduced velocity range of $0.6 < \mathcal{U}_R = \frac{U_0}{fc} < 13$, they have measured the response of a NACA 0021 mounted on springs for a large range of angle of attack between 50° and 130°.

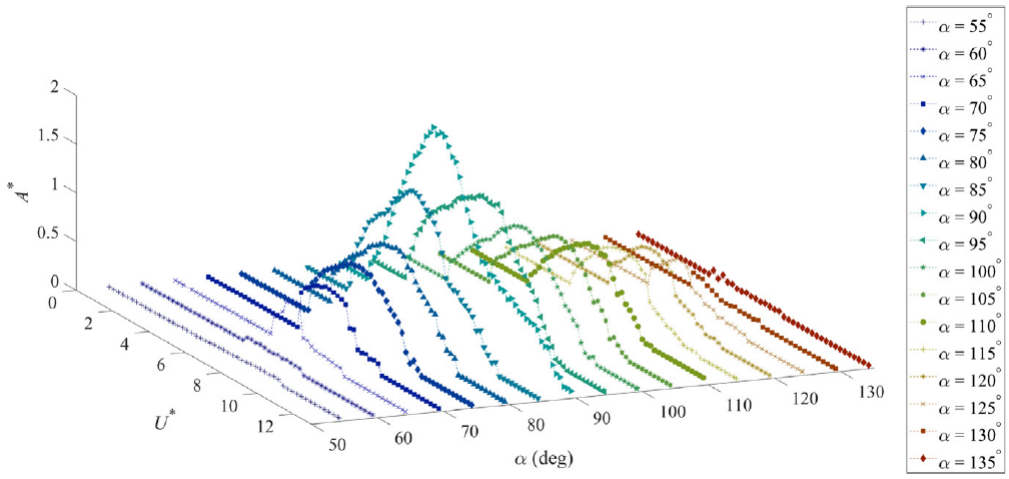

Figure 1.8: Dimensionless amplitude of the crossflow oscillations A^* versus the reduced velocity for angles of attack in the range 55° to 135° [12]

The figure 1.8 shows that VIV can occur in a large range of angle of attack going from 65° to 125° and a reduced velocity between 6 and 10 for this airfoil in water. The maximum amplitude $A^* = A/c$ of vibrations is obtained at 90° of AOA, when the projected surface is the highest. The amplitude of the vibrations reaches 2 chords. The level of vibration and reduced velocity range of lock-in are larger in the water because the mass ratio leads to a lower Scruton number.

1.2.3 Vortex induced vibrations past wind turbine blades

The next step in the investigation of VIV on wind turbines is to simulate the response of a complete 3D blade. It has been shown by Dose et al. [40] that common wind turbine solvers based on Blade Element Momentum Theory (BEMT) are not capable of simulating VIV and coupled CFD/CSM was necessary to capture the 3D unsteady flow required for VIV simulations on a blade in standstill position. A visualization of the flow during VIV with an isosurface of criterion Q is shown in Figure 1.9 for a wind at 50m/s coming with a pitch angle of 90° and no inclination. Due to the twist and variable chord of the blade, the vortex shedding frequency is different for each section. It leads to an induced flow that presents complex structures with many vortices.

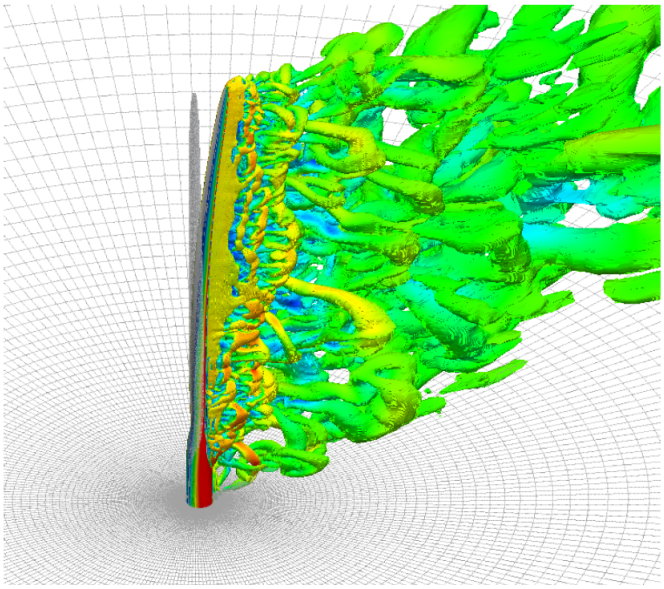

Figure 1.9: Instantaneous isosurface for the vortex criterion Q coloured by velocity magnitude. The initial blade geometry is shown in grey. The inflow speed is 50m/s at 90° pitch with no inclination. [40]

To gather information on VIV on the DTU 10-MW RWT blade, Heinz et al. [67] have coupled a structural solver to a CFD solver and explored the effect of three main parameters: the angle of attack, the inclination angle and the wind speed. The inclination angle allows to take into account the azimuth position in which the wind turbine has been stopped. As observed for the 2D airfoils, the angle of attack range in which VIV arise on a blade is limited around 90°. For the DTU 10-MW RWT blade, this range is between 80° and 110° for the tip angle of attack. Moreover, a minimum angle of inclination is required to correlate the vortex shedding behind the blade to initiate VIV. Vibrations have not been observed for angles of inclination less than 20°. For several couples of angle of attack and angle of inclination, the wind speed has been increased from 16m/s to 26m/s. It appeared that the wind velocity range of lock-in was depending on both angles. In general, higher wind speeds are required to start VIV when the inclination angle is increased because the velocity perpendicular to the blade is reduced. The minimum wind speed that provoked vibrations was 16m/s. This is a velocity that has a relatively high probability of occurrence and may lead to fatigue. The maximum peak-to-peak amplitude of the edgewise tip displacement detected is 5m for a blade of 86m long at 26m/s. The edgewise direction of a blade is the average direction of the chordwise direction of its section.

Further investigations have been conducted by Horcas et al. [70] and Horcas et al. [71] on a blade of the IEA 10MW at a wind speed of 18m/s. The impact of blade pitch angle and flow

inclination angle (Figure 1.10) have been analyzed and a map of peak-to-peak amplitude has been made in the edgewise direction. It has been observed that only certain combinations of pitch and inclination angles lead to vortex induced vibration. A high inclination regime with a C shape, between 40° and 60° inclination, and a low inclination regime without a clear shape, around 30° inclination, can be noticed. Both regimes concern pitch angle between 80° and 105°, which is more narrow than the range for 2D airfoil. The main difference between the two regimes is the frequency content of the wake. In the high inclination regime, the wake is defined by a single frequency which corresponds to vibration frequency of the blade. Whereas in the low inclination regime, the wake contains a broadband shedding in addition to the dominating frequency of motion.

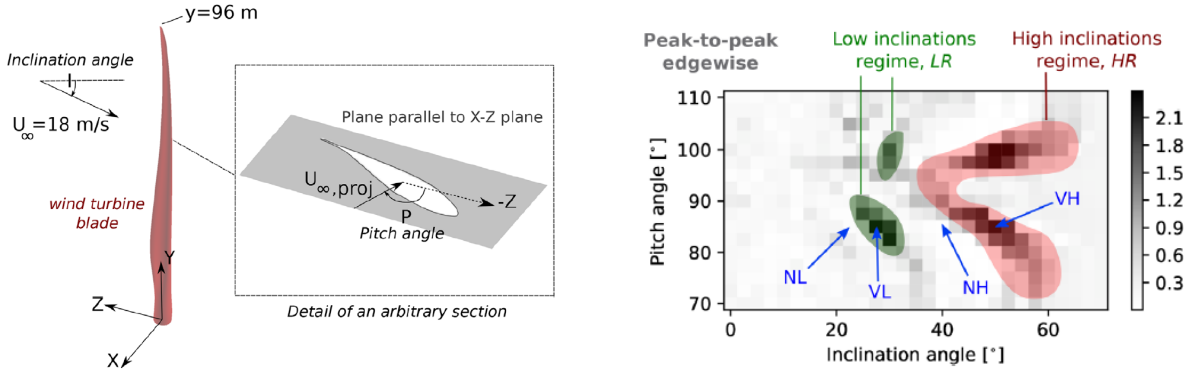

(a) Definition of the pitch angle and the inclination angle [71]

(b) Peak-to-peak amplitudes of the tip motion in edgewise [71]

Figure 1.10

Furthermore, the VIV observed in this study is different from classical VIV in the way that no vortex shedding was observed with rigid blades. However with flexible blades, a reconfiguration of the wake occurs due to vibration and triggers vortex shedding (Figure 1.11). Mittal and Singh [97] also observed a similar case with no vortex shedding in the wake when a rigid cylinder is fixed at subcritical Re but appears when the cylinder is flexible. However, it is not clear if it is the same phenomenon or not.

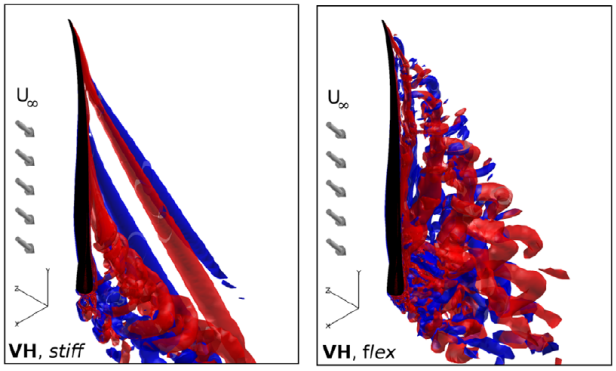

Figure 1.11: Wake visualization by iso-surfaces of Q-criterion. Includes both pure CFD simulations (stiff) and FSI ones (flex) [71]

By looking more closely at the energy exchange along the span during the limit cycle oscillations (LCO), it can be observed that some areas of the blade are receiving energy from the fluid while others are losing energy. In total, the average power is positive. This means that to maintain a

constant amplitude of vibration, the excess power is dissipated by structural damping. Since fully coupled fluid-structure interaction simulations are dependent on initial conditions, changing the initial conditions can lead to other solutions as the equations are non-linear. Then Grinderslev et al. [59] have extended the study of Horcas et al. [71] by performing forced motion simulations. By applying a prescribed motion, the limit cycle oscillation can be reached more quickly. Good agreement has been seen between the two approaches. Finally, it has been found that some configurations that do not exhibit VIV under coupled simulations can build up VIV if perturbed by turbulence. The turbulence itself may impact the VIV but turbulence is complicated to simulate and experimental data, on site or in wind tunnel, would be necessary to validate the high fidelity modeling.

VIV on a full rotor

A last step has been made by Pirrung et al. [108] who have extended the study to a full rotor CFD/CSM simulation. Some simulations have been chosen based on the mapping of Horcas et al. [71] and the one that has led to the larger vibrations has been detailed. It corresponds to a rotor placed in a uniform flow of 18m/s with a yaw angle of 90°. All blades are pitched to 80°. The azimuth position is such that blade 1 has an angle of inclination of 60°. In this configuration, the isolated blade simulation of Horcas et al. [71] has led to vibration in edgewise with an amplitude of the tip of 0.6m. However, as it can be noticed in Figure 1.12b, the vibrations have reached an amplitude peak to peak of around 30m for a 96m long blade. It is larger than any VIV obtained with an isolated blade. A flow visualization during the LCO (Figure 1.12a) shows that the vortex shedding of blade 1 is well correlated. The wake of blade 3 is composed of spanwise vortices due to the large motion on top of an uncorrelated background. No spanwise correlation is visible in the wake of Blade 2.

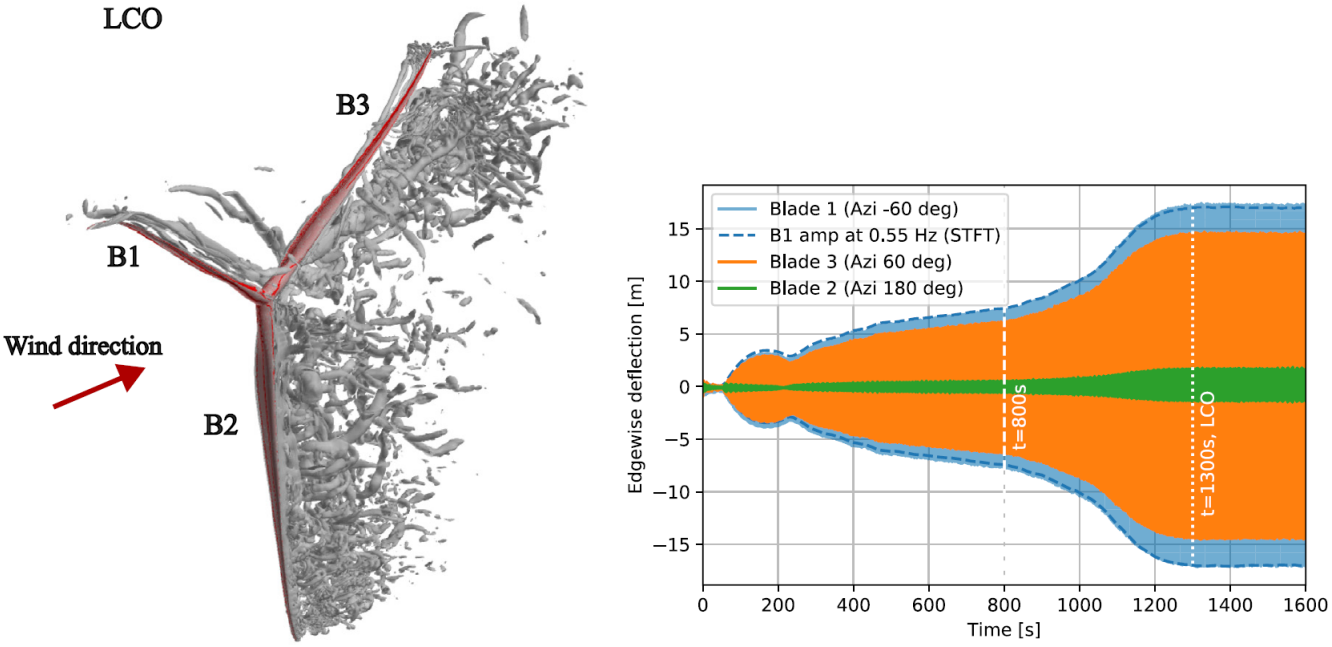

(a) Shed vortices displayed using iso-surfaces of the Q-criterion of 5 during LCO at 1600 s. [108]

(b) Buildup of edgewise vibrations of the three blades. [108]

Figure 1.12

1.2.4 Summary

To sum up, vortex induced vibrations on wind turbines are possible and have already been observed in the field. High-fidelity simulations have permitted to identify configurations in yaw and inclination at risk. Angles of attack between 80° and 100° associated with angles of inclination between 20° and 60° may lead to VIV if the wind speed is around 18m/s. Such conditions of wind speed has a relatively high probability of occurrence and represents a concerning issue for the fatigue of the blade. Especially with respect to the high level of vibration obtained with the full rotor simulations.

The effect of the turbulence on wind turbine VIV still remains to be investigated numerically and experimentally.

1.3 Stall-induced vibrations

Stall-induced vibrations (SIV) is an aeroelastic instability mostly encountered in civil engineering. However, it can also appear for airfoils in a stall regime. In contrast to classical flutter, SIV can appear even if the structure motion is described by only one degree of freedom in flexion or torsion. It is characterized by negative aerodynamic damping. The vibration velocity of the blade induces aerodynamic loads that in return promote the motion. The oscillations are amplified until the system reaches a limit cycle oscillation (LCO) due to non-linearities. Even if the SIV are similar in civil engineering and in aeronautics, the methods to study it differ depending on the field. With profiled bodies, the flow can only be partially separated justifying the use of dynamic stall model. On the contrary, bluff bodies are generally fully stalled and the critical velocity is mainly estimated with quasisteady aerodynamics.

Within stall-induced vibrations, the instabilities are of two kinds. The first kind regroups stall flutter and torsional galloping, which refers to torsional vibrations. The term stall flutter is used in aeronautics where the bodies are profiled whereas the term galloping is used in civil engineering where the bodies are bluff. A famous example of torsional galloping in civil engineering is the Tacoma bridge. The H shape of the bridge was generating vortices on the leading part that produced unsteady aerodynamic loads with a phase shift making the bridge unstable for some wind speed. The second kind of SIV contains the flexion galloping which refers to vibrations in flexion. It mainly affects bodies for which the lift or transverse coefficient has a negative slope. For example, stall regulated wind turbines were prone to edgewise vibrations during operation. Unlike modern pitch regulated wind turbines, this kind of wind turbine had their blades attached with a fixed pitch angle. To limit over-speed in operation, it used the fact that the blade will enter a stall regime when the wind speed exceeds a specific value. Moreover, with tilt, the blades were experiencing an angle of attack varying with time, leading to dynamic stall. However, this kind of wind turbine is not much used. The other kind of wind turbine, the pitch regulated wind turbine, do not enter in stall during operation because the pitch is controlled to limit the rotor speed and does not need the passive saturation of the stall regime. Thus, they are not likely to experience SIV in operation. However, pitch regulated wind turbine blades can experience high angle of attack (AOA) when the wind turbine is stopped or in idling operation mode (rotating very slowly) if the wind is coming with yaw. It means that wind turbine blades can stall in such conditions and potentially be subject to SIV.

Stall-induced vibrations are different from vortex induced vibrations, as SIV are motion induced vibrations whereas VIV are flow induced vibrations. It means that SIV needs an initial perturbation (for example turbulence) to start whereas VIV is triggered by the establishment of vortex shedding, a pure fluid phenomenon. As a consequence, the reduced velocities triggering

VIV or SIV are different. For VIV, the reduced velocity needs to be close to the inverse of the Strouhal number so that the vortex shedding synchronized with the structure, whereas for SIV, the aerodynamic damping decreases and becomes negative with increasing reduced velocity, thus the instability appears when the reduced velocity reaches a specific value corresponding to the moment when the negative aerodynamic damping overcomes the structural damping. In general, VIV occurs for lower reduced velocity. Moreover, the range of angle of attack of the instabilities also differs. VIV concerns angle of attack between 80° and 105° whereas SIV can arise for all angles of attack satisfying conditions on the lift, drag and moment. In general, it occurs when the lift slope is negative, meaning that it can be just after the stall angle when the flow around the airfoil is still partially separated or in much higher angles of attack.

In order to well understand what is stall-induced vibrations on a wind turbine blade, the phenomenon is progressively explained. First, the focus is put on the flow side. It begins with the static stall of 2D airfoils : why does the boundary layer detach and what is the consequence on the loads. It continues with the introduction of a movement of the airfoil leading to dynamic stall. Then, the three dimensionality of stall around a wing is highlighted. First with fixed wings and next with moving wings. Finally, the coupling with the structure is addressed.

1.3.1 Static stall

An airfoil is often aerodynamically characterized by its polars. It consists of plotting the time-averaged load coefficient C_L, C_D and C_M as a function of the angle of attack. An example is given in Figure 1.13.

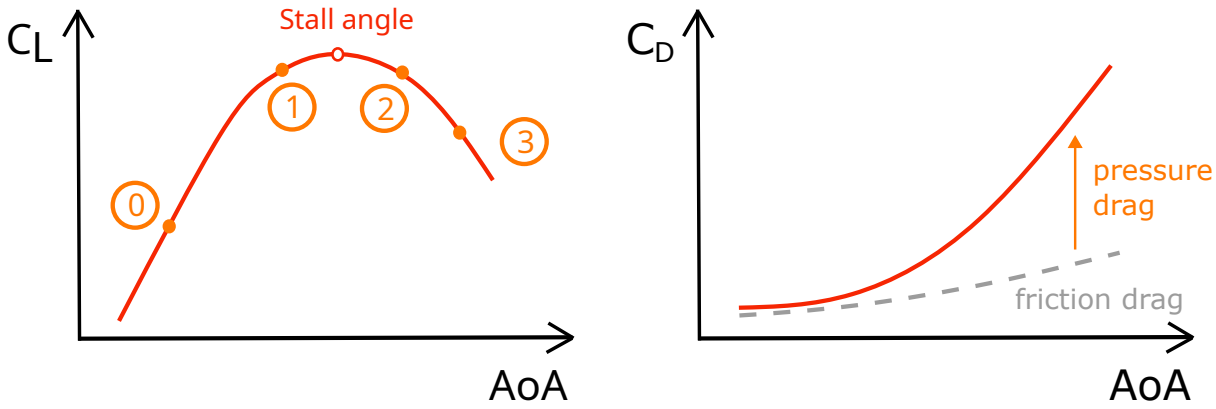

(a) Lift (b) Drag

Figure 1.13: Scheme of a static polar

For low angles of attack (0 in Figure 1.13a), the flow is attached to the airfoil and the lift coefficient is increasing linearly. When the angle of attack is large, the lift coefficient is no longer linear (1 in Figure 1.13a). It is due to the formation of a separated area at the trailing edge as schematized in Figure 1.14a. Increasing further the angle of attack, the lift coefficient passes by a maximum. The corresponding angle is named the stall angle. The growth of the separated area (Figure 1.14b) causes the lift coefficient to drop (2 in Figure 1.13a). Finally, comes an angle of attack where the flow is completely separated (Figure 1.14c and 3 in Figure 1.13a).

Concerning the drag (Figure 1.13b), for low angle of attack the drag is nearly constant. The majority of the drag is skin-friction drag. However, with the increasing angle of attack, the total drag rapidly rises due to the pressure drag provoked by the flow separation.

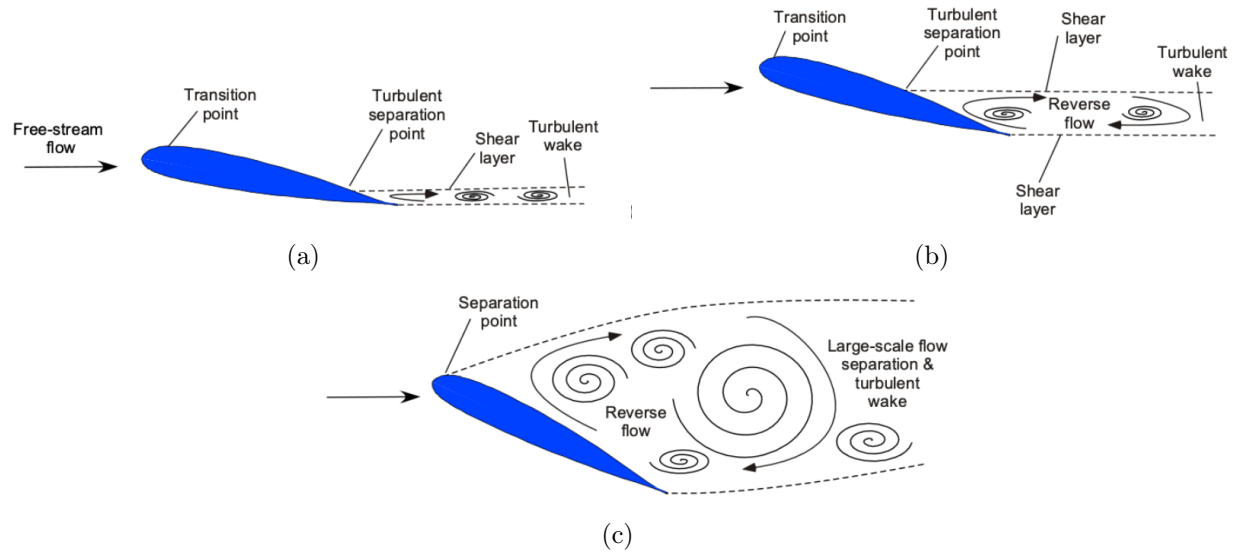

Figure 1.14: Flow about an airfoil section at increasing angles of attack showing the progressive forward movement of flow separation and the onset of stall [80]

Separation mechanism To provide some physical intuition, a simplified explanation is as follows: flow separation occurs due to the detachment of the boundary layer imposed by high adverse pressure gradient. In the case of an airfoil, its angle of attack and shape generate a pressure field that leads to pressure gradients within the boundary layer. The modification of the boundary layer due to a pressure gradient is illustrated in figure 1.15.

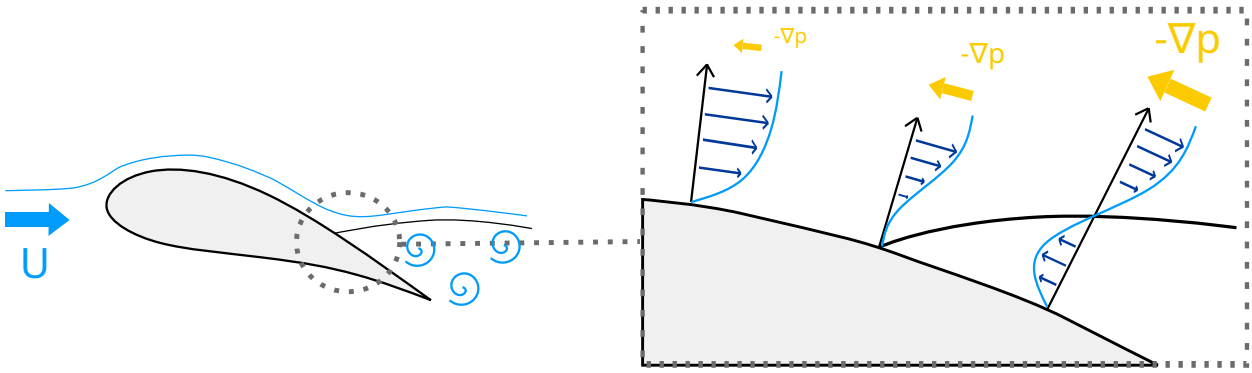

Figure 1.15: Scheme of the boundary layer separation

Due to the shape of the airfoil, the adverse pressure gradient gets stronger when approaching the trailing edge. As a consequence, when the pressure gradient becomes too strong it forces the boundary layer to detach at a specific area.

Trailing-edge versus leading-edge type stall The stall mechanism explained above is the trailing-edge type stall. But there exists another type of stall: the leading edge type stall. This one is caused by the bursting of a laminar suction bubble (LSB). This bursting happens before the separation point could reach the leading edge. It is common for thin airfoils. This way of stall is more sudden and causes the static polar to be sharper after the stall angle (Figure 1.16). Airfoil section are generally thick for wind turbine blade and thus more concerned by the trailing edge type of stall.

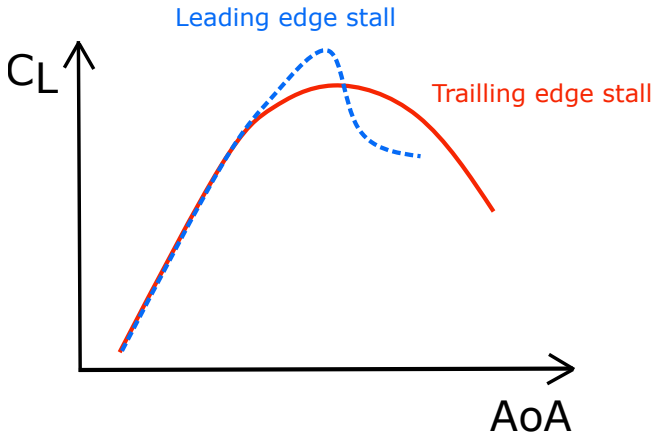

Figure 1.16: Comparison of lift static polars between leading edge stall and trailing edge stall

1.3.2 Dynamic stall

The fluid flow reacts to the motion of the structure. For an airfoil section operating close to the static stall angle of attack, a harmonic motion in either plunge or pitch can lead to a complex dynamic stall process for which the flow separates and reattaches partially or completely during each cycle of oscillation. It leads to unsteady lift, drag and moment drawing loops around the steady polar.

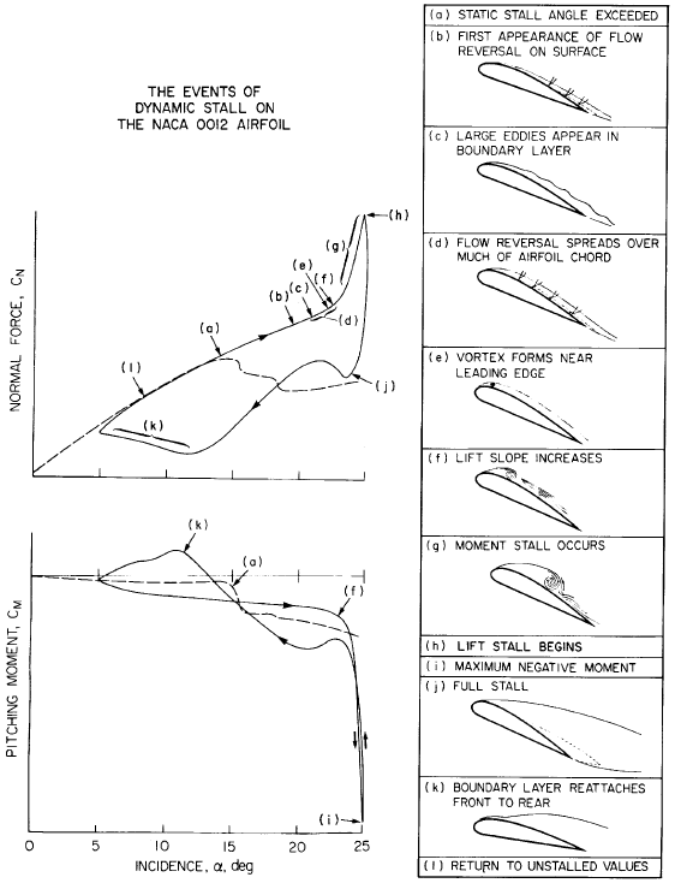

Figure 1.17: Dynamic stall events on a NACA0012 airfoil around 15° with an amplitude of 10° and a reduced frequency $k = 0.15$ at $Re = 2.5 \cdot 10^6$ [23]

The dynamic stall behavior mainly depends on the airfoil shape, operating mean angle of attack, amplitude of motion and reduced frequency $k = \frac{\omega c}{2U_0}$, where ω is the pulsation of oscillation, c the chord and U_0 the flow velocity. The turbulence characteristic of the incoming flow (intensity, spatio-tempporal scales) can also significantly affect the dynamic stall process. Dynamic stall process and associated non-linear unsteady aerodynamic behavior have been mainly studied for harmonic pitching motion.

It highlights the fact that passing through the static stall angle dynamically produces an overshoot of lift. This additional lift is due to a complex fluid behavior that introduces a delay of adaptation of the fluid flow to the structure motion. The details of this flow behavior will be examined later but an overview is given by the figure 1.17. The aerodynamic delay involves an exchange of energy between the flow and the structure. That's why this delay needs to be modeled in order to correctly predict the aeroelastic behavior of a system. However, it is not simple because the loops depend on the geometry, the type of movement, the frequency and the amplitude of the motion. Amandolese and Széchényi [3] and Damiola et al. [31] experimentally measured these loops for wind turbine designs.

Deep vs light dynamic stall Dynamic stall can be categorized in two kinds. Deep dynamic stall refers to a dynamic stall process with emission of a dynamic stall vortex (DSV) whereas no DSV is emitted in light dynamic stall, the separation point only moves back and forth on the suction side. For example, Figure 1.17 describes a deep dynamic stall whereas dynamic stall loops of light dynamic stall look like Figure 1.23. As it will be seen later, many parameters affect the dynamic stall process and the emission of a DSV. In general, thin airfoils experience a leading edge stall which leads to deep dynamic stall. Thick airfoils undergoing trailing edge stall can experience light dynamic stall but if the angle of attack becomes too high, vortices are emitted and there is deep dynamic stall.

In this work, the wind turbine airfoils are thick and the angle of attack will be limited in order to stay in a light dynamic stall regime. Deep dynamic stall is more challenging to simulate because the turbulence modeling needs to correctly capture the dissipation of the vortices.

1.3.2.1 Dynamic stall process in 2D

Dynamic stall is a complex phenomenon in which the flow separates and reattaches partially or completely during each cycle of oscillation. As CFD approaches can provide detailed spatial and temporal information, it is a promising way to investigate dynamic stall. Several numerical studies have been conducted in which the blade motion is imposed. Good agreement has been obtained between the numerical and experimental data for the dynamic loops of the S809 airfoil in [147]. Bangga et al. [7] have also simulated dynamic loops for the same airfoil and obtained similar results. They however pointed out the importance of the turbulence model as it has a significant impact on the flow structures. The Spalart-Allmaras model seems to show better prediction than the SST model. With the increase of numerical capacities, it is possible to simulate dynamic stall with higher fidelity. Visbal and Garmann [139] and Benton and Visbal [13] performed LES simulations of a NACA 0012 airfoil in a ramp-type pitching motion. They provided a precise description of the onset of dynamic stall, depicting the complex interaction between the turbulent-separation vortex (TSV) and the leading edge vortex (LEV) that produces the dynamic stall vortex (DSV).

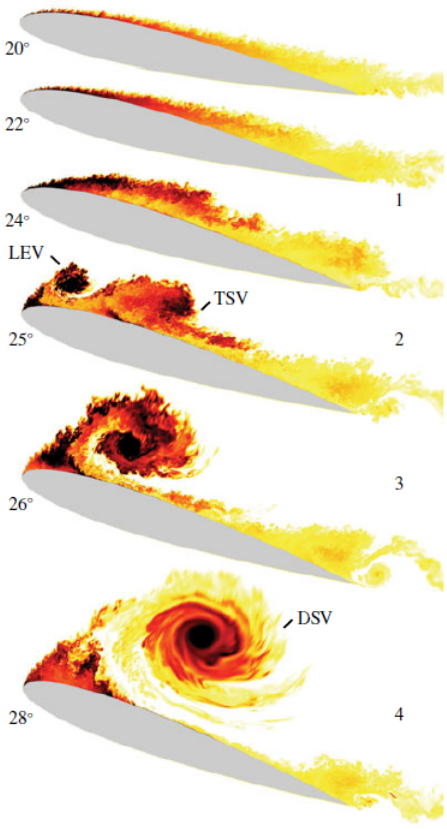

Figure 1.18: Instantaneous contours of entropy at the mid-span showing overall process of dynamic stall during a ramp motion from 8° up to 30° with a pitch rate of 2.8° by U_0/c second. (Re = 1e6) [13]

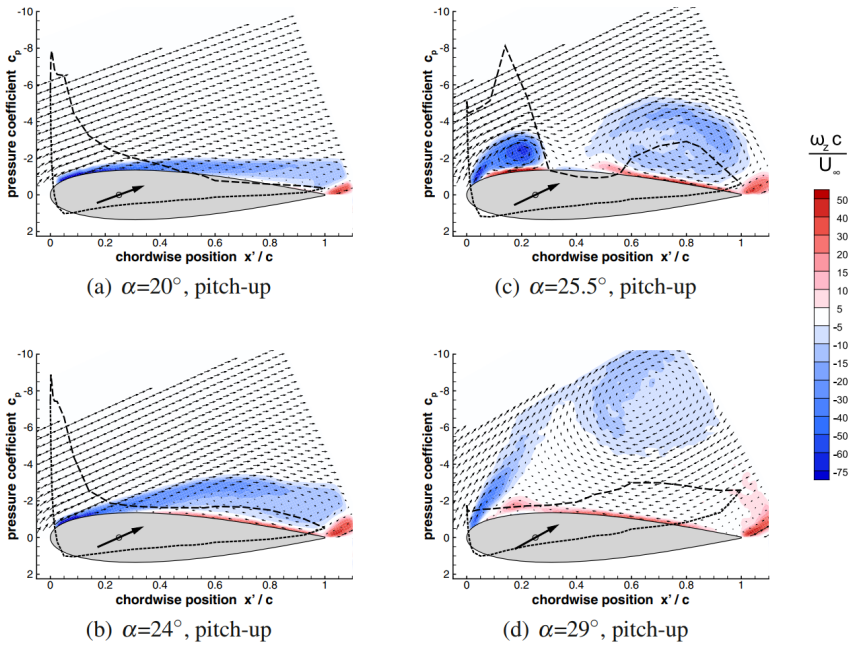

Figure 1.19: Phase averaged normalized vorticity fields and surface pressure coefficients illustrating various stages of the dynamic stall mechanism, $\alpha = 0° + 30° \sin(\omega t)$, $k = 0.074$, $Re = 2.5e5$ [99].

A turbulent separation (TS) appears near the trailing edge at $\alpha \approx 15°$ and propagates upstream with increasing α. At Re=1e6, the laminar separation bubble (LSB) is stable until the TS reaches it. This causes a bursting event that results in the development of a small leading-edge vortex (LEV) structure (Figure 1.18). At the same moment, the turbulent boundary layer that has been separated by the passage of the TS rolls up to form a second vortex structure named the turbulent-separation vortex (TSV). The two vortices combine to form the well-known dynamic stall vortex (DSV). The DSV then propagates downstream as it is typically observed [13].

Mueller-Vahl et al. [99] conducted experimental PIV measurements on a NACA0018 during dynamic stall at $Re = 2.5e5$. They observed the vorticity field represented in figure 1.19. In (a), the turbulent separation appears at the trailing edge. In (b), the separation has moved toward the leading edge. In (c), additionally to the leading edge vortex, another vortex has been reported across the rear half of the blade, probably the TSV. Finally, in (d), the two vortices have merged to generate a DSV.

Effect of the Reynolds number As it affects the boundary layer evolution, the Reynolds number can have a significant impact on the dynamic stall process. Benton and Visbal [13] performed LES simulations on a NACA 0012 airfoil in ramp-type pitching motion for three different values of the Reynolds number. Spatio-temporal (x–α) contours of span-averaged wall skin friction coefficient on the airfoil suction surface are reported in figure 1.20.

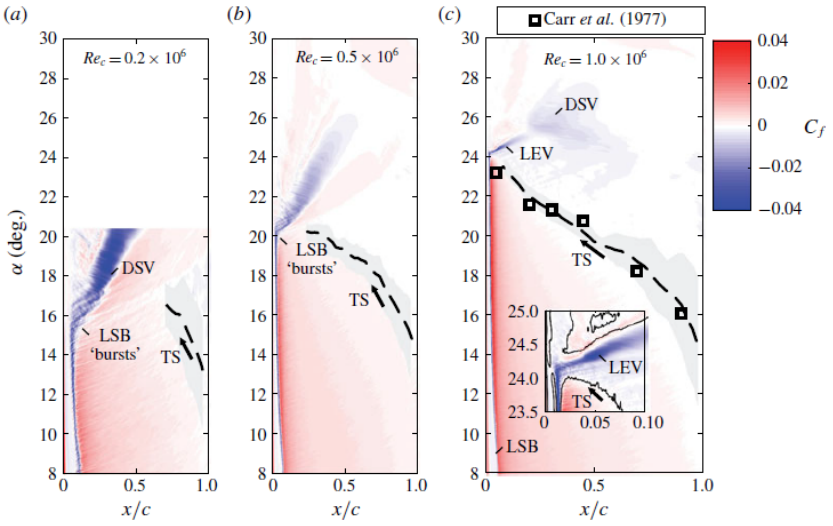

Figure 1.20: Spatio-temporal (x–α) contours of span-averaged wall skinfriction coefficient on the airfoil suction surface [13].

It can be seen that for $Re = 2e5$ the LSB bursts before the TS could reach the leading edge, at an angle of 16°. With higher Reynolds numbers, the LSB is more stable and bursts for higher angles of attack. For $Re = 1e6$, the LSB does not burst, the LEV has been produced because the TS has reached the leading edge.

Effect of the airfoil thickness As mentioned previously thin and thick airfoil section exhibit different type of static stall behavior. Sharma and Visbal [122] investigated numerically the effect of airfoil thickness by comparing numerically the onset of dynamic stall for NACA airfoils of varying thickness (9%, 12%, 15% and 18%) at $Re = 2e5$. They observed in figure 1.21 that the onset of dynamic stall is triggered by LSB bursting for the thin airfoils whereas the LSB remains stable until its interaction with the turbulent separation for the thick airfoils. As a consequence, the onset of deep dynamic stall occurs at an higher angle of attack for thick airfoils than thin airfoils. Bangga et al. [9] also compared the dynamic stall process between airfoils of various thicknesses. They concluded that the LEV is smaller with increasing airfoil thickness.

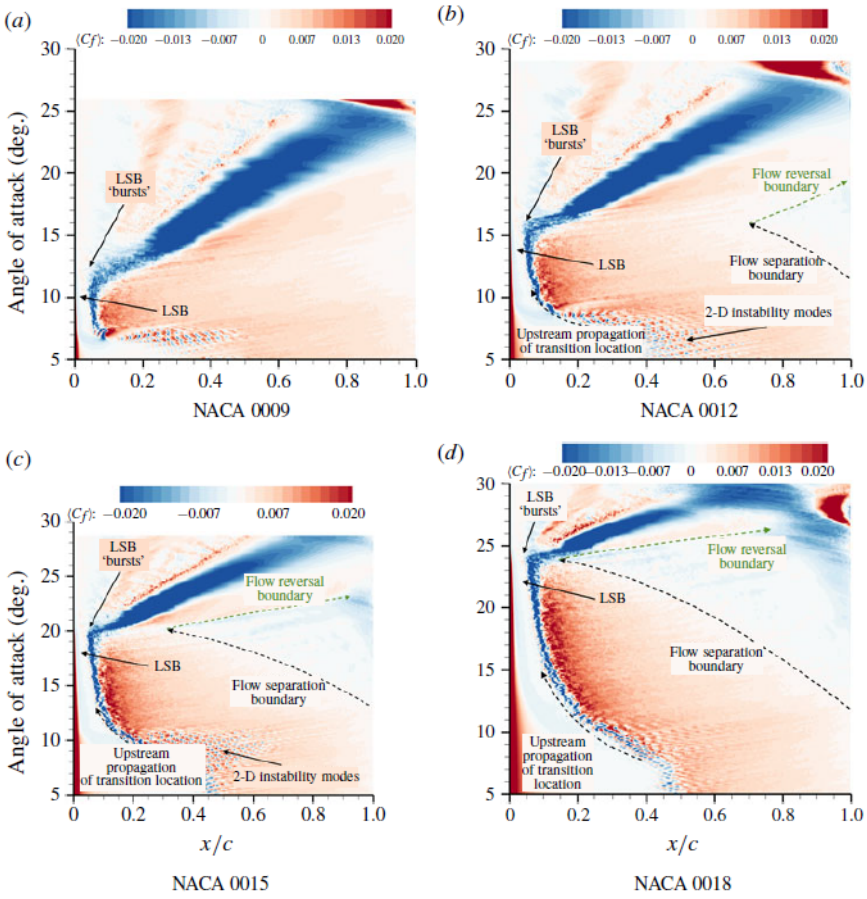

Figure 1.21: Contours of spanwise-averaged skin friction coefficient $< C_f >$ on the suction side of the four airfoils through the constant pitch-rate motion. [122]

Effect of the reduced frequency As for the motion-induced fluid behavior in the linear domain (i.e. small angle of attacks), the reduced frequency has a major impact on the dynamic stall process. This is illustrated in figure 1.22 from the experimental work of Kiefer et al. [75], showing the temporal change of the suction-side surface pressure on a NACA0021 airfoil section, in ramp-type pitching motion from 19° to 29° with three different reduced frequencies is reported in figure 1.22. The mean angle and amplitude of the motion as well as the Reynolds number are held constant. In the early times, the instantaneous lift is the result of two counteracting mechanisms. The first one is the suction magnitude near the leading edge ($x/c \approx 0$). It adapts almost instantly to the motion as indicated by the decrease in pressure during the pitching motion in the figure 1.22. The second mechanism is the progressive separation of the boundary layer from the trailing

edge to the leading edge. This one presents a delay from the passage of the static stall angle which has a low dependency about the reduced frequency. Thus, for this ramp motion with a limited pitch angle, there exists a reduced frequency for which higher reduced frequencies do not influence the maximum lift and the stall process evolution.

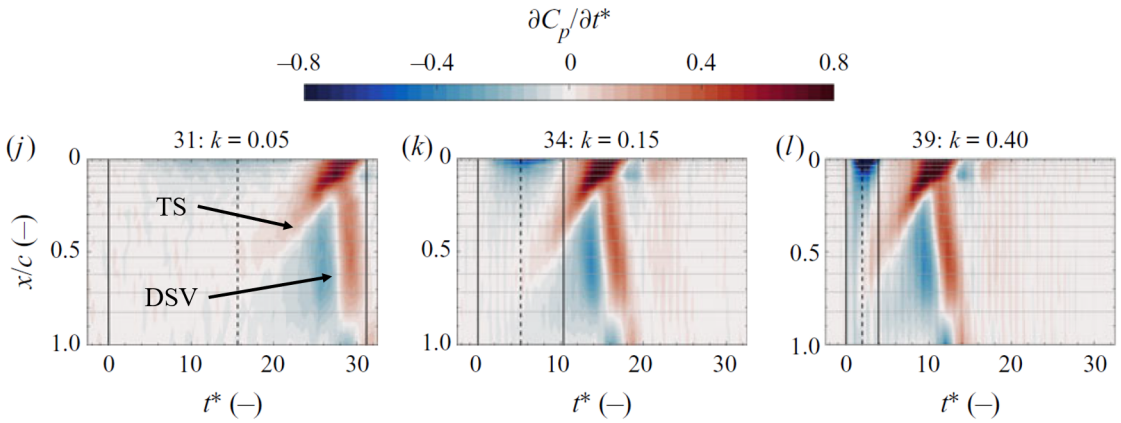

Figure 1.22: The temporal change of suction-side surface pressure presented for selected test cases of the reduced frequency series. Black solid lines mark the start and end of the piching motion; black dotted lines specify the passage of the static stall angle. [75]

Numerous experimental and numerical results regarding the unsteady lift and/or pitching moment coefficients of airfoil section forced in harmonic pitching motion for various reduced frequencies have been published. Results regarding a typical wind turbine blade airfoil section are reported in figure 1.23.

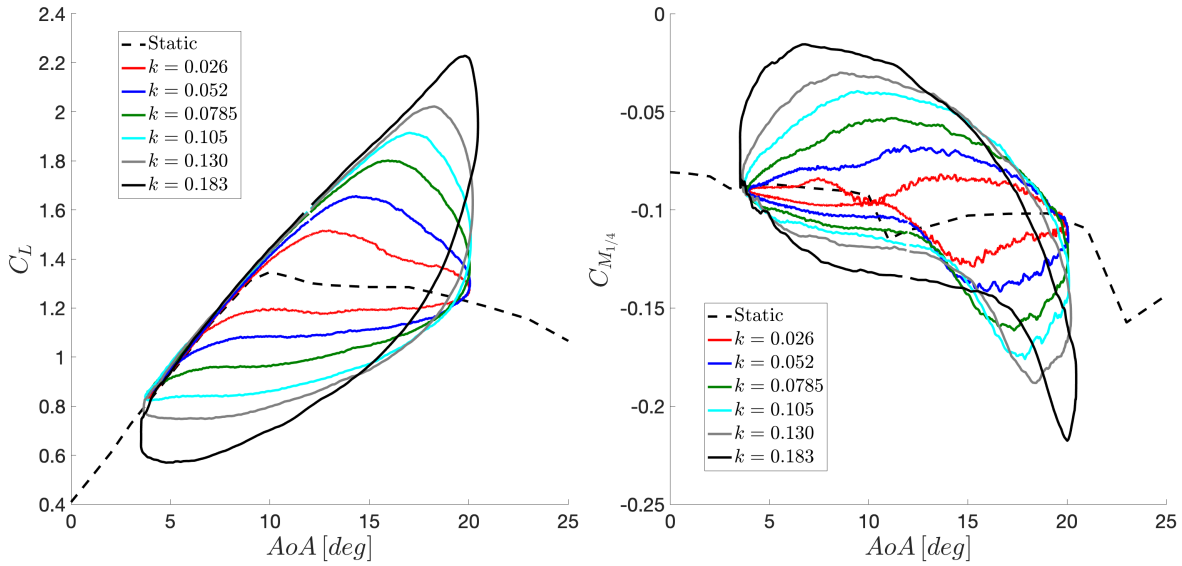

Figure 1.23: Influence of the reduced frequency $k = \frac{\pi f c}{U_0}$ on the lift and moment coefficient; Experiments on a NACA63421 section model in harmonic pitching motion of mean angle of attack 12° and mean amplitude 8°, for $Re = 10^6$ and $I_{tu} = 1.1\%$. [3]

Effect of the turbulence intensity The effect of the turbulence intensity has been investigated both experimentally [3, 31] and numerically [73, 76] on several airfoils : NACA0012 [76], NACA0018 [31], NACA63421 [3] and ClarkY airfoil [73]. In all studies, a delayed flow separation during upstroke and enhanced flow reattachment during downstroke have been observed by increasing the turbulence intensity. The dynamic loops in both lift and moment coefficients are thus significantly affected, in particular the lift for which the swept area is reduced due to an increase of the lift coefficient during downstroke (see: Figure 1.24).

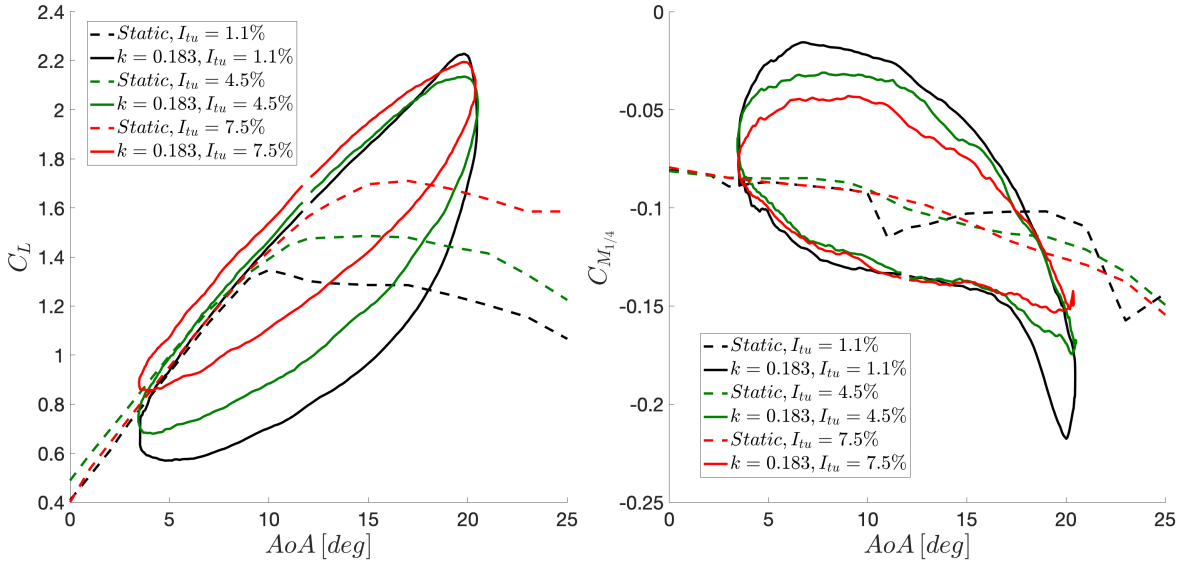

Figure 1.24: Influence of the turbulence intensity on the lift and moment coefficients; Experiments on a NACA63421 section model in harmonic pitching motion of mean angle of attack 12° and mean amplitude 8°, for $Re = 10^6$ and reduced frequency $k = \frac{\pi fc}{U_0} = 0.183$. [3]

It should nevertheless be mentioned that the impact of the incoming turbulence is a complex and open question for lifting surfaces operating in the atmospheric boundary layer. The turbulence intensity is a relevant parameter but only if it is associated to a proper spatio-temporal distribution of the turbulence. Regarding the experimental results reported in Figure 1.24, a turbulence grid was used in the wind tunnel, allowing to increase the turbulence intensity but for a mean turbulence length scale more than 100 times smaller than the one that should be used to scale a realistic atmospheric turbulence to the wind turbine blade section model in the wind tunnel.

1.3.2.2 Dynamic stall models

Dynamic stall process generates unsteady lift, drag and moment loops around the steady polar. Various semi-empirical models have been developed to simulate this unsteady nonlinear aerodynamic behavior. The two most popular models are the Beddoes-Leishman model [81] and the ONERA model developed by Tran and Petot [136] and improved by Petot [104]. Both are based on the airfoil steady characteristics (steady lift, drag and moment coefficients evolution with the angle of attack), and a set of parameters that need to be identified using specific dynamic tests. The Beddoes-Leishman model describes dynamic stall by modeling separately the attached flow behavior, the leading edge separation, the trailing separation and the effect of the leading edge vortex (LEV). The ONERA model is not directly based on the flow behavior but consists in a semi-empirical set of non-linear differential equations that generate dynamic stall loops. The unsteady response in lift, drag and moment, is calculated using two terms. The first term is associated to the

dynamic response in the linear or unstalled region. For low amplitude harmonic motions, it gives unsteady lift, drag and moment close to those obtained using the linear Theodorsen formulations. The second term represents the dynamic response in the non linear stalled region. It is the solution of an harmonic oscillator (i.e. a second order differential equation) forced by a term proportional to the first derivative of an effective angle of attack and a term proportional to the nonlinear aerodynamic force deviation, defined as the difference between the linear lift coefficient (from an extrapolation of the linear region) and the static lift coefficient. A time delay can also be used to compute the nonlinear aerodynamic force deviation and delay the dynamic stall onset. More recently, the IAG model [8] has been developed in order to take into account the higher harmonics of the vortex shedding during deep stall. In addition to these three models, many others exist. A comparison of several dynamic stall models that could be used for wind turbine blade have been done by Larsen et al. [77]. It should be noticed that all those dynamic stall models are purely sectional model and their use for continuous wing or blade application are often done in the strip theory assumption, neglecting any 3D stall effects. The only dynamic stall model found to take into account the tip vortex is the one of Lu and Wang [88]. It adapts the Beddoes-Leishman model by delaying the separation near the tip.

ONERA dynamic stall models In this paragraph, the extended version of the ONERA model to pitch α and plunge y is presented based on Dimitriadis [37], the drag is added based on Petot [104]. This model will be used in the following chapter of the thesis.

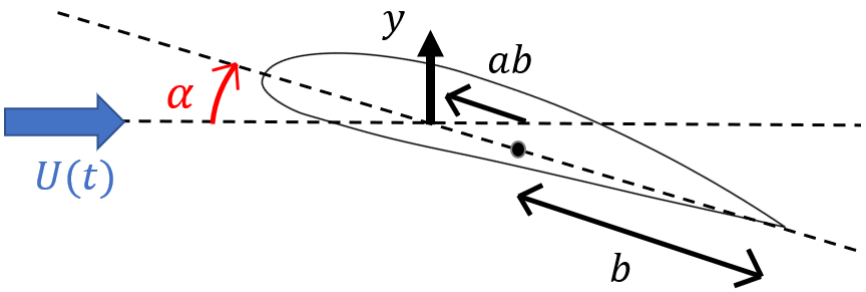

Figure 1.25: Scheme for the ONERA model. a is negative on the scheme.

First, two downwash velocities are defined as:

$$W_0(t) = -\dot{y}\cos(\alpha) + U(t)\sin(\alpha) - b(a+1/2)\dot{\alpha} \tag{1.1a}$$

$$W_1(t) = b\dot{\alpha} \tag{1.1b}$$

where U_0 is the absolute velocity, $b = c/2$ is the half chord and a is the dimensionless distance between the mid-chord and the elastic center. W_0 is the relative velocity at the quarter chord and W_1 is the difference between the relative velocity at the three quarter-chord and the relative velocity at the quarter-chord.

These velocities are used to calculate the lift, drag and moment acting on the airfoil:

$$L = \frac{1}{2}\rho c\left(s_l b\dot{W}_0 + k_l b\dot{W}_1 + U(\Gamma_1 + \Gamma_2)\right) \tag{1.2a}$$

$$M = \frac{1}{2}\rho c^2\left(U^2 c_{m_L}(W_0/U) + b(\bar{\sigma}_m + d_m)\dot{W}_0 + \sigma_m U W_1 + s_m b\dot{W}_1 + U\Gamma_3\right) \tag{1.2b}$$

$$D = \frac{1}{2}\rho c\left(U^2 c_{d_L}(W_0/U) + b(\sigma_d + d_d)\dot{W}_0 + U\Gamma_4\right) \tag{1.2c}$$

where Γ_1 is the circulation generated by the attached flow and Γ_2 is the circulation generated by the stalled flow.

The circulation variables are calculated from two ordinary differential equations, given by:

$$\dot{\Gamma}_1 + \lambda_l \tau \Gamma_1 = \lambda_l \tau U c_{l_L}(W_0/U) + \lambda_l \tau W_1 + \left(\alpha_l \frac{dc_{l_s}}{d\alpha} + d_l\right) \dot{W}_0 + \alpha_l \sigma_l \dot{W}_1 \tag{1.3a}$$

$$\ddot{\Gamma}_2 + a_l \tau \dot{\Gamma}_2 + r_l \tau^2 \Gamma_2 = -r_l \tau^2 U \Delta c_l (W_0/U) - E_l \tau \dot{W}_0 \tag{1.3b}$$

$$\ddot{\Gamma}_3 + a_m \tau \dot{\Gamma}_3 + r_m \tau^2 \Gamma_3 = -r_m \tau^2 U \Delta c_m (W_0/U) - E_m \tau \dot{W}_0 \tag{1.3c}$$

$$\ddot{\Gamma}_4 + a_d \tau \dot{\Gamma}_4 + r_d \tau^2 \Gamma_4 = -r_d \tau^2 U \Delta c_d (W_0/U) - E_d \tau \dot{W}_0 \tag{1.3d}$$

The coefficients s_l, k_l, λ_l, α_l, d_l, σ_l, a_l, r_l and E_l are empirical and don't have real physical meaning. Same for the coefficients used for the moment and the drag. τ is a time constant defined as $\tau = U_0/b$. The term $c_{l_L}(W_0/U)$ denotes the attached flow linear static lift coefficient extrapolated to the effective angle of attack W_0/U. The term Δc_l denotes the difference between the linear static lift c_{l_L} and the measured static lift c_{l_s} (Figure 1.26). Δc_d and Δc_m are defined in a same manner.

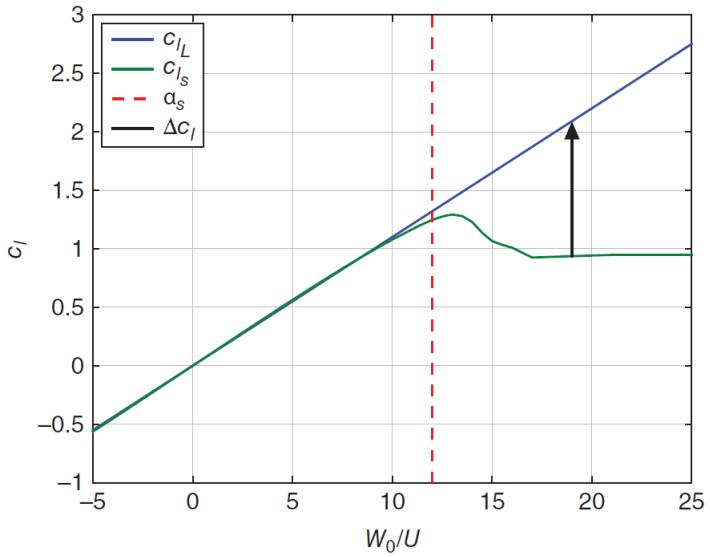

Figure 1.26: Definition of Δc_l [37]

Finally, the stall delay effect is described by the following condition through the parameter $\Delta\tau_{d_l}$:

$$\Delta c_l\,(W_0/U_0) = \begin{cases} 0 & \text{if } t - t_s \leq \Delta\tau_{d_l} b/U_0 \\ c_{l_L}\,(W_0/U_0) - c_{l_s}\,(W_0/U_0) & \text{otherwise} \end{cases}$$

where t_s is the time instance at which (W_0/U_0) exceeded the static stall angle α_s.

The range of validity of the ONERA model is said to be around -15° to 30° [110].

Effects of the parameters on the loops Donnard [39] has explored the effects of the parameters of the ONERA model on the dynamic stall loop of a NACA 63-215. The effect of a_0, a_2, r_0, r_2 and E_2, defined by $a_l = a_0 + a_2 \Delta c_l^2$, $r_l = (r_0 + r_2 \Delta c_l^2)^2$ and $E_l = E_2 \Delta c_l^2$, are presented in the Figures 1.27, 1.28 and 1.29.

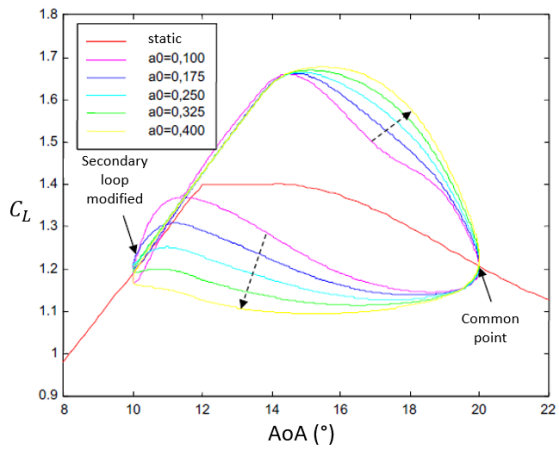

(a) a_0

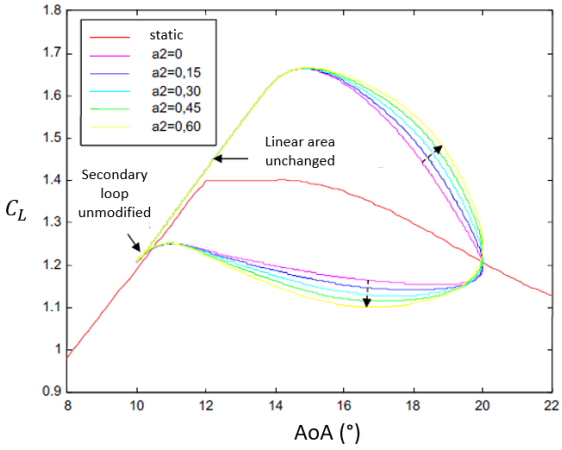

(b) a_2

Figure 1.27: Effect of the parameters a_0 and a_2 on the lift dynamic stall loop. [39]

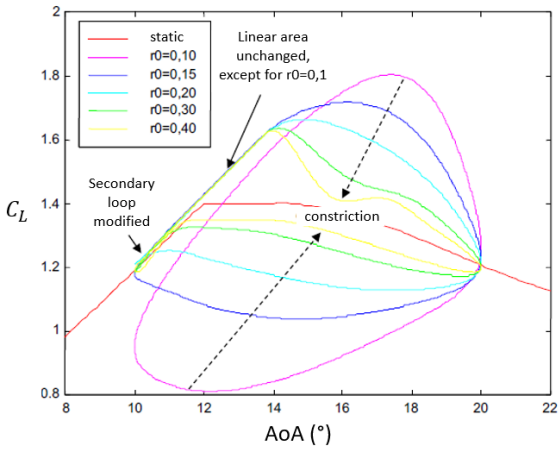

(a) r_0

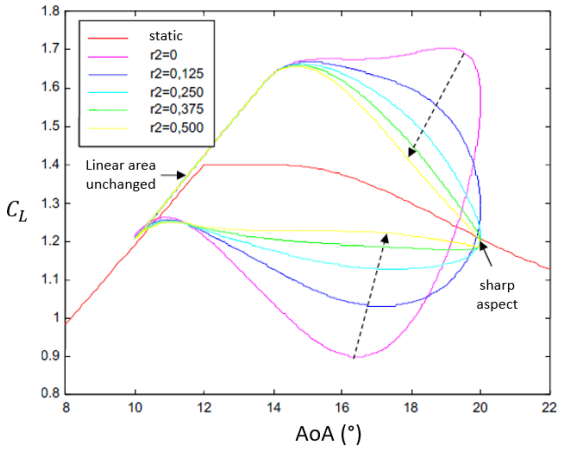

(b) r_2

Figure 1.28: Effect of the parameters r_0 and r_2 on the lift dynamic stall loop. [39]

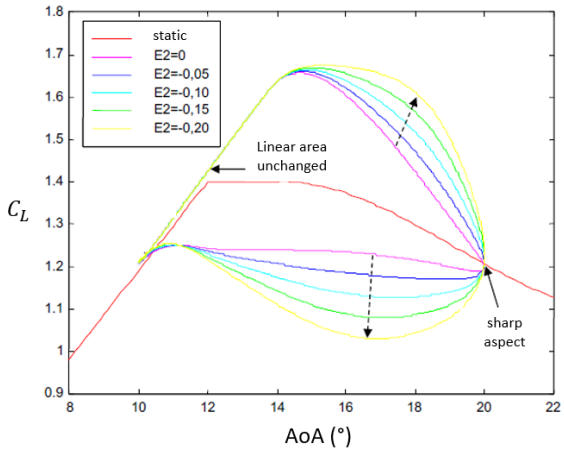

Figure 1.29: Effect of the parameter E_2 on the lift dynamic stall loop. [39]

The diminution of the parameter a_0 provokes a constriction of the dynamic stall loop and amplifies the secondary loop. The parameter a_2 has no effect on the linear area but its decrease makes the loop more slender. Then, the parameters r_0 and r_2 have more impacts. The rise of r_0 induces a constriction as a_0 but in a different manner, when r_0 is low, the loop has a rounded shape. The parameter r_2, like a_2, has no effect on the linear area. However, r_2 distends the dynamic loops for high angle of attack when reduced. Finally, the effect of E_2 is similar effect to that of r_2. [39]

1.3.3 3D Stall

In some cases, the stall flow is inherently 3D, making the 2D description insufficient. The major example is the stall cells.

1.3.3.1 3D Static stall : the stall cells

Stall cells were first observed in the 70s with experiments like the one of Gregory et al. [57]. Stall cells are 3D pattern of a stall flow introducing spatial oscillations of the separation line. It looks like mushrooms, as shown in Figure 1.30. Stall cells appear on the suction side of airfoils concerned by trailing edge type stall for angle of attack around and just above the maximum lift angle [21].

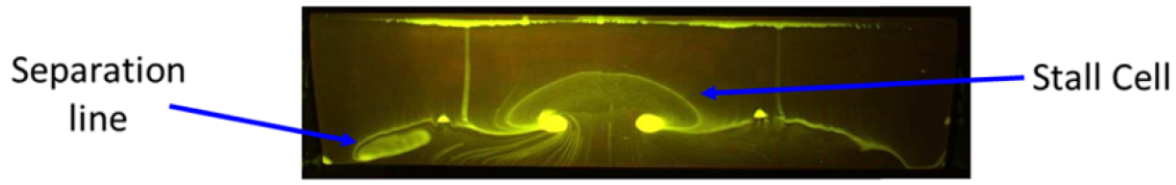

Figure 1.30: Stall-cell flow pattern observed in the suction side of a NACA0015 wing model with aspect ratio AR=4 at the angle of attack 16° and Reynolds number $4.04 \cdot 10^5$; oil flow visualization; the mean flow is coming from to bottom. [36]

Using linear stability analysis around an extruded 2D mean flow, Sarras et al. [120] have shown that the stall cells emanate from a 3D fluid instability. The unstable mode can inform on the initial shape of the stall cells, but the real structure of the stall cells is the result of the saturation of this unstable mode.

The 3D structure of a stall cell Manolesos et al. [92] has analyzed the structure of a stall cell using stereo PIV flow measurements. Their experimental results confirm a flow structure obtained with CFD (Figure 1.31). The stall cells are composed of three vortices. The stall cell (SC) vortex is the ones visible on the surface of the wing. It starts normal to the wall and then it bends to align with the flow direction. It has also a small movement toward the center of the cell. The other vortices are the trailing edge line (TEL) vortex and the separation line (SL) vortex. They are two counter rotative vortices that run parallel to the trailing edge. They grow and get away from each other in the middle of the cell.

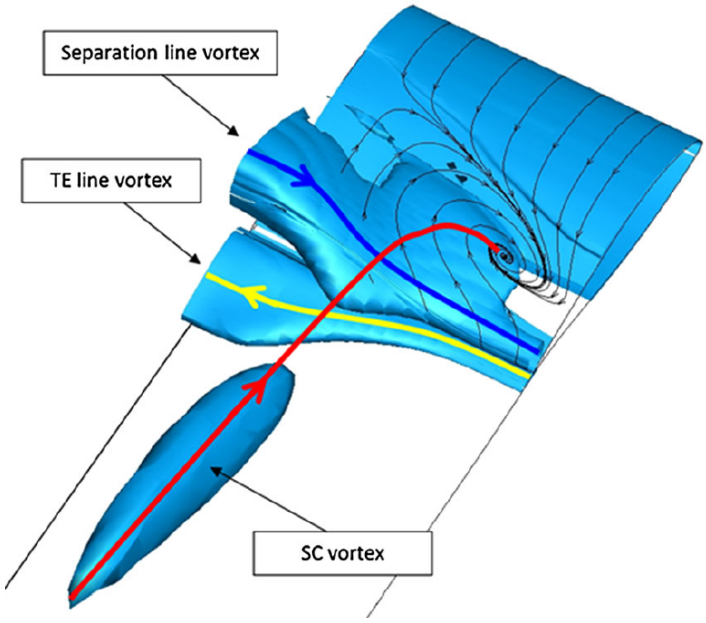

Figure 1.31: The CFD obtained SC structure. Q = 1 iso-surface. Interpreted vortex core lines with vorticity direction are also shown.[92]

Effect of the Reynolds number and the angle of attack In order to identify the conditions that lead to the presence of stall cells, Dell'Orso et al. [36] conducted a parametric study in Reynolds number and angle of attack. The experiments show that the Reynolds number needs to be higher than a critical value to allow the observation of stall cells. For a fixed angle of attack, at low Reynolds number there is no stall cell but passing the critical value, the stall cells abruptly appear. They noted that the critical Reynolds number increases with angle of attack. However, stall cells do not occur at all angles of attack. For each Reynolds number, there is a range of AoA within which stall cells can be observed. In their experiments, it was between 16° and 20° for $Re = 4.5e5$. Moreover, a growth of the stall cells has been observed with the increase of angle of attack.

Unsteadiness of the stall cells At high Reynolds numbers, the stall cells are unsteady in most cases. At $Re = 620000$, Yon and Katz [146] found that the stall cells on a NACA0015 airfoil of AR=3 were oscillating at a frequency ($St \approx 0.04$ where the length of reference is the projected chord) lower than the bluff body vortex shedding ($St \approx 0.15$). Manolesos and Voutsinas [91] observed unsteady stall cells switching between several possible configurations (one unique stall cell, two stall cells or one stall cell and a half). Liu and Nishino [85] realized URANS simulations of a stalled NACA0012 at $Re = 1e6$. They also observed oscillations of the stall cells at low frequency ($St \approx 0.05$ where the length of reference is the projected chord). The separation line between the stall cells was going back and forth. The attached region between the stall cells was growing and decreasing periodically. In that context they observed low frequency modulation of the lift coefficient with an amplitude $\Delta C_L = 0.1$.

1.3.3.2 Dynamic stall on finite wings

Static stall exhibits 3D characteristics. The 2D behavior of dynamic stall presented in 1.3.2.1 should then be modified by 3D stall cells. For finite wing moving in either pitch and/or plunge harmonic motion, tip vortices may also interact with stall cells and complexify the 3D dynamic stall behavior. Hammer et al. [61] investigated the effects of aspect ratio on the dynamic stall of finite wing using Large Eddy Simulation (LES). They analyzed the fluid flow of wings constituted of NACA0012 for three aspect ratios (4, 8 and 16) at a reduced frequency of $k = 0.18$. Figure 1.32 shows the main flow structures that Hammer et al. [61] observed during a dynamic stall cycle of the AR=4 wing. The tip vortices (TV) are visible and reduce the effective angle of attack seen by the sections near the tip. As a consequence, the leading edge vortex (LEV) is weaker near the tip than in the middle. When the downstroke begins, the LEV partially detaches to form an arch vortex (AV) that is still connected to the wing by vortex legs (VL). Finally, when the angle of attack further decreases, the AV completely separates from the wing and forms a ring vortex (RV) that is emitted into the wake.

For higher aspect ratio wings, the flow behavior is different as the tip vortices have less influence. A front view of the 3D flow structure of the AR=16 wing is given in Figure 1.33. The influence of the tip vortices is still visible but is constrained to the near tip regions. In the middle part, instabilities provoke undulations of the vortex tube. As a result, ejections occur first at localized areas. Such stall cells have also been observed experimentally by Winkelmann [144] and Zarutskaya and Arieli [150].

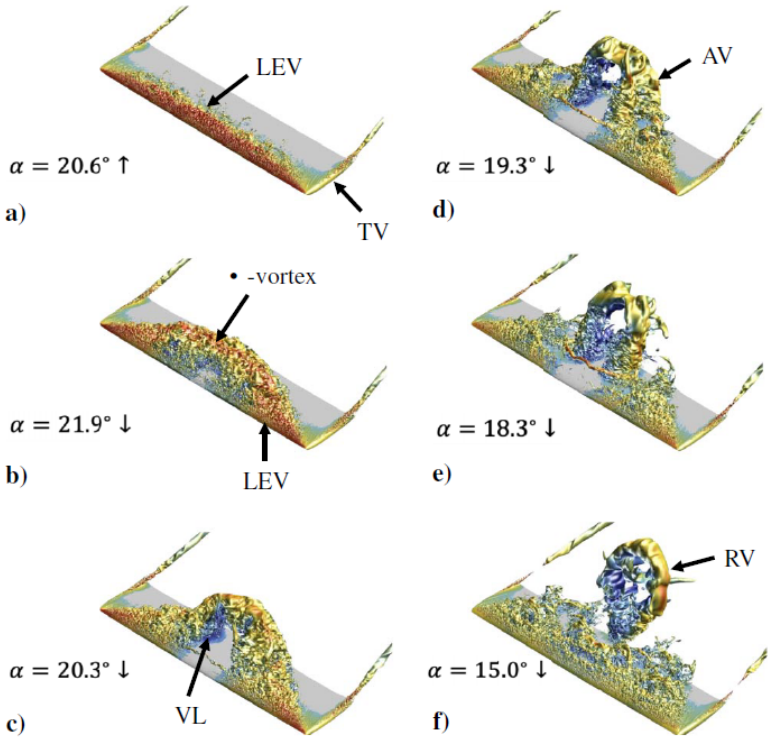

Figure 1.32: Evolution of the instantaneous 3D flow structure of the pitching AR=4 wing using isosurfaces of normalized stagnation density at different instants of the pitching cycle [61]

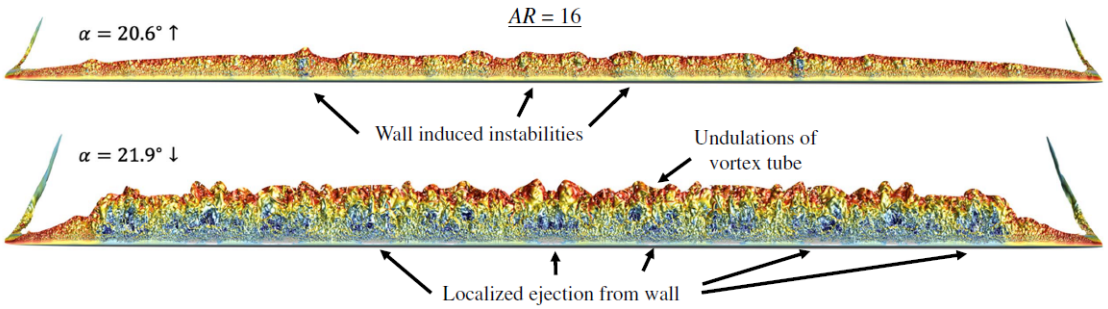

Figure 1.33: Front view of instantaneous 3D flow structure evolution of the AR=16 wing using isosurfaces of normalized stagnation density [61]

Hammer et al. [62] also investigated the dynamic stall over a swept wing of aspect ratio AR=8. A pitching motion of the root section was imposed, and due to the sweep, the tip section of the wing experienced a combined pitch-plunge motion. A flow visualization is given Figure 1.34. As the tip has also a plunge motion, each section along the span experiences an increasing angle of attack. For the motion under study, it leads to a 7.2° difference of angle of attack between the tip and the root of the wing. This inhomogeneity of angle of attack along the span promotes the formation of arch vortices and ring vortices, that were less present in the unswept configuration for large AR. Such mechanisms should also be involved for twisted blade.

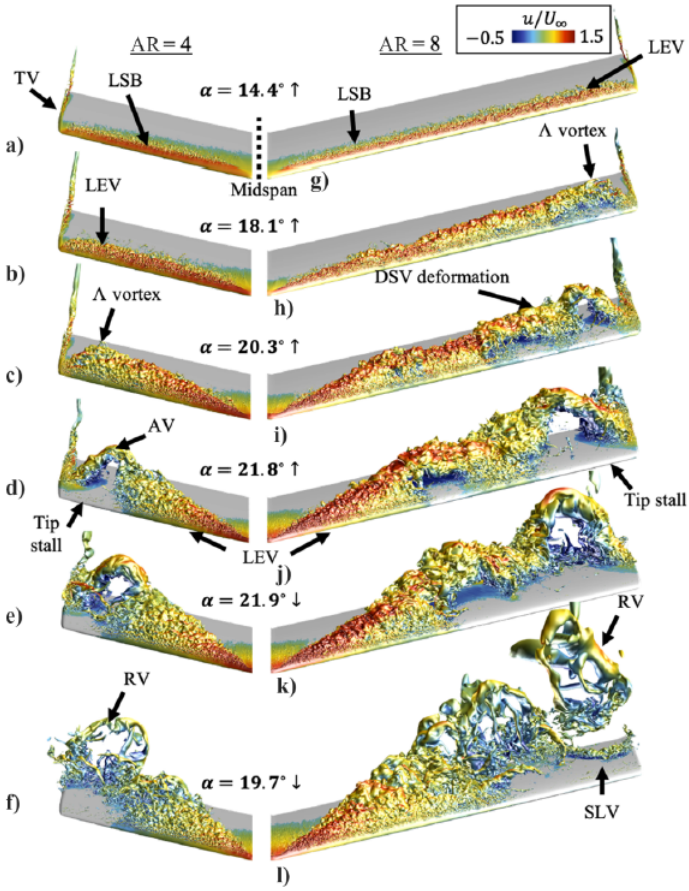

Figure 1.34: Front view of instantaneous 3D flow structure evolution of the AR=8 wing using isosurfaces of normalized stagnation density [62]

Finally, Sørensen and Schreck [128] analyzed the dynamic stall of a wind turbine blade at standstill at a reduced frequency of $k = 0.1$. The behavior of the flow is different as the airfoils of the blade are thicker. There is no LSB burst before the turbulent separation reaches the leading edge. Moreover, the flow is more chaotic due to the atmospheric turbulence.

1.3.4 Aeroelastic studies on SIV

According to Holierhoek [69] there is at least three types of stall-induced vibrations. Each one is associated to a pure motion in either edgewise, flapwise or torsion. It occurs when the vibration of an edgewise, flapwise or torsional mode allow a transfer of energy from the flow to the structure that can not be fully dissipated by the structural damping. Edgewise SIV has been reported for stall-regulated wind turbines by Stiesdal [131] and Anderson et al. [5]. Flapwise SIV has also been reported on stall regulated wind turbines by Lundsager et al. [89]. Both edgewise and flapwise SIV are sometimes addressed using quasi-static formulation for the aerodynamic loading. Such simplified approach, used close to the static stall angle of attack, is however controversial regarding the dynamic stall process. Stall flutter is a dynamic instability in torsion (Figure 1.35) of particular importance for lifting surface operating at high angle of attack. It has then been widely studied for helicopters and wing, but according to Eggleston and Stoddard [44], stall flutter may also occur on wind turbines with flexible pitch control without dampers. In fact, it has been observed in the test of FLEXTEETER test [69]. Unlike SIV in either pure edgewise or flapwise, the stall flutter mechanism for energy transfer totally relies on the dynamic stall process for which the flow separates partially or completely during each cycle of oscillation and produces complex unsteady moment coefficient patterns. Due to the non-linear nature of the aerodynamic load involved, stall flutter is also limited in amplitude, leading to LCOs (Amandolese [2], Dimitriadis and Li [38], McCroskey et al. [95]).

1.3.4.1 Stall flutter

Prediction of stall flutter critical velocity relies on a correct evaluation of the dynamic stall process and induced aerodynamic pitching moment that depend on the airfoil geometry, mean angle of attack and reduced velocity. The amplitude of pitching oscillation also strongly affects the dynamic stall process and is responsible for the aerodynamic saturation mechanism [4, 114], which are parameters that modifies the dynamic stall process. As seen in section 1.3.2, the behavior of the dynamic stall process is far from quasiteady aerodynamics, making it difficult to predict.

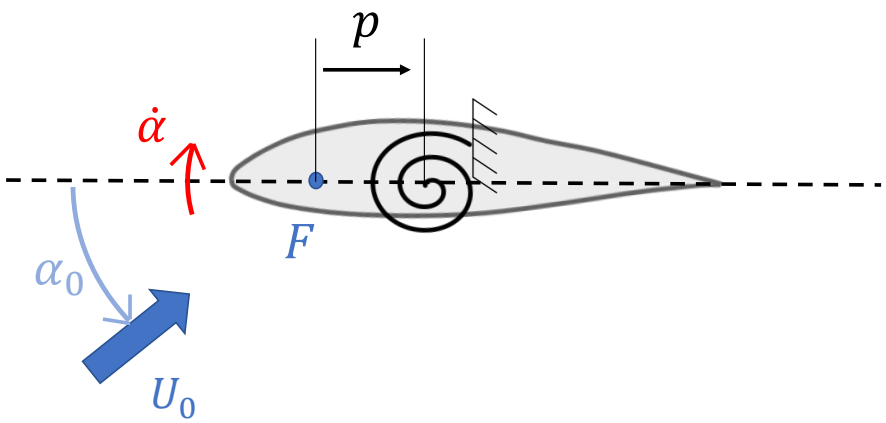

Figure 1.35: Typical section with one degree of freedom in torsion

Validation of numerical methods then relies on experimental dynamic tests mainly performed on section models forced to oscillate in pitch for various mean angles of attack, reduced velocities and amplitudes [7, 83, 147]. Simulating dynamic stall loops in moment allows to evaluate if the work of the aerodynamic loads on the structure is positive or not. A positive work over a cycle is equivalent to a negative aerodynamic damping which can lead to stall flutter if it overcomes the structural damping.

For example, the dynamic stall loop of moment of a NACA0012 airfoil illustrated in Figure 1.17 is reported in Figure 1.36.

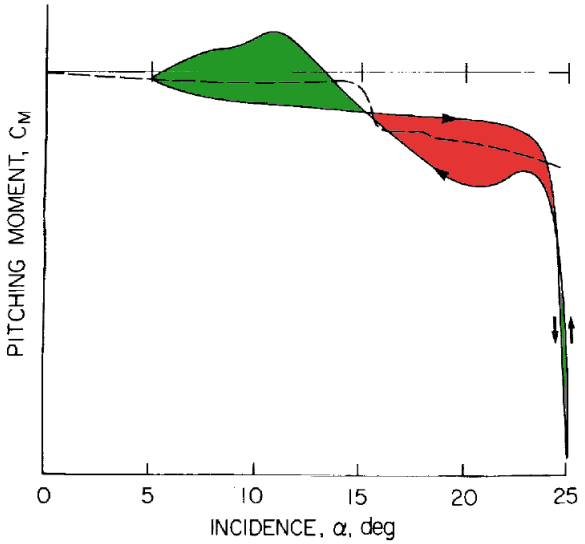

Figure 1.36: Dynamic stall loop of a NACA0012 forced to oscillate in pitch around 15° with an amplitude of 10° and a reduced frequency $k = 0.15$ at $Re = 2.5 \cdot 10^6$ [23].

The work of the aerodynamic loads for a pitching airfoil is:

$$W = \frac{1}{2}\rho c^2 U_0^2 \oint C_M d\alpha$$

It depends on both the area and the direction of rotation of the dynamic stall loops. If the loop is clockwise the work is positive and if the loop is counter-clockwise, the work is negative. In the example (Figure 1.36), the dynamic pitching moment shows two main loops. The counter-clockwise area is colored in green while the clockwise area is colored in red. The energy balance between those two areas will give the sign of the energy transfer. This example highlights the complexity of predicting the energy transfer associated with the dynamic stall process.

Moreover, let us remark that the shape of the dynamic stall loop in moment depends on the amplitude of vibration, which can lead to subcritical Hopf bifurcation, as encountered by Razak et al. [114].

1.3.4.2 Flapwise/Edgewise instability

As mentioned previously both edgewise and flapwise SIV are sometimes addressed using quasi-static formulation for the aerodynamic loading. Such simplified approach is recalled here.

First analytical approach A first simple approach to study SIV is to use a quasisteady aerodynamics approach. It is based on the evaluation of static lift, drag and moment curves at an effective angle of attack, which is an angle of attack corrected with the relative wind speed induced by the movement of the airfoil. By taking any arbitrary direction of vibration x defined by its angle θ with the rotor plane, it is possible to calculate the aerodynamic damping for an airfoil of chord c moving along this direction (Figure 1.37) [135]. The airfoil has an angle of attack α_0 and is placed at an incidence ϕ_0 relative to the rotor plane. It allows to identify the directions at risk and check if they are compatible with some vibration mode directions. The development presented here is a reformulation of the one done by Hansen [64].

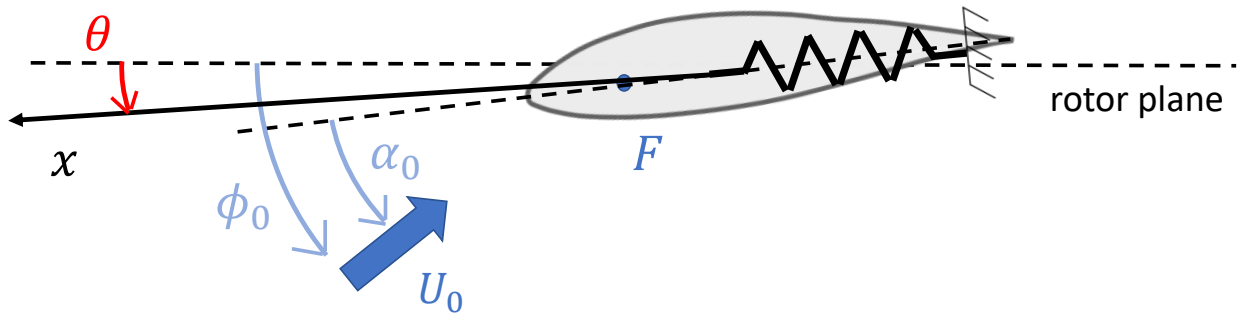

Figure 1.37: A typical blade section with one degree of freedom x(t) in the direction of vibration θ relative to the rotor plane [64]

The aerodynamics is modeled by a quasi-steady approach. It means that the fluid adapts instantaneously to the structure motion. It then consists in calculating an effective wind speed U_{eff} and an effective angle of attack α_{eff} that take into account the velocity of the blade section $\dot{x}$:

$$U_{\text{eff}} = \sqrt{(U_0 \cos\phi_0 + \dot{x}\cos\theta)^2 + (U_0 \sin\phi_0 + \dot{x}\sin\theta)^2} \tag{1.4}$$

$$\alpha_{\text{eff}} = \phi - \phi_0 + \alpha_0 \tag{1.5}$$

where U_0 is the mean wind velocity and ϕ is the effective incidence relative to the rotor plane:

$$\phi = \arctan\left(\frac{U_0 \sin\phi_0 + \dot{x}\sin\theta}{U_0 \cos\phi_0 + \dot{x}\cos\theta}\right) \tag{1.6}$$

The lift and drag are evaluated using these effective wind speed and effective angle of attack. Then the loads are projected onto the direction of vibration:

$$F_x = \frac{1}{2}\rho c U_{\text{eff}}^2 C_L(\alpha_{\text{eff}})\sin(\phi-\theta) - \frac{1}{2}\rho c U_0^2 C_D(\alpha_{\text{eff}})\cos(\phi-\theta) \tag{1.7}$$

This force can be linearized around $\dot{x} = 0$ in order to exhibit an aerodynamic damping coefficient: $F_x \approx F_0 - \eta\dot{x}$. The damping coefficient is given by :

$$\begin{aligned}\eta = \frac{1}{2}\rho c U_0 \Big[& C_D(\alpha_0)(3+\cos(2\theta-2\phi_0)) + \frac{\partial C_L}{\partial\alpha}(\alpha_0)(1-\cos(2\theta-2\phi_0)) \\ & + (C_L(\alpha_0) + \frac{\partial C_D}{\partial\alpha}(\alpha_0))\sin(2\theta-2\phi_0)\Big]\end{aligned} \tag{1.8}$$

Depending on the mean angle of attack and the direction of vibration, each term does not have the same contribution. It is discussed in [64]. Nevertheless, the quasisteady approach has restrictive assumptions. The dimensionless frequency has to be very low in order to use the steady polars. These results cannot be conclusive for higher dimensionless frequencies and, as for stall flutter, further investigations taking into account the dynamic stall process are needed.

Application to the FFA-W3-211 airfoil An example of application of the quasisteady analysis is proposed for the FFA-W3-211 airfoil which is the airfoil of the IEA15MW around 80%. The evolution of the aerodynamic damping with the incidence ϕ_0 and the direction of vibration θ is represented in Figure 1.38, with $\phi_0 = \alpha_0$ and $\frac{1}{2}\rho c U_0 = 1$. Around 0° of incidence, the aerodynamic damping is positive for any directions of vibration. The aerodynamic damping may be negative when the airfoil is stalled. It is the case around 20° and -30° of incidence. The minimum aerodynamic damping is found around 20° of incidence for a direction of vibration of -50°. In practice, the preferential directions of vibration are determined by the structural modes. The flapwise vibrations are near $\theta = 90°$ while the edgewise vibrations are around $\theta = 0°$. For both directions, negative aerodynamic damping can be encountered.

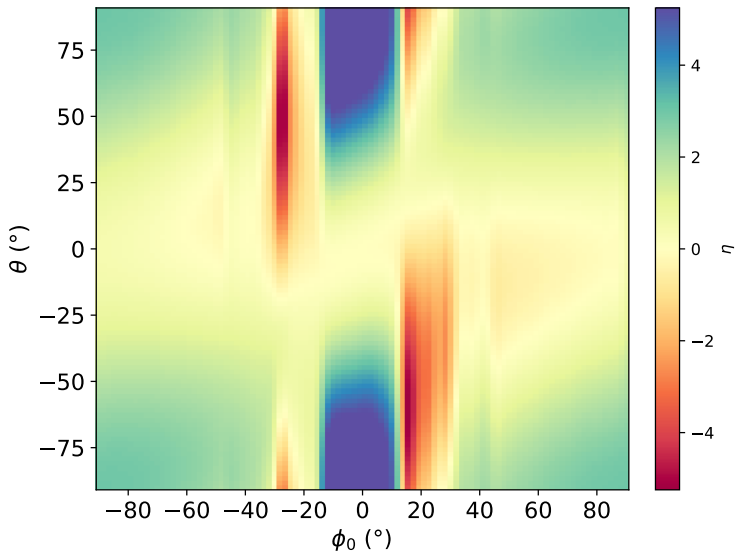

Figure 1.38: Evolution of the aerodynamic damping of the FFA-W3-211 airfoil with the incidence ϕ_0 and the direction of vibration θ for stall-induced vibrations in linear translation.

It is proposed here to compute the critical velocity for two potentially unstable configurations : ($\Phi_0 = 20°$, $\theta = 90°$ flapwise) and ($\Phi_0 = 20°$, $\theta = 0°$ edgewise). The linearized dynamic equation on the x direction writes:

$$\ddot{x} + \left(2\omega_0\xi + \frac{\eta}{m}\right)\dot{x} + \omega_0^2 x = F_0 \tag{1.9}$$

where ξ is the structural damping and ω_0 is the pulsation of either the flapwise or the edgwise mode.

The system becomes unstable if a negative aerodynamic damping overcome the structural damping:

$$2\omega_0\xi + \frac{\eta}{m} = 0$$

By injecting the expression of η (Equation 1.8) with the term under bracket noted $C_A(\phi_0, \theta)$,

it gives the critical reduced velocity:

$$\mathcal{U}_R = \frac{U_c}{c\omega_0} = -\frac{4}{C_A(\phi_0,\theta)} S_c \tag{1.10}$$

where U_c is the critical wind speed and the Scruton number $S_c = \frac{\xi m}{\rho c^2}$ has been introduced. Thus, it appears that for given conditions, the critical reduced velocity is proportional to the Scruton number and strongly depends on the sign and value of $C_A(\phi_0, \theta)$.

Taking the section at 80% of the IEA15MW blade, numerical values of the critical velocity can be estimated for our two configurations: ($\Phi_0 = 20°$, $\theta = 90°$ flapwise) and ($\Phi_0 = 20°$, $\theta = 0°$ edgewise). The chord c is 2.8m, the mass per meter m is 129.3kg/m and the structural damping ξ is 3%, leading to a Scruton number Sc of 0.4. For the flapwise mode, $C_A(\phi_0 = 20°, \theta = 90°) = -1.59$, while for the edgewise mode, $C_A(\phi_0 = 20°, \theta = 0°) = -0.9$. Thus, the critical reduced velocity is equal to 1 for the flapwise mode and 1.78 for the edgewise mode. Finally, using the frequency of the modes (0.51Hz for the flapwise and 0.71Hz for the edgewise), we obtain a critical velocity of 9m/s for the flapwise mode and 22.2m/s for the edgewise mode. Based on this quasisteady approach, it appears that the instability first rises on the flapwise mode.

However, as for stall flutter, further investigation of the potential instabilities addressing the dynamic stall process are required because, as for stall flutter, the dynamic stall loops should also have a large impact on the aerodynamic damping.

Investigations of SIV for wind turbine SIV were first reported by Moeller [98] for stall-regulated wind turbines. Several blades of 19m long have been damaged by serious longitudinal cracks due to severe edgewise vibrations. It apparently starts for winds of 16-17 m/s [98]. Numerous research works thus concern wind turbines in operation (i.e. rotating blades without yaw). Chaviaropoulos [25] investigated such vibrations using a section model approach combining flap/lead-lag (i.e. flap/edgewise) motion and the ONERA dynamic stall model. The stability of the system has been investigated through linearization and eigenvalue analysis. As it was reported by Moeller [98], the edgewise mode of vibration can become unstable, but it also appeared that the flapwise mode can turn unstable for low reduced rotational velocity $\kappa = \frac{\Omega c}{U_0}$ (where Ω is the rotational speed, c is the chord and U_0 is the wind speed) [25]. The analysis was extended to a full blade in [26] by using a finite beam element model coupled with the ONERA dynamic stall model. It was confirmed that the first lead-lag (edgewise) and flapwise modes can be unstable for wind speed higher than 15m/s. With quasisteady aerodynamics, the edgewise mode was unstable for the same wind speeds but the flapwise mode stayed stable. In the VISCEL project [27], CFD tools have also started to be employed in the study of SIV for "rotating" wind turbine. 2D URANS simulations coupled with blade section model have been conducted. It was highlighted that the aerodynamic damping prediction was in good agreement between URANS results and the ONERA model, leading to the same condition of stability in terms of reduced rotational velocity: the system was unstable for $\kappa < 0.06$. However, it was not precised if the instability came from the flapwise or the edgewise mode. In the KNOW-BLADE project [109], 3D URANS simulations coupled with full wind turbine blade structural model were realized. The flapwise mode was stable because the reduced rotational velocity was higher than 0.1 and the edgewise mode was neutrally stable (damping near zero). It is coherent with the previous studies where the edgewise mode was found unstable with a damping close to zero for $\kappa > 0.1$. Sarkar and Bijl [119] also explored the influence of structural stiffness, the effects of initial conditions and geometric structural nonlinearity using a section model approach and the ONERA dynamic stall model. They found that an initial perturbation can make the flapwise direction unstable for $\kappa > 0.06$ while it is stable without

the perturbation. Moreover, it has been observed that higher flexibility can produce nonlinear behavior like period-3 attractor.

The growing interest for pitch-regulated wind turbines that are not concerned by SIV in operation significantly reduced SIV studies. However, pitch-regulated wind turbine are still prone to aeroelastic instabilities at standstill. With the increase in diameter and flexibility of the blades, SIV could also become a concerning issue. Politis et al. [110] realized a linear stability analysis on an isolated parked 40m blade of the UPWIND project, with wind coming from any direction. Using a quasi-steady aerodynamics formulation, results have shown that the first flapwise mode became unstable in a narrow stalled region encountered for yaw between 9° and 13° for any wind speeds, because structural damping was not taken into account. The edgewise mode were also negatively damped and unstable, for any wind speed, in a larger stalled region encountered for yaw between 8° and 120°. A comparison was also done with the results obtained using the ONERA dynamic stall model under strip theory assumption for yaw between -15° and 30°. It was shown that the quasi-steady aerodynamic model underestimated the negative aerodynamic damping associated to the unstable edgewise mode for yaw between 8° and 30° for all the wind speed studied (<70m/s). For the flapwise mode, the minimum negative damping predicted with the ONERA model was similar to the one obtained with the quasisteady aerodynamics, but the unstable conditions covered a wider range of yaw going from 9° to the largest yaw studied (30°). A 2D CFD study has been conducted by Skrzypiński et al. [127] on the DU96-W-180 airfoil section at 24° angle of attack, forced to oscillate in translational motion along the edgewise direction, for various reduced velocities. Positive fluid-structure energy transfer were observed in two distinct regions. The first one, associated to a Karman vortex wake loading was for reduced velocities $\mathcal{U}_R = U_0/c\omega$ from $1/2\pi$ up to $15/2\pi$. The second, for $\mathcal{U}_R > 44/2\pi$, was attributed to a stall-induced loading. Skrzypiński and Gaunaa [124] have further explored the aerodynamic damping on a 2D section. They found out that the lag in the aerodynamic response is a key parameter controlling the aerodynamic damping as an increase of the time lag can significantly increase the damping in the deep stall region and thus reduce the range of incidence where the edgewise mode is unstable. Wang et al. [141] investigated numerically the stall-induced vibration of a full DTU 10MW wind turbine in idling operation (i.e. very low RPM of 0.8rpm in average). They conducted a temporal simulation with the ONERA dynamic stall model at 30° yaw and 42.5m/s wind speed that exhibited severe edgewise vibrations. Then, they proceeded to eigenvalue stability analysis using either a quasi steady aerodynamics or ONERA dynamic stall model. For both models, the damping of the rotor modes were depending on the azimuth position of the rotor, but in general the ONERA model predicted higher damping than quasisteady aerodynamics. It is however in contradiction with the results obtained by Politis et al. [110] for a isolated blade. Moreover, the eigenvalue analysis of Bir and Jonkman [16], Wang et al. [141] shows that the damping of the out of plane (edgewise) modes are negative for a larger range of incidence than the in-plane (flapwise) modes, explaining the edgewise vibrations observed in the temporal simulation. The stability of the full 15MW wind turbine at standstill has been explored by Loubeyres et al. [87], using a quasi-static aerodynamic formulation under the strip theory assumption. Unstable yaw ranges were identified in stall. The vibrations observed were a combination of the edge and flap modes. Bangga et al. [10] compared the effect of the Beddoes-Leishman dynamic stall model and the IAG model on the vibrations of the full IEA15MW wind turbine in idling operation with yaw misalignment. They have reported that the dynamic stall models have a large influence on the amplitude of vibration.

To further investigate this phenomenon, some experimental studies were conducted. Chen et al. [28] have carried out an on-site vibration experiment with a 137m radius wind turbine at idling state. Fluctuations in the edgewise bending moment have been observed for wind speed around 18m/s and wind deviation around $-20°$. Gao et al. [54] focused on wind tunnel test of a

scaled model of blade and explored the blade behavior for wind coming from any direction. They observed flapwise vibration when the blade was in the near stall region. Moreover, it has been noted that the turbulence has a significant influence on the vibration level [143].

Limits Previous studies have highlighted that large wind turbine blades can be prone to SIV at standstill in either flapwise, edgewise or a combination of flapwise and edgewise modes. Risk assessment requires experiments or relevant FSI simulation for different wind conditions (direction and speed). The former are very rare and the latter are still too fragmentary using high-fidelity approach. In this context, the majority of works are based on either quasi-steady or semi-empirical dynamic stall models coupled with either a sectional or a full blade model. If the validity of both those low-fidelity approaches still needs to be clarified, it is clear that they can not be used to fully understand such a complex, 3D, unsteady and coupled phenomenon. More details can be obtained with coupled 3D CFD-CSM simulations but this kind of study is lacking concerning stall-induced vibrations.

1.4 Conclusion

In this chapter, an overview of the main aeroelastic phenomena that a wind turbine can experience has been given. The coupled-mode flutter is a destructive instability occurring when two structural modes couple through the flow. For actual wind turbine designs, this flutter velocity is above the operational regime [111]. At standstill such a dynamic instability may also occur at very high velocity [19]. Anyway, this aeroelastic problem can be addressed using a linear structure solver coupled with a linear fluid solver. For the latter, either analytical unsteady aerodynamics formulations or unsteady potential solvers can be used. VIV is also to be studied as it can concern low wind speed under a relatively large range of wind directions around 90° angle of attack. It has been shown that high fidelity approaches could be of interest in that context, in particular to highlight the complex unsteady 3D wake behavior. The impact of the incoming turbulence is however an important issue. Finally, stall-induced vibration also concerns wind turbines in standstill position. It may happen under yaw misalignment around 20° for high wind speeds. The conditions triggering the aeroelastic instabilities are summarized in Figure 1.39. And the Table 1.1 summarized values of critical speed of the aeroelastic instabilities found in the literature.

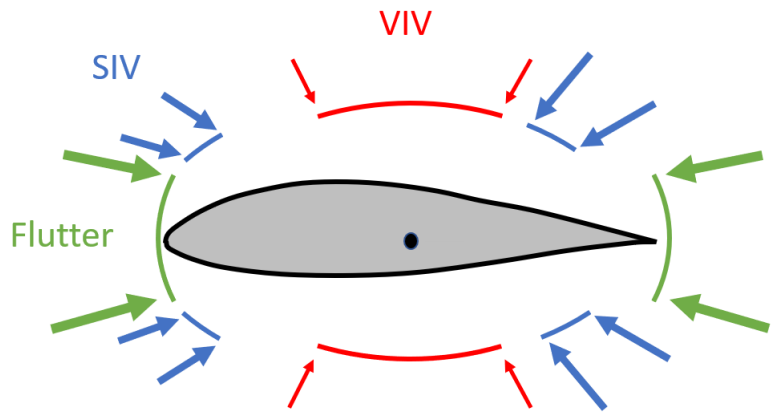

Figure 1.39: Schematic representation showing the wind direction likely to trigger aeroelastic instabilities. The range of direction depends on the airfoil. The size of the arrow gives an idea of the critical velocity. Small arrow means low critical velocity.

Wind turbine	VIV	SIV	Flutter | flutter ratio
5MW	40 - 50 m/s [40]	<50 m/s [16]	20 - 24 rpm | 1.65 - 2 [58, 64, 111] 230 m/s [19]
10MW	16 - 26 m/s [67] 18 m/s [71]	<42.5 m/s [141]	| 1.4 - 1.6 [72]
15MW	?	<45 m/s [87]	6.87-13.51 rpm | 0.91-1.79 [45, 82, 116]

Table 1.1: Table of the critical velocity for three aeroelastic instabilities

Based on this literature review, it has been identified that among coupled-mode Flutter, VIV and SIV, the phenomenon that was the most lacking of understanding and high-fidelity details was the SIV. That's why, it has been decided to focus on SIV during this thesis.

Chapter 2

Numerical methods for high-fidelity aeroelasticity simulations

In aeroelasticity, the fluid and the structure dynamics interact. Thus, it is necessary to simulate both physics, using one as boundary conditions for the other. Several ways allow to do it numerically. The objective of this chapter is to present the procedures, models and numerical methods that can be used to simulate an aeroelastic response. It mainly concern high fidelity approaches.

Contents

2.1 General fluid structure coupling 45
2.2 Fluid solver : FastS 46
2.2.1 Numerical schemes 46
2.2.2 Arbitrary Lagrangian Eulerian formulation 48
2.2.3 Chimera method 49
2.3 Mesh Deformation : Quantum 49
2.4 Structural solver : Project Chrono 50
2.4.1 Data entry of the beam model 50
2.5 Spatial coupling between a fluid solver and structural solver 51
2.5.1 Conservative vs Consistent approach 52
2.5.2 Transfer methods 53
2.6 Temporal coupling 55
2.6.1 Static coupling 55
2.6.2 Dynamic coupling 55
2.7 Summary 57

2.1 General fluid structure coupling

There are two main approaches to deal with multi-field problems involving different physical domains. The monolithic coupling approach regroups the different physics in one single system and solves all together. In contrast to this, a partitioned coupling approach solves the different physics separately and the interaction is achieved by exchanging the necessary data through a common interface [68, 116].

Monolithic coupling

The monolithic approach is usually used for specific coupling problems. The full system of equations is rather inflexible making this approach computationally challenging and software-wise unmanageable for industrial application [107]. It is mostly used in an academic context in order to allow a detailed mathematical analysis [68].

In the present work, a monolithic approach is used in the Chapter 4 with a sectional model. But the high-fidelity simulations of Chapter 5 are using a partitioned approach.

Partitioned coupling

From a numerical point of view, the partitioned approach has several advantages over the monolithic approach. Since the subsystems are treated independently, it is possible to use well-tested stand-alone solvers specialized for each domain of the global system. This approach is quite flexible and allows software modularity. In return, partitioned approaches need additional models to deal with the interactions between the solvers [68, 116]. It is also generally harder to achieve orders of convergence as good as with monolithic solvers. Moreover, with monolithic approaches it is possible to use very efficient Newton solvers that use the full Jacobian of the coupled system, whereas in partitioned approaches it is very difficult to assemble such Jacobian matrix.

In aeroelasticity, the fluid solver computes the flow behavior and provides the fluid loading (i.e. the wall pressure and shear stress). Then a loads transfer module transforms this fluid loading into the loads format accepted by the structural solver. This one deforms the structure accordingly to its loading. Finally, a motion transfer module moves the fluid interfaces based on the structure position. With CFD, the boundary conditions are moved and the mesh is also deformed. A scheme of this procedure is presented in Figure 2.1.

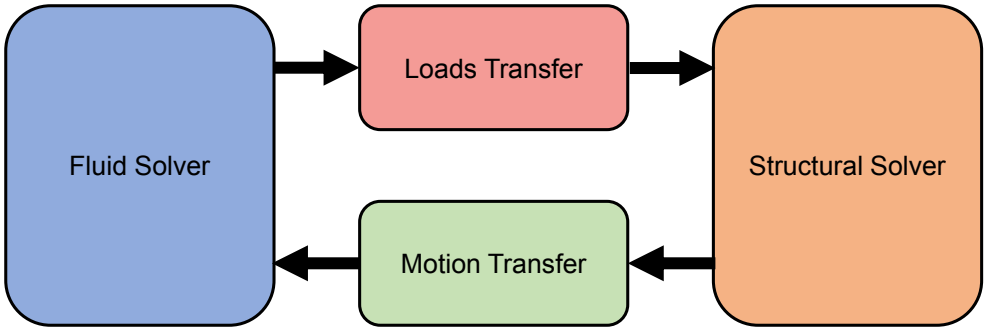

Figure 2.1: Scheme of the partitioned coupling

In the following, each step, represented by a block, is explained.

2.2 Fluid solver : FastS

The CFD solver used in the present study to simulate the fluid dynamics is the solver FastS developed at ONERA [78]. It is a research solver optimized for structured mesh that can realize (U)RANS, LES and (U)RANS/LES simulations. The solver is able to handle chimera mesh.

The numerical schemes used are presented. Then, a brief explanation of the Arbitrary Lagrangian Eulerian (ALE) formulation is given. Next, the chimera method is tackled.

2.2.1 Numerical schemes

The compressible Navier-Stokes equations are resolved using finite volumes discretization technique. It consists in subdividing the space with a mesh and solving the conservative form of the Navier-Stokes equations in each volume. The average value of the flow quantities in a volume is then obtained by summing all the fluxes at each of its faces over time.

Discretization of the fluxes Three numerical schemes for the discretization of the fluxes are available: the Roe scheme, the AUSM+(P) [43, 94] and a "sensor" scheme based on the AUSM scheme. The scheme that will be used for the simulations is the AUSM+(P) because it allows to do low Mach simulations with the compressible equations. This advantage comes from the split of the inviscid flux $\mathbf{F}_{i+\frac{1}{2}}$ into a convective contribution $\mathbf{F}^{\text{conv}}_{i+\frac{1}{2}}$ and a pressure contribution $\mathbf{F}^{\text{press}}_{i+\frac{1}{2}}$.

$$\mathbf{F}_{i+\frac{1}{2}} = \mathbf{F}^{\text{conv}}_{i+\frac{1}{2}} + \mathbf{F}^{\text{press}}_{i+\frac{1}{2}} \tag{2.1}$$

Each contribution is processed separately. The convective flux contains the part linked to the mass flow.

$$\mathbf{F}^{\text{conv}}_{i+\frac{1}{2}} = \dot{m}_{i+\frac{1}{2}} \begin{bmatrix} 1 \\ u_{i+\frac{1}{2}} \\ v_{i+\frac{1}{2}} \\ w_{i+\frac{1}{2}} \\ H_{i+\frac{1}{2}} \end{bmatrix} \tag{2.2}$$

The values of u, v, w and H are taken either from the left state or right state of the face depending on the direction of the flow.

The mass flow is based on a split Mach number.

$$\dot{m}_{i+\frac{1}{2}} = a_{i+\frac{1}{2}} \left(M^{+}_{L} \rho_L + M^{-}_{R} \rho_R \right) \tag{2.3}$$

where a is the sound velocity, ρ is the density and $M^{\pm}$ are polynomials of the Mach number of the left (L) or right (R) state.

The pressure flux models the acoustics.

$$\mathbf{F}^{\text{press}}_{i+\frac{1}{2}} = \begin{bmatrix} 0 \\ p_{i+\frac{1}{2}} n_x \\ p_{i+\frac{1}{2}} n_y \\ p_{i+\frac{1}{2}} n_z \\ p_{i+\frac{1}{2}} u^n_{i+\frac{1}{2}} \end{bmatrix} \tag{2.4}$$

where (n_x, n_y, n_z) is the normal of the face and $p_{i+\frac{1}{2}}$ is calculated from the left and right pressure state and polynomials of the Mach number.

Unsteady Reynolds averaged Navier-Stokes In RANS equations, the flow variables are separated into a mean component and a fluctuating component. It simplifies the Navier-Stokes equations but a Reynolds stress tensor, describing the turbulence, still remains. To close the equations, this Reynolds stress tensor needs to be modeled by additional equations. RANS simulations only allow to compute a stationary flows. To compute unsteady flows, it is possible to keep the variables decomposition in a mean component and a fluctuating component but relax the hypothesis that the mean flow is independent of time. This way the temporal derivative of the mean velocity is kept in the URANS equations and large turbulent structures can be computed.

The turbulence model In *FastS*, the turbulence is modeled with the Spalart-Allmaras model [129]. First, the Reynolds stress tensor is assumed to follow the Boussinesq assumption that introduced a turbulent viscosity. The Spalart-Allmaras model is a one equation model that gives temporal and spatial evolution of this turbulent viscosity.

URANS simulations with the Spalart-Allmaras model are effective to simulate attached or slightly detached flows around wings and blades [7]. For stall-induced vibrations, if the angle of attack is too large, the flow can widely detach. In such cases, higher fidelity models like ZDES are needed [14]. ZDES is available in *FastS* but it requires much more resources due to the necessity of a fine mesh. In order to limit the computational cost, it has been decided to focus on the range of angle of attack in the near stall region that still can be simulated with URANS. A validation will be proposed in Chapter 3.

The temporal scheme The temporal scheme used in FastS is the Gear scheme [55, 56]. It is based on a backward differentiation formula that uses two previous time steps to compute the flow solution $\mathbf{Q}^{n+1}$ at time t_{n+1}. By using the Gear scheme to evaluate the time derivative of the Navier-Stokes equations, it gives:

$$\frac{3\boldsymbol{Q}^{n+1} - 4\boldsymbol{Q}^{n} + \boldsymbol{Q}^{n-1}}{2\Delta t} = -\boldsymbol{R}(\boldsymbol{Q}^{n+1}) \tag{2.5}$$

where $\mathbf{R}(\mathbf{Q}^{n+1})$ is the residual at time t_{n+1} which makes the Gear scheme implicit.

As a result, the Gear scheme is unconditionally stable as long as the spatial discretization is stable. Equation 2.5 is nonlinear, thus a Newton method has to be used to compute the solution at each time step. More details on the resolution are given by Suss [132].

For steady simulations, the resolution of the non-linear system with the Newton method does not converge well [32]. To improve the convergence, an additional terms with a local pseudo time step $\Delta\tau$ is added:

$$\left(\frac{1}{\Delta\tau}\mathbf{I} + \mathbf{A}\right)\Delta\boldsymbol{Q}^{n+1} = -\boldsymbol{R}(\boldsymbol{Q}^{n+1}) \tag{2.6}$$

where $\mathbf{I}$ is the identity matrix, $\mathbf{A}$ is the Jacobian matrix associated to the residual $\boldsymbol{R}$ and $\Delta\boldsymbol{Q}^{n+1} = \boldsymbol{Q}^{n+1} - \boldsymbol{Q}^{n}$. The local pseudo time step is chosen so that the CFL is constant over the domain. Typically, a CFL around 5 is chosen.

2.2.2 Arbitrary Lagrangian Eulerian formulation

In structural mechanics, the common approach is the lagrangian. A set of material points of the solid are chosen and grouped into a mesh that follows the deformations of the solid. Each material point moves with the structure in such a way that a point always refers to the same part of the solid. However, in fluid mechanics, if the mesh follows the fluid particles, it will rapidly be distorted. That's why, it is more convenient to use Eulerian formulation. The mesh is fixed in space and at each position the evolution of the velocity is observed over time. In aeroelasticity, both solid and fluid are present. There are several ways to accommodate with this difference. For example, the immersed boundary method keeps the lagrangian formulation for the solid and the eulerian for the fluid. Within the fluid solver, a cartesian grid fills all the space and the presence of the solid is added through source terms of loads. But in FastS, the solution chosen is to use an arbitrary lagrangian eulerian formulation. The mesh is body fitted, thus the boundary conditions follow the structure motion and the mesh deforms. The ALE formulation allows to adapt the eulerian formulation in case of moving grid. Compared to the eulerian formulation, an additional term

with the grid velocity allows to pass from an eulerian formulation if the grid velocity is zero to a lagrangian formulation if the grid velocity is equal to the flow velocity. Thus, the ALE formulation is an in-between. A demonstration can be found in [50, 105].

2.2.3 Chimera method

Mesh deformation is numerically costly. The idea is then to only deform the mesh around the structure. Thanks to the chimera method, it is possible to do it by using several grids. The grid that will be deformed can be limited to a small area around the structure and immersed in a cartesian grid. The communication between the grids is handled by interpolations. Some cells of the cartesian grid are not calculated in regions already calculated by an other grid, these cells are said masked. The overlapping regions of interpolation need to be large in order to interpolate the cells of one grid with calculated cells of the other grid and not other interpolated cells. An example is given for a cylinder in the Figure 2.2.

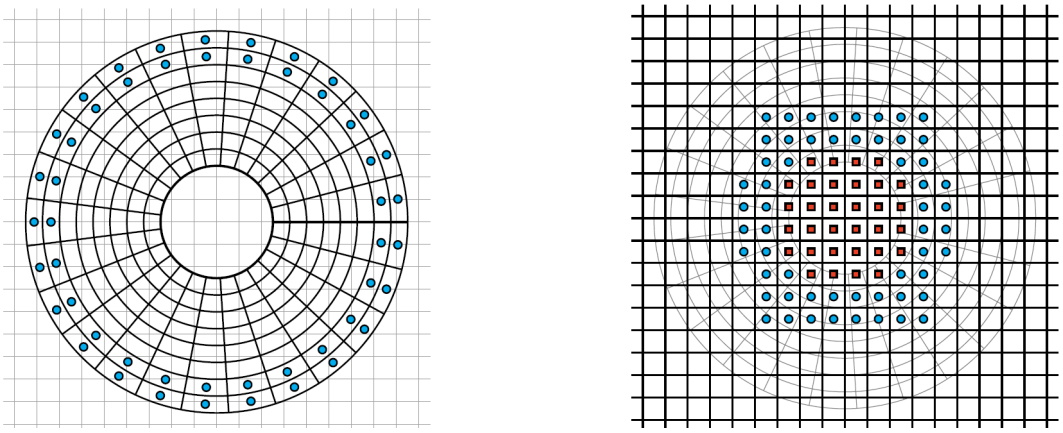

(a) Point of view of the cylinder mesh

(b) Point of view of the cartesian grid

Figure 2.2: Illustration of the chimera method. The interpolated cells are in blue and the masked cells are in red. [96]

2.3 Mesh Deformation : Quantum

It exists several methods to deform a mesh. It is possible to use structural analogy by placing a spring at each edge and solving the system or by using finite element method as in CSM. However, the mesh deformation module used, Quantum, is based on Inverse Distance Weighting interpolation (IDW) on the quaternions. The advantage of Quantum is that it allows large deformations while maintaining the orthogonality of the mesh near the boundaries.

First, the displacements of the points of the moving boundary condition are separated in a translation part and a rotational part. Each part needs to be propagated into the volume in order to deform the mesh. The Inverse Distance Weighting interpolation method consists in evaluating the translation part and rotational part of each point of the mesh separately in function of the displacement of all the boundary nodes depending on their distance.

In its simplest form, the IDW can be written for the translation as:

$$u(x) = \frac{\sum_{k=0}^{N} w_k(x) u_k}{\sum_{k=0}^{N} w_k(x)} \tag{2.7}$$

with $w_k(x) = \frac{1}{d(x,x_k)}$

However, the rotation can not be propagated as easily because rotational matrices can not be summed in 3D. The choice made in Quantum is to use quaternions in order to describe the rotations. The mathematical framework of the Lie algebra then permits the propagation of the associated vector of the Lie algebra into the volume. More details are given in [93].

Such a mesh deformation method allows the mesh to preserve its orthogonality near the boundary.

2.4 Structural solver : Project Chrono

For a wind turbine blade, a beam model seems appropriate and the Euler-Bernoulli corotational beam solver included in *projectChrono* [115] has been chosen. The model used in the solver is described in [49]. The corotational formulation consists in decomposing the motion of each element into a rigid motion and a motion of deformation. The rigid motion is described by the movement of a corotational frame attached to the element, thus the rotation can be as large as wanted. Then the deformation is resolved in the corotational frame (Figure 2.3). This way, the hypothesis of small perturbation can be taken in this local frame. Finally, the local quantities are transformed to the global coordinate frame in order to be assembled into the global system matrices.

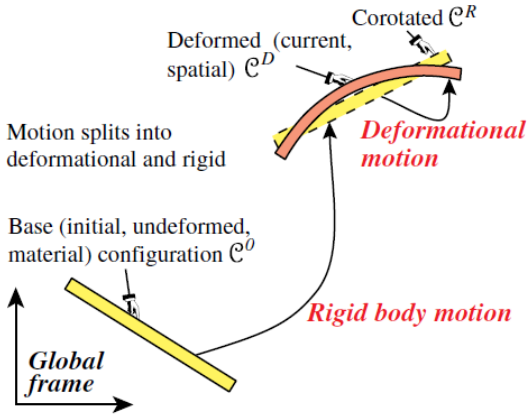

Figure 2.3: The corotational kinematic description [49]

The structural system is solved by finite element method and the temporal scheme is constant-average-acceleration version of the Newmark integration scheme ($\gamma = 1/2$ and $\beta = 1/4$). Moreover, as the stiffness matrix depends on the beam state due to large rotations, a Newton-Raphson method is used for the non-linear systems at each time step.

2.4.1 Data entry of the beam model

To initialize the beam model, the mass and stiffness properties of each element have to be set. As the wind turbine blade is a complex geometry made of composite material, there are flexion-torsion coupling and flexion-flexion coupling. The needed properties are:

- Axial rigidity EA and Torsion rigidity GJ
- Flexion rigidity in Y EI_y and Flexion rigidity in Z EI_z
- Section rotation θ_p
- Position of the centroid (y_C, z_C)

- Position of the shear center (y_S, z_S)
- Mass per unit length ρA
- Inertia in X J_{xx}
- Inertia in Y I_{yy} and Inertia in Z I_{zz}
- Product of inertia I_{xy}
- Position of the center of mass (y_G, z_G)

The couplings come from the section rotation, the product of inertia and the positions of the centroid, shear center and mass center.

The data available in the github[1] of the IEA are the sectional mass and stiffness matrices along the blade. The previous properties are obtained from the matrices using the procedure given in the OpenFAST documentation [2] and [11]. The validation of the structural model is proposed in the Chapter 3.

2.5 Spatial coupling between a fluid solver and structural solver

To couple a fluid solver with a structural solver, aerodynamic loads computed by the fluid solver need to be transformed into structural loads accepted by the structural solver. The displacements computed by the structural solver also need to be transferred to the fluid solver. The transfer methods deal with satisfying the kinematic and dynamic boundary conditions at the interface Γ given by:

$$\mathbf{u}_f = \mathbf{u}_s \quad \text{on} \quad \Gamma, \tag{2.8}$$

$$p_s \mathbf{n}_s = p_f \mathbf{n}_f \quad \text{on} \quad \Gamma, \tag{2.9}$$

where $\mathbf{u}_{f,s}$ are the displacements of the fluid and structure respectively at the interface and $p_{f,s}$ are the stress tensors at the interface [33].

These boundary conditions can be formulated in the discrete form as:

$$\mathbf{U}_f = H_{fs} \mathbf{U}_s \tag{2.10}$$

$$\mathbf{P}_s = H_{sf} \mathbf{P}_s \tag{2.11}$$

where H_{fs} and H_{sf} are the transformation matrices between the flow and structure interface. These matrices depend on the transfer methods chosen. The way to transfer aerodynamic loads is not exactly the same if it is toward a structural finite element model or a beam model. $\mathbf{U}$ and $\mathbf{P}$ contain the discrete values of the displacements and the stress tensor. They are defined by the approximations:

$$\mathbf{u}(\mathbf{x}) = \sum_{i=1}^{n^u} N^i(\mathbf{x}) \mathbf{U}_i, \quad p(\mathbf{x}) \mathbf{n}(\mathbf{x}) = \sum_{j=1}^{n^p} D^j(\mathbf{x}) \mathbf{P}_j \tag{2.12}$$

where $N(x)$ is a function that depends on the spatial discretization method used for the displacement and $D(x)$ is a function that depends on the discretization method used for the pressure and shear stress [33].

[1] https://github.com/IEAWindTask37/IEA-15-240-RWT

[2] https://openfast.readthedocs.io/en/v3.5.3/_downloads/fd7a8bc10f2371a50828391f75170032/beamdyn_inputs_sectional_props.pdf

When a CFD solver is used, the mesh has to be deformed accordingly to the structural solver. It can be done either directly in the volume based on the structural mesh displacement or by moving the fluid interface in a first step and then deforming the volume mesh.

2.5.1 Conservative vs Consistent approach

Conservative approach

The conservative approach consists in implementing a coupling that conserves the energy over the interface. It means that:

$$\int_{\Gamma_f} \mathbf{u}_f \cdot p_f \mathbf{n}_f ds = \int_{\Gamma_s} \mathbf{u}_s \cdot p_s \mathbf{n}_s ds \tag{2.13}$$

Combining Equation 2.12 with Equation (2.13) and developing:

$$\int_{\Gamma_f} \mathbf{u}_f \cdot p_f \mathbf{n}_f ds = \sum_{j=1}^{n_f^p} \left[\sum_{i=1}^{n_f^u} \mathbf{U}_{f_i}^T \left(\int_{\Gamma_f} N_f^i D_f^j ds \right) \right] \mathbf{P}_{f_j} = \mathbf{U}_f^T M_{ff} \mathbf{P}_f \tag{2.14}$$

Doing the same thing for the right hand side, it can be found that the energy is conserved when:

$$\mathbf{U}_f^T M_{ff} \mathbf{P}_f = \mathbf{U}_s^T M_{ss} \mathbf{P}_s \tag{2.15}$$

It then imposed the transformation of pressure over the interface:

$$H_{sf} = M_{ss}^{-1} H_{fs}^T M_{ff} \tag{2.16}$$

This results obtained by De Boer [33] is the same that the one obtained by Farhat et al. [47].

Unfortunately, although the conservation of energy over the interface is desirable, it can lead to unphysical oscillations in the pressure forces [33, 116].

Consistent approach

The consistent approach consists in exactly interpolating the displacements and the loads over the interface. This means that the row-sum of H_{sf} and H_{fs} should be equal to one. In the conservative approach, it is the case for H_{fs} as it is calculated with a transfer method but in general it is not the case for $H_{sf} = M_{ss}^{-1} H_{fs}^T M_{ff}$.

To ensure a consistent interpolation of the pressure, the matrix H_{sf} can be directly obtained by using one of the transfer methods. Thus H_{sf} is independent of H_{fs} and both can be consistent interpolations. However, it means that global conservation of energy over the interface is not guaranteed [33].

2.5.2 Transfer methods

For non-matching fluid and structural meshes but for which the interfaces are close, it is common to use the Nearest-Neighbor Interpolation, the Weighted Residual Method or the Radial basis function interpolation (RBFI) [34, 47]. Farhat et al. [47] presents some procedures to transfer displacements and forces between a CFD mesh and a FEM mesh. The two meshes do not share a matching interface but the fluid-structure interfaces of each mesh are close to each other. After using a pairing algorithm between interface boundary elements of the two meshes like the one of Maman and Farhat [90], it is possible to proceed to consistent interpolations. A mortar based algorithm is also presented in [47]. However, in the case of a CFD mesh on one side and a beam model on the other side, it is not possible to use the methods developed in [47]. The two meshes are too different and the structural model does not extend to the fluid structure interface. It is better to use specific methods for the load transfer and the motion transfer.

Transfer of loads with slices

Heinz et al. [68] performed a transfer of loads between the CFD solver *EllipSys3D* and the CSM solver *HAWC2* for wind turbine applications. The structure was modeled by a beam finite element model, making the two meshes highly non matching. To provide the aerodynamic load per unit of span to the beam, line integrations of the pressure and shear stress along the airfoil sections were computed. The resulting moments were calculated around the mid-chord for *HAWC2*.

However, section orientation used for the integrations was not the exact orientation. Their routine was only able to proceed to horizontal cuts (Figure 2.4). It means that with large displacements, the difference of orientation can produce spurious moment in flexion.

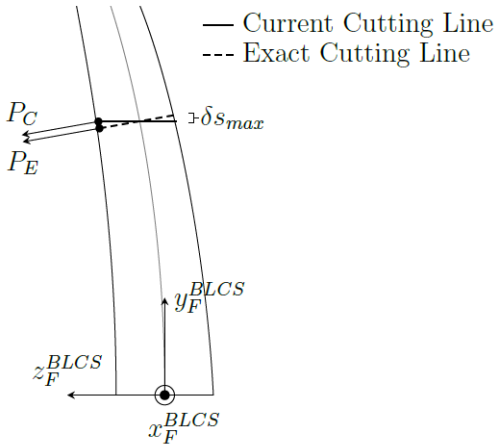

Figure 2.4: Cutting Lines and Pressure Force Orientation during Force Read-Out in EllipSys3D [68]

After extracting the aerodynamic forces from the fluid mesh at specific radial blade positions, they assumed the loads to vary linearly between these points.

Kinematic transfer of motion

Brown [22] presents a discussion on the use of extrapolation functions allowing to determine the displacements at points outside of the modeled structural elements. To explain the method, he took an example of a wing section modeled by a beam element (Figure 2.5).

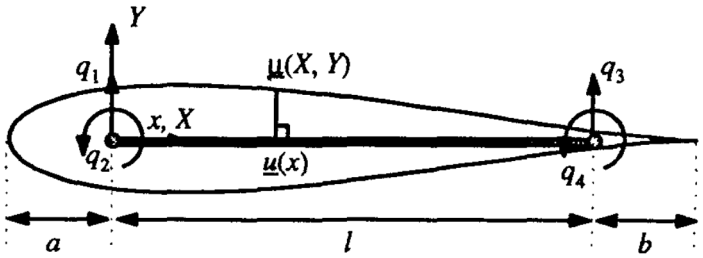

Figure 2.5: Wing structure modeled as a simple beam finite element [22]

First, each point $\underline{X}$ of the fluid structure interface (can correspond to CFD Mesh node) needs to be associated to a point $\underline{x}$ belonging to the beam by defining the mapping function $\underline{x}(\underline{X})$. It is as if each point $\underline{X}$ were now connected by a rigid bar to $\underline{x}(\underline{X})$. The displacements and rotations at $\underline{X}$ can be calculated with the beam kinematics:

$$\underline{\mu}(\underline{X}) = \underline{u}(\underline{x}) - (\underline{X} - \underline{x}) \times \underline{u}_\theta(\underline{x}) \tag{2.17}$$

$$\underline{\mu}_\theta(\underline{X}) = \underline{u}_\theta(\underline{x}) \tag{2.18}$$

where $\underline{u}(\underline{x})$ and $\underline{u}_\theta(\underline{x})$ are the displacement and rotation of the beam at $\underline{x}$. The displacements and rotations of the beam can be written with the nodal displacements $\underline{q}$:

$$\underline{\mu}(\underline{X}) = \left[\eta\right]^T \underline{q} - (\underline{X} - \underline{x}) \times \left[\eta_\theta\right]^T \underline{q} \tag{2.19}$$

$$\underline{\mu}_\theta(\underline{X}) = \left[\eta_\theta\right]^T \underline{q} \tag{2.20}$$

In the example Figure 2.5, the element is along the chord to model a stringer. It allows to deform the airfoil itself but in the case of a wing or a blade, the airfoils are supposed rigid and the beam elements are along the span in order to deform the blade. Heinz et al. [68] applied the method described by Brown [22] to a wind turbine blade.

Using the transfer of loads with the slices and this motion transfer does not lead to a conservative transfer. To conserve the energy from the fluid interface to the structure, Heinz et al. [68] multiplied the loads by a scaling factor before giving them to the structure.

2.6 Temporal coupling

All the steps have been presented, it simply remains to chain them in order to compute a static equilibrium or advance in time.

2.6.1 Static coupling

It begins with the stress-free configuration of the structure. The loads are computed with the fluid solver using a stationary method and transferred to the structure using one of the methods presented. Then, the static deformation of the structure is computed with the solid solver. However, as this new configuration is different from the initial one, the aerodynamic loads need to be evaluated one more time. The structural displacements are passed to the fluid solver using a motion transfer method in order to compute the new fluid stationary state. The cycle continues until convergence to an aeroelastic equilibrium.

To help the convergence, it is common to add some damping in the cycle. It is done by multiplying the update of loads or displacement by a factor γ between 0 and 1 during the transfer.

$$\mathbf{F_s}^n = \mathbf{F_f}^{n-1} + \gamma \left(\mathbf{F_f}^n - \mathbf{F_f}^{n-1} \right) \tag{2.21}$$

with $\mathbf{F_f}$ the loads computed by the fluid solver and $\mathbf{F_s}$ the loads given to the structural solver.

2.6.2 Dynamic coupling

Loose coupling

A common way to realize the coupling in a partitioned system is by using a loose coupling method. This kind of method minimizes the transfer of data between the fluid and structure solvers as the participating models exchange their data only once per time step. Several variations of loosely coupled schemes exist. The elementary loose coupling scheme (Figure 2.6a) is the simplest but is only first order accuracy in time. This scheme is used when little consideration is given to the coupling method. It consists of the following step cycle [68]:

1. Transfer the actual aerodynamic forces to the structural solver and apply them on the structures.
2. Use the actual aerodynamic forces and a time integration in order to calculate the structural deflections of the new time step.
3. Transfer the new deflections from the structural solver to the fluid solver.
4. Solve the fluid subdomain and calculate the new aerodynamic forces corresponding to the new deflection state.

A better way to realize a loose coupling has been developed by Piperno and Farhat [106], Piperno et al. [107] with their Conventional Serial Staggered (CSS) scheme then improved in a Generalized Serial Staggered (GSS) scheme [48] which can be second order accuracy in time (Figure 2.6b). It consists of the following step cycle :

1. Predict the motion of the wet surface of the structure, transfer it to the fluid subsystem. Piperno and Farhat [106] advice to use the following predictor:

$$u_\Gamma^{n+1^P} = u_\Gamma^n + \alpha_0 \Delta t \dot{u}_\Gamma^n + \alpha_1 \Delta t^2 \ddot{u}_\Gamma^n \tag{2.22}$$

2. Update the corresponding predicted positions of the fluid dynamic mesh.
3. Solve the fluid subdomain and calculate the new pressure field corresponding to the predicted deflection state.
4. Convert the pressure into aerodynamic load and transfer it to the structure.
5. Compute a corrected aerodynamic force and solve the structure subsystem to obtain the structural deflections. Several choices for the corrected aerodynamic forces are proposed in [48].

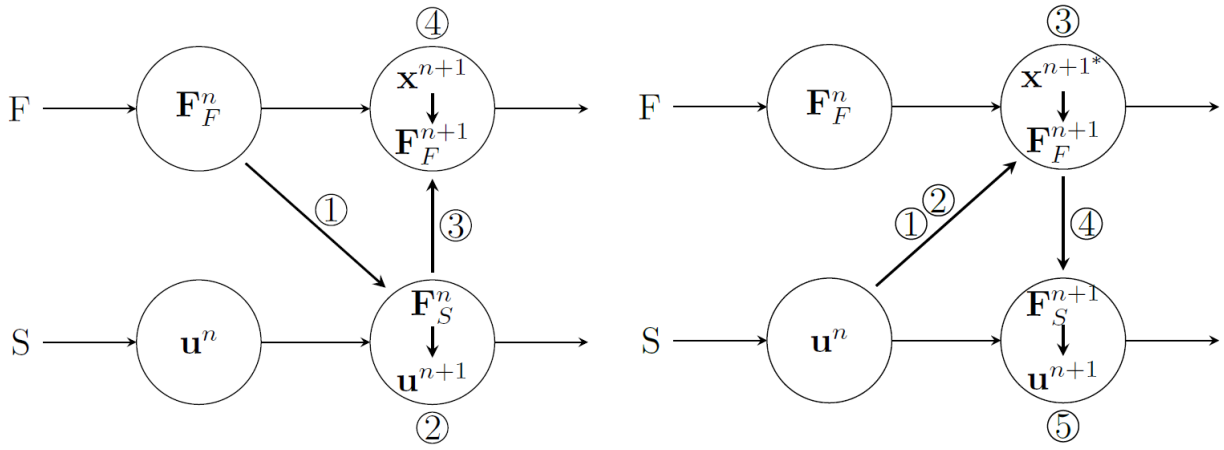

(a) Elementary loose coupling scheme

(b) Generalised Serial Staggered (GSS) scheme

Figure 2.6: Loose coupling schemes [68]

Strong coupling

Strong coupling schemes proceed to subiterations in order to reach an equilibrium between the aerodynamic loads and the internal forces of the structure before passing to the next time step (Figure 2.7). As a consequence, such schemes are generally more accurate and more stable than loose coupling schemes. However, this gain of accuracy and stability has a significant computational cost. Both solvers have to compute and exchange their solution multiple times per time step [68].

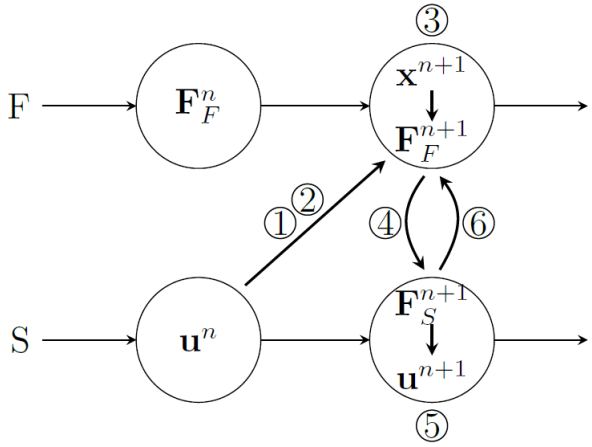

Figure 2.7: Strong coupling scheme [68]

In the field of biomechanics, strong coupling schemes are preferred due to a high mass ratio amplifying numerical instabilities [24]. But in the case of wind turbines, the mass ratio is low and loose coupling schemes can give satisfying results [68]. So we will use an elementary loose coupling scheme.

2.7 Summary

This chapter presented a brief theoretical background for high-fidelity numerical aeroelasticity simulations. The numerical methods used in the fluid solver *FastS* were introduced, in particular the discretization of the fluxes, the time integration scheme and the arbitrary lagrangian eulerian formulation to deal with deforming grids. Then, mesh deformation technique used in *Quantum* was explained. The solid solver, based on Euler-Bernoulli corotated beam model of *Project Chrono* was also presented. As the fluid mesh and the beam mesh are highly non-matching, specific transfer methods of loads and motion between the two solvers were introduced. Finally, the two ways of coupling a fluid solver with a structural solver, the loose and strong coupling, were explained. Some of these methods will be implemented and validated in the next chapter which focuses on a modular python framework. Low-fidelity approaches will also be introduced and discussed.

Chapter 3

Implementation and validation of a modular python framework for coupled fluid-structure simulations

To simulate aeroelastic phenomena numerically, a modular approach based on partitioned coupling between fluid and structure solvers has been chosen. It allows to switch easily between several levels of fidelity for the fluid and/or the structure computation. To work together, both those solvers need to exchange information. The coupling between several solvers has been implemented but the main development concerns the coupling between Chrono and *FastS*. The general ideas are the following. *Chrono* needs the aerodynamic loads on each node of the beam. These loads are integrated from the CFD wall pressure and shear stress for each section linked to a structural node. The structural solver deforms the blade according to the fluid forces. Then, the CFD solver *FastS* needs a mesh of the new configuration of the blade. To do so, the boundary of the mesh has to be deformed according to the beam displacement. As the fluid mesh and the beam mesh are not matching, a method based on the assumption of rigid beam section has to be employed. Next, the mesh deformer Quantum allows the propagation of the deformation into the mesh volume.

This chapter deals with the implementation and the validation of all these steps, introduced in Chapter 2.

Contents

3.1 General organization of the framework 60
3.2 Validation of the IEA15MW blade beam model 61
3.3 Identification of the ONERA dynamic stall model parameters 63
3.4 Validation of the dynamic stall modeling with CFD 65
3.4.1 Methodology 65
3.4.2 Results and discussion for fixed-wing cases 67
3.4.3 Results and discussion for oscillating-wing cases 69
3.4.4 Fully resolved flow field 70
3.5 Implementation and Validation of the motion transfer 71
3.5.1 Coupling with the sectional models 71
3.5.2 Coupling with the CFD solver 72
3.6 Implementation of the load transfer 76
3.6.1 Orientation of the slices and integration 76
3.6.2 Comparison between the CFD and the strip theory models 77
3.6.3 Calculation of the generalized forces for the beam FEM model 78
3.6.4 Precautions with the slices 80
3.7 Comparison of the static aeroelastic coupling between the CFD and the strip theory models 81
3.8 Restart of dynamic aeroelastic simulations 83

3.9 Conclusion 83

3.1 General organization of the framework

The aim of the present python framework which has been developed during the thesis is to interact with the various fluid and structure solvers and regroup the transfer methods. The framework is organized around a main file containing the "Driver" that calls the different classes: "Fluid", "Struct", "Transfert_deplacement" and "Transfert_Forces". It is the bandmaster. The "Driver" reads the inputs and initializes the corresponding solvers. Next, two modes are implemented into the "Driver": static coupling that calculate the aeroelastic equilibrium, and a dynamic coupling that simulate temporal responses. An UML diagram is presented in Figure 3.1. The "Driver" is at the center and interacts with the four main class of the coupling as well as an "Utils" class. The "Fluid" and "Struct" classes are parent classes that give some general attributes and functions to their respective child classes. Their main role is to create the right fluid and struct class according to the user inputs. The dependencies of each class is also indicated.

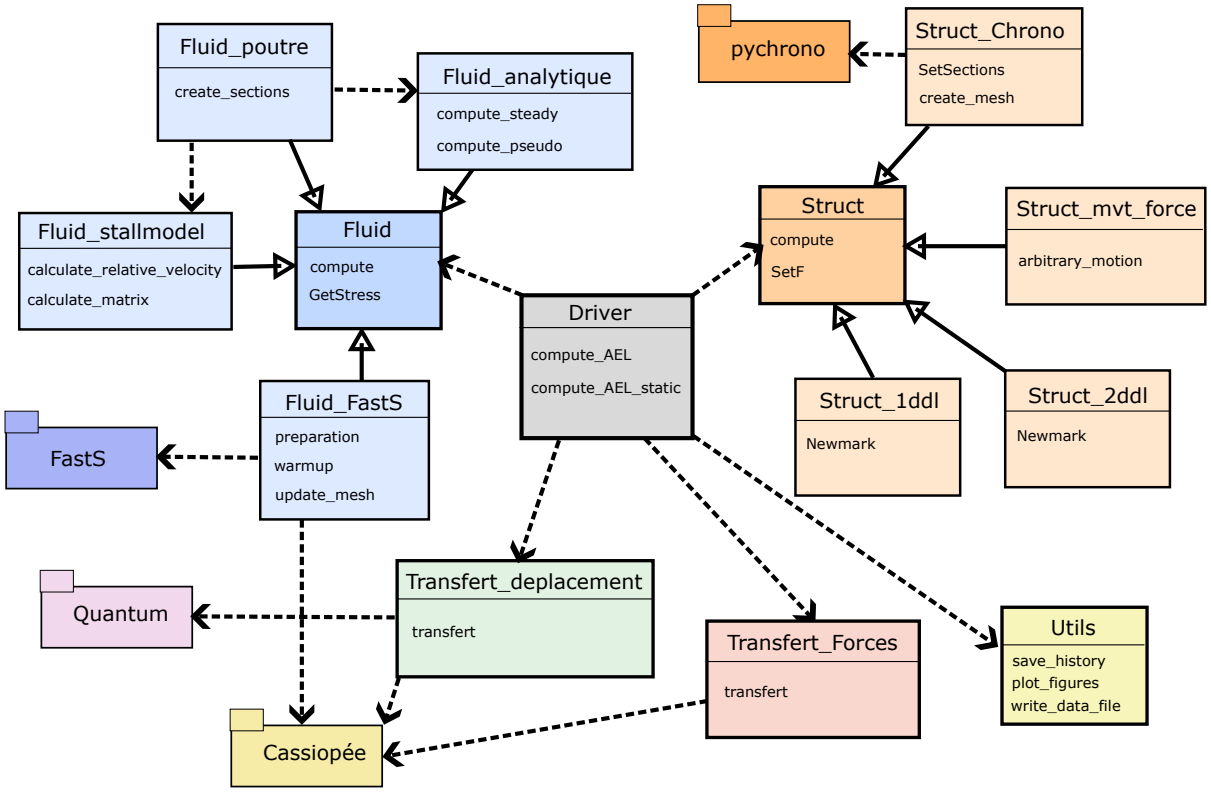

Figure 3.1: UML diagram of the aeroelastic python framework

The fluid classes are constituted of a class "Fluid_FastS" that wraps *FastS*, a class "Fluid_stallmodel" for the sectional dynamic stall model, a class "Fluid_analytique" for the sectional analytical models and a class "Fluid_poutre" that can distribute the sectional models along the blade under the strip theory assumption:

- The wrapping of *FastS* consists in managing the CGNS tree with *Cassiopée* (version 4.0) in order to prepare and conduct CFD simulations but also extract the data. The blanking of

the background grid and the setting of interpolated points, needed for the use of chimera mesh, are also realized in this class.
- The dynamic stall class contains the ONERA dynamic stall model as described in [37].
- The class for the sectional analytical models regroups the static aerodynamic curves, the quasi-steady aerodynamic model and the Theodorsen model in a Wagner formulation [65].
- The class "Fluid_poutre" for the beams allows to manage a set of the previous sectional models distributed on each section of the beam. This class calls the other classes and gathers the calculated forces.

The structure classes are composed of a class that wraps *pychrono*, two classes "Struct_1ddl" and "Struct_2ddl" for section models elastically supported in either 1dof or 2dof, and a class for the imposed motion of the structure:

- The wrapping of *pychrono* (version 8.0.0) allows to create a beam with varying properties along the length. The full sectional matrices of mass and stiffness can be given to each section.
- The classes "Struct_1ddl" and "Struct_2ddl" compute the response, using a Newmark scheme, of section models elastically supported in either 1dof or 2dof.
- The last class "Struct_mvt_force" can be used to impose predefined motion on sections or beams. It can be harmonic oscillations of a structural mode or a complete arbitrary motion.

In the transfer classes, there are one class for the transfer of the motion and one class for the transfer of the loads:

- The class for the transfer of the motion contains the kinematic method to displace the skin mesh for a 2D section and for a whole blade. It also calls Quantum to deform the volume mesh.
- In the class for the load transfer, the slices of the skin mesh and the integration of the wall pressure and shear stress are realized.

Finally, there is also an Utils class that carries out the plots and a Postprocess class to effectuate some treatment during the simulations.

In the following sections, each main class is validated.

3.2 Validation of the IEA15MW blade beam model

The first class to be validated is the wrapper of *pychrono* (version 8.0.0). The Corotated Euler-Bernoulli beam model has been chosen to describe the blade. In the following sections, a static and dynamic validations are presented for a single blade of the IEA15MW that is clamped at its root, without rotation. The structural properties of the blade are extracted from the github of the IEA15MW [1]. These properties are quickly presented in Appendix A.

Convergence study regarding the spatial discretization

To set the spatial discretization of the finite element model of the beam, a convergence study was conducted focusing on the natural frequencies. The evolution of the seven first natural frequencies with the number of nodes evenly distributed are represented in Figure 3.2. Results show that 100 points evenly distributed ensure a good convergence.

[1] https://github.com/IEAWindTask37/IEA-15-240-RWT

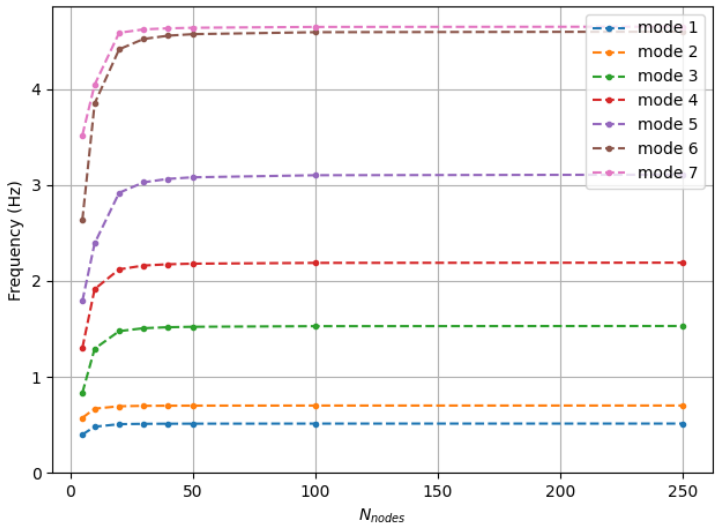

Figure 3.2: Evolution of the natural frequencies with the number of nodes

Dynamic validation : blade natural frequencies

No experimental data are available regarding the natural frequencies of the IEA15MW blade. Results obtained with our Beam model can however be compared with those obtained numerically by DTU, IFPEN and NREL as part of the IEA Task 47[2]. Results are reported in Figure 3.3.

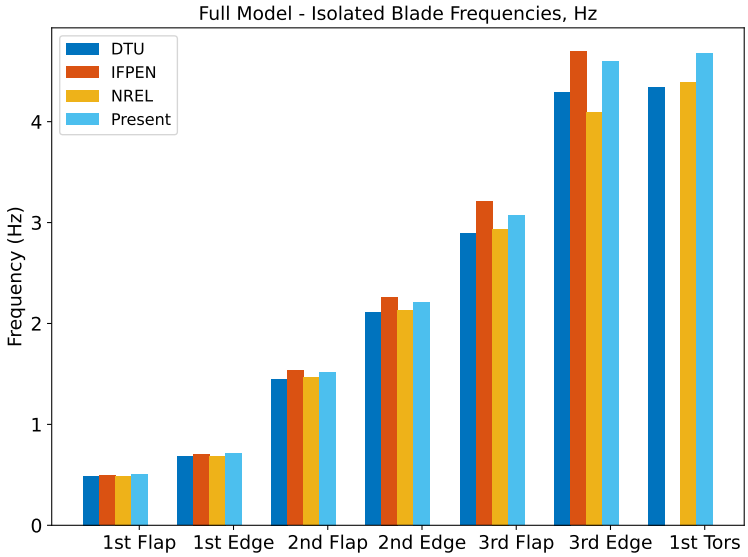

Figure 3.3: Natural frequencies of the IEA15MW blade obtained as part of the IEA Task 47

For the two first modes, there is a good agreement between all the actors. But as the modes get higher, the natural frequencies go apart from each other. The frequencies obtained by the DTU and the NREL stay close to each other except for the 3rd edgewise mode. The frequencies computed with *Chrono* and the ones calculated by IFPEN are higher than those of DTU and NREL. In our aeroelastic study, the most involved modes are the first flapwise and first edgewise mode, which only have a gap of 4% in frequency compared to the DTU.

[2] https://iea-wind.org/task47/

Static validation: tip displacement

A static validation is performed here using the reference results of Loubeyres et al. [87] regarding the tip displacements for axial, in plane or out-of-plane tip loads of various intensity. These results were obtained using two solvers based on geometrically exact beam theory models allowing large displacements and rotations: *DeepLines* and *BeamDyn*. The first one, *DeepLines*, uses a formulation similar to the one developed by Simo and Vu-Quoc [123], while *BeamDyn* relies on a spectral method [142]. Comparison with *Chrono* results are reported in Figure 3.4.

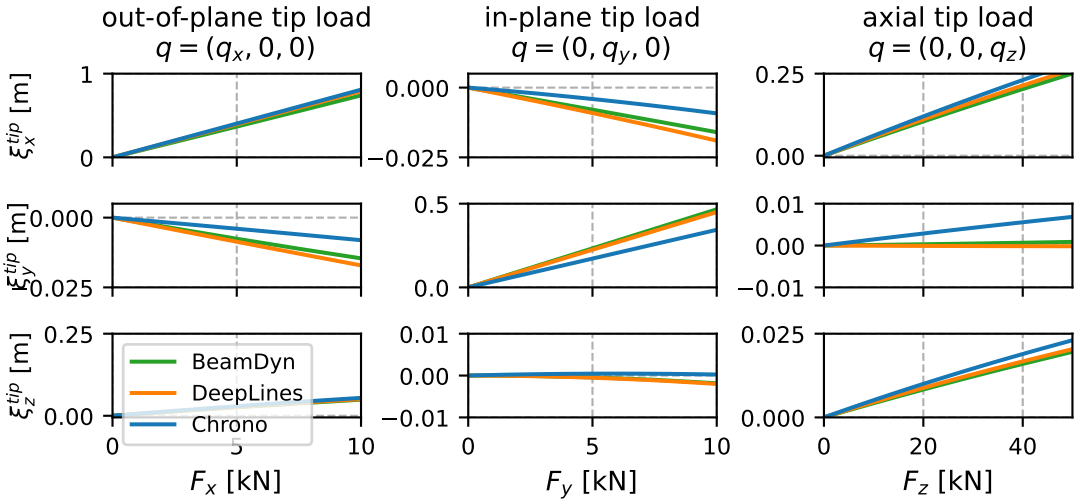

Figure 3.4: Comparison of the tip displacements with Loubeyres et al. [87]. (The axes are the ones of Loubeyres et al. [87])

Chrono results are in good agreement with those obtained with both the *BeamDyn* and *DeepLines* solvers. Significant differences are nevertheless observed for the in-plane tip displacement due to a pure in-plane tip load. It seems that our finite element *Chrono* model is stiffer in the in-plane direction. Otherwise, the flexion-flexion coupling is a little lower.

3.3 Identification of the ONERA dynamic stall model parameters

The version of the ONERA dynamic stall model is the one described by Dimitriadis [37] and given in section 1.3.2.2. As mentioned previously this unsteady nonlinear aerodynamic model relies on the steady aerodynamic curves associated to an airfoil section and a set of parameters that need to be identified using specific dynamic tests. The dynamic parameters have been set using the experimental results of Fuglsang et al. [51] who measured the unsteady lift, drag and moment coefficient of a FFA-W3-241 airfoil, which is the airfoil section at 64% of the IEA15MW blade, forced to oscillate in pitch at a reduced frequency $k = \frac{\omega c}{2U_0} = 0.093$, with an amplitude of two degrees, for different mean angles of attack in and beyond the static stall angle of attack. The Reynolds number was $1.6 \cdot 10^6$ and the turbulence intensity was about 1%. Note that in the experimental work of Fuglsang et al. [51] the airfoil model was equipped with vortex generators The parameters are given in Table 3.1. The comparison between experimental and numerical loops are shown in Figure 3.5

Table 3.1: Parameters used in the ONERA model (set for the FFA-W3-241 airfoil)

Drag	Value	Lift	Value	Moment	Value	General	Value
σ_{0_d}	0.5					λ_l	$0.17 - 0.13M$
σ_{1_d}	-0.5	σ_{1_l}	-0.1	σ_{1_m}	-0.1	β	$\sqrt{1-M^2}$
a_{0_d}	0.7	a_{0_l}	0.7	a_{0_m}	0.3	α_l	$0.6 + 0.25(\beta - 1)$
a_{2_d}	0.15	a_{2_l}	0.15	a_{2_m}	0.7	σ_l	$3\pi/\beta$
r_{0_d}	0.4	r_{0_l}	0.13	r_{0_m}	0.1	d_l	$0.6\sigma_{1_l}\lvert\Delta c_l\rvert$
r_{2_d}	0.04	r_{2_l}	0.04	r_{2_m}	0.1	α_{stall}	12°
E_{2_d}	-0.1	E_{2_l}	3	E_{2_m}	50		
$\Delta\tau_{d_d}$	1	$\Delta\tau_{d_l}$	1	$\Delta\tau_{d_m}$	0		

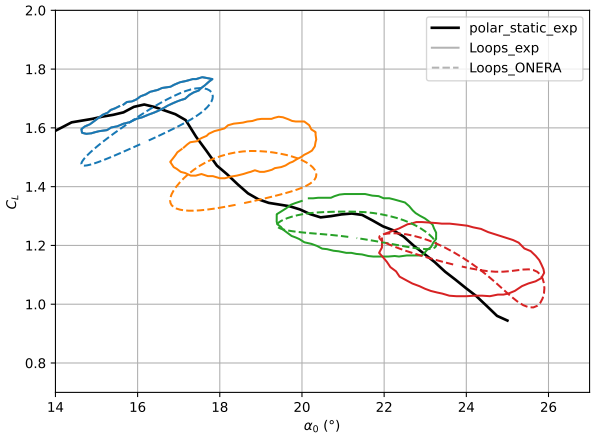

(a) Lift coefficient

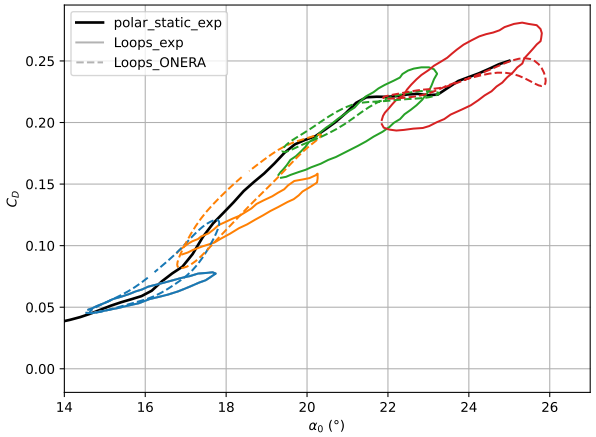

(b) Drag coefficient

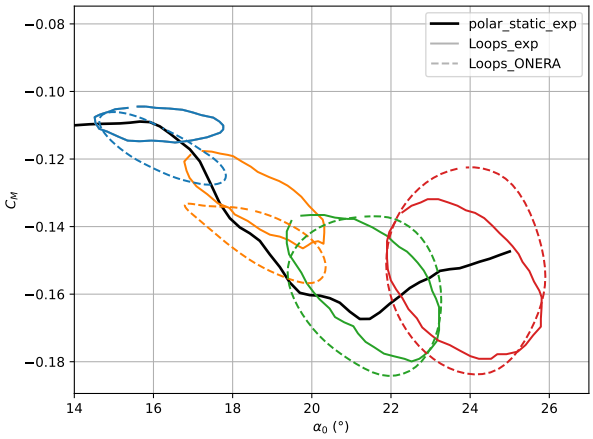

(c) Moment coefficient

Figure 3.5: Comparison between the experimental results of Fuglsang et al. [51] with the results obtained with the ONERA dynamic stall model using the set of parameter reported in Table 3.1. Unsteady lift, drag and moment coefficient of the FFA-W3-241 airfoil forced to oscillate in pitch with an amplitude of two degrees, for different mean angles of attack, at a reduced frequency $k = \frac{\omega c}{2U_0} = 0.093$.

The slope is an important feature of the loops, as it will be argued later, the lift coefficient

parameters have then been determined so as to conserved the mean slope for most of the loops. It has however been difficult to maintain the loop aspect ratio with a unique set of parameters and priority was given to the loops close to the static stall angle of attack. We can nevertheless observed that for $\bar{\alpha} = 17°$ and 19° the ONERA model slightly translate the loops vertically. It is expected that this shift in C_L will modify the static aeroelastic equilibrium but its effect on the stability should be limited. Regarding the drag coefficient, we were unable to identify a set of parameters allowing to reproduce the experimental loops. As shown in Figure 3.5b the ONERA model stick to the static polar. As a consequence, neither the mean slope nor the aspect ratio are correctly reproduced. For the moment coefficient, the aspect ratio of the ONERA dynamic stall loops is respected for the $\bar{\alpha} = 17°$ and 19° loops, but for higher mean angles of attack, the swept area is overestimated. Moreover, it can be noticed that the slope of the $\bar{\alpha} = 17°$ loop differs from the experiment, while the mean slope of the $\bar{\alpha} = 19°$ loop is well reproduced. For the two last loops, the rounded shape is similar. Nevertheless, in our case since stall-induced vibrations involve mainly flapwise and edgewise motion, the moment dynamic stall loops are of less importance than the lift and drag ones.

This set of parameters, identified for a unique airfoil section, an unique reduced frequency and an unique amplitude of harmonic pitching motion will be used for aeroelastic simulations using either a section or continuous blade model. In addition to the limitations mentioned above, one should mention that those parameters should also depend on the airfoil section (that vary along the IEA15MW blade), reduced frequency and amplitude of motion. Dynamic aeroelastic results that will be obtained using this fluid solver should therefore be considered with caution. Other unsteady aerodynamic data would have been needed to improve such a "low fidelity" approach.

3.4 Validation of the dynamic stall modeling with CFD

Among the CFD codes available at ONERA, *FastS* was chosen as it has better flexibility, evolutivity and efficiency. The objective of this section is to validate the capability of the CFD solver *FastS* to capture the dynamic stall process for a thick airfoil section, representative of a wind turbine blade, forced to oscillate in pitch. *FastS* results will be compared to experiments performed on a NACA 63_4421 airfoil and with the results obtained with the ONERA dynamic stall model. This section has been published in Cortes et al. [29] and is reproduced here with minor additions.

3.4.1 Methodology

Benchmark experiments

The experimental reference data previously published in [3] were obtained from static and dynamic tests performed on a NACA 63_4421 section model in a $5m \times 3m$ wind tunnel, for Reynolds numbers, $Re = \frac{Uc}{\nu} = 10^6$, using an experimental rig which forces the section model to oscillate in pitch, around its fore quarter-chord axis, at different values of mean angle of attack $\bar{\alpha}$, reduced frequency $k = \frac{\pi f c}{U}$ and amplitude of motion $\tilde{\alpha}$. The aerodynamic lift, drag and pitching moment about the quarter chord were obtained through unsteady surface pressure measurements (see [3] for further information on the experimental process and results).

As the *FastS* CFD solver assumes a fully turbulent boundary layer over the blade section, numerical predictions will be compared with the experimental results obtained for a grid turbulence intensity $Tu = 4\%$. As shown in Figure 3.7, the *FastS* steady results in lift match very well the experiments for $Tu = 4\%$.

Numerical setup

The NACA 63_4421 rigid airfoil model of 0.5m chord was immersed in a reference flow of 30m/s. It corresponds to a Reynolds number $Re = 10^6$ and Mach $M = 0.05$. The simulations are realized with the solver *FastS* that has been presented in Chapter 2.

A mesh of the NACA 63_4421 was generated with Construct2D. An O-grid type mesh is used. A convergence study on both the domain size and the number of points has been realized, leading us to generate a mesh with a diameter of 1000 chords composed of 10^5 points. To describe the boundary layer, the first cell height is small enough to satisfy an y^+ value lower than one. The outer limit of the CFD domain has been defined as a farfield boundary condition. To account for the pitching motion of the airfoil, the mesh is rotated around the quarter chord in a rigid motion.

A convergence time step study was first performed. Several simulations of the dynamic stall loop for different reduced frequencies have been realized with decreasing time steps. Results for $k = 0.183$ are reported and compared to experiments in fig 3.6.

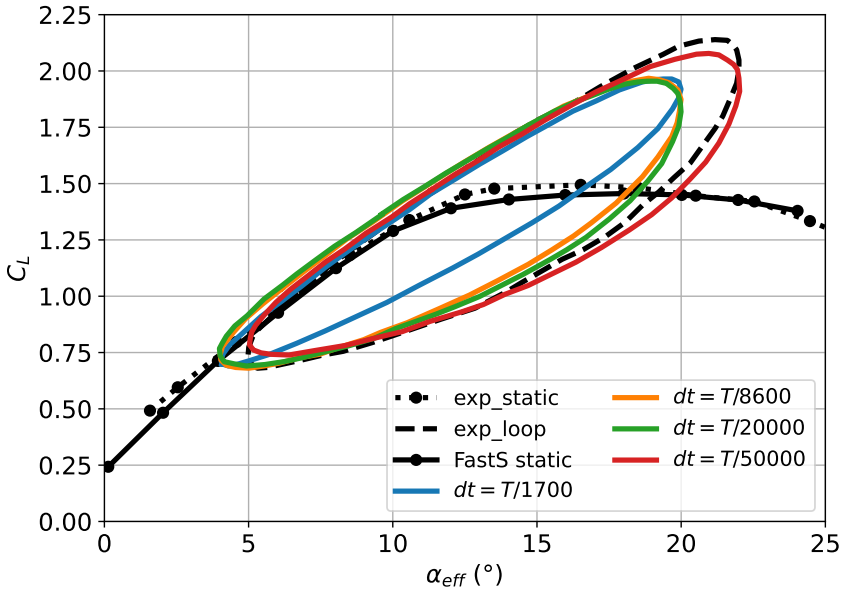

Figure 3.6: Convergence of time step for the dynamic stall loop of reduced frequency $k = 0.183$ and turbulence intensity 4%.

A total of 50 000 time-steps per period of oscillation were required to achieve the convergence of the dynamic stall loops for $k_2 = 0.0785$ and $k_3 = 0.183$ whereas 100 000 time-steps per period has been necessary for the lowest reduced frequency $k_1 = 0.0183$ (It corresponds to a flow displacement of 0.002 chord by time-step).

Regarding the ONERA dynamic stall model, a parametric study has been performed in order to identify the parameters' values that best fit the dynamic stall loops in the reduced frequency range. The ONERA dynamic stall results presented in Figure 3.9 have been computed with the parameters of Table 3.2. Compared to the parameters used for the FFA-W3-241 airfoil (Table 3.1), a_{0_l} is lower and r_{0_l} is higher. As shown in Figure 1.27 and 1.28, it increases the constriction of the lift loops. Moreover, the sign of E_{2_l} is different and the amplitude is lower. Concerning the moment, a_{0_m} and a_{2_m} are lower.

Table 3.2: Parameters used in the ONERA model (set for the NACA 63421 airfoil)

Coefficient	Value	Coefficient	Value	Coefficient	Value	Coefficient	Value
σ_{1_l}	-0.1	σ_{1_m}	-0.1	r_{0_l}	0.175	r_{0_m}	0.1
a_{0_l}	0.25	a_{0_m}	0.1	r_{2_l}	0.04	r_{2_m}	0.1
a_{2_l}	0.15	a_{2_m}	0.1	E_{2_l}	-0.1	E_{2_m}	60
$\Delta\tau_{d_l}$	4	$\Delta\tau_{d_m}$	0				
β	$\sqrt{1-M^2}$	α_l	$0.6+0.25(\beta-1)$	σ_l	$3\pi/\beta$	d_l	$0.6\sigma_{1_l}\lvert\Delta c_l\rvert$

3.4.2 Results and discussion for fixed-wing cases

Static polars

In this section, 2D unsteady RANS simulations were conducted so as to calculate the aerodynamic lift and moment time-averaged polar curves. The data points have been gathered by successive steps of angle of attack. For each angle of attack, the transient regime induced by increasing the angle of attack has been ignored and the mean aerodynamic coefficients have been computed over $25\frac{c}{U} = 0.4167$ seconds. Results are reported in Figure 3.7.

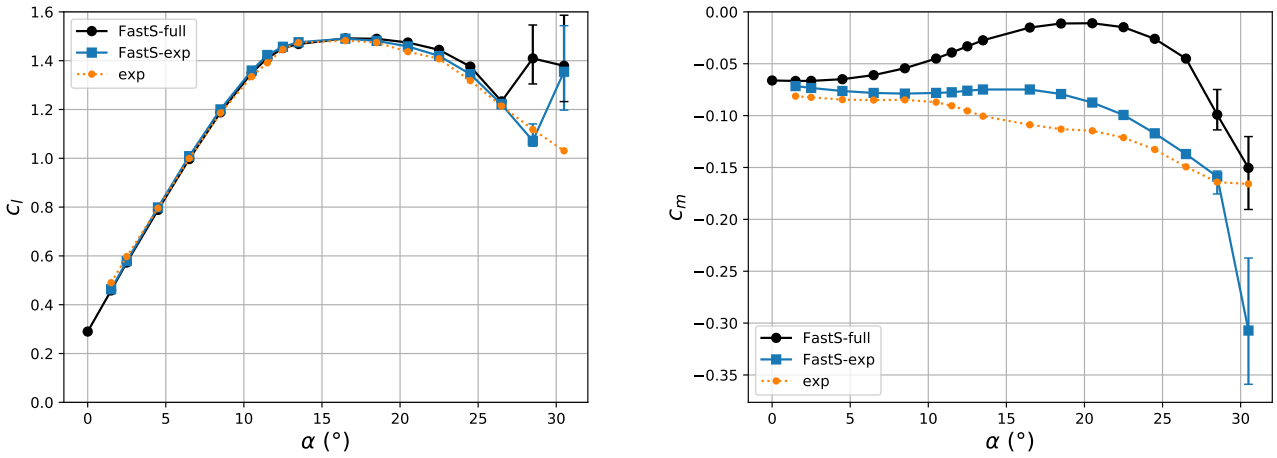

Figure 3.7: Steady lift coefficient (left) and moment coefficient about the quarter chord (right) results. FastS-full is obtained with a full integration of the stress over the airfoil while FastS-exp is calculated using the same integration method as the experiment [3].

The experimental results from [3] are reported with orange plain circles. Plain circles in black are used for the FastS-full results for which coefficients were calculated with a full integration of the stress over the airfoil using all the surface mesh points. FastS-exp results, reported with blue plain squares, are computed using the same integration method as the experiment, using 25 pressure points. Regarding the lift coefficient, FastS-full and FastS-exp results are very close and well reproduce the lift coefficient evolution for angles of attack up to 26°. For higher angles of attack, one can observe a sudden increase of the *FastS* mean lift coefficient along with an unsteady behavior. In this region, the flow is fully detached and CFD exhibits vortices that are alternately emitted from the leading and trailing edge into the wake, leading to a strong unsteady aerodynamic load and an increase of the mean value of the lift coefficient. Note that the frequency of the vortex emission observed here corresponds to a Strouhal of 0.32 (based on the chord), which is consistent

with the one expected for the Von Kármán vortex street downstream a planar plate in incidence [18]. No mention of this unsteady behavior and its impact on the steady results has however been reported in [3].

Regarding the moment coefficient about the quarter chord, significant discrepancies can be observed between the experiments and FastS-full results (full integral of stress over the airfoil). While experimental results show a gradual decrease of the moment coefficient beyond 10°, FastS-full results show an increase up to 20°, with an inflection point close to 7°, followed by a fall down of the moment coefficient that is abrupt for angle of attack beyond 26° where a strong unsteady vortex wake signature was observed. Using the same integration method as the experiment, i.e. using the pressure at the same positions as the pressure taps of the experiment, numerical predictions are closer to the experiment. This seems to show that the experiment was lacking of taps to correctly capture the impact of the dynamic stall fluid mechanism on the moment coefficient.

C_p curves

The remaining difference between experiments and FastS-exp results can be understood by looking at the pressure coefficient curves. In Figure 3.8, the pressure data from the CFD (FastS-full and FastS-exp) are compared to the experimental pressure data for three angles of attack: 1.5°, 11.5° and 24.5°.

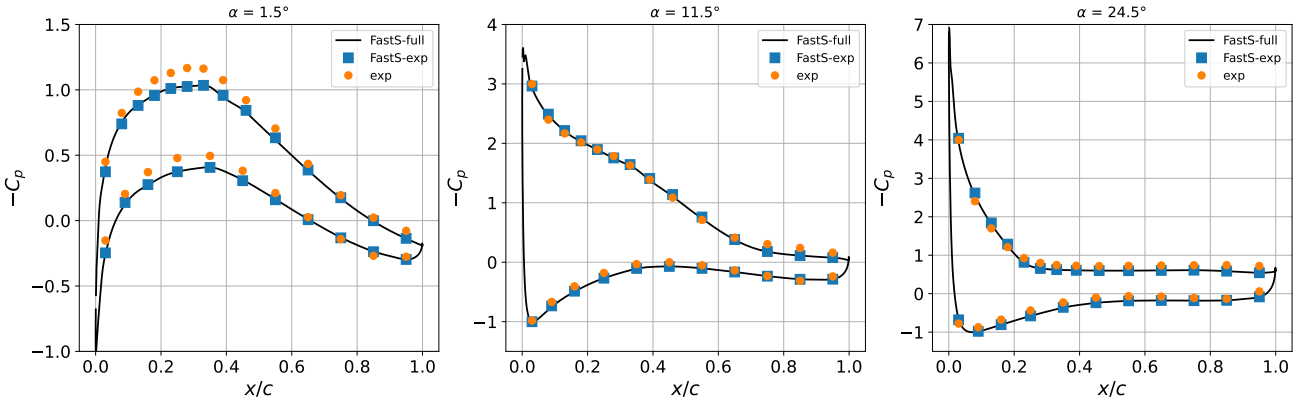

Figure 3.8: Mean pressure coefficient comparison between simulation (FastS-exp, FastS-full) and experiment (exp) for three angles of attack.

At 1.5° of angle of attack, the simulation underestimates depression in both the upper and lower surfaces of the airfoil. It does not affect the lift coefficient and slightly underestimates the negative moment coefficient about the quarter chord. At 11.5°, the pressure coefficient is well predicted. However, a deviation appears at the upper surface near the trailing edge. The lift is however balanced by a slightly overestimation of the suction around the quarter chord of the lower surface. However, it causes the moment to diverge even more from the experimental data. At 24.5°, a large part of the upper surface is stalled – corresponding to the constant C_p area. In this region, the CFD code predicts slightly lower values of $-C_p$ than the experiment. It appears to be the reason for the major misalignment in the curve of moment coefficient.

By looking at the leading and trailing edges, it can be noticed that important values of C_p in FastS-full are not measured by the experiment. The large value of C_p at the leading edge for $\alpha = 24.5°$ causes an increase of the moment. Therefore, greater number of pressure taps in the leading and trailing edge should improve the measure of the moment.

3.4.3 Results and discussion for oscillating-wing cases

Tests with an oscillating wing have been simulated using the CFD *FastS* solver for $\bar{\alpha} = 13.5°$, $\tilde{\alpha} = 8°$ and three different reduced frequencies $k_1 = 0.0183$ (slow oscillation), $k_2 = 0.0785$ and $k_3 = 0.183$ (fast oscillation). The airfoil is forced to oscillate in pitch around its quarter chord following the expression :

$$\alpha = \bar{\alpha} + \tilde{\alpha}\sin(2\pi f t) \tag{3.1}$$

where the frequency f is chosen so as to match the prescribed reduced frequency.

In this section experiments will be compared with FastS-exp results for which the lift and moment coefficients are computed using the same integration method as the experiment. Results obtained with the ONERA dynamic stall model using a unique set of dynamic parameters (see Table 3.2) that best fit the experimental dynamic loops will also be reported.

Regarding the unsteady lift coefficient results (see top of the Figure 3.9), both the *FastS* solver and the dynamic stall model correctly reproduce the experimental loops for $k_1 = 0.0183$ and $k_2 = 0.0785$. For the highest reduced frequency ($k_3 = 0.183$), the CFD solver slightly underestimates the lift overshoot beyond 17° while the ONERA dynamic stall model produces a loop for which the lift coefficient is significantly underestimated during the recovery process.

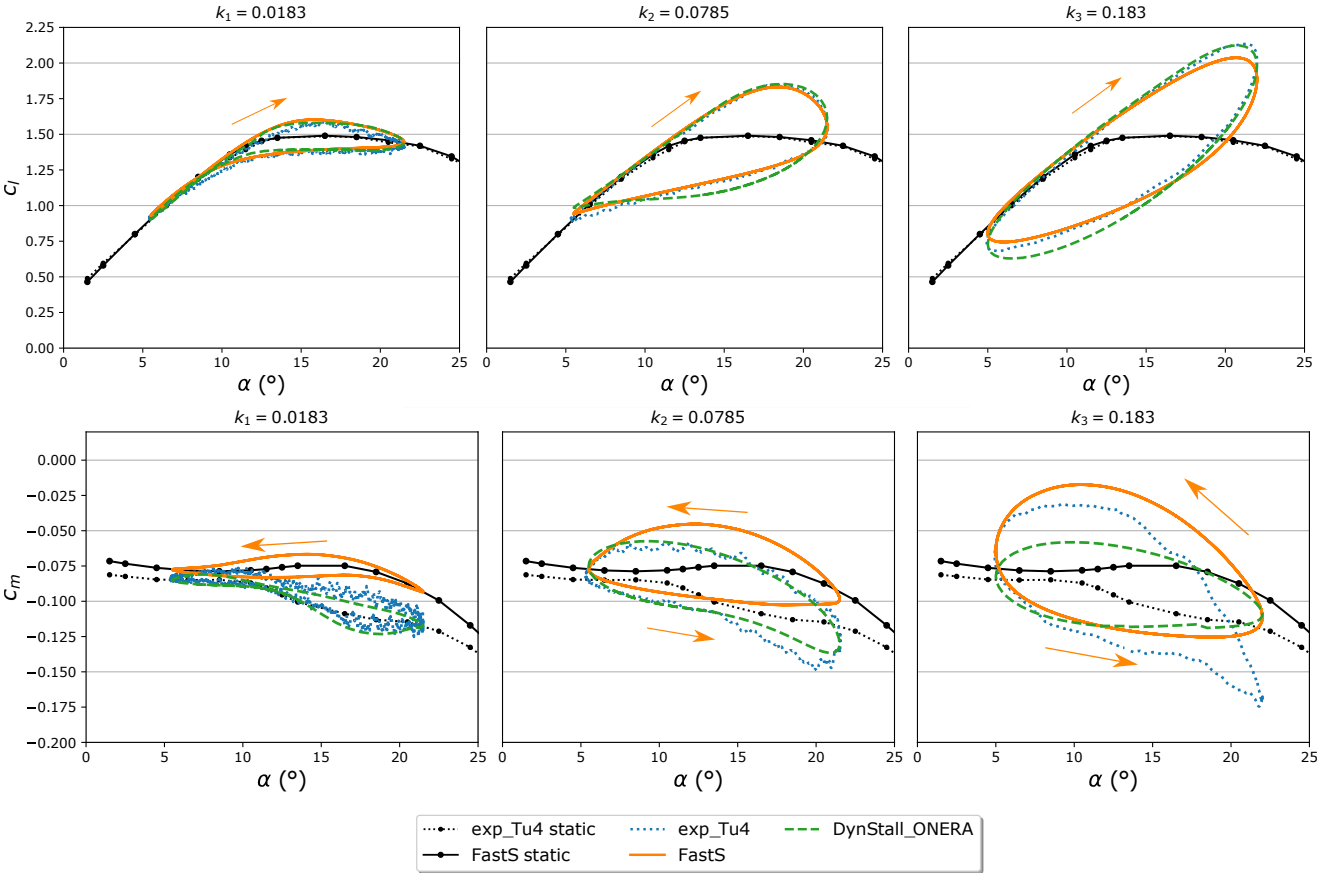

Figure 3.9: Static and dynamic lift coefficients (top) and moment coefficients (bottom) for three reduced frequencies; comparison of numerical predictions (FastS-exp and Onera dynamic stall model) with experiments reported in [3]. The lift loops turn clockwise while the moment loops turn counter-clockwise. The letters indicate specific states used in the following figures.

Unsteady moment coefficient results are compared with experiments at the bottom of Figure 3.9. As the experimental static curve was used to compute the ONERA dynamic stall model,

the loops obtained for $k_1 = 0.0183$ and $k_1 = 0.0785$ are in good agreement with the experiment. However, for $k_3 = 0.183$, the ONERA dynamic stall model underestimates the size and area of the loop and fails to capture the minimum of the moment coefficient occurring at the maximum angle of attack. Because of the discrepancies between the static curves of *FastS* and the experiments, the dynamic loops obtained with *FastS* significantly differs from the experiments. However their dynamic behaviors in regards to the associated steady curve are coherent.

3.4.4 Fully resolved flow field

For illustration, the dynamic flow field associated to a dynamic stall loop is presented in this section. Vorticity field is displayed for the reduced frequency $k_3 = 0.183$ in Figure 3.10. The snapshots show the delay for the flow to reattach. Clear differences in the vorticity field can be observed between the upstroke and the downstroke for a same angle of attack. The pressure gradient helps the flow to stay longer attached during the upstroke while it encourages stall during the downstroke. For the range of angles of attack under study, the stall point has never reached the leading edge and no shedding of leading edge dynamic stall vortex has been observed.

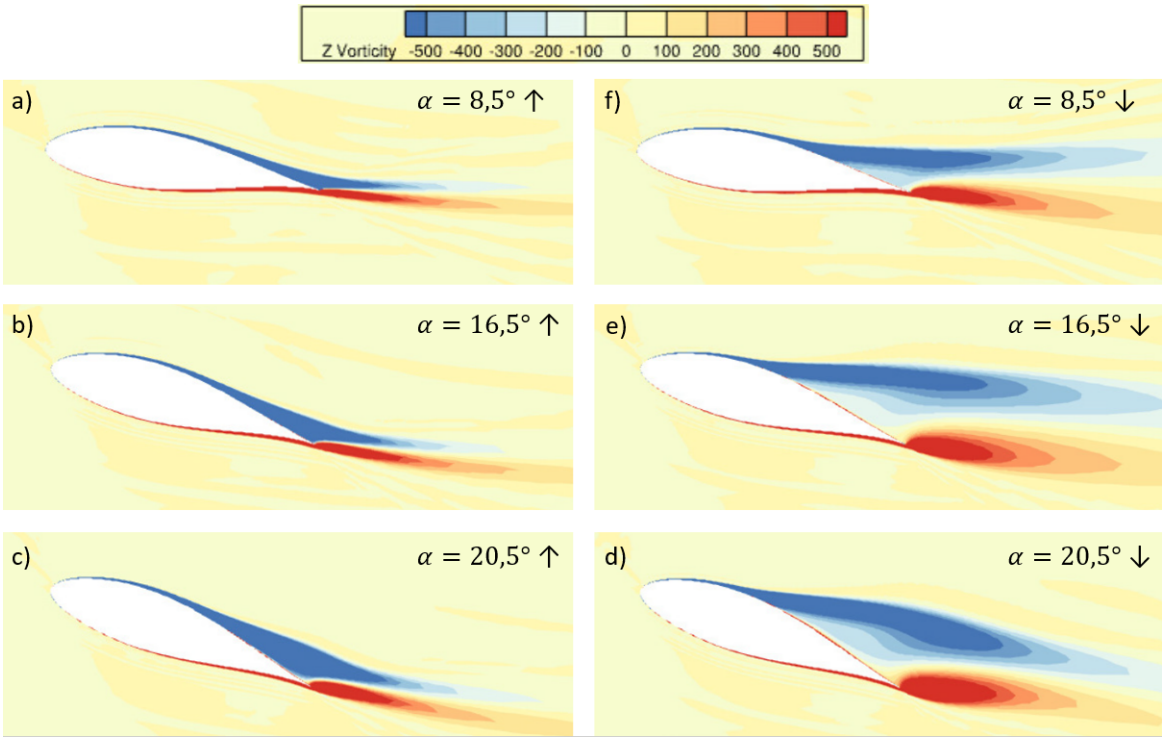

Figure 3.10: Snapshots of the vorticity field for the reduced frequency $k_3 = 0.183$ at three angles of attack during the upstroke (a, b, c) and the downstroke (d, e, f), for the NACA63421 airfoil.

3.5 Implementation and Validation of the motion transfer

After the structural solver and the fluid solver, the transfer methods now need to be validated. In chapter 2, several methods of the motion transfer have been presented. The one chosen here is a kinematic transfer similar to Heinz et al. [66]. The motion of the mesh surface nodes are based on the beam kinematics. It allows to stay consistent with the structural model.

3.5.1 Coupling with the sectional models

Just before dealing with the main motion transfer between the FEM beam model and the CFD fluid mesh, the motion transfer to the sectional aerodynamic model of the strip theory is explained. This subsection shows how to process the beam quantities, which are the positions and rotation matrices of each section, in order to use them in the sectional aerodynamic models. The idea is to project the beam displacement at each node into the section plane, use the 2D aerodynamics models and project back the forces to the beam frame. A scheme of the frames used is given in Figure 3.11.

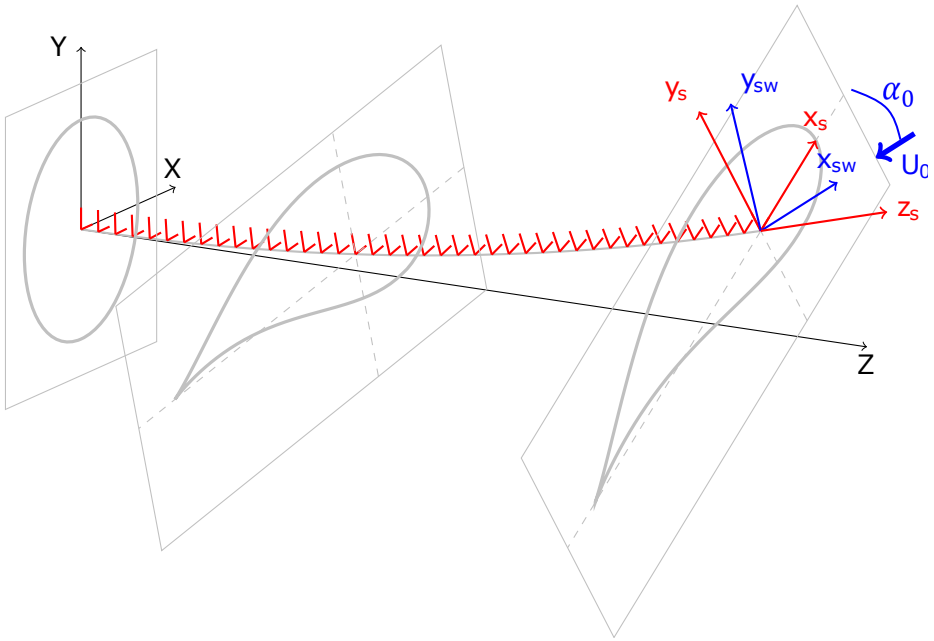

Figure 3.11: Scheme of the different frames: global frame $\mathcal{R}$ (black), section frame $\mathcal{R}_s$ (red) and section wind frame $\mathcal{R}_{sw}$ (blue).

First, the wind speed $\boldsymbol{U_s}$ in the section frame $\mathcal{R}_s$ is

$$\boldsymbol{U_s} = \mathbf{R}^T \boldsymbol{U}$$

where $\boldsymbol{U}$ is the wind velocity vector expressed in the global frame $\mathcal{R}$ and $\mathbf{R}$ is the rotation matrix of the section given by *pychrono*.

From this velocity, the mean angle of attack can be found with:

$$\alpha_0 = \arctan\left(\frac{\boldsymbol{U_s} \cdot \boldsymbol{e_y}}{-\boldsymbol{U_s} \cdot \boldsymbol{e_x}}\right)$$

The minus sign comes from the fact that the leading edge is toward positive x.

The position of the airfoil in the section frame is not needed in the sectional models but, as the aerodynamics models are written with the x axis aligned with the wind, the pitch α is taken equal to α_0. The velocity of the airfoil in the section frame can be obtained from the component $\dot{\boldsymbol{X}}_{\boldsymbol{C}}$ of the absolute velocity of the node resolved in the global frame $\mathcal{R}$ and the rotational velocity matrix $\dot{\mathbf{R}}$. The airfoil velocity is expressed in the section frame:

$$\dot{\boldsymbol{X}}_{\boldsymbol{s}} = \mathbf{R_s} \mathbf{R}^T \dot{\boldsymbol{X}}_{\boldsymbol{C}}$$

where $\mathbf{R_s} = \begin{pmatrix} \cos(\alpha_0) & -\sin(\alpha_0) & 0 \\ \sin(\alpha_0) & \cos(\alpha_0) & 0 \\ 0 & 0 & 1 \end{pmatrix}$ allows to pass from the section frame $\mathcal{R}_s$ into section wind frame $\mathcal{R}_{sw}$.

The angular velocity of the airfoil is obtained by transforming the rotational velocity matrix into an antisymmetric matrix in which a rotation vector can be extracted.

$$\boldsymbol{\Omega} = \mathbf{R}^T \dot{\mathbf{R}}$$

with $\boldsymbol{\Omega} = \begin{pmatrix} 0 & -\omega_z & \omega_y \\ \omega_z & 0 & -\omega_x \\ -\omega_y & \omega_x & 0 \end{pmatrix}$ leading to $\boldsymbol{\omega} = \begin{pmatrix} \omega_x \\ \omega_y \\ \omega_z \end{pmatrix}$.

Then this rotation vector is expressed in the section frame in order to extract the pitch rate which is the third component.

$$\boldsymbol{\omega_s} = \mathbf{R}^T \boldsymbol{\omega}$$

Thus, $\dot{\alpha} = \boldsymbol{\omega_s} \cdot \boldsymbol{e_z}$

The acceleration of the elastic center of the airfoil in the section frame is obtained in a same manner.

$$\ddot{\boldsymbol{X}}_{\boldsymbol{s}} = \mathbf{R_s} \mathbf{R}^T \ddot{\boldsymbol{X}}_{\boldsymbol{C}} + \mathbf{R_s} \dot{\mathbf{R}}^T \dot{\boldsymbol{X}}_{\boldsymbol{C}}$$

The pitch acceleration is calculated from the acceleration matrix given by *pychrono* using:

$$\dot{\boldsymbol{\Omega}} = \mathbf{R}^T \ddot{\mathbf{R}} + \boldsymbol{\Omega}^T \boldsymbol{\Omega}$$

Thus, $\ddot{\alpha} = \dot{\boldsymbol{\omega}}_{\boldsymbol{s}} \cdot \boldsymbol{e_z}$ with $\dot{\boldsymbol{\omega}}_{\boldsymbol{s}} = \mathbf{R}^T \dot{\boldsymbol{\omega}}$

3.5.2 Coupling with the CFD solver

Contrary to the sectional models, the CFD solver *FastS* is based on a mesh that discretized the volume around the blade. For the CFD solver to take into account the motion of the blade, the mesh needs to be deformed. This is done in two steps. First, each point of the fluid mesh belonging to the boundary corresponding to the blade skin have to be moved. Then, the volume mesh is deformed using the module *Quantum* introduced in section 2.3. This section focuses on the motion of the skin mesh.

Motion of the mesh surface nodes

At each time step, the blade moves. The goal is thus to calculate the new coordinates of each point of the fluid skin mesh at each iteration.

The coordinates of a point P_i of the fluid mesh, represented in Figure 3.12, can be decomposed into the coordinates of the projected point on the beam centerline and the position into the section associated to this point:

$$\boldsymbol{X}^{(i)} = \boldsymbol{X_C}\left(s^{(i)}\right) + \mathbf{R}\left(s^{(i)}\right) \boldsymbol{X_l}\left(s^{(i)}\right) \tag{3.2}$$

where $\boldsymbol{X}^{(i)}$ is the coordinate in the global frame of point P_i, $s^{(i)}$ is the curvilinear abscissa of the projected point on the beam centerline, $\boldsymbol{X_C}\left(s^{(i)}\right)$ is the coordinate of the centerline point, $\mathbf{R}\left(s^{(i)}\right)$ is the rotation matrix of the centerline point and $\boldsymbol{X_l}\left(s^{(i)}\right)$ is the position of the point P_i within the beam section with respect to the section frame $\mathcal{R}_s$.

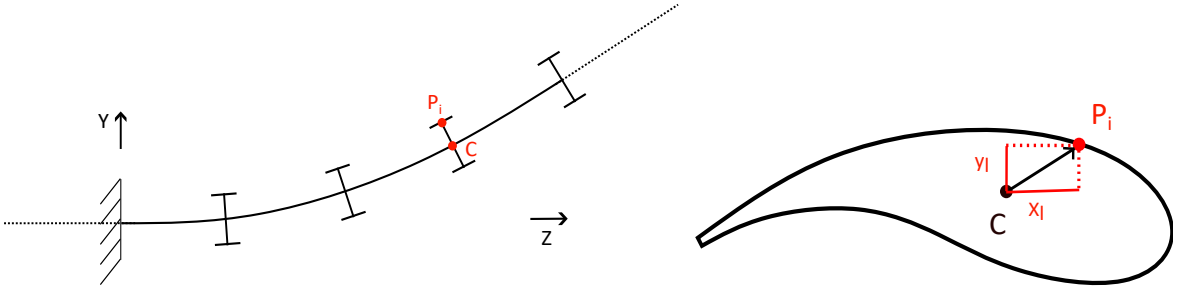

(a) Deformed beam. P_i is a point of the fluid mesh of coordinates $\boldsymbol{X}^{(i)}$ and C is its projected point on the centerline which the coordinates are $\boldsymbol{X_C}$

(b) Coordinates of P_i within the rigid section in the section frame $\mathcal{R}_s$

Figure 3.12: Scheme of the displacement transfer method

$s^{(i)}$ and $\boldsymbol{X_l}\left(s^{(i)}\right)$ need to be found at the initialization of the simulation. The procedure to obtain it is detailed in the next section. $\boldsymbol{X_C}$ and $\mathbf{R}$ are only calculated at the structural nodes. When $s^{(i)}$ is within an element, the values have to be interpolated. Heinz et al. [66] uses spline interpolations but in the present work, an interpolation based on the shape functions of the FEM model, available in *pychrono*, is used. Within *pychrono* the rotations are manipulated with quaternions.

The ALE formulation of the Navier-Stokes equations of the CFD solvers also needs the grid velocities. They can be computed by finite differences but it introduces little errors. So, it is better to calculate skin velocities with the kinematic and propagate it with *Quantum*. The expression of the velocity of a node P_i of the skin mesh is:

$$\boldsymbol{V}^{(i)} = \boldsymbol{V_C}\left(s^{(i)}\right) + \dot{\mathbf{R}}\left(s^{(i)}\right)\boldsymbol{X_l}\left(s^{(i)}\right) \tag{3.3}$$

where $\dot{\mathbf{R}}$ is the derivative of the rotation matrix of the centerline reconstructed based on the interpolation of the rotation vectors with cubic splines.

Attribution of the mesh surface nodes to a span of the beam

For now, $s^{(i)}$ and $\boldsymbol{X_l}\left(s^{(i)}\right)$ are unknown. To find them, the Euler-Bernoulli assumption of the orthogonality of the sections can be used. It means that the scalar product between the vector $\boldsymbol{X}^{(i)} - \boldsymbol{X_C}\left(s^{(i)}\right)$ and tangential vector of the beam at abscissa $s^{(i)}$ is zero.

$$\left(\boldsymbol{X}^{(i)} - \boldsymbol{X_C}\left(s^{(i)}\right)\right) \cdot \mathbf{R}\left(s^{(i)}\right)\boldsymbol{Z} = 0 \tag{3.4}$$

where $\boldsymbol{Z}$ is the third vector of the global frame $\mathcal{R}$.

$\mathbf{R}$ and $\boldsymbol{X_C}$ can be evaluated at any abscissa of the span s, even for $s < 0$ and $s > 1$ the beam has been extended by infinite rigid straight line, as represented in Figure 3.12. Thus, this inverse problem can be resolved with a Newton method to find $s^{(i)}$. The solution is illustrated in the Figure 3.13. The CFD skin mesh of the IEA15MW blade is constituted of successive iso-Z contours that are not perpendicular to the beam.

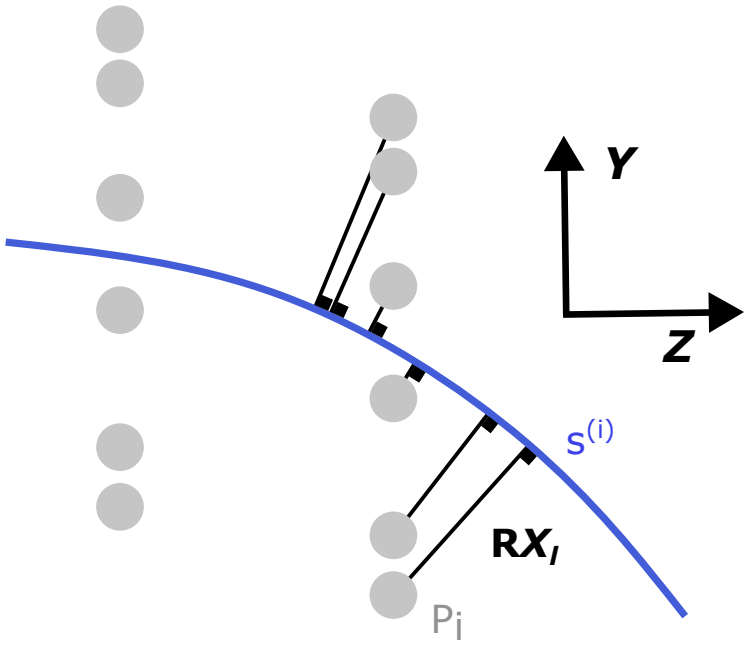

Figure 3.13: Scheme of the attribution of the mesh point to a curvilinear abscissa. The blue line is centerline of the beam while the grey dots are the skin fluid mesh points projected in the YZ plane.

For some nodes around the root and the tip, $s^{(i)}$ may not belong to the beam and be associated with the rigid line. Then, $\boldsymbol{X_l}\left(s^{(i)}\right)$ can be found using Equation 5.2. For nodes being farther than the tip, it means that they are moved according to a rigid motion of the tip. This treatment needs to be done just once at the initialization and saved. It has been added compared to Heinz et al. [66] where the abscissa $s^{(i)}$ are taken equal to the abscissa z.

Implementation

This method has been implemented in a python class named *Transfert_ deplacements*. The fluid mesh is collected either by association with the Fluid class *Fluid_ FastS* using the function **SetFluid** or by directly giving the mesh using **SetTree**. The fluid mesh is saved in the CGNS format and manipulated using the ONERA software *Cassiopee*.

The dot product in equation 3.4 is implemented in the function **section_othogonality**. For a given point and abscissa s, the dot product is calculated. The blade may not be oriented in the same direction in the structural frame and the fluid mesh. In *Chrono*, the beam span is toward the X direction whereas the blade is orientated along the Z axis in the fluid mesh. That's why a change-of-basis matrix P is defined in *Transfert_ deplacements*. It modifies $\boldsymbol{X_C}$ and $\mathbf{R}$ extracted from the beam solver before using them in the dot product. The Newton method to found $s^{(i)}$ is implemented in **associate_rigid_section**. For each point, $s^{(i)}$ and $\boldsymbol{X_l}\left(s^{(i)}\right)$ are saved in np.array.

Finally, the rigid motion described in eq 5.2 is implemented in **calcul_grid_displacement_beam**. This function returns the displacement of the surfaces that are then given to *Quantum*.

Validation

To verify the method and its implementation, the loads obtained with a rigid CFD simulation at $U_0 = 40m/s$ and $\alpha_0 = 3°$ (see Figure 3.16) are imposed to the beam model. A static structural simulation is done to calculate the deformed state. This new state is used to compute the new geometry of skin mesh. The initial and deformed geometry of the skin mesh are compared with the initial and deformed state of the beam in Figure R.6.

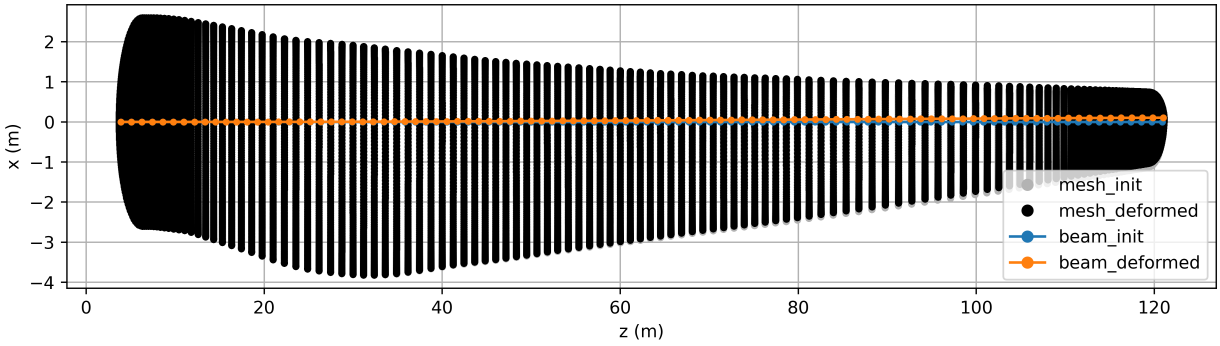

(a) X direction

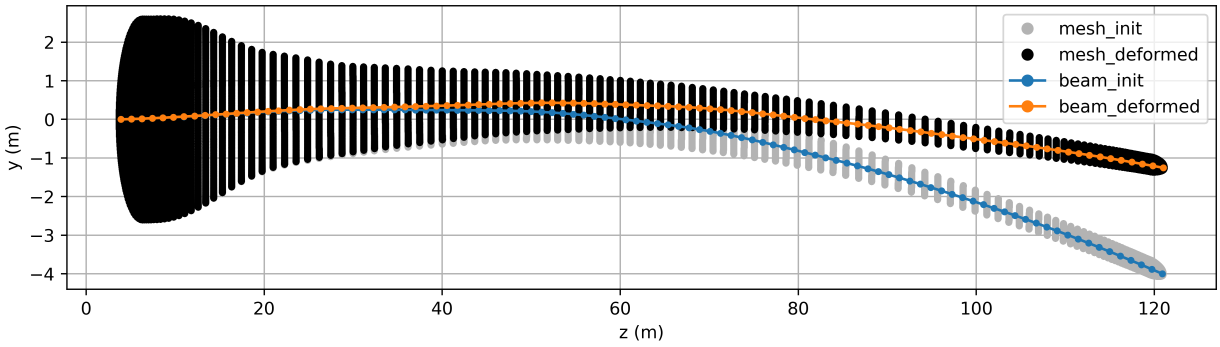

(b) Y direction

Figure 3.14: Deformation of the skin mesh

The undeformed shape of the beam in blue has been initially placed in the initial skin mesh of the blade in grey. It is in this configuration that each gray dot, representing the mesh node, is associated to an abscissa $s^{(i)}$ of the beam. Then, the beam has been deformed into the orange shape. Thus, each node in black has correctly followed the deformation and are around the deformed state of the beam.

3.6 Implementation of the load transfer

The second transfer method to implement is the load transfer. As described in chapter 2, there are several methods to transfer the loads. Given that the structural mesh and the fluid mesh are highly non-matching, it has been chosen to use a method similar to Heinz et al. [66] with slices of the fluid skin mesh. To pass from the CFD wall pressure and shear stress to structural loads adapted to the FEM beam model, two steps are needed. First, to obtain sectional loads, slices are realized on the skin mesh along the blade. The orientation of the slices is determined by the structure position. Then, the wall pressure and shear stress are integrated along the contours defined by the slices, leading to sectional loads. Secondly, these sectional loads are transformed into generalized loads by integrating them with the shape functions of the FEM model.

3.6.1 Orientation of the slices and integration

Contrary to Heinz et al. [66] who realized the slices in the XY plane (as explained in chapter 2), the slices are oriented according to the beam kinematics. For Euler-Bernoulli beams the sections are perpendicular to the local direction of the blade. Therefore, for each structural node, a slice along the section plane defined by the section frame $\mathcal{R}_s$ is realized, i.e the plane equation of the slices is deduced from the rotation matrix $\mathbf{R}$ of the nodes given by *pychrono*. A scheme is given in the Figure 3.15.

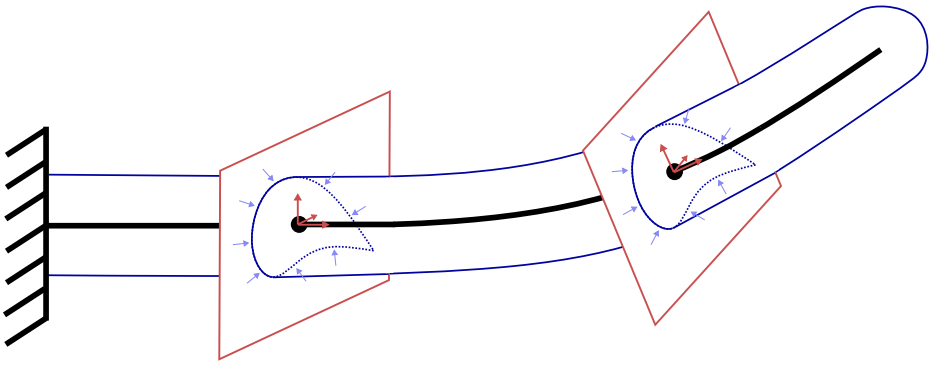

Figure 3.15: Scheme of the slices. The red frames are the local section frame $\mathcal{R}_s$.

Then, the wall pressure and shear stress on the intersection of the slices and the skin mesh is integrated in order to obtain the sectional forces and moments in the three directions of the global frame $\mathcal{R}$. As the slices are based on the blade configuration, most of the time they do not intersect the computation point of the CFD. It means that the wall pressure and the shear stress used in the integration come from linear interpolations within the CFD cells.

Implementation This is implemented in the python class named *Transfert_Forces*. First, a function calculates the equation of the plan corresponding to the section of a node and returns the coefficients. The slice is constructed with *Cassiopee* using the coefficients of the plane. Next, the integration is done in another function using *Cassiopee*.

3.6.2 Comparison between the CFD and the strip theory models

No experimental data are available for the IEA15MW. So, to verify that the loads transfer is working, a steady RANS simulation of the undeformed IEA15MW blade has been done with *FastS* and the loads have been compared with quasi-steady aerodynamics. The blade has been placed in a uniform wind of 40m/s at 3° of incidence in order to have an attached flow. The polars used with the quasi-steady aerodynamic model are the one of the github of the IEA15MW [3]. The loads from both models are reported in Figure 3.16.

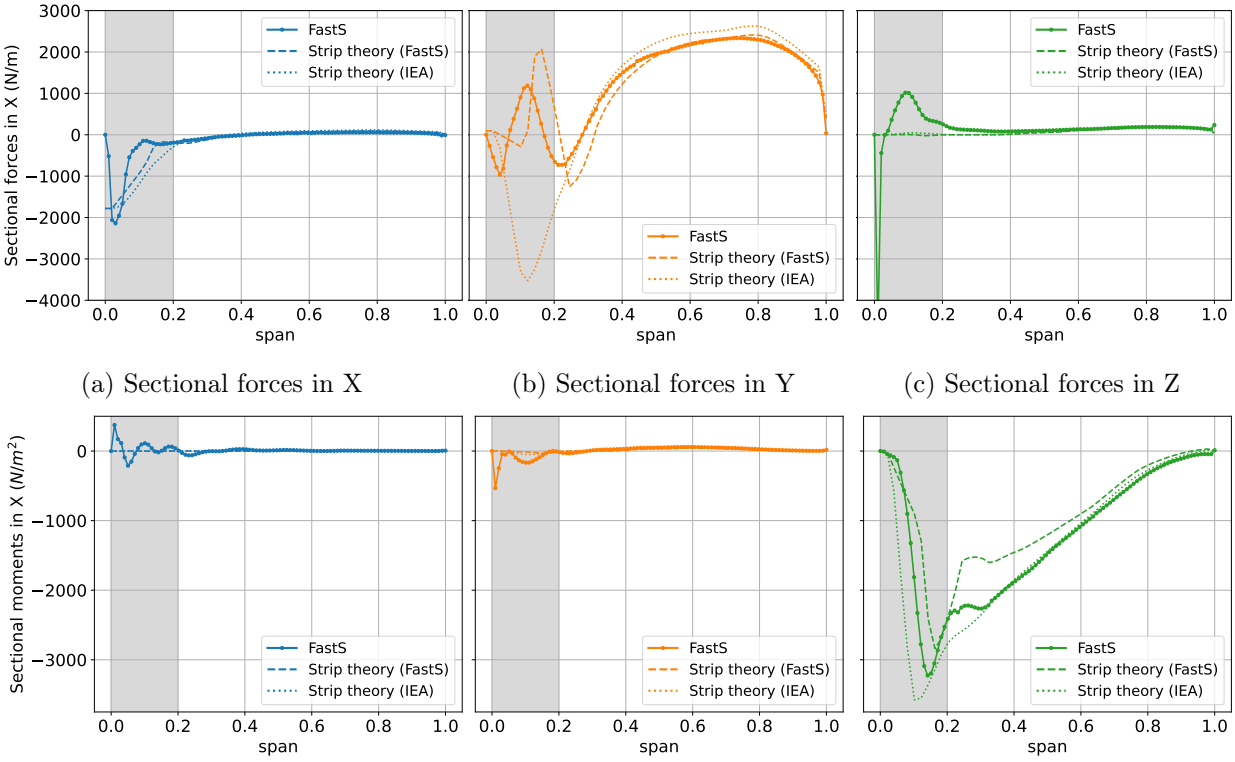

(a) Sectional forces in X (b) Sectional forces in Y (c) Sectional forces in Z

(d) Sectional moment in X (e) Sectional moment in Y (f) Sectional moment in Z

Figure 3.16: Comparison between the loads obtained with CFD and the loads obtained with the strip theory ($U_0 = 40m/s$ and $\alpha_0 = 3°$). The two set of polars is explained in Appendix A.

For most of the blade (span > 0.2), *FastS* and the strip theory with the IEA polars agree for the sectional forces and moments. The sectional forces in Y obtained with the CFD are slightly lower than the reading of the IEA polars. The strip theory with the *FastS* polars also agree with the CFD for the sectional forces but a gap is present for the sectional moment. Based on the Figure 3.16, the transfer of loads is satisfying. For the part of the blade near the root indicated by the shaded area, the sections are close to a cylinder. As a consequence, the CFD struggles to correctly predict the loads, notably because no boundary layer transition model is used. Nevertheless, as it will be seen in the next chapter, this area does not generate any power and does not affect the aeroelastic behavior of the system.

[3] https://github.com/IEAWindTask37/IEA-15-240-RWT

3.6.3 Calculation of the generalized forces for the beam FEM model

However, these loads cannot be passed directly to the beam FEM model. The loads needed for the FEM model are generalized loads in Newtons and not Newtons per meter. In the FEM formulation, the sectional loads have to be multiplied by the FEM shape functions and integrated in span. This applies for the sectional loads obtained with both the CFD and the strip theory models. The sectional loads are only known at the structural nodes and must be interpolated in between, that's why, in order to be integrated, the sectional loads are assumed to evolve linearly between the structural nodes.

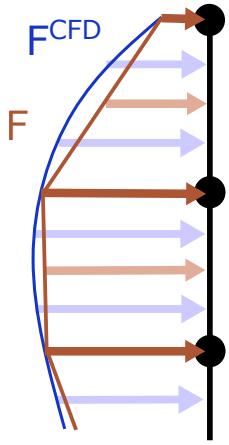

Figure 3.17: Illustration of the hypothesis of linear evolution of the loads within the beam elements

To calculate the generalized loads, let's take a Euler-Bernoulli beam element oriented in the x direction from $-\frac{l}{2}$ and $\frac{l}{2}$, as it is implemented in *pychrono*. The work of the external forces can be calculated in two manners. The first one consists in multiplying the generalized loads by the displacements and rotations of the two nodes. And the second one passes by a continuous approach by integrating the local work over the element. Put into equations, it gives:

$$\boldsymbol{q}^T \boldsymbol{F}_{FEM} = \int_{-\frac{l}{2}}^{\frac{l}{2}} \boldsymbol{u}^T(x) \boldsymbol{F}(x) dx \tag{3.5}$$

where $\boldsymbol{q}^T = \begin{bmatrix} u_x^1 & u_y^1 & u_z^1 & \theta_x^1 & \theta_y^1 & \theta_z^1 & u_x^2 & u_y^2 & u_z^2 & \theta_x^2 & \theta_y^2 & \theta_z^2 \end{bmatrix}$ is the displacements and rotations of the two nodes, $\boldsymbol{u}^T = \begin{bmatrix} u_x & u_y & u_z & \theta_x & \theta_y & \theta_z \end{bmatrix}$ is the local displacements and rotations, and $\boldsymbol{F}$ is the sectional loads. All the quantities are written in the structure global frame $\mathcal{R}_b$ used in *pychrono*, which is rotated by 90° around Y compared to the fluid global frame $\mathcal{R}$.

In the finite element method, the continuous displacements and rotations $\boldsymbol{u}$ are interpolated from the nodal displacements and rotations $\boldsymbol{q}$ using shape functions regrouped in the matrix $\mathbf{N_e}$:

$$\boldsymbol{u} = \mathbf{N_e}(x) \boldsymbol{q} \tag{3.6}$$

The axial displacements and the torsion only depend on the axial displacements and torsion of the nodes respectively. But due to the Euler-Bernoulli assumption that imposed the section to be perpendicular to the centerline, the rotation of the nodes can introduced displacements within the element and vice versa. It leads to the following form of the matrix $\mathbf{N_e}$:

$$\mathbf{N_e} = \begin{bmatrix} N_0 & 0 & 0 & 0 & 0 & 0 & N_3 & 0 & 0 & 0 & 0 & 0 \\ 0 & N_1 & 0 & 0 & 0 & N_2 & 0 & N_4 & 0 & 0 & 0 & N_5 \\ 0 & 0 & N_1 & 0 & -N_2 & 0 & 0 & 0 & N_4 & 0 & -N_5 & 0 \\ 0 & 0 & 0 & N_0 & 0 & 0 & 0 & 0 & 0 & N_3 & 0 & 0 \\ 0 & 0 & -N_6 & 0 & N_8 & 0 & 0 & 0 & -N_7 & 0 & N_9 & 0 \\ 0 & N_6 & 0 & 0 & 0 & N_8 & 0 & N_7 & 0 & 0 & 0 & N_9 \end{bmatrix} \tag{3.7}$$

To ensure the continuity of the displacements and the rotations, the shape functions are typically Hermit polynomials. Then, the coefficients of the polynomials can be identified using the condition that $\boldsymbol{u}$ should be equal to the value of $\boldsymbol{q}$ at the nodes:

$$N_0(x) = 0.5\left(1 - 2\frac{x}{l}\right)$$
$$N_1(x) = 0.25\left(1 - 2\frac{x}{l}\right)^2\left(2 + 2\frac{x}{l}\right)$$
$$N_2(x) = \frac{l}{8}\left(1 - 2\frac{x}{l}\right)^2\left(1 + 2\frac{x}{l}\right)$$
$$N_3(x) = 0.5\left(1 + 2\frac{x}{l}\right)$$
$$N_4(x) = 0.25\left(1 + 2\frac{x}{l}\right)^2\left(2 - 2\frac{x}{l}\right)$$

$$N_5(x) = \frac{l}{8}\left(1 + 2\frac{x}{l}\right)^2\left(2\frac{x}{l} - 1\right)$$
$$N_6(x) = \frac{1}{2l}\left(-3 + 3\left(\frac{2x}{l}\right)^2\right)$$
$$N_7(x) = \frac{1}{2l}\left(3 - 3\left(\frac{2x}{l}\right)^2\right)$$
$$N_8(x) = \frac{1}{4}\left(-1 - 4\frac{x}{l} + 3\left(\frac{2x}{l}\right)^2\right)$$
$$N_9(x) = -\frac{1}{4}\left(1 - 4\frac{x}{l} - 3\left(\frac{2x}{l}\right)^2\right)$$

The shape functions are illustrated in the Figure 3.18.

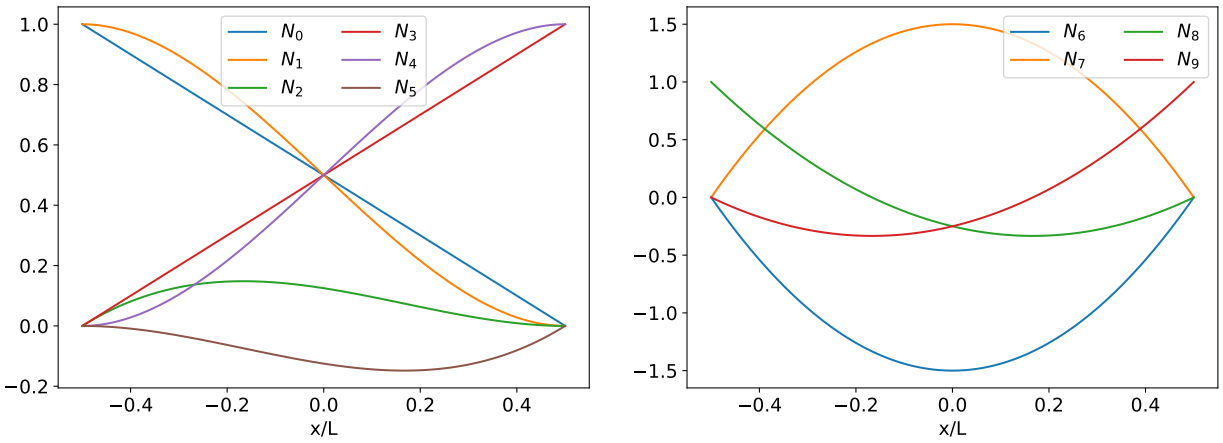

Figure 3.18: Shape functions

In addition, the linear evolution of the loads between the nodes gives the following expression

of the sectional loads:

$$\boldsymbol{F}(x) = \begin{bmatrix} F_{xi}^{\text{CFD}}\left(\frac{1}{2}-\frac{x}{l}\right) + F_{xj}^{\text{CFD}}\left(\frac{1}{2}+\frac{x}{l}\right) \\ F_{yi}^{\text{CFD}}\left(\frac{1}{2}-\frac{x}{l}\right) + F_{yj}^{\text{CFD}}\left(\frac{1}{2}+\frac{x}{l}\right) \\ F_{zi}^{\text{CFD}}\left(\frac{1}{2}-\frac{x}{l}\right) + F_{zj}^{\text{CFD}}\left(\frac{1}{2}+\frac{x}{l}\right) \\ M_{xi}^{\text{CFD}}\left(\frac{1}{2}-\frac{x}{l}\right) + M_{xj}^{\text{CFD}}\left(\frac{1}{2}+\frac{x}{l}\right) \\ M_{yi}^{\text{CFD}}\left(\frac{1}{2}-\frac{x}{l}\right) + M_{yj}^{\text{CFD}}\left(\frac{1}{2}+\frac{x}{l}\right) \\ M_{zi}^{\text{CFD}}\left(\frac{1}{2}-\frac{x}{l}\right) + M_{zj}^{\text{CFD}}\left(\frac{1}{2}+\frac{x}{l}\right) \end{bmatrix} \tag{3.8}$$

where $\boldsymbol{F}^{CFD}$ and $\boldsymbol{M}^{CFD}$ are the loads per unit length obtained by the integrations over the slices of node i and j in the CFD and projected into the structure global frame $\mathcal{R}_b$.

Thus, the generalized loads can be calculated with $\boldsymbol{F}_{FEM} = \int_{-\frac{l}{2}}^{\frac{l}{2}} \mathbf{N_e}^T(x)\boldsymbol{F}(x)dx$, which gives:

$$\boldsymbol{F}_{FEM} = \begin{bmatrix} \frac{l}{6}\left(2F_{xi}^{\text{CFD}} + F_{xj}^{\text{CFD}}\right) \\ \frac{7l}{20}F_{yi}^{\text{CFD}} + \frac{3l}{20}F_{yj}^{\text{CFD}} - \frac{1}{2}M_{zi}^{\text{CFD}} - \frac{1}{2}M_{zj}^{\text{CFD}} \\ \frac{7l}{20}F_{zi}^{\text{CFD}} + \frac{3l}{20}F_{zj}^{\text{CFD}} + \frac{1}{2}M_{yi}^{\text{CFD}} + \frac{1}{2}M_{yj}^{\text{CFD}} \\ \frac{l}{6}\left(2M_{xi}^{\text{CFD}} + M_{xj}^{\text{CFD}}\right) \\ \frac{l}{60}\left(-3lF_{zi}^{\text{CFD}} - 2lF_{zj}^{\text{CFD}} + 5M_{yi}^{\text{CFD}} - 5M_{yj}^{\text{CFD}}\right) \\ \frac{l}{60}\left(3lF_{yi}^{\text{CFD}} + 2lF_{yj}^{\text{CFD}} + 5M_{zi}^{\text{CFD}} - 5M_{zj}^{\text{CFD}}\right) \\ \frac{l}{6}\left(F_{xi}^{\text{CFD}} + 2F_{xj}^{\text{CFD}}\right) \\ \frac{3l}{20}F_{yi}^{\text{CFD}} + \frac{7l}{20}F_{yj}^{\text{CFD}} + \frac{1}{2}M_{zi}^{\text{CFD}} + \frac{1}{2}M_{zj}^{\text{CFD}} \\ \frac{3l}{20}F_{zi}^{\text{CFD}} + \frac{7l}{20}F_{zj}^{\text{CFD}} - \frac{1}{2}M_{yi}^{\text{CFD}} - \frac{1}{2}M_{yj}^{\text{CFD}} \\ \frac{l}{6}\left(M_{xi}^{\text{CFD}} + 2M_{xj}^{\text{CFD}}\right) \\ \frac{l}{60}\left(2lF_{zi}^{\text{CFD}} + 3lF_{zj}^{\text{CFD}} - 5M_{yi}^{\text{CFD}} + 5M_{yj}^{\text{CFD}}\right) \\ \frac{l}{60}\left(-2lF_{yi}^{\text{CFD}} - 3lF_{yj}^{\text{CFD}} - 5M_{zi}^{\text{CFD}} + 5M_{zj}^{\text{CFD}}\right) \end{bmatrix} \tag{3.9}$$

This is the contribution from one element, so for a specific node, the contribution from each adjacent element needs to be summed.

This procedure is valid if the beam element is oriented in the x direction, however to take into account the prebend and the large displacements, the matrix $\mathbf{N_e}$ should be modified using rotation matrices.

Remark 1 *Due to the linear interpolation of the loads between the nodes, this transfer method is not consistent.*

3.6.4 Precautions with the slices

A limit of the method has been identified. When the fluid mesh skin is coarse, the integration of the loads over the slices can produce unphysical moments. For example, a blade with a tubular geometry over a circular-shaped span is represented in Figure 3.19. The pressure forces are normal to the wall and should produce moment only in the direction of the beam. However, due to the discretization of the mesh and the curvature of the beam, moments within the section can be induced. The curvature of the blade is low enough so that this effect does not appear in the Figure 3.16. Otherwise, the mesh should be refined.

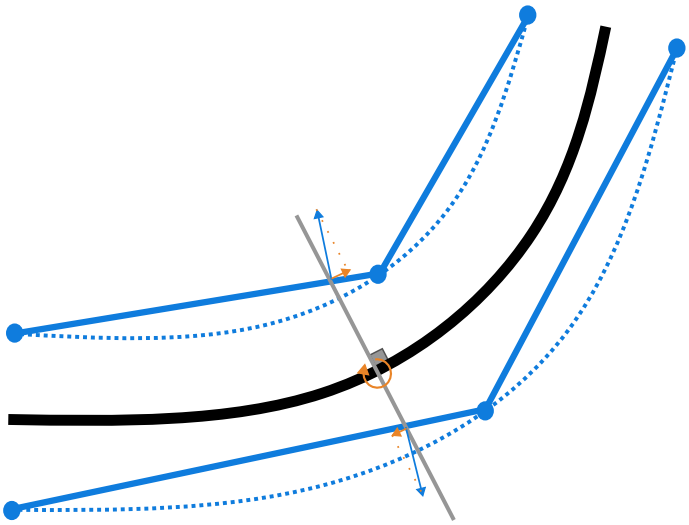

Figure 3.19: Scheme explaining the production of an unwanted moment. The black line is the beam. The dotted blue line is the exact geometry of the blade while the solid blue line is the discretized geometry. The slice is represented in grey.

Remark 2 *When running parallel simulations, the loads need to be copied over all the processors that run the structural solver in order to be exactly identical. Without this copy, if the loads are not exactly the same for all the processors, it can lead to a divergence of the beam model between the tasks and then a dislocation of the mesh afterwards because each task only moves one part of the mesh.*

3.7 Comparison of the static aeroelastic coupling between the CFD and the strip theory models

Now that each step has been validated, everything can be put together in order to verify that all the steps chain correctly. In that purpose, static aeroelastic simulations have been conducted at $U_0 = 40m/s$ and an incidence of 3°. The convergence toward the static aeroelastic equilibrium is observed through the evolution of the tip position in Y over the coupling iterations in Figure 3.20.

The initial position is the undeformed configuration. The loads are computed with a stationary CFD simulation and transferred to the structure. A structural static simulation allows to calculate a new state leading to the Y tip position in iteration 1. However, the previous loads does not correspond to the actual blade state and needs to be updated. After few coupling iterations, the simulations using the strip theory assumption have converged but the simulation using CFD needs more iterations to converge. The final states of the three aeroelastic simulations are compared in Figure 3.21.

All the final states are close, especially for the torsion. However, the equilibriums obtained with the polars under the strip theory assumption are more deflected than the one computed with CFD. It was expected as the loads were higher for the IEA polars in Figure 3.16. Moreover, 3D effects that are not modelled under the strip theory could have an impact on the equilibrium state. Nevertheless, the coupling chain has worked properly with CFD and has given a consistent equilibrium state.

Remark 3 *No dynamic validation has been done due to a lack of reference.*

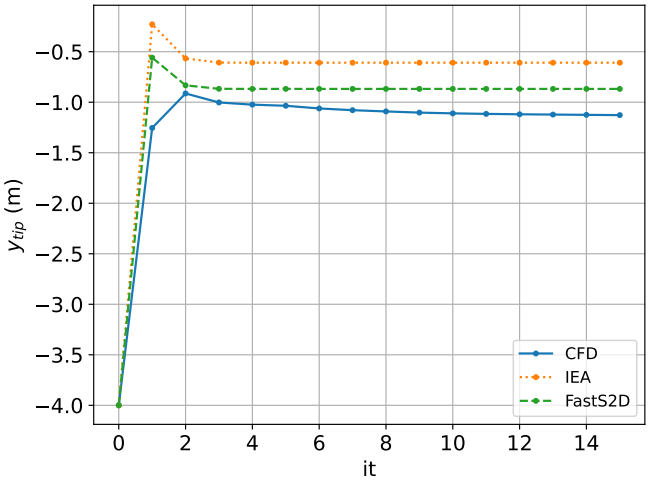

Figure 3.20: Evolution of the tip position in Y over the coupling iterations for the beam/CFD simulation and simulations with the strip theory assumption.

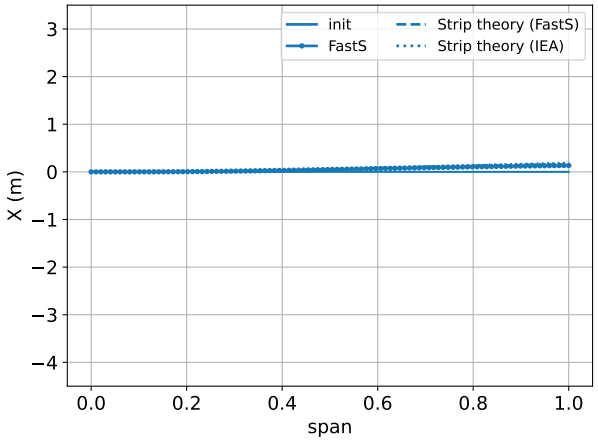

(a) Flexion in X

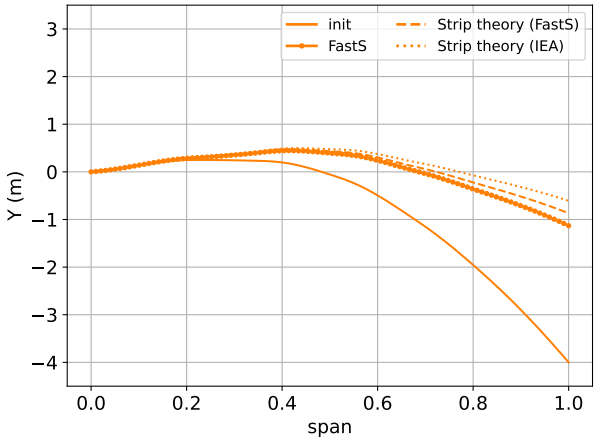

(b) Flexion in Y

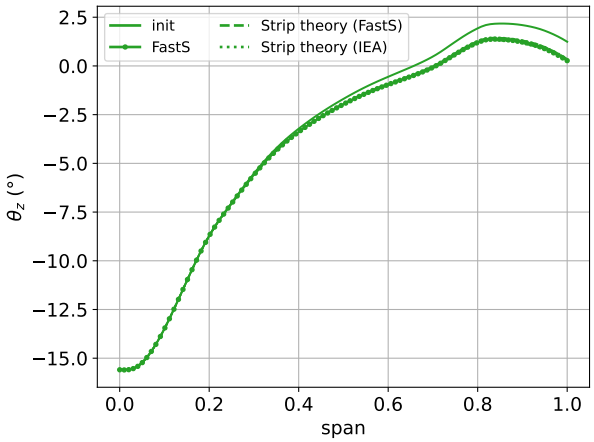

(c) Torsion

Figure 3.21: Deformation of the blade for $\phi_0 = 3°$ and $U_0 = 40$m/s calculated with CFD and the strip theory assumption. The solid line represents the initial configuration.

3.8 Restart of dynamic aeroelastic simulations

As the characteristic time of the fluid is brief compared to the period of the flexion modes, a large number of time steps is necessary to simulate several periods of oscillation of the blade. However, the maximum time duration of a job is limited on clusters. On Adastra, the limit is 24 hours. To overcome this duration, the solver needs to save the current state and the ones of previous iterations in order to restart the simulation in a new job. For the restart to be smooth and to not generate spurious density, everything needs to be numerically perfect. The mesh deformer operator has to be generated on the initial mesh at any restart, otherwise, even if the mesh deformation is good, it could be incompatible with the operator of the previous job. Finally, the restart procedure in *FastS* was not adapted for aeroelastic simulation because the time derivative of the cell volumes was set to zero, leading to a numerical error in the ALE formulation at the first iteration. To correct this, the volumes of the cells were saved for the three last iterations and given to *FastS* at the restart. Thus, some modifications in *FastS* were made.

3.9 Conclusion

In this chapter, a python framework has been developed in order to use and couple easily fluid and structure models of different levels of fidelity. First, the structural model has been verified by comparing the natural frequency of the IEA15MW blade with other institution results. Then, the CFD solver *FastS* has been used to reproduce experimental dynamic stall loops in 2D. It appeared that the URANS simulations were valid until some angle of attack where vortex shedding occurs and makes the lift coefficient diverging from experiment. Next, the load transfer method has been compared with quasi-steady aerodynamics and has shown a satisfying match. Finally, the motion transfer has been qualitatively validated.

All these developments will be integrated in Mimas, the modular code that groups advanced methods for coupling fluid and structure at ONERA.

Chapter 4

Study of stall-induced vibrations at standstill with low fidelity models

Previous studies have highlighted that large wind turbine blades can be prone to SIV at standstill on either flapwise, edgewise or a combination of flapwise and edgewise modes. Risk assessment requires FSI calculations for different wind conditions (direction and speed), which may be prohibitive using high fidelity approach. Many studies investigating stall-induced vibrations have been done using sectional approaches. More simple and computationally cheap, such approach allow to easily study various wind conditions but can be questioned for twisted and flexible blades with variable sections. In that context: how to choose the most relevant section of a specific blade? Is it possible to define an equivalent section? Questions also concern the motion-induced aerodynamic model. Quasi-static approach like the one presented in chapter 1 are often used but further investigation of the potential instabilities addressing the dynamic stall process are required. Indeed, as for stall flutter, the dynamic stall loops should also have an impact on the aerodynamic damping. However, as mentioned in chapter 1, dynamic stall models are very dependent on the section profiles, mean angle of attack and reduced frequency (that is proportional to the chord), which again raises the question of choosing the best section along the blade or identifying an equivalent section. In that context the goal of this chapter is to assess the potential of section model approaches to study stall-induced vibrations at standstill using the modular framework exposed in the previous chapter with low fidelity models. Following the idea of Branlard et al. [20], our aim is to build an equivalent section model that is the closest possible to a specific full blade, the IEA15MW blade. To do so, an equivalent 2dof (flapwise and edgewise) section model based on either quasi-steady or the ONERA dynamic stall aerodynamic formulation will be compared to a continuous approach for which the blade, modeled by a finite element model using corotated Euler-bernoulli beam elements is coupled, under strip theory assumption, to the ONERA dynamic stall model.

Furthermore, this study aims at preparing high fidelity simulations by identifying few relevant SIV configurations.

Contents

4.1 Development of an equivalent section model 86
4.1.1 Step 1 : Equations of motion of a 2dof equivalent section model 87
4.1.2 Step 2: Modal equations of the blade 90
4.1.3 Step 3: Identification of the section model edgewise direction and equivalent chord 94
4.1.4 Step 4: Identification of an equivalent polar 96
4.1.5 Step 5: Identification of the flexion-torsion coupling stiffness and the angle of torsion 97
4.1.6 Summary and implementation 99
4.2 Effect of the dynamic stall model 101
4.2.1 Stability map 102
4.2.2 Stability analysis for a wind of fixed angle of incidence 103

4.2.3 Stability analysis for a wind of fixed velocity . . . 104
4.2.4 Effect of the loops orientation . . . 105
4.3 Stability analysis using a finite element model of the blade . . . 106
4.3.1 Spanwise distribution of the fluid-structure energy transfer . . . 107
4.3.2 Stability analysis . . . 108
4.4 Discussions . . . 109
4.4.1 Equivalent dynamic stall . . . 109
4.4.2 The equilibrium modification . . . 110
4.4.3 Comparison with a simpler sectional model . . . 111
4.4.4 Sensitivity to a parameter of the ONERA model . . . 113
4.5 Conclusion . . . 114

4.1 Development of an equivalent section model

A section model that could simulate the behavior of a full blade is build in this section. Branlard et al. [20] developed such a reduced-order model with three degrees of freedom, the flapwise and edgewise flexions as well as the torsion. It allows to simulate the dynamic behavior of a specific section of the blade with a variety of aerodynamic model for a low cost. In [20] the model is scaled with respect to a particular section of the blade, considering generalized mass, inertia and stiffness computed with shape functions of the blade. The motion-induced aerodynamic loads are computed from unsteady 2D CFD performed on an chosen section and then scaled in order to take into account the aerodynamic loads acting on the full blade. This scaling is based on load shape functions obtained from steady aerodynamic simulation on the full blade.

The model developed in the present study is an equivalent section, not linked to any specific section of the blade. It has two degrees of freedom, edgewise in the x direction and flapwise in the y direction, perpendicular to the edgewise direction. The latter is defined with an angle α_{edgewise} according to a reference direction chosen to facilitate the comparison between the equivalent section model and the continuous blade model. The reference direction is the one used in the github of the IEA15MW, it is the chord direction at 66% of the blade. As the blade is twisted, the chord of the equivalent section is not necessarily aligned with the edgewise direction. An angle $\alpha^{2D}_{\text{twist}}$ is then introduced in Figure 4.1. The angle of incidence of the wind ϕ_0, is also defined according to the reference direction. In so far as the aerodynamic pitching moment can deform the blade, a torsional equilibrium equation will also be considered, along with the contribution in torsion of both the edgewise and flapwise deformations. Note that a 3dof (edgewise-flapwise-torsion) model could have been used but as the torsion is stiffer than both the edgewise and flapwise modes, with a torsion frequency of 4.67Hz compared to the 0.51Hz and 0.7Hz of the flapwise and edgewise modes, it has been shown that its role in the dynamic of the system can be neglected regarding the study of SIV at standstill.

All the parameters of the equivalent section are chosen in order to model the dynamics of the IEA15MW as closest as possible. The general idea is to compare the equations of motion of the equivalent section with the modal equations of the blade, considering only the first flapwise and edgewise mode, in order to identify the best section parameters. This identification process is done considering a quasisteady aerodynamic formulation introducing an effective velocity vector that will depend on the motion in both edgewise and flapwise but also on torsional deformations. The procedure is constituted of five steps. The first step consists of writing the dimensionless linearized

equation of the 2dof section model. In the step two, the same treatment is done for the modal equations of the blade. The step three allows the identification of an equivalent chord and angle α_{edgewise} by comparing a simplified formulation of the dominant modal aerodynamic damping term for the flapwise mode with the one associated to the linearized section model. This step three is done neglecting both the twist and prebend of the blade. In step 4, a more general identification between the two linearized models allows to compute an equivalent polar taking into account the twist and the prebend of the blade. Finally, the coefficient of the flexion-torsion coupling are identified in a fifth step.

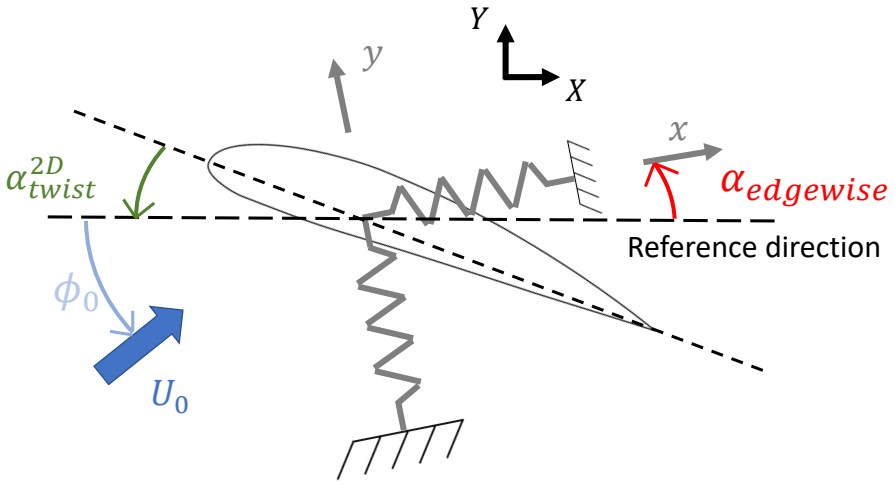

Figure 4.1: Scheme of a 2dof section

4.1.1 Step 1 : Equations of motion of a 2dof equivalent section model

Using the Lagrange equations, and assuming a quasi-static behavior of the aerodynamic loads, the equation of motion of the equivalent section model writes:

$$m_{\text{eq}}\ddot{x}+d_x\dot{x}+k_x x = \frac{1}{2}\rho c_{\text{eq}} U^2_{\text{eff}_{2D}} \begin{pmatrix}\cos(\alpha_{\text{edgewise}})\\ \sin(\alpha_{\text{edgewise}})\end{pmatrix}\cdot\begin{bmatrix}\cos(\alpha^{2D}_{\text{eff}}-\alpha^{2D}_{\text{twist}}) & -\sin(\alpha^{2D}_{\text{eff}}-\alpha^{2D}_{\text{twist}})\\ \sin(\alpha^{2D}_{\text{eff}}-\alpha^{2D}_{\text{twist}}) & \cos(\alpha^{2D}_{\text{eff}}-\alpha^{2D}_{\text{twist}})\end{bmatrix}\begin{pmatrix}C^{2D}_D(\alpha^{2D}_{\text{eff}})\\ C^{2D}_L(\alpha^{2D}_{\text{eff}})\end{pmatrix} \tag{4.1a}$$

$$m_{\text{eq}}\ddot{y}+d_y\dot{y}+k_y y = \frac{1}{2}\rho c_{\text{eq}} U^2_{\text{eff}_{2D}} \begin{pmatrix}-\sin(\alpha_{\text{edgewise}})\\ \cos(\alpha_{\text{edgewise}})\end{pmatrix}\cdot\begin{bmatrix}\cos(\alpha^{2D}_{\text{eff}}-\alpha^{2D}_{\text{twist}}) & -\sin(\alpha^{2D}_{\text{eff}}-\alpha^{2D}_{\text{twist}})\\ \sin(\alpha^{2D}_{\text{eff}}-\alpha^{2D}_{\text{twist}}) & \cos(\alpha^{2D}_{\text{eff}}-\alpha^{2D}_{\text{twist}})\end{bmatrix}\begin{pmatrix}C^{2D}_D(\alpha^{2D}_{\text{eff}})\\ C^{2D}_L(\alpha^{2D}_{\text{eff}})\end{pmatrix} \tag{4.1b}$$

$$k_{\alpha_{\text{torsion}}}\alpha_{\text{torsion}} = \frac{1}{2}\rho c^2_{\text{eq}} U^2_{\text{eff}_{2D}} C^{2D}_M(\alpha^{2D}_{\text{eff}}) \tag{4.1c}$$

where m_{eq} is an equivalent mass, c_{eq} is an equivalent chord, d_x and d_y are lineic damping coefficients, k_x and k_y are lineic stiffness in edgewise and flapwise allowing to match the first modal frequencies of the IEA15MW blade (0.51 Hz in flapwise and 0.7 Hz in edgewise). These frequencies where obtained with an eigenvalue analysis using matrices calculated by the finite element solver project Chrono. As mentioned previously a torsional equilibrium equation has been added to the system. It introduces a generalized stiffness $k_{\alpha_{\text{torsion}}}$ also computed with the finite element solver.

A quasisteady aerodynamic model is considered here. It assumes that the flow reacts instantaneously to an effective wind condition (in modulus and direction). Several quasi-steady aerodynamic models exist as described in [41] in section 3.4.2.2. The approach chosen here is

to calculate an effective wind speed $U_{\text{eff}_{2D}}$ and an effective angle of attack α_{eff}^{2D}, induced by the movement of the airfoil, and to evaluate the load by using the static polars as if the airfoil were steady with a wind velocity $U_{\text{eff}_{2D}}$ and an angle of attack α_{eff}^{2D} defined as :

$$U_{\text{eff}_{2D}}^2 = (U_0\cos(\phi_0 - \alpha_{\text{edgewise}}) - \dot{x})^2 + (U_0\sin(\phi_0 - \alpha_{\text{edgewise}}) - \dot{y})^2 \tag{4.2a}$$

$$\alpha_{\text{eff}}^{2D} = \alpha_{\text{twist}}^{2D} + \arctan\left(\frac{U_0\sin(\phi_0 - \alpha_{\text{edgewise}}) - \dot{y}}{U_0\cos(\phi_0 - \alpha_{\text{edgewise}}) - \dot{x}}\right) + \alpha_{\text{edgewise}} + k_{\alpha x}\frac{x}{c_{\text{eq}}} + k_{\alpha y}\frac{y}{c_{\text{eq}}} + \alpha_{\text{torsion}}(U_0, \phi_0) \tag{4.2b}$$

Note that the last three terms in the expression of α_{eff}^{2D} (Eq. 4.2b) introduce $k_{\alpha x}$ and $k_{\alpha y}$ coefficients to model the contribution in torsion of both the edgewise and flapwise deformations, but also α_{torsion} that is a static equilibrium angle of torsion under the pitching aerodynamic moment about the elastic center C_M^{2D}.

The loads in Equations 4.1a and 4.1b are written with a scalar product between the spring direction in the global frame and the aerodynamic loads coefficients transferred into the global frame by a rotation matrix. With a flexion-torsion coupling, the moment around the elastic center should also induce a displacement in the flexion direction but this effect has been neglected.

Step 1a: Dimensionless form of the section equations

To analyze the physics of the system, it's better to write it in a dimensionless form. The distances are nondimensionalized by the chord c_{eq} and the time by the flapwise pulsation ω_y.

$$\tilde{x} = x/c_{\text{eq}} \qquad \tilde{y} = y/c_{\text{eq}} \qquad \tilde{t} = \omega_y t \qquad \tilde{U}_{\text{eff}_{2D}} = U_{\text{eff}_{2D}}/U_0$$

It gives the following equations:

$$\frac{\partial^2\tilde{x}}{\partial\tilde{t}^2} + 2\xi_x\beta\frac{\partial\tilde{x}}{\partial\tilde{t}} + \beta^2\tilde{x} = \frac{1}{2}\mathcal{M}\mathcal{U}_R^2\tilde{U}_{\text{eff}_{2D}}^2\begin{pmatrix}\cos(\alpha_{\text{edgewise}})\\ \sin(\alpha_{\text{edgewise}})\end{pmatrix}\cdot\begin{bmatrix}\cos(\alpha_{\text{eff}}^{2D} - \alpha_{\text{twist}}^{2D}) & -\sin(\alpha_{\text{eff}}^{2D} - \alpha_{\text{twist}}^{2D})\\ \sin(\alpha_{\text{eff}}^{2D} - \alpha_{\text{twist}}^{2D}) & \cos(\alpha_{\text{eff}}^{2D} - \alpha_{\text{twist}}^{2D})\end{bmatrix}\begin{pmatrix}C_D^{2D}(\alpha_{\text{eff}}^{2D})\\ C_L^{2D}(\alpha_{\text{eff}}^{2D})\end{pmatrix} \tag{4.3a}$$

$$\frac{\partial^2\tilde{y}}{\partial\tilde{t}^2} + 2\xi_y\frac{\partial\tilde{y}}{\partial\tilde{t}} + \tilde{y} = \frac{1}{2}\mathcal{M}\mathcal{U}_R^2\tilde{U}_{\text{eff}_{2D}}^2\begin{pmatrix}-\sin(\alpha_{\text{edgewise}})\\ \cos(\alpha_{\text{edgewise}})\end{pmatrix}\cdot\begin{bmatrix}\cos(\alpha_{\text{eff}}^{2D} - \alpha_{\text{twist}}^{2D}) & -\sin(\alpha_{\text{eff}}^{2D} - \alpha_{\text{twist}}^{2D})\\ \sin(\alpha_{\text{eff}}^{2D} - \alpha_{\text{twist}}^{2D}) & \cos(\alpha_{\text{eff}}^{2D} - \alpha_{\text{twist}}^{2D})\end{bmatrix}\begin{pmatrix}C_D^{2D}(\alpha_{\text{eff}}^{2D})\\ C_L^{2D}(\alpha_{\text{eff}}^{2D})\end{pmatrix} \tag{4.3b}$$

$$\beta_\alpha^2\alpha_{\text{torsion}} = \frac{1}{2}\mathcal{M}_\alpha\mathcal{U}_R^2\tilde{U}_{\text{eff}_{2D}}^2 C_M^{2D}(\alpha_{\text{eff}}^{2D}) \tag{4.3c}$$

with

$$\tilde{U}_{\text{eff}_{2D}}^2 = \left(\cos(\phi_0 - \alpha_{\text{edgewise}}) - \frac{1}{\mathcal{U}_R}\frac{\partial\tilde{x}}{\partial\tilde{t}}\right)^2 + \left(\sin(\phi_0 - \alpha_{\text{edgewise}}) - \frac{1}{\mathcal{U}_R}\frac{\partial\tilde{y}}{\partial\tilde{t}}\right)^2 \tag{4.4a}$$

$$\alpha_{\text{eff}}^{2D} = \alpha_{\text{twist}}^{2D} + \arctan\left(\frac{\sin(\phi_0 - \alpha_{\text{edgewise}}) - \frac{1}{\mathcal{U}_R}\frac{\partial\tilde{y}}{\partial\tilde{t}}}{\cos(\phi_0 - \alpha_{\text{edgewise}}) - \frac{1}{\mathcal{U}_R}\frac{\partial\tilde{x}}{\partial\tilde{t}}}\right) + \alpha_{\text{edgewise}} + k_{\alpha x}\tilde{x} + k_y\tilde{y} + \alpha_{\text{torsion}}(\mathcal{U}_R, \phi_0) \tag{4.4b}$$

Several dimensionless parameters, as the mass ratio $\mathcal{M}$, the torsional mass ratio $\mathcal{M}_\alpha$, the reduced velocity $\mathcal{U}_R$ and the frequency ratio β, can be defined. They are regrouped in the Table 4.1.

Table 4.1: Dimensionless parameters of the 2D section

Name	Symbol	Expression	Name	Symbol	Expression
Reduced velocity	$\mathcal{U}_R$	$\frac{U_0}{c_{\text{eq}}\omega_y}$			
Mass ratio	$\mathcal{M}$	$\frac{\rho c_{\text{eq}}^2}{m_{\text{eq}}}$	Torsional mass ratio	$\mathcal{M}_\alpha$	$\frac{\rho c_{\text{eq}}^4}{I_{\text{eq}}}$
Frequency ratio	β	$\frac{\omega_x}{\omega_y}$	Torsional frequency ratio	β_α	$\frac{\omega_\alpha}{\omega_y}$
Edgewise damping	ξ_x	$\frac{d_x}{2\sqrt{k_x m_{\text{eq}}}}$	Flapwise damping	ξ_y	$\frac{d_y}{2\sqrt{k_y m_{\text{eq}}}}$

The reduced velocity $\mathcal{U}_R$ and the angle of incidence ϕ_0 will be varied during this study but all the other parameters have to be chosen according to the dynamic of the IEA15MW. The frequency ratio β is the ratio between the first edgewise flexion mode pulsation and the first flapwise flexion mode of the IEA15MW, it equals 1.42. According to the documentation [53], the damping is 3% for both modes. The equivalent chord c_{eq}, the equivalent mass m_{eq}, the equivalent polars of the airfoil, the flexion-torsion coupling coefficients $k_{\alpha x}$ and $k_{\alpha y}$ as well as α_{torsion} still need to be chosen. These characteristics are identified by comparing the linearized dynamic equations of the section model with those of the blade obtained by modal projection, considering the first flapwise and the first edgewise mode.

Step 1b: Linearization of the section equations

By linearizing the section model equations around $(\tilde{x},\dot{\tilde{x}},\tilde{y},\dot{\tilde{y}})=\mathbf{0}$, the following equations can be obtained:

$$\frac{\partial^2 q_i}{\partial \tilde{t}^2} + 2\xi\beta_i \frac{\partial q_i}{\partial \tilde{t}} + \beta_i^2 q_i \simeq \tilde{F}_i^{2D}(\mathbf{0}) + \sum_j \left(\left.\frac{\partial \tilde{F}_i^{2D}}{\partial q_j}\right|_{\mathbf{0}} q_j + \left.\frac{\partial \tilde{F}_i^{2D}}{\partial \dot{q}_j}\right|_{\mathbf{0}} \dot{q}_j \right) \tag{4.5}$$

with $q_1 = \tilde{y}$ and $q_2 = \tilde{x}$

The terms of the linearization are written in the following. The mean force is:

$$\tilde{F}_i^{2D}(\mathbf{0}) = \frac{1}{2}\mathcal{M}\mathcal{U}_R^2 \boldsymbol{\phi_i} \cdot \mathbf{R}_{\boldsymbol{\phi_0}} \begin{pmatrix} C_D^{2D}(\phi_0 + \alpha_{\text{twist}}^{2D}) \\ C_L^{2D}(\phi_0 + \alpha_{\text{twist}}^{2D}) \end{pmatrix} \tag{4.6}$$

with $\boldsymbol{\phi_1} = \begin{pmatrix} -\sin(\alpha_{\text{edgewise}}) \\ \cos(\alpha_{\text{edgewise}}) \end{pmatrix}$ and $\boldsymbol{\phi_2} = \begin{pmatrix} \cos(\alpha_{\text{edgewise}}) \\ \sin(\alpha_{\text{edgewise}}) \end{pmatrix}$ which are the direction of the springs and with $\mathbf{R}_{\boldsymbol{\phi_0}} = \begin{bmatrix} \cos(\phi_0) & -\sin(\phi_0) \\ \sin(\phi_0) & \cos(\phi_0)) \end{bmatrix}$ which is the matrix of rotation from the wind frame to the global frame.

The aerodynamic stiffness depends on the flexion-torsion coupling introduced by $k_{\alpha i}$:

$$\left.\frac{\partial \tilde{F}_i^{2D}}{\partial q_j}\right|_{\mathbf{0}} = \frac{1}{2}\mathcal{M}\mathcal{U}_R^2 k_{\alpha i} \boldsymbol{\phi_i} \cdot \left(\mathbf{R}_{\boldsymbol{\phi_0}} \begin{pmatrix} \frac{\partial C_D^{2D}}{\partial \alpha_{\text{eff}}^{2D}}(\phi_0 + \alpha_{\text{twist}}^{2D}) \\ \frac{\partial C_L^{2D}}{\partial \alpha_{\text{eff}}^{2D}}(\phi_0 + \alpha_{\text{twist}}^{2D}) \end{pmatrix} + \left.\frac{\partial \mathbf{R}_{\boldsymbol{\phi}}}{\partial \alpha_{\text{eff}}^{2D}}\right|_{\mathbf{0}} \begin{pmatrix} C_D^{2D}(\phi_0 + \alpha_{\text{twist}}^{2D}) \\ C_L^{2D}(\phi_0 + \alpha_{\text{twist}}^{2D}) \end{pmatrix} \right) \tag{4.7}$$

Then, the aerodynamic damping is:

$$\begin{aligned} \left.\frac{\partial \tilde{F}_i^{2D}}{\partial \dot{q}_j}\right|_{\mathbf{0}} = \frac{1}{2}\mathcal{M}\mathcal{U}_R^2 \boldsymbol{\phi_i} \cdot \Bigg[\frac{\partial}{\partial \dot{q}_j}\left(\tilde{U}_{\text{eff}_{2D}}^2\right) \mathbf{R}_{\boldsymbol{\phi_0}} \begin{pmatrix} C_D^{2D}(\phi_0 + \alpha_{\text{twist}}^{2D}) \\ C_L^{2D}(\phi_0 + \alpha_{\text{twist}}^{2D}) \end{pmatrix} \\ + \frac{\partial \alpha_{\text{eff}}^{2D}}{\partial \dot{q}_j} \left(\mathbf{R}_{\boldsymbol{\phi_0}} \begin{pmatrix} \frac{\partial C_D^{2D}}{\partial \alpha_{\text{eff}}^{2D}}(\phi_0 + \alpha_{\text{twist}}^{2D}) \\ \frac{\partial C_L^{2D}}{\partial \alpha_{\text{eff}}^{2D}}(\phi_0 + \alpha_{\text{twist}}^{2D}) \end{pmatrix} + \left.\frac{\partial \mathbf{R}_{\boldsymbol{\phi}}}{\partial \alpha_{\text{eff}}^{2D}}\right|_{\mathbf{0}} \begin{pmatrix} C_D^{2D}(\phi_0 + \alpha_{\text{twist}}^{2D}) \\ C_L^{2D}(\phi_0 + \alpha_{\text{twist}}^{2D}) \end{pmatrix} \right) \Bigg] \end{aligned} \tag{4.8}$$

with

$$\frac{\partial}{\partial \dot{\tilde{x}}}\left(\tilde{U}^2_{\text{eff}_{2D}}\right) = -\frac{2}{\mathcal{U}_R}\cos(\phi_0 - \alpha_{\text{edgewise}}) \qquad \frac{\partial}{\partial \dot{\tilde{y}}}\left(\tilde{U}^2_{\text{eff}_{2D}}\right) = -\frac{2}{\mathcal{U}_R}\sin(\phi_0 - \alpha_{\text{edgewise}})$$

$$\frac{\partial \alpha^{2D}_{\text{eff}}}{\partial \dot{\tilde{x}}} = \frac{\sin(\phi_0 - \alpha_{\text{edgewise}})}{\mathcal{U}_R} \qquad \frac{\partial \alpha^{2D}_{\text{eff}}}{\partial \dot{\tilde{y}}} = -\frac{\cos(\phi_0 - \alpha_{\text{edgewise}})}{\mathcal{U}_R}$$

$$\left.\frac{\partial \mathbf{R}_{\boldsymbol{\phi}}}{\partial \alpha^{2D}_{\text{eff}}}\right|_{\mathbf{0}} = \begin{bmatrix} -\sin(\phi_0) & -\cos(\phi_0) \\ \cos(\phi_0) & -\sin(\phi_0) \end{bmatrix}$$

4.1.2 Step 2: Modal equations of the blade

The same process is done for the blade. The modal equations are written keeping only the two first modes of the blade (the first flapwise mode and the first edgewise mode). A torsion shape function (here the shape function associated to the first torsional mode), is also considered for the static equilibrium. Note that both the flapwise and edgewise modes are not pure and contains a little part of torsion because of material and geometry coupling.

Introducing the generalized coordinates q_1 (flapwise), q_2 (edgewise) and q_3 (torsion) the equations of motion reads:

$$m_{\text{eq},1} L_{blade}\ddot{q_1} + d_{eq,1} L_{blade}\dot{q_1} + k_{eq,1} L_{blade} q_1 = F_1 \tag{4.9a}$$
$$m_{\text{eq},2} L_{blade}\ddot{q_2} + d_{eq,2} L_{blade}\dot{q_2} + k_{eq,2} L_{blade} q_2 = F_2 \tag{4.9b}$$
$$k_{eq,3} L_{blade} q_3 = F_3 \tag{4.9c}$$

$m_{\text{eq,i}} = \frac{\boldsymbol{\phi_i}^T \mathbf{M} \boldsymbol{\phi_i}}{L_{blade}\|\boldsymbol{\phi_i}\|^2}$ are the normalized modal mass divided by the length of the blade L_{blade}. The division by L_{blade} has been made in order to obtain a quantity per span unite. As the modes can contain torsion, this quantity is in fact an inertia per span unite. The norm is defined as : $\|\boldsymbol{\phi}\|^2 = \|\frac{\boldsymbol{\phi_X}}{c_{\text{eq}}}\|^2_{L_2} + \|\boldsymbol{\phi_\Theta}\|^2_{L_2}$. This norm is made to deal with the different dimensions within $\boldsymbol{\phi_\Theta}$, $\boldsymbol{\phi_X}$ (translation) and $\boldsymbol{\phi_\Theta}$ (rotation), and obtain a dimensionless quantity. F_1 and F_2 are the modal projection of the aerodynamic forces on the mode 1 (flapwise) and 2 (edgewise) respectively. A quasisteady aerodynamic model under the strip theory assumption is considered here.

The coordinate system of the blade is represented Figure 4.2.

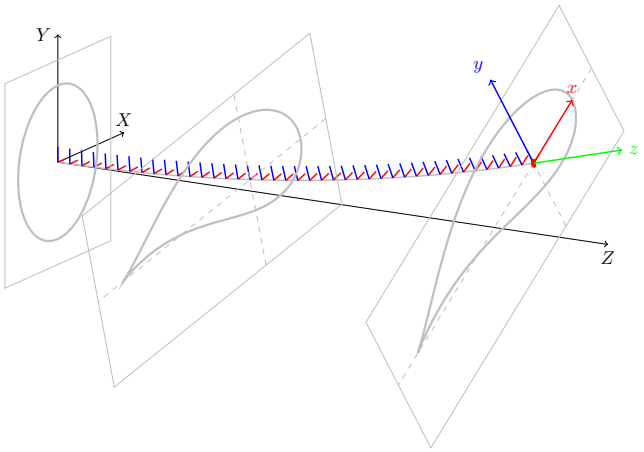

Figure 4.2: Scheme indicating the coordinate system of the blade

The generalized loads are calculated through the power of the external forces f which is written:

$$\mathcal{P}_{ext} = \int_S \boldsymbol{f} \cdot \dot{\boldsymbol{r}}_{\boldsymbol{P}} dS \tag{4.10}$$

where r_P is the position of a point belonging to the surface of the blade. It can be decomposed into the position of the centerline r and the position of the point on the associated section. Using the rotation matrix R of the section from the global frame to the local frame, and knowing the position $\boldsymbol{\xi}$ of P in the local frame of the section:

$$\mathcal{P}_{ext} = \int_S \boldsymbol{f} \cdot \left(\dot{\boldsymbol{r}} + \dot{\mathbf{R}}\boldsymbol{\xi} \right) dS \tag{4.11}$$

Introducing the velocity $\boldsymbol{v} = \dot{\boldsymbol{r}}$ and the rotation speed vector $\boldsymbol{\omega} \times \boldsymbol{\Xi} = \dot{\mathbf{R}}\mathbf{R}^T\boldsymbol{\Xi}$, with $\boldsymbol{\Xi} = \mathbf{R}\boldsymbol{\xi}$ the position of P in the global frame, the generalized loads reads:

$$\mathcal{P}_{ext} = \int_S \boldsymbol{f} \cdot \boldsymbol{v} dS + \int_S \boldsymbol{f} \cdot (\boldsymbol{\omega} \times \boldsymbol{\Xi}) dS \tag{4.12}$$

Introducing the sectional aerodynamic coefficients expressed in the global frame, $\mathcal{P}_{ext}$ can be written:

$$\mathcal{P}_{ext} = \frac{1}{2}\rho \int_0^{L_{blade}} c(l) U_{\text{eff}}^2 \left[\boldsymbol{v} \cdot \begin{pmatrix} C_X \\ C_Y \\ C_Z \end{pmatrix} + c(l)\boldsymbol{\omega} \cdot \begin{pmatrix} C_{M_X} \\ C_{M_Y} \\ C_{M_Z} \end{pmatrix} \right] dl \tag{4.13}$$

Using the rotation matrix R, one can then write the generalized loads using the aerodynamic coefficients in the local section frame:

$$\mathcal{P}_{ext} = \frac{1}{2}\rho \int_0^{L_{blade}} c(l) U_{\text{eff}}^2 \left[\boldsymbol{v} \cdot \mathbf{R}^T \begin{pmatrix} C_x \\ C_y \\ C_z \end{pmatrix} + c(l)\boldsymbol{\omega} \cdot \mathbf{R}^T \begin{pmatrix} C_{M_x} \\ C_{M_y} \\ C_{M_z} \end{pmatrix} \right] dl \tag{4.14}$$

As the aerodynamic model is a sectional model, C_z, C_{M_x} and C_{M_y} are neglected.

Introducing the mode shapes and generalized coordinates with $\boldsymbol{v} = \sum \frac{\boldsymbol{\phi_{X,i}}}{\|\boldsymbol{\phi_i}\|}\dot{q}_i$ and $\boldsymbol{\omega} = \sum \frac{\boldsymbol{\phi_{\Theta,i}}}{\|\boldsymbol{\phi_i}\|}\dot{q}_i$, $\mathcal{P}_{ext}$ reads:

$$\mathcal{P}_{ext} = \sum_i \dot{q}_i \frac{1}{2}\rho \int_0^{L_{blade}} c(l) U_{\text{eff}}^2 \left[\frac{\boldsymbol{\phi_{X,i}}}{\|\boldsymbol{\phi_i}\|} \cdot \mathbf{R}^T \begin{pmatrix} C_x \\ C_y \\ 0 \end{pmatrix} + c(l) \frac{\boldsymbol{\phi_{\Theta,i}}}{\|\boldsymbol{\phi_i}\|} \cdot \mathbf{R}^T \begin{pmatrix} 0 \\ 0 \\ C_{M_z} \end{pmatrix} \right] dl \tag{4.15}$$

As a consequence, the generalized forces on mode i is:

$$F_i = \frac{1}{2}\rho \int_0^{L_{blade}} c(l) U_{\text{eff}}^2 \left[\frac{\boldsymbol{\phi_{X,i}}}{\|\boldsymbol{\phi_i}\|} \cdot \mathbf{R}^T \begin{pmatrix} C_x \\ C_y \\ 0 \end{pmatrix} + c(l) \frac{\boldsymbol{\phi_{\Theta,i}}}{\|\boldsymbol{\phi_i}\|} \cdot \mathbf{R}^T \begin{pmatrix} 0 \\ 0 \\ C_{M_z} \end{pmatrix} \right] dl \tag{4.16}$$

where $\boldsymbol{\phi_{X,i}}$ is the translational part of the modal shape, $\boldsymbol{\phi_{\Theta,i}}$ is the rotational part of the modal shape and $\mathbf{R}$ is the rotation matrix of the section from the global frame to the local frame.

Step 2a: Dimensionless form of the modal equations

As for the sectional model, the modal equations of the blade are written in a dimensionless form.

$$\frac{\partial^2 q_1}{\partial \tilde{t}^2} + 2\xi\frac{\partial q_1}{\partial \tilde{t}} + q_1 = \frac{1}{2}\mathcal{M}_1\mathcal{U}_R^2\int_0^1 \tilde{c}(s)\tilde{U}_{\text{eff}}^2\left[\frac{\boldsymbol{\phi_{X,1}}}{c_{\text{eq}}\|\boldsymbol{\phi_1}\|}\cdot\mathbf{R}^T\begin{pmatrix}C_x\\C_y\\0\end{pmatrix} + \tilde{c}(s)\frac{\boldsymbol{\phi_{\Theta,1}}}{\|\boldsymbol{\phi_1}\|}\cdot\begin{pmatrix}0\\0\\C_{M_z}\end{pmatrix}\right]ds \tag{4.17a}$$

$$\frac{\partial^2 q_2}{\partial \tilde{t}^2} + 2\xi\beta\frac{\partial q_2}{\partial \tilde{t}} + \beta^2 q_2 = \frac{1}{2}\mathcal{M}_2\mathcal{U}_R^2\int_0^1 \tilde{c}(s)\tilde{U}_{\text{eff}}^2\left[\frac{\boldsymbol{\phi_{X,2}}}{c_{\text{eq}}\|\boldsymbol{\phi_2}\|}\cdot\mathbf{R}^T\begin{pmatrix}C_x\\C_y\\0\end{pmatrix} + \tilde{c}(s)\frac{\boldsymbol{\phi_{\Theta,2}}}{\|\boldsymbol{\phi_2}\|}\cdot\begin{pmatrix}0\\0\\C_{M_z}\end{pmatrix}\right]ds \tag{4.17b}$$

$$\beta_3^2 q_3 = \frac{1}{2}\mathcal{M}_3\mathcal{U}_R^2\int_0^1 \tilde{c}(s)\tilde{U}_{\text{eff}}^2\left[\frac{\boldsymbol{\phi_{X,3}}}{c_{\text{eq}}\|\boldsymbol{\phi_3}\|}\cdot\mathbf{R}^T\begin{pmatrix}C_x\\C_y\\0\end{pmatrix} + \tilde{c}(s)\frac{\boldsymbol{\phi_{\Theta,3}}}{\|\boldsymbol{\phi_3}\|}\cdot\begin{pmatrix}0\\0\\C_{M_z}\end{pmatrix}\right]ds \tag{4.17c}$$

with $\mathcal{M}_i = \frac{\rho c_{\text{eq}}^4}{m_{\text{eq,i}}}$, $\tilde{c} = c/c_{\text{eq}}$ and $\tilde{U}_{\text{eff}} = U_{\text{eff}}/U_0$.

$$\begin{aligned}\tilde{U}_{\text{eff}}^2 = &\left[\cos(\phi_0) + \frac{1}{\mathcal{U}_R}\left(-\sum_j \frac{\phi_{X,j,x}(s)}{c_{\text{eq}}\|\boldsymbol{\phi_j}\|}\dot{q}_j + \left(\frac{\tilde{c}(s)}{2} - \frac{e(s)}{c_{\text{eq}}}\right)\sin(\alpha)\dot{\alpha}\right)\right]^2\\ &+ \left[\sin(\phi_0) + \frac{1}{\mathcal{U}_R}\left(-\sum_j \frac{\phi_{X,j,y}(s)}{c_{\text{eq}}\|\boldsymbol{\phi_j}\|}\dot{q}_j + \left(\frac{\tilde{c}(s)}{2} - \frac{e(s)}{c_{\text{eq}}}\right)\cos(\alpha)\dot{\alpha}\right)\right]^2\end{aligned} \tag{4.18a}$$

$$\alpha_{\text{eff}} = \alpha + \arctan\left(\frac{\sin(\phi_0) + \frac{1}{\mathcal{U}_R}\left(-\sum_j \frac{\phi_{X,j,y}(s)}{c_{\text{eq}}\|\boldsymbol{\phi_j}\|}\dot{q}_j + \left(\frac{\tilde{c}(s)}{2} - \frac{e(s)}{c_{\text{eq}}}\right)\cos(\alpha)\dot{\alpha}\right)}{\cos(\phi_0) + \frac{1}{\mathcal{U}_R}\left(-\sum_j \frac{\phi_{X,j,x}(s)}{c_{\text{eq}}\|\boldsymbol{\phi_j}\|}\dot{q}_j + \left(\frac{\tilde{c}(s)}{2} - \frac{e(s)}{c_{\text{eq}}}\right)\sin(\alpha)\dot{\alpha}\right)}\right) \tag{4.18b}$$

where $\alpha = \alpha_{\text{twist}}(s) + \sum \frac{\phi_{\Theta,j,z}(s)}{\|\boldsymbol{\phi_j}\|}q_j$ and e is the distance between the aerodynamic center and the elastic center.

As the mode shapes are note pure, it introduces coupling between modes.

Step 2b: Linearization of the modal equations

The dimensionless modal equations are linearized around $(q_1, \dot{q_1}, q_2, \dot{q_2}) = \mathbf{0}$.

$$\frac{\partial^2 q_i}{\partial \tilde{t}^2} + 2\xi\beta_i \frac{\partial q_i}{\partial \tilde{t}} + \beta_i^2 q_i \simeq \tilde{F}_i(\mathbf{0}) + \sum_j \left(\left.\frac{\partial \tilde{F}_i}{\partial q_j}\right|_{\mathbf{0}} q_j + \left.\frac{\partial \tilde{F}_i}{\partial \dot{q}_j}\right|_{\mathbf{0}} \dot{q}_j \right) \tag{4.19}$$

The aerodynamic stiffness will be use to adjust the flexion-torsion coupling of the equivalent section, it reads:

$$\left.\frac{\partial \tilde{F}_i}{\partial q_j}\right|_{\mathbf{0}} = \frac{1}{2}\mathcal{M}_i \mathcal{U}_R^2 \int_0^1 \tilde{c}(s) \left[\frac{\boldsymbol{\phi_{X,i}}}{c_{\text{eq}}\|\boldsymbol{\phi_i}\|} \cdot \left(\frac{\partial \mathbf{R}^T}{\partial q_j} \begin{pmatrix} C_x(\phi_0 + \alpha_{\text{twist}}) \\ C_y(\phi_0 + \alpha_{\text{twist}}) \\ 0 \end{pmatrix} + \frac{\phi_{\Theta,j,z}}{\|\boldsymbol{\phi_j}\|} \mathbf{R_0}^T \begin{pmatrix} \frac{\partial C_x}{\partial \alpha_{\text{eff}}}(\phi_0 + \alpha_{\text{twist}}) \\ \frac{\partial C_y}{\partial \alpha_{\text{eff}}}(\phi_0 + \alpha_{\text{twist}}) \\ 0 \end{pmatrix} \right) \right.$$
$$\left. + \tilde{c}(s) \frac{\phi_{\Theta,j,z} \boldsymbol{\phi_{\Theta,i}}}{\|\boldsymbol{\phi_j}\|\|\boldsymbol{\phi_i}\|} \cdot \begin{pmatrix} 0 \\ 0 \\ \frac{\partial C_{M_z}}{\partial \alpha_{\text{eff}}}(\phi_0 + \alpha_{\text{twist}}) \end{pmatrix} \right] ds \tag{4.20}$$

As stall-induced vibrations arise from negative aerodynamic damping, the following expression will be used to calculate the other parameters of the equivalent section:

$$\left.\frac{\partial \tilde{F}_i}{\partial \dot{q}_j}\right|_{\mathbf{0}} = \frac{1}{2}\mathcal{M}_i \mathcal{U}_R^2 \int_0^1 \tilde{c}(s) \left[\frac{\partial \left(\tilde{U}_{\text{eff}}^2\right)}{\partial \dot{q}_j} \left(\frac{\boldsymbol{\phi_{X,i}}}{c_{\text{eq}}\|\boldsymbol{\phi_i}\|} \cdot \mathbf{R_0}^T \begin{pmatrix} C_x(\phi_0 + \alpha_{\text{twist}}) \\ C_y(\phi_0 + \alpha_{\text{twist}}) \\ 0 \end{pmatrix} + \tilde{c}(s) \frac{\boldsymbol{\phi_{\Theta,i}}}{\|\boldsymbol{\phi_i}\|} \cdot \begin{pmatrix} 0 \\ 0 \\ C_{M_z}(\phi_0 + \alpha_{\text{twist}}) \end{pmatrix} \right) \right.$$
$$\left. + \frac{\partial \alpha_{\text{eff}}}{\partial \dot{q}_j} \left(\frac{\boldsymbol{\phi_{X,i}}}{c_{\text{eq}}\|\boldsymbol{\phi_i}\|} \mathbf{R_0}^T \begin{pmatrix} \frac{\partial C_x}{\partial \alpha_{\text{eff}}}(\phi_0 + \alpha_{\text{twist}}) \\ \frac{\partial C_y}{\partial \alpha_{\text{eff}}}(\phi_0 + \alpha_{\text{twist}}) \\ 0 \end{pmatrix} + \tilde{c}(s) \frac{\boldsymbol{\phi_{\Theta,i}}}{\|\boldsymbol{\phi_i}\|} \cdot \begin{pmatrix} 0 \\ 0 \\ \frac{\partial C_{M_z}}{\partial \alpha_{\text{eff}}}(\phi_0 + \alpha_{\text{twist}}) \end{pmatrix} \right) \right] ds \tag{4.21}$$

with

$$\frac{\partial \left(\tilde{U}_{\text{eff}}^2\right)}{\partial \dot{q}_j} = \frac{2\cos(\phi_0)}{\mathcal{U}_R} \left(-\frac{\phi_{X,j,x}}{c_{\text{eq}}\|\boldsymbol{\phi_j}\|} + \left(\frac{\tilde{c}(s)}{2} - \frac{e}{c_{\text{eq}}} \right) \sin(\alpha_{\text{twist}}) \frac{\phi_{\Theta,j,z}}{\|\boldsymbol{\phi_j}\|} \right)$$
$$+ \frac{2\sin(\phi_0)}{\mathcal{U}_R} \left(-\frac{\phi_{X,j,y}}{c_{\text{eq}}\|\boldsymbol{\phi_j}\|} + \left(\frac{\tilde{c}(s)}{2} - \frac{e}{c_{\text{eq}}} \right) \cos(\alpha_{\text{twist}}) \frac{\phi_{\Theta,j,z}}{\|\boldsymbol{\phi_j}\|} \right) \tag{4.22a}$$

$$\frac{\partial \alpha_{\text{eff}}}{\partial \dot{q}_j} = \frac{\cos(\phi_0) \left(-\frac{\phi_{X,j,y}}{c_{\text{eq}}\|\boldsymbol{\phi_j}\|} + \left(\frac{\tilde{c}}{2} - \frac{e}{c_{\text{eq}}} \right) \cos(\alpha_{\text{twist}}) \frac{\phi_{\Theta,j,z}}{\|\boldsymbol{\phi_j}\|} \right) - \sin(\phi_0) \left(-\frac{\phi_{X,j,x}}{c_{\text{eq}}\|\boldsymbol{\phi_j}\|} + \left(\frac{\tilde{c}}{2} - \frac{e}{c_{\text{eq}}} \right) \sin(\alpha_{\text{twist}}) \frac{\phi_{\Theta,j,z}}{\|\boldsymbol{\phi_j}\|} \right)}{\mathcal{U}_R} \tag{4.22b}$$

From expression (4.21), it can be noticed that the aerodynamic damping can be either due to translational and/or rotational terms proportional to square velocity gradient (Eq. 4.22a) or angle of attack gradient (Eq. 4.22b).

All these four terms do not have the same level of contribution to the aerodynamic damping. A numerical evaluation has been realized for both the flapwise and edgewise modes in a range of angle of attack for which stall-induced vibration can be observed. Results are reported in Figure 4.3.

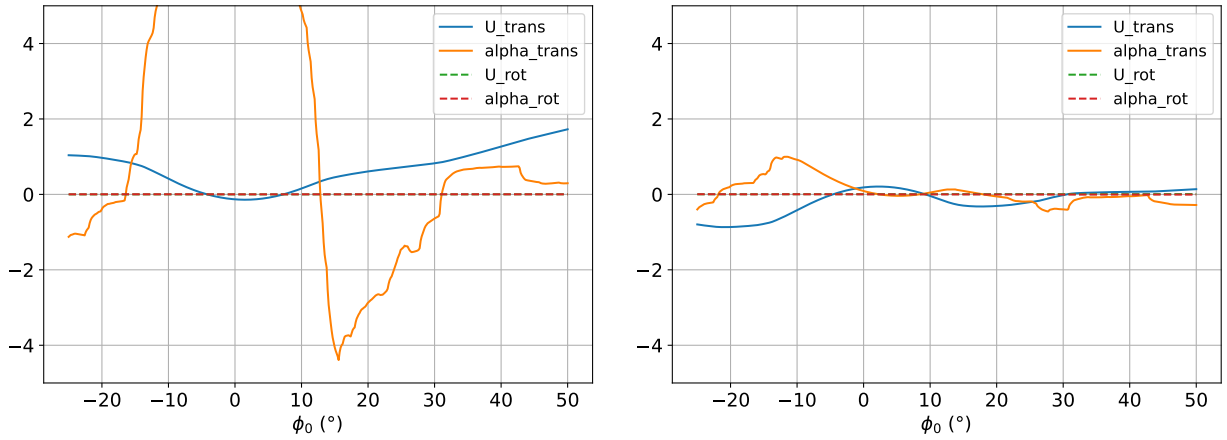

(a) Flapwise mode

(b) Edgewise mode

Figure 4.3: Comparison of the different terms of the aerodynamic dampings

Based on Figure 4.3, rotational contributions can be neglected. Regarding results for the flapwise mode, the term proportional to the angle of attack gradient is also of major importance on the aerodynamic damping. This term will then be used in the next section to identify the two first equivalent section model parameters.

4.1.3 Step 3: Identification of the section model edgewise direction and equivalent chord

The section model edgewise direction α_{edgewise} and equivalent chord are here identified by comparing a simplified formulation of the dominant modal aerodynamic damping term for the flapwise mode with the one associated to the linearized section model

The dominant modal aerodynamic damping for the flapwise mode (named alpha_trans in Figure 4.3), reads:

$$\frac{1}{2}\mathcal{M}_1\mathcal{U}_R^2\int_0^1 \tilde{c}(s)\frac{\partial\alpha_{\text{eff}}}{\partial\dot{q}_1}\frac{\boldsymbol{\phi_{X,1}}}{c_{\text{eq}}\|\boldsymbol{\phi_1}\|}\cdot\mathbf{R_0}^T\begin{pmatrix}\frac{\partial C_x}{\partial\alpha_{\text{eff}}}(\phi_0+\alpha_{\text{twist}})\\ \frac{\partial C_y}{\partial\alpha_{\text{eff}}}(\phi_0+\alpha_{\text{twist}})\\ 0\end{pmatrix}ds \tag{4.23}$$

In a simplified case were the blade has no twist ($\alpha_{\text{twist}}=0$), no prebend ($\mathbf{R_0}=\mathbf{1}$), the same airfoils all along the blade and a negligible part of torsion within the two first modes ($\boldsymbol{\phi_\Theta}\approx 0$), the expression (4.23) becomes:

$$\frac{1}{2}\mathcal{M}_1\mathcal{U}_R\int_0^1 \tilde{c}(s)\left(-\cos(\phi_0)\frac{\phi_{X,1,y}}{c_{\text{eq}}\|\boldsymbol{\phi_1}\|}+\sin(\phi_0)\frac{\phi_{X,1,x}}{c_{\text{eq}}\|\boldsymbol{\phi_1}\|}\right)\frac{\boldsymbol{\phi_{X,1}}}{c_{\text{eq}}\|\boldsymbol{\phi_1}\|}ds\cdot\begin{pmatrix}\frac{\partial C_x}{\partial\alpha_{\text{eff}}}(\phi_0)\\ \frac{\partial C_y}{\partial\alpha_{\text{eff}}}(\phi_0)\\ 0\end{pmatrix} \tag{4.24}$$

In comparison, the same term writes for the linearized sectional model:

$$\frac{1}{2}\mathcal{M}_1\mathcal{U}_R\left[-\cos(\phi_0-\alpha_{\text{edgewise}})\begin{pmatrix}-\sin(\alpha_{\text{edgewise}})\\ \cos(\alpha_{\text{edgewise}})\\ 0\end{pmatrix}\right]\cdot\begin{pmatrix}\frac{\partial C_X}{\partial\alpha_{\text{eff}}}(\phi_0)\\ \frac{\partial C_Y}{\partial\alpha_{\text{eff}}}(\phi_0)\\ 0\end{pmatrix} \tag{4.25}$$

By imposing the equality between the expressions (4.24) and (4.25), it gives two relations that allow to obtained α_{edgewise} and c_{eq}.

$$-\cos(\phi_0-\alpha_{\text{edgewise}})\,(-\sin(\alpha_{\text{edgewise}})) = \int_0^1 \tilde{c}(s)\left(-\cos(\phi_0)\frac{\phi_{X,1,y}}{c_{\text{eq}}\|\boldsymbol{\phi_1}\|}+\sin(\phi_0)\frac{\phi_{X,1,x}}{c_{\text{eq}}\|\boldsymbol{\phi_1}\|}\right)\frac{\phi_{X,1,x}}{c_{\text{eq}}\|\boldsymbol{\phi_1}\|}ds \tag{4.26a}$$

$$-\cos(\phi_0-\alpha_{\text{edgewise}})\cos(\alpha_{\text{edgewise}}) = \int_0^1 \tilde{c}(s)\left(-\cos(\phi_0)\frac{\phi_{X,1,y}}{c_{\text{eq}}\|\boldsymbol{\phi_1}\|}+\sin(\phi_0)\frac{\phi_{X,1,x}}{c_{\text{eq}}\|\boldsymbol{\phi_1}\|}\right)\frac{\phi_{X,1,y}}{c_{\text{eq}}\|\boldsymbol{\phi_1}\|}ds \tag{4.26b}$$

Dividing (4.26a) by (4.26b) and taking the arctan, α_{edgewise} can be isolated:

$$\alpha_{\text{edgewise}} = -\arctan\left(\frac{\int_0^1 c(s)(\cos(\phi_0)\phi_{X,1,y}-\sin(\phi_0)\phi_{X,1,x})\phi_{X,1,x}ds}{\int_0^1 c(s)(\cos(\phi_0)\phi_{X,1,y}-\sin(\phi_0)\phi_{X,1,x})\phi_{X,1,y}ds}\right) \tag{4.27}$$

By definition $\|\boldsymbol{\phi_1}\|$ depends on c_{eq}, but as the torsion part of the mode is neglected: $c_{\text{eq}}\|\boldsymbol{\phi_1}\| = \|\boldsymbol{\phi_{X,1}}\|_{L_2}$.

Thus, both (4.26a) and (4.26b) can be elevated to square and summed in order to cancel out $\sin(\alpha_{\text{edgewise}})$ and $\cos(\alpha_{\text{edgewise}})$. Isolating c_{eq}^2 and dividing by $\cos(\phi_0-\alpha_{\text{edgewise}})^2$, c_{eq} is obtained by taking the square root:

$$c_{\text{eq}} = \frac{\sqrt{\left(\int_0^1 c(s)\frac{(\cos(\phi_0)\phi_{X,1,y}-\sin(\phi_0)\phi_{X,1,x})}{\|\boldsymbol{\phi_{X,1}}\|_{L_2}}\frac{\phi_{X,1,x}}{\|\boldsymbol{\phi_{X,1}}\|_{L_2}}ds\right)^2+\left(\int_0^1 c(s)\frac{(\cos(\phi_0)\phi_{X,1,y}-\sin(\phi_0)\phi_{X,1,x})}{\|\boldsymbol{\phi_{X,1}}\|_{L_2}}\frac{\phi_{X,1,y}}{\|\boldsymbol{\phi_{X,1}}\|_{L_2}}ds\right)^2}}{\cos(\phi_0-\alpha_{\text{edgewise}})} \tag{4.28}$$

Expressions (4.27) and (4.28) come from the identification of the dominant terms of the added aerodynamic damping of the flapwise mode. It means that using relations (4.27) and (4.28) for α_{edgewise} and c_{eq}, the added aerodynamic damping should be correctly estimated in the sectional model. It is not necessarily the case for the edgewise mode for which the added aerodynamic damping term proportional to the angle of attack gradient is not dominant.

Remark 4 *In simpler cases where the chord is constant over the span and the modes are uniform, the equivalent chord reduces to the actual chord.*

With $c(s) = c$, $\phi_{X,1,y}(s) = \Phi_y$ *and* $\phi_{X,1,x} = \Phi_x$.

With this simplification α_{edgewise} *verifies* $\cos(\alpha_{\text{edgewise}}) = \frac{\Phi_y}{\sqrt{\Phi_x^2+\Phi_y^2}}$ *and* $\sin(\alpha_{\text{edgewise}}) = -\frac{\Phi_x}{\sqrt{\Phi_x^2+\Phi_y^2}}$

c_{eq} *becomes:*

$$c_{\text{eq}} = \frac{c}{\cos\left(\phi_0-\alpha_{\text{edgewise}}\right)}\frac{|\Phi_x\sin(\phi_0)-\Phi_y\cos(\phi_0)|}{\sqrt{\Phi_x^2+\Phi_y^2}}$$

Thus, it leads to $c_{\text{eq}} = c$

4.1.4 Step 4: Identification of an equivalent polar

To take into account the twist and the prebend of the blade, the simplification on the twist and prebend of the Step 3 are released and an equivalent polar is defined with only the hypothesis that the torsion part of the flexion modes is negligible. This equivalent polar aims at summarizing the steady aerodynamic of the whole blade. The equivalent polar should verify that the aerodynamic damping in the flapwise and edgewise direction between the equivalent section and the blade modal model is equal. The choice to conserve the aerodynamic damping instead of the aerodynamic stiffness or the mean force has been made because the SIV come from a negative aerodynamic damping. The angle $\alpha^{2D}_{\text{twist}}$ is also identified in this section as it allows to translate the equivalent polar through the angles of attack and thus estimate an equivalent twist angle.

To identify the equivalent drag and lift coefficient C_D^{2D} and C_L^{2D}, the two relations between the flapwise and edgewise dampings can be regrouped in a system of the form:

$$A(\alpha)\frac{d}{d\alpha}\begin{pmatrix}C_D^{2D}\\C_L^{2D}\end{pmatrix} + B(\alpha)\begin{pmatrix}C_D^{2D}\\C_L^{2D}\end{pmatrix} = C(\alpha) \tag{4.29}$$

with A, B and C defined in Appendix B.

Numerical resolution of the equivalent polar

Careful attention is needed to solve this differential equation as the determinants of A and B are zero for some α, which produce singularities. These singularities occur when the wind direction is align with the edgewise or flapwise ($\alpha = \alpha_{\text{edgewise}} + k\frac{\pi}{2}$). In this cases, $\frac{\partial}{\partial \dot{q}}\left(\tilde{U}^2_{\text{eff}}\right)$ or $\frac{\partial \alpha_{\text{eff}}}{\partial \dot{q}}$ become zero and the nature of the relation in the edgewise or flapwise direction changes. It prevents the resolution of Equation (4.29) on the full 2π interval in one time. The equation then needs to be solved in each interval separately and connected afterwards.

The method is to first solve the homogeneous equation using the resolvent. It consists in solving the following equation with initial condition $\mathbf{R}(\alpha_i) = \mathbf{1}$ where α_i is an arbitrary angle of attack taken to begin the resolution.

$$\frac{d\mathbf{R}}{d\alpha} + A^{-1}(\alpha)B(\alpha)\mathbf{R} = 0 \tag{4.30}$$

When α is approaching a singularity $A^{-1}(\alpha)B(\alpha)$ diverges. The time step of integration needs to be adapted in order to solve correctly the equation. Even if $A^{-1}(\alpha)B(\alpha)$ diverges, $\mathbf{R}$ converges towards finite values. Beginning from α_i, the Equation (4.29) has to be solved in increasing and decreasing α to cover the interval between two singularities.

Then, the solution on each interval can be obtain with the following formula:

$$\begin{pmatrix}C_D^{2D}\\C_L^{2D}\end{pmatrix}(\alpha) = \mathbf{R}(\alpha,\alpha_i)\begin{pmatrix}C_D^{2D}\\C_L^{2D}\end{pmatrix}(\alpha_i) + \int_{\alpha_i}^{\alpha}\mathbf{R}(\alpha,s)A^{-1}(s)C(s)ds \tag{4.31}$$

There are four intervals. Thus, there are four initial conditions $\begin{pmatrix}C_D^{2D}\\C_L^{2D}\end{pmatrix}(\alpha_i)$ to identify, representing eight unknowns. Due to the properties of A and B of Equation (4.29), the continuity of C_D^{2D} is automatic but four conditions are needed to imposed the continuity of C_L^{2D}. Finally, the four remaining unknowns are obtained by minimizing the distance between the aerodynamic coupled dampings of the section and the ones of the blade model on all the angle of incidence.

The equivalent polars obtained for the IEA15MW blade are shown in Figure 4.4, along with the drag and lift coefficients associated with the blade section airfoil at 75% of radius. As the first blade mode is larger at the tip of the blade, it leads the equivalent polar to be close to the polar

of blade sections near the tip. We can indeed observe that the equivalent polars are similar to that at 75% of radius. However, some differences can be observed. The drag and lift coefficients are shifted due to the twist of the blade. The angle $\alpha^{2D}_{\text{twist}}$ of the equivalent section has the effect of translating the equivalent polar. Its value, corresponding to an equivalent twist, can then be identified so that the origin of the equivalent polar matches the origin of the polar of the airfoil at 75% of the blade. Moreover, the drag equivalent polar cd_eq has a little slope around 0° angle of attack that increases the drag at low positive angles of attack and reduces it for low negative angles of attack. This effect comes from the mode shape of the blade. For the 2D profil, the flapwise vibration is only towards one direction, but the beam mode is more complex, each section of the blade does not oscillate exactly in the same direction, causing disparities in effective angles of attack along the blade. This is compensated by the equivalent polar. Otherwise, if the beam mode was a pure flapwise flexion, the drag would have been flat around 0° angle of attack.

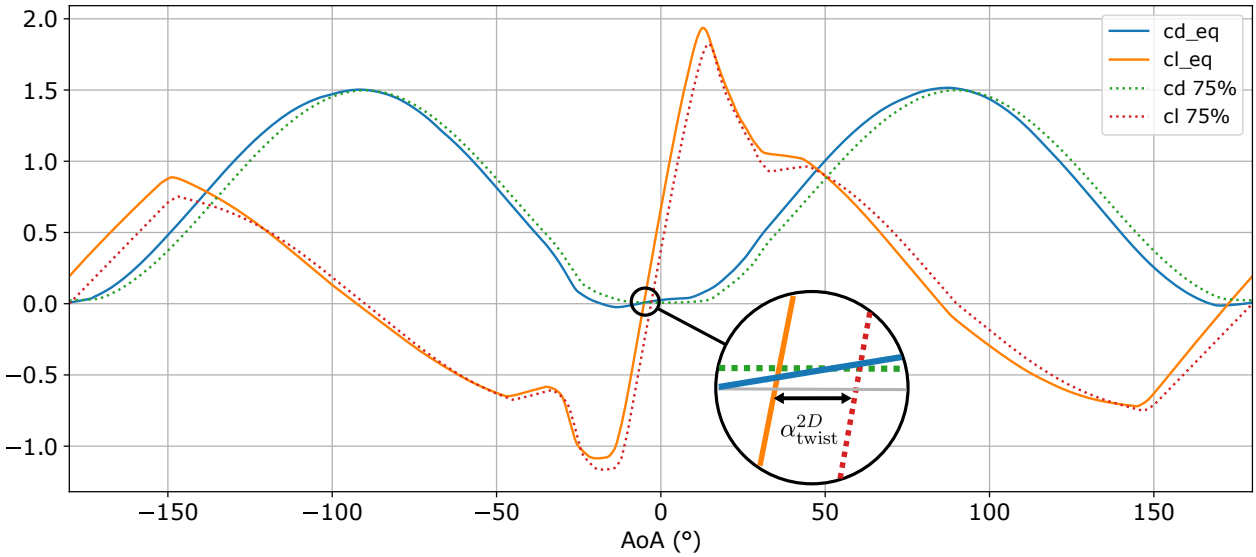

Figure 4.4: Equivalent polars of the IEA15MW before the translation by $\alpha^{2D}_{\text{twist}}$. The polar at 75% of radius is added for comparison.

4.1.5 Step 5: Identification of the flexion-torsion coupling stiffness and the angle of torsion

The last quantity to identify to complete the equivalent section model are the flexion-torsion parameters $k_{\alpha x}$ and $k_{\alpha y}$ and the angle of torsion α_{torsion}.

The flexion-torsion parameters $k_{\alpha x}$ and $k_{\alpha y}$

Now that the equivalent polar has been calculated, it is possible to identify $k_{\alpha x}$ and $k_{\alpha y}$ by comparing the aerodynamic stiffness of the sectional model (Eq. 4.7) and the blade model (Eq. 4.20). The stiffness introduced by the moment coefficient can be neglected. It leads to the following equality:

$$k_{\alpha i}\boldsymbol{\phi_i}\cdot\left(\mathbf{R_{\phi_0}}\begin{pmatrix}\frac{\partial C_D^{2D}}{\partial\alpha_{\text{eff}}^{2D}}(\phi_0+\alpha_{\text{twist}}^{2D})\\ \frac{\partial C_L^{2D}}{\partial\alpha_{\text{eff}}^{2D}}(\phi_0+\alpha_{\text{twist}}^{2D})\end{pmatrix}+\left.\frac{\partial\mathbf{R_\phi}}{\partial\alpha_{\text{eff}}^{2D}}\right|_0\begin{pmatrix}C_D^{2D}(\phi_0+\alpha_{\text{twist}}^{2D})\\ C_L^{2D}(\phi_0+\alpha_{\text{twist}}^{2D})\end{pmatrix}\right)$$
$$=\int_0^1\tilde{c}(s)\left[\frac{\phi_{\Theta,i,z}}{\|\boldsymbol{\phi_i}\|}\frac{\boldsymbol{\phi_{X,i}}}{c_{\text{eq}}\|\boldsymbol{\phi_i}\|}\cdot\left(\frac{\partial\mathbf{R_\phi}}{\partial\alpha_{\text{eff}}}^T\begin{pmatrix}C_D(\phi_0+\alpha_{\text{twist}})\\ C_L(\phi_0+\alpha_{\text{twist}})\\ 0\end{pmatrix}+\mathbf{R_{\phi_0}}^T\begin{pmatrix}\frac{\partial C_D}{\partial\alpha_{\text{eff}}}(\phi_0+\alpha_{\text{twist}})\\ \frac{\partial C_L}{\partial\alpha_{\text{eff}}}(\phi_0+\alpha_{\text{twist}})\\ 0\end{pmatrix}\right)\right]ds \tag{4.32}$$

From Equation 4.32, $k_{\alpha x}$ and $k_{\alpha y}$ can be easily isolated.

The angle of torsion α_{torsion}

The expression of the angle of torsion α_{torsion} of the aeroelastic equilibrium α_{torsion} can be obtained by the linearization of the moment equation (Eq. 4.3c) of the sectional model around ($\tilde{x}$,$\dot{\tilde{x}}$,$\tilde{y}$,$\dot{\tilde{y}}$, α_{torsion})=$\mathbf{0}$:

$$\alpha_{\text{torsion}}=\frac{\frac{1}{2}\mathcal{M}_\alpha\frac{\mathcal{U}_R^2}{\beta_\alpha^2}C_M^{2D}(\phi_0+\alpha_{\text{twist}}^{2D})}{1-\frac{1}{2}\mathcal{M}_\alpha\frac{\mathcal{U}_R^2}{\beta_\alpha^2}\frac{\partial C_M^{2D}}{\partial\alpha_{\text{eff}}}(\phi_0+\alpha_{\text{twist}}^{2D})} \tag{4.33}$$

Thus, the equivalent moment polar C_M^{2D} is necessary to compute the angle of torsion α_{torsion}. And as this angle of torsion is an angle at equilibrium, the construction of the equivalent moment polar is based on the equality of the mean load of the linearized torsion equation of the equivalent section and the one of the blade model.

From torsional equation of the equivalent section (Eq. 4.3c), taking the mean moment around ($\tilde{x}$,$\dot{\tilde{x}}$,$\tilde{y}$,$\dot{\tilde{y}}$, α_{torsion})=$\mathbf{0}$, gives:

$$\tilde{F}_3^{2D}(\mathbf{0})=\frac{1}{2}\mathcal{M}_\alpha\mathcal{U}_R^2C_M^{2D}(\phi_0+\alpha_{\text{twist}}^{2D}) \tag{4.34}$$

On the other hand, for the blade, the mean load of the linearized modal equation in torsion (Eq. 4.19 with $i=3$) is:

$$\tilde{F}_3(\mathbf{0})=\frac{1}{2}\mathcal{M}_3\mathcal{U}_R^2\int_0^1\tilde{c}(s)\left[\frac{\boldsymbol{\phi_{X,3}}}{c_{\text{eq}}\|\boldsymbol{\phi_3}\|}\cdot\mathbf{R_{\phi_0}}^T\begin{pmatrix}C_D(\phi_0+\alpha_{\text{twist}})\\ C_L(\phi_0+\alpha_{\text{twist}})\\ 0\end{pmatrix}+\tilde{c}(s)\frac{\boldsymbol{\phi_{\Theta,3}}}{\|\boldsymbol{\phi_3}\|}\cdot\begin{pmatrix}0\\ 0\\ C_{M_z}(\phi_0+\alpha_{\text{twist}})\end{pmatrix}\right]ds \tag{4.35}$$

By taking $\mathcal{M}_\alpha=\mathcal{M}_3$ and equalizing equations (4.34) and (4.35), it gives the equivalent moment polar:

$$C_M^{2D}(\phi_0+\alpha_{\text{twist}}^{2D})=\int_0^1\tilde{c}(s)\left[\frac{\boldsymbol{\phi_{X,3}}}{c_{\text{eq}}\|\boldsymbol{\phi_3}\|}\cdot\mathbf{R_{\phi_0}}^T\begin{pmatrix}C_D(\phi_0+\alpha_{\text{twist}})\\ C_L(\phi_0+\alpha_{\text{twist}})\\ 0\end{pmatrix}+\tilde{c}(s)\frac{\boldsymbol{\phi_{\Theta,3}}}{\|\boldsymbol{\phi_3}\|}\cdot\begin{pmatrix}0\\ 0\\ C_{M_z}(\phi_0+\alpha_{\text{twist}})\end{pmatrix}\right]ds \tag{4.36}$$

The equivalent polar in moment obtained for the IEA15MW blade are shown in Figure 4.5, along with the moment coefficient around the elastic center associated with the blade section airfoil at 75% of radius. It can be noticed that the global shape of the equivalent polar in moment is similar. However, the variations of the coefficient are modified by the contribution of the flexion part of the torsion mode.

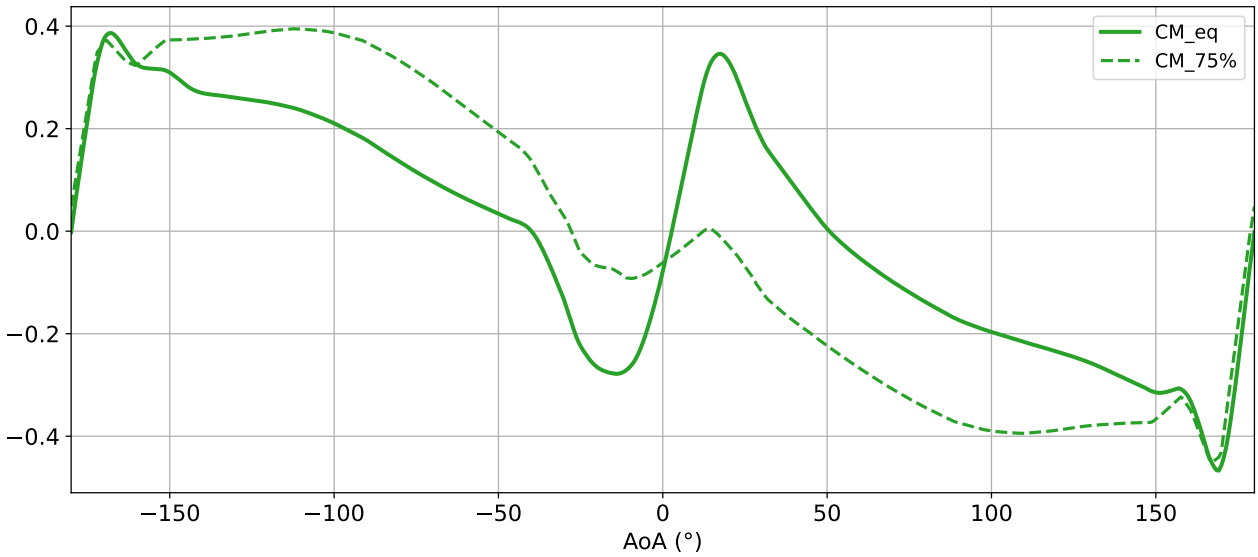

Figure 4.5: Equivalent polar in moment of the IEA15MW before the translation by $\alpha^{2D}_{\text{twist}}$. The polar at 75% of radius is added for comparison.

4.1.6 Summary and implementation

The development of the equivalent section model is structured around five steps. The first two steps are based on the linearization of the section and blade equations in order to obtain the aerodynamic stiffness and dampings expressions. In the third step, the edgewise direction α_{edgewise} and the equivalent chord c_{eq} are identified, neglecting the twist and the prebend of the blade, by comparing a simplified formulation of the dominant modal aerodynamic damping term for the flapwise mode with the one associated to the linearized section model. In the fourth step, the simplification on the twist and prebend is released in order to identify an equivalent polars and $\alpha^{2D}_{\text{twist}}$ parameter. Finally, in a fifth step, the confrontation of the aerodynamic stiffness has allowed to evaluate the flexion-torsion coupling coefficient of the equivalent section. An equivalent curve of the moment coefficient, allowing to compute the angle of torsion α_{torsion} of the aeroelastic equilibrium, has also been identified in this last fifth step. A flowchart summarising the development is given in Figure 4.6.

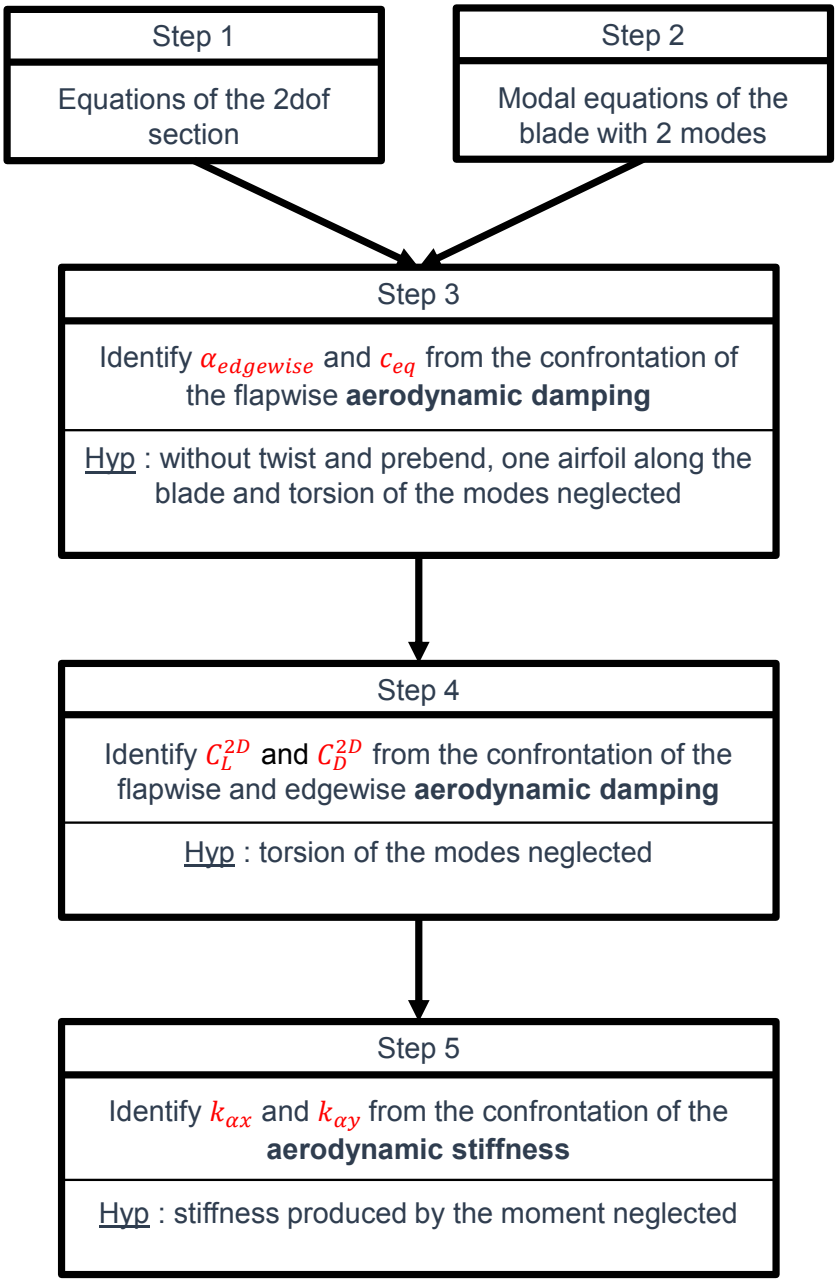

Figure 4.6: Flowchart of the equivalent section model development.

Parameters of the equivalent section model of the the IEA15MW blade are reported in table 5.3.

Table 4.2: Parameters of the equivalent section

Parameter	Value	Parameter	Value	Parameter	Value
c_{eq}	2.35 m	$\mathcal{M}$	0.0706	$\mathcal{M}_\alpha$	0.08
$k_{\alpha x}$	-0.123 rad	$k_{\alpha y}$	-0.0178 rad	β	1.373
ξ_{edge}	0.03	ξ_{flap}	0.03	β_α	9.11
α_{edgewise}	7.37°	$\alpha^{2D}_{\text{twist}}$	2.2°		

In order to validate this equivalent section model, including the parameters reported in Table 5.3, it has been confronted to a linearized modal blade model, constituted of the 7 first structural modes, using the quasi-steady aerodynamic formulation. A stability analysis has been performed for both the model for angles of attack ranging from 10 up to 25° and for wind velocity up to $70m/s$. Results reported in Figure 4.7 show that the section model is equivalent to the modal blade model for low amplitude dynamic analysis. The two unstable areas match well, except for a small shift along the angle of attack axis, probably due to a slightly overestimation of the $\alpha_{\text{twist}}^{2D}$.

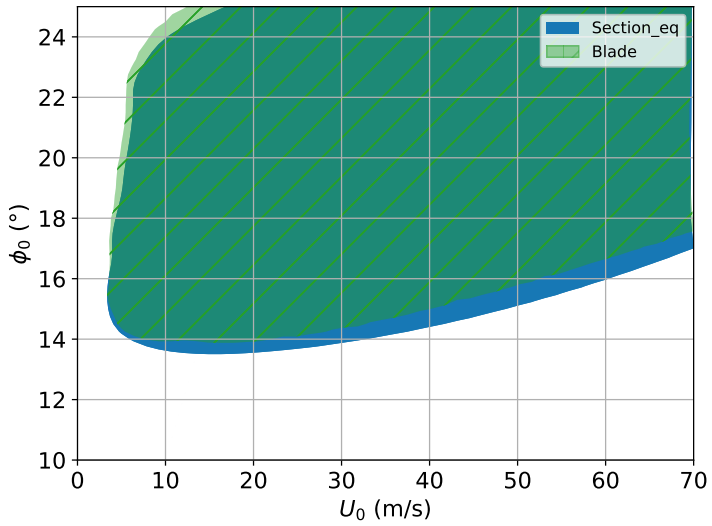

Figure 4.7: Stability map of the equivalent section model using quasi-steady aerodynamics and a linearized modal blade model with the 7 first modes using quasi-steady aerodynamics. The colored areas are unstable.

In the next section a stability map, obtained with either the quasi-steady or dynamic stall aerodynamic model will be compared.

Remark 5 *Based on the way it has been constructed, the $\tilde{x}$ and $\tilde{y}$ displacement of the section model are equivalent to the modal coordinates q_2 and q_1 of the 2nd and 1st structural modes respectively. To effectively compare the displacement of the equivalent section and the one of the blade, it remains to multiply $\tilde{x}$ and $\tilde{y}$ by the values of the mode shapes of the section of interest.*

Remark 6 *This equivalent section model is not compatible with 2D CFD in its current state as it would involve the generation of an equivalent airfoil that would reproduce the equivalent polar. The construction of such an equivalent airfoil is out of the scope of this study.*

4.2 Effect of the dynamic stall model

The effect of the ONERA dynamic stall model on the aeroelastic behavior of the equivalent section is investigated here. The question being addressed is how dynamic stall loops affect the stability and the energy transfer.

The equations of the equivalent section are written and implemented in a monolithic form with both the quasi-steady aerodynamic model and the ONERA dynamic stall model. It allows to easily calculate the eigenvalues and eigenvectors of the coupled system.

Implementation of the ONERA dynamic stall model for the equivalent section When coupled with the equivalent section, the ONERA dynamic stall model is adapted from the formulation of Dimitriadis [37], presented in section 1.3.2.2, in order to make appear the variables of the equivalent section defined previously.

$$W_0(t) = -\dot{y}\cos(\alpha + \alpha_{\text{edgewise}}) + U_0 \sin(\phi_0 + \alpha) - \dot{x}\sin(\alpha + \alpha_{\text{edgewise}}) \tag{4.37a}$$
$$W_1(t) = 0 \tag{4.37b}$$

with $\alpha = \alpha^{2D}_{\text{twist}} + k_{\alpha x}\frac{x}{c_{\text{eq}}} + k_{\alpha y}\frac{y}{c_{\text{eq}}} + \alpha_{\text{torsion}}(U_0, \phi_0)$

The derivative of α has been neglected in W_0 because $k_{\alpha x}$ and $k_{\alpha y}$ are small compared to 1. Taking the derivative of W_0 with time and neglecting $\dot{\alpha}$, it leads to:

$$\dot{W}_0(t) = -\ddot{y}\cos(\alpha + \alpha_{\text{edgewise}}) - \ddot{x}\sin(\alpha + \alpha_{\text{edgewise}}) \tag{4.38a}$$
$$\dot{W}_1(t) = 0 \tag{4.38b}$$

The term $\ddot{x}\sin(\alpha + \alpha_{\text{edgewise}})$ is also neglected as the edgewise motion does not affect much the normal velocity.

The circulation equations (see Eqs. 1.3) now read with the effective angle of attack:

$$\dot{\Gamma}_1 + \lambda_l \tau \Gamma_1 = \lambda_l \tau U c_{l_L}(\alpha^{2D}_{\text{eff}}) + \left(\alpha_l \frac{dc_{l_S}}{d\alpha} + d_l\right)\dot{W}_0 \tag{4.39a}$$
$$\ddot{\Gamma}_2 + a_l \tau \dot{\Gamma}_2 + r_l \tau^2 \Gamma_2 = -r_l \tau^2 U \Delta c_l(\alpha^{2D}_{\text{eff}}) - E_l \tau \dot{W}_0 \tag{4.39b}$$
$$\ddot{\Gamma}_4 + a_d \tau \dot{\Gamma}_4 + r_d \tau^2 \Gamma_4 = -r_d \tau^2 U \Delta c_d(\alpha^{2D}_{\text{eff}}) - E_d \tau \dot{W}_0 \tag{4.39c}$$

It allows to compute the unsteady lift and drag using Eqs. (1.2).

4.2.1 Stability map

The equivalent section model with either the quasi-steady or dynamic stall aerodynamic formulation are confronted under the linear point of view. As the two systems are in a monolithic form, they are numerically linearized in order to obtain their stability matrix A, such that $\dot{X} = AX$. Eigenvalues and eigenvectors of A are calculated over a range of angle of incidence and wind speed. The study of these eigenvalues gives information about the stability of the systems as well as their natural frequencies. By looking to the real part of the eigenvalues, the stability of the system can be deduced. For a wind condition described by its direction and velocity, if at least one eigenvalue has a positive real part then the equivalent section is unstable. A (U_0, ϕ_0) map of instability for angles of attack ranging from 10 up to 25° and for wind velocity up to $70m/s$ is represented in Figure 4.8 for both the quasi-steady or dynamic stall aerodynamic formulation. The colored areas depict the regions of instability for both aerodynamic models.

With quasi-steady aerodynamics, the instability arises over 13.75° of incidence. It mostly corresponds to the range of angle of attack where the derivative of the aerodynamic coefficient C_y with respect to the angle of attack is negative, which is similar to a transverse galloping instability [101]. The critical velocity depends on the incidence and reaches a minimum of 3.8m/s for an incidence of 15°. The critical velocity is the velocity at which the negative aerodynamic damping offsets the structural damping. It means this velocity also depends on the level of damping in the structure. For higher wind speed, the unstable area moves towards higher angles of incidence. This behavior is due to the torsion introduced in the aeroelastic equilibrium due to flexion-torsion

coupling. With the ONERA dynamic stall model, the internal dynamic of the fluid modifies strongly the stability of the system. For angle of incidence lower than 19°, the system has become stable. However, above 19° of incidence, the critical velocity is still very low, below $10m/s$.

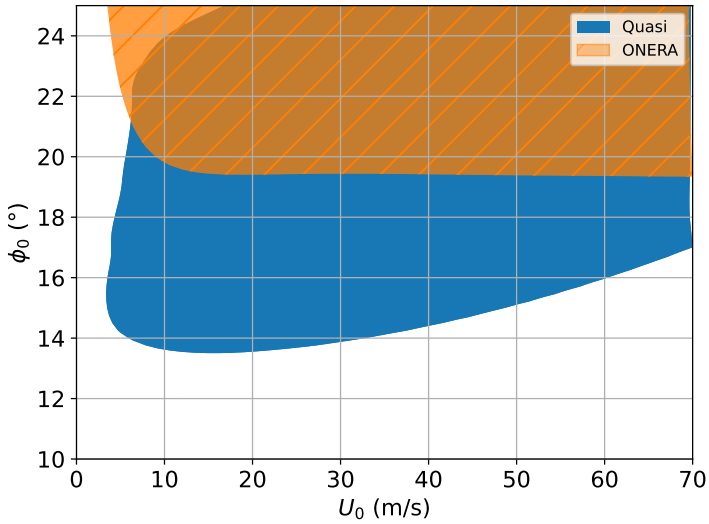

Figure 4.8: Stability map of the equivalent section using quasi-steady aerodynamics or the ONERA dynamic stall model. The colored areas are unstable.

According to Hansen [64] from quasi-steady SIV analysis, the main source of instability in this range of angle of attack is the negative slope of the lift polar. That's why the instability occurs after the stall angle using a quasi-steady aerodynamic formulation. With dynamic stall loops, it is not the static slope of the lift polar which triggers the instability but the mean slope of the loops. It will be detailed later (§4.2.4) but, for low reduced velocities, the mean slope of the lift dynamic loops can significantly depart from the quasi-steady ones. They also depend on the mean angle of attack (see Figure 3.5). When the wind speed rises, the aerodynamics tends to quasi-steady aerodynamics, meaning that the loops get closer to the static polar. The range of incidence of the instability then converges to the range of incidence obtained with quasi-steady aerodynamics. This particular behavior of the slopes of the lift coefficient loop also explains why the unstable zone almost does not move towards higher incidence increasing the velocity.

4.2.2 Stability analysis for a wind of fixed angle of incidence

The angle of incidence ϕ_0 of the wind is fixed at 22° and its velocity is risen from from 0.75 to 70 m/s (i.e. a the reduced velocity from 0.1 to 9.26). For each velocity, the eigenvalues are plotted in Figure 4.9.

With quasi-steady aerodynamics (Fig. 4.9a), there are two eigenvalues, one mostly in the edgewise direction and the other mostly in the flapwise direction. The rise of reduced velocity increases mainly the real part of the flapwise eigenvalue for the whole range of velocity, which crosses the imaginary axis at 4.54 m/s ($\mathcal{U}_R = 0.6$) without coupling with an other eigenvalue. Its eigenvector stays in majority composed of the flapwise degree of freedom for velocity lower than 30.2 m/s ($\mathcal{U}_R = 4$). This stall-induced vibrations can then be defined as a 1dof instability similar to transverse galloping. Figure 4.9a also shows that the real part of the edgewise eigenvalue crosses the imaginary axis at 60.5 m/s ($\mathcal{U}_R = 8$). Its eigenvector contains more and more flapwise structural mode.

With the ONERA dynamic stall model (Fig. 4.9b), the dynamic behavior is different. In addition to the two previous eigenvalues, four eigenvalues are associated to the internal states of the ONERA model. Tang and Dowell [133] performed similar stability analysis for a pitch-plunge section model coupled with the ONERA dynamic stall model. They highlighted possible interactions between a "structural" eigenvalue and a "fluid" eigenvalue. No such interaction can be noticed in Figure 4.9b. Results show that the real part of the flapwise eigenvalue increases and becomes unstable at 5 m/s ($\mathcal{U}_R = 0.66$). Contrary to the quasi-steady aerodynamics results the edgewise eigenvalue does not become unstable. The frequencies of the modes also remains nearly constant.

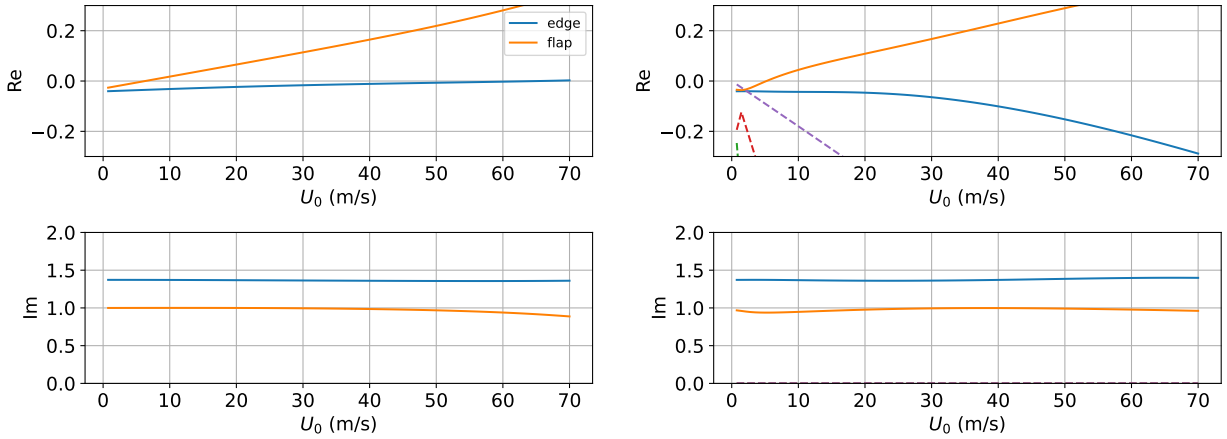

(a) Quasi-steady aerodynamics

(b) ONERA dynamic stall model

Figure 4.9: Eigenvalues for $\phi_0 = 22°$ with increasing reduced velocity from 0.75m/s to 70m/s ($\mathcal{U}_R$ from 0.1 to 9.26)

4.2.3 Stability analysis for a wind of fixed velocity

The velocity U_0 is fixed at 40m/s, corresponding to a reduced frequency $\mathcal{U}_R = 5.31$, and the angle of incidence ϕ_0 is varied from 10° to 25°. The evolution of the eigenvalues with the angle of incidence is reported in Figure 4.10 using quasi-steady aerodynamics (Fig. 4.10a) and the ONERA dynamic stall model (Fig. 4.10b).

With quasi-steady aerodynamics, the flapwise eigenvalue becomes unstable at 14.3°. Its real part reaches a maximum around 16.4° and then linearly decreases. The edgewise eigenvalue stays stable while being very close to zero until 25°. Looking at the imaginary part, it can be noticed that the frequency of the flapwise mode is lower than the natural structural frequency for low angle of incidence but gradually increases with the incidence. Like in the previous section, the eigenvector associated to the flapwise mode is mainly made up of the flapwise structural degree of freedom.

With the ONERA dynamic stall model, the real part of the eigenvalues evolves differently than with quasi-steady aerodynamics. As seen in the stability map, the flapwise mode destabilizes at an higher incidence of 19.4° and the real part continues to rise during the whole range of incidence. The real part of the edgewise eigenvalue remains slightly negative up to 17° and then gradually decreases with the angle of incidence. The evolution of the imaginary part of the edgewise mode stays approximately constant. For the flapwise eigenvalue, a singular drop-and-rise behavior is observed for $13 < \phi_0 < 19$ which seems to be linked to the interaction with a fluid mode associated with the ONERA dynamic stall model.

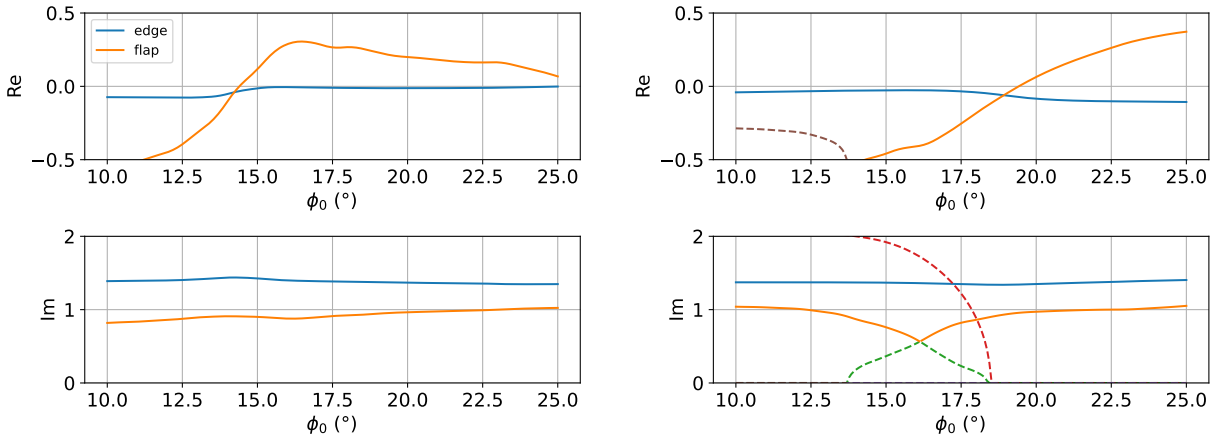

(a) Quasi-steady aerodynamics

(b) ONERA dynamic stall model

Figure 4.10: Eigenvalues for $\mathcal{U}_R = 5.31$ ($U_0 = 40$m/s) with increasing incidence from 10° to 25°

4.2.4 Effect of the loops orientation

When dealing with dynamic stall, the shape and orientation of the unsteady aerodynamic loop is very important to assess the risk of instability. In stall flutter when the torsion is involved, the area and the direction of rotation of the unsteady pitching moment as a function of the angle of attack, allow to quantify the transfer of energy from the fluid to the structure (positive for clockwise area and negative otherwise). For stall-induced vibrations in flexion, the stability is determined by the sens and the surface of the Lissajous graph according to the generalized coordinate (i.e the plot of the generalized load along the displacement versus the displacement). As a consequence, regarding the unsteady load plotted as a function of an effective angle of attack, the criteria on the shape of the loops is different. Instead of the surface and direction of rotation, it involves its mean slope.

As an example, a sinusoidal motion in the flapwise direction is imposed to the equivalent section with an amplitude of $0.085c_{\text{eq}}$ for the angles of incidence 18° and 22° and a wind speed of 40m/s. The load coefficients along the flapwise direction are represented in Figure 4.11a as a function of the effective angle of attack. The Lissajous graphs are given in Figure 4.11b.

Like in the experiment of Fuglsang et al. [51], the dynamic stall loop plotted as a function of the effective angle of attack, is clockwise for $\phi_0 = 18°$ and has a positive mean slope (see Figure 4.11a). When representing this loop in a Lissajou graph, it gives a new loop that is counter-clockwise. It means that the work of the aerodynamic loads is negative (i.e. no risk of instability). The dynamic stall loop versus α_{eff} is almost flat for $\phi_0 = 22°$ but has a negative mean slope. In the Lissajous graph, it gives a thicker loop that is clockwise, meaning that the work of the aerodynamic loads is positive.

The link between the slope of the dynamic stall loop plotted as a function of the effective angle of attack and the direction of rotation in a Lissajous graph can be understood following a cycle of harmonic motion (step 1 to 4 in Figure 4.11). Step 1 corresponds to a maximum of q_{flap} where $\dot{q}_{flap} = 0$. The effective angle of attack is equal to the angle of incidence. From Step 1 to step 3, $\dot{q}_{flap}$ is negative. The effective angle of attack increases up to point 2, then decreases to reach point 3 where q_{flap} is minimum and $\dot{q}_{flap} = 0$. From step 3 to step 1, $\dot{q}_{flap}$ is positive. The effective angle of attack decreases to reach its minimum at point 4, then it increases back to point 1. Comparing the relative height of points 2 and 4 gives the direction of rotation of the loop on the Lissajous graph. When 2 is higher than 4, like for the loop around 19.5°, it is counter-clockwise in a Lissajous representation (i.e. no risk of instability). But when 2 is below 4, like for the loop

around 23.5°, it is clockwise in a Lissajous representation (i.e. risk of instability).

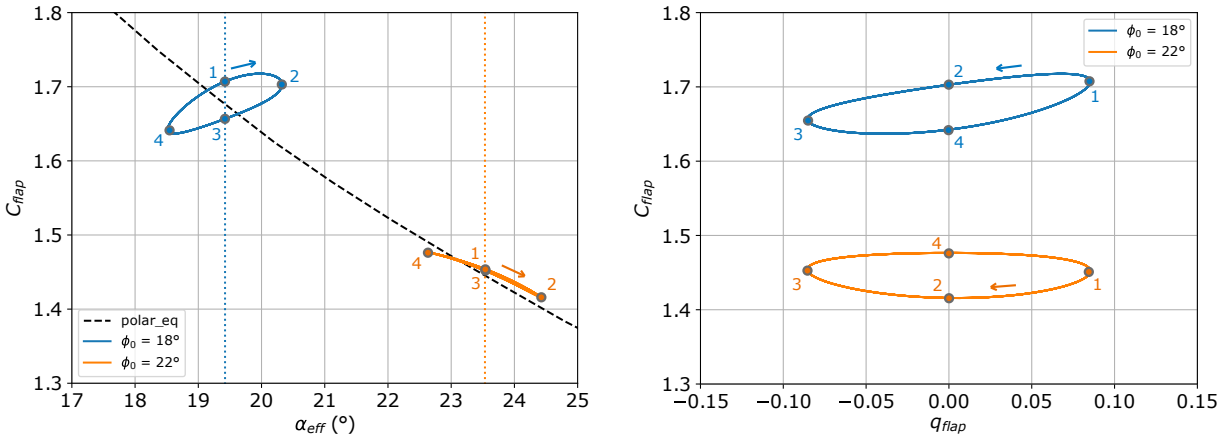

(a) Dynamic stall loops of the load coefficient in flapwise direction as a function of the effective angle of attack.

(b) Lissajous graph: Load coefficient versus flapwise coordinate. The oriented surface of the loop gives the work of the load.

Figure 4.11: Evolution of the load coefficient in flapwise direction in function of (a) the effective angle of attack and (b) the flapwise coordinate. The imposed motion is a sinusoid translation along the flapwise direction. The wind speed is 40m/s ($\mathcal{U}_R = 5.3$).

These dynamic stall loops can be put in perspective with the stability map in Figure 4.8. The dynamic stall loop for $\phi_0 = 18°$ (positive mean slope) is located outside the unstable area of the ONERA model whereas the loop for $\phi_0 = 22°$ (negative mean slope) is inside.

4.3 Stability analysis using a finite element model of the blade

In this section, the equivalent section model is compared to a finite element model of the full blade which uses corotated Euler-Bernoulli beam elements that take into account geometric non-linearities. This comparison will allows to evaluate the representativeness and the limits of the equivalent section model.

The finite element blade modelis constituted of 100 beam elements using the material mass and stiffness matrix of the IEA15MW. A partitioned approach has been chosen to couple the finite element beam solver with the ONERA dynamic stall model. The temporal coupling method is a conventional serial staggered (CSS) procedure [46] without predictor. 200 time steps per period of flapwise oscillation are used, it corresponds to a time step of 2.55ms. Spatially, a dynamic stall model has been placed on each node of the beam, under the strip theory assumption. It means that no corrections are implemented to take into account the three dimensionality of the flow. The static polars used for the profiles constituting the blade are the one provided in the github of the IEA15MW [1]. The displacements, velocities and accelerations of the blade are used in the dynamic stall model to compute the loads. Between the nodes, the loads are supposed to vary linearly. They are integrated by the finite element form functions to obtain generalized forces that can be given to the structural solver.

[1] https://github.com/IEAWindTask37/IEA-15-240-RWT

4.3.1 Spanwise distribution of the fluid-structure energy transfer

The blade model allows to calculate the distribution along the span of the power associated to the aerodynamic load by multiplying the aerodynamic force with the velocity at each node. It gives information about the localization of the fluid-structure transfer of energy along the blade. The distribution of the averaged power over a period, for a forced harmonic motion of the flapwise mode with an amplitude of 0.085 at $U_0 = 50m/s$ and $\phi_0 = 19°$ is shown on the Figure 4.12a.

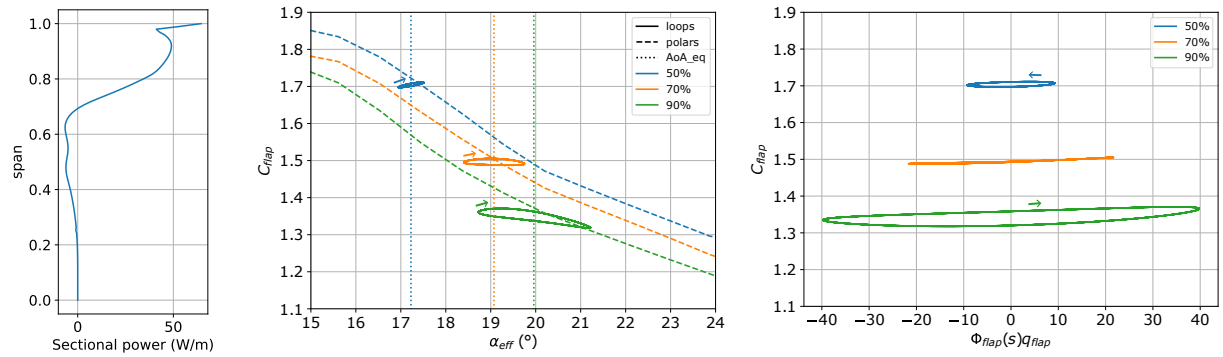

(a) Sectional power along the blade

(b) Dynamic stall loop for the 50%, 70% and 90% blade sections

(c) Load coefficient as a function of the dimensionless displacement of the sections

Figure 4.12: Impact of the dynamic stall loops on the sectional power along the blade for forced flapwise motion at $U_0 = 50m/s$ and $\phi_0 = 19°$

It appears that the power does not have the same sign along the blade. The blade can be divided in three regions from root to tip. The first 20% of the blade does not exchange energy with the fluid. As the root is clamped, the beam as not much velocity in this region. Until 70%, the power is negative. It means that the flow damp the blade motion. Finally, the power is positive in the last region. The flow is giving energy to the blade and powers the oscillations. If the blade receives more energy than the one dissipated by the structural damping, then the vibrations will grow.

This specific distribution of power comes from the shapes of the loops along the blade. They are represented in the Figure 4.12b. Due to the twist and the torsion of the blade, the outer sections have a higher mean angle of attack than the other sections. Between 50% and 90% of the blade, the mean angle of attack has augmented by 2.8°. Consequently, at the mid span the loop has a positive mean slope whereas at 90%, the loop has a negative mean slope (cf Figure 3.5). It induces loops as a function of the displacement that are counter-clockwise at 50%, closed at 70% and clockwise at 90% (see Figure 4.12c). Moreover, because of the flapwise mode motion, the outer sections have larger displacements. That's why the dynamic stall loops are larger and the energy exchanged near the tip is higher. It can be seen by the greater surface in Figure 4.12c.

For other wind angles of incidence, the repartition of mean power along the span differs.

4.3.2 Stability analysis

In this section the stability of the blade model is investigated and compared to the stability of the equivalent section. As a partitioned approach has been chosen to couple the finite element beam solver with the ONERA dynamic stall model, the stability of the blade model is assessed by temporal simulation in a staggered way. It consists in 56 simulations uniformly distributed within the area $U_0 \in [10, 70] m/s$ and $\phi_0 \in [16°, 21°]$. The results are reported in Figure 4.13 where the dots indicate that the vibration are damped whereas the crosses marked growing oscillations. The unstable area of the equivalent section coupled with the ONERA dynamic stall model is added for comparison.

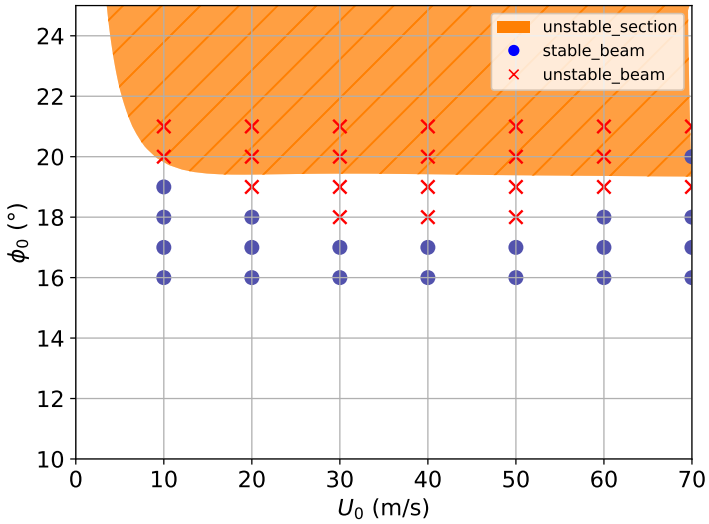

Figure 4.13: $\phi_0 - U_0$ map comparing the stability of the sectional model and the FEM blade model. Both models are coupled with the ONERA dynamic stall model using parameters reported in Table 3.1

Results are mainly coherent between the two models. However, close to the neutral line, some crosses (i.e. unstable results for the FEM blade model) are outside the unstable area of the equivalent section model. The shape of the neutral line of the FEM model exhibits a smooth V-shape. The shift of the unstable area towards higher angle of attacks, beyond 50m/s, is probably due to the amplification of the mean torsional deformation that can be attributed to geometric nonlinearities (see Fig. 4.15c). The differences observed below 50m/s also highlight that using the ONERA dynamic stall model with an equivalent polar has limitations in capturing the combined effect of the dynamic stall along the blade.

4.4 Discussions

The differences observed between the stability of the FEM blade model and the equivalent section model (Fig. 4.13) are discussed in this section. A comparison with a simpler section model is also provided. Finally, the sensitivity of the stability map to an important parameter of the ONERA dynamic stall model is highlighted.

4.4.1 Equivalent dynamic stall

Contrary to the quasi-steady aerodynamics, the dynamic stall has its own dynamic. As each section has a different chord, the delay introduced by the dynamic stall, that depends on the local reduced frequency, is unique to the section. When calculating the generalized force on the blade, the behavior of each section needs to be combined. It is expected to lead to a more complex dynamic that can only be described by high orders equations. Technically, the generalized force on the blade is the integral of the force coefficients. The force coefficient at each section evolves in time following the differential equations of the ONERA dynamic stall model. The idea of an equivalent dynamic stall model would then be to build a set of equations dictating the evolution in time of the integral.

For example, let's take the quantities x_1 and x_2 that follow the differential equations:

$$\frac{dx_1}{dt} + \lambda_1 x_1 = 0 \tag{4.40}$$

$$\frac{dx_2}{dt} + \lambda_2 x_2 = 0 \tag{4.41}$$

The question is : which differential equation follows $X = x_1 + x_2$?

The answer is :

$$\frac{d^2X}{dt^2} + (\lambda_1 + \lambda_2)\frac{dX}{dt} + \lambda_1\lambda_2 X = 0 \tag{4.42}$$

It can be notice that the order of the differential equation has risen according to the number of initial differential equations. For the continuous integral of a quantity (lift along the blade), as it represents an infinite sum of the lift over infinitesimal sections, it leads to a differential equation of infinite order.

As it is too complex, the ONERA dynamic stall model has been a posteriori associated to the equivalent section model for which the structural parameters and polar curves have been identified considering a quasisteady aerodynamic formulation. The effect of this simplification is evaluated in this section.

To compare the equivalent section model to the blade model, both coupled with the ONERA dynamic stall model, the same flapwise motion is imposed to both models. It means that in both cases, the generalized coordinate q_{flap} is forced by a sinusoid of the same amplitude. For the equivalent section model, q_{flap} corresponds to y/c_{eq} while it correspond to the modal amplitude of the flapwise mode for the beam. The generalized force coefficient is then represented as a function of q_{flap} in Figure 4.14a.

The first thing to notice is that the mean value of the generalized force coefficient of the blade model is lower than the one of the equivalent section. It comes from the fact that the polars of the equivalent section have been build in order to reproduce the aerodynamic damping and not the mean force. It means that expression (4.6) is not conserved between the two models. Secondly, the rotation direction of the two loops is different. The loop of the beam is clockwise, indicating that there is a transfer of energy from the fluid to the structure whereas for the equivalent section,

the loop is counter-clockwise, indicating that the transfer of energy is from the structure to the fluid. As exposed previously, it comes from the simplification of the dynamic stall behavior. If equivalence was perfect, the two loops would have been superposed.

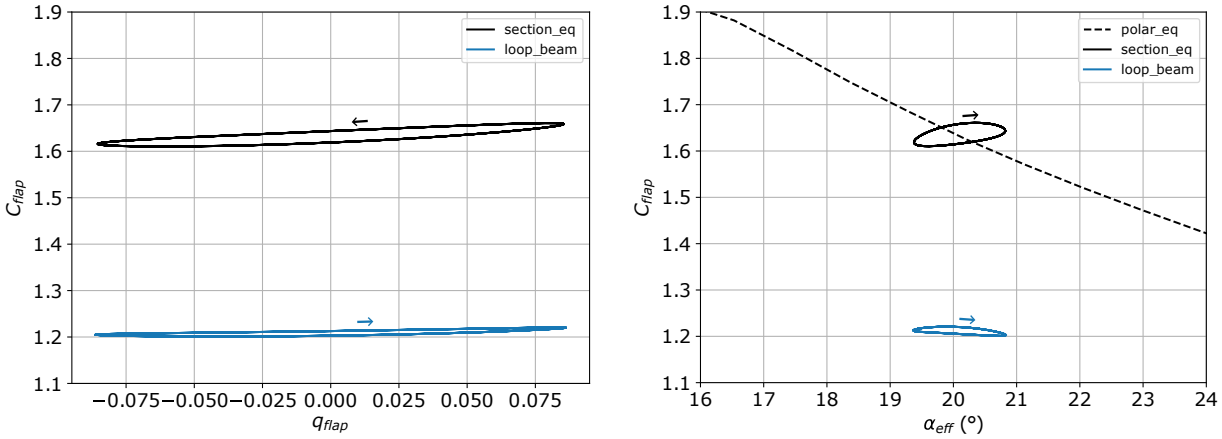

(a) Load coefficient versus the flapwise coordinate. The surface of the loop is the work of the load.

(b) Dynamic stall loops

Figure 4.14: Comparison of the generalized force between the equivalent section and the blade model for forced flapwise motion at $U_0 = 50m/s$ and $\phi_0 = 19°$

The generalized force coefficient is now plotted for both the models as a function of the effective angle of attack of the equivalent section model in Figure 4.14b. It can be noted that the loop is finer for the FEM blade model and its mean slope is negative. This loop looks like the dynamic stall loop occurring at higher angles of attack using the section model.

4.4.2 The equilibrium modification

As the mean generalized force is not conserved between the equivalent section and the blade model, a deviation in the equilibrium state is expected. To better understand this effect, the evolutions of the edgewise and flapwise relative displacement of the blade tip have been plotted as a function of the reduced velocity in Figure 4.15a and 4.15b. To allow a comparison of both model, the displacement of the equivalent section is scaled by the value of the blade flapwise or edgewise mode at the tip. The relative torsional deformation of the blade at the tip is also reported in Figure 4.15c.

Until 15 m/s ($\mathcal{U}_R = 2$), the displacements in edgewise and flapwise predicted by the two models are close. But as the mean forces and the aerodynamic stiffness are not equivalent between the two models, the displacements are moving away from each other increasing the reduced velocity. The torsion of the two models can not be compared directly, because the torsion angle of the equivalent section model is constituted of multiple part that should be scaled at the tip using multiple blade modes, but nevertheless their trends should be similar. What is shown in Figure 4.15c is that the modeling of the flexion-torsion coupling and the torsion mode in the equivalent section allows to capture the initial decrease of the angle of torsion. However, beyond 45 m/s ($\mathcal{U}_R = 6$) the section model underestimates the torsional blade deformation. This highlights the limit of the linear based equivalent section model to catch the impact of geometric non-linearities.

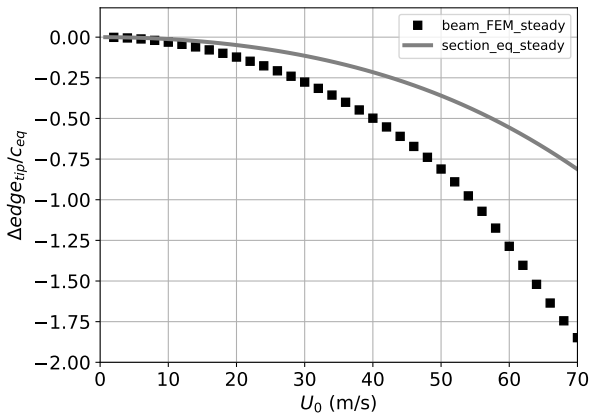

(a) Relative displacement at the tip in the edgewise direction (x in Fig. 4.1)

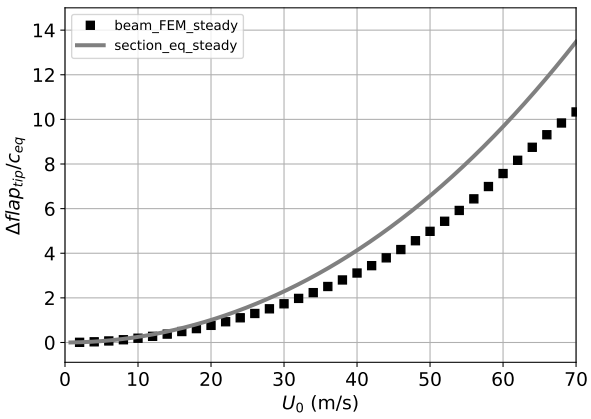

(b) Relative displacement at the tip in the flapwise direction (y in Fig. 4.1)

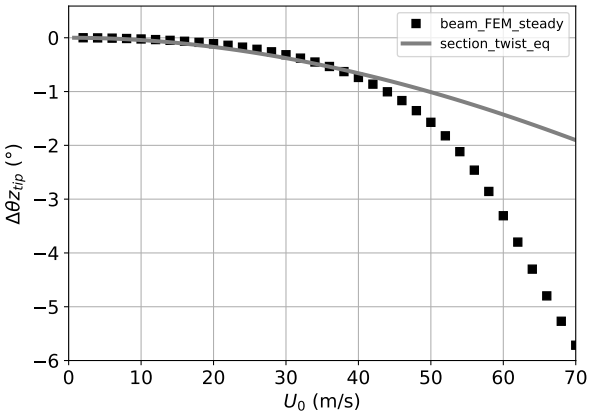

(c) Relative torsional deformation at the tip

Figure 4.15: Comparison of the equilibrium between the equivalent section model and the blade model at $\phi_0 = 17°$. ($\mathcal{U}_R = 9.25$ approximately correspond to $U_0 = 70m/s$)

4.4.3 Comparison with a simpler sectional model

The proposed equivalent section is not straight forward to use as the calculation of the equivalent polars in Step 5 is not easy. Moreover, all the characteristics of the equivalent section do not have the same significance. To evaluate what feature is of main importance, the equivalent section is compared to a simpler section model obtained by choosing one arbitrary section of the blade, for example the one at 75% of the blade for which the lift and drag coefficients polars are very close, as shown in Figure 4.4. The sectional mass, the chord and the polar of this section are picked for this simpler model. Then, the stiffness of the springs can be taken so as to match the natural frequencies of the blade. The flexion-torsion coupling parameters are also picked by looking at the 75% blade's section of the structural modes.

The stability map obtained with this 75% section model is drawn in the Figure 4.16b. Results obtained with the equivalent section model are recalled in Figure 4.16a. The range of angle of incidence leading to an instability are pretty similar for both those section models. The shape of the unstable areas using either a quasi-steady or dynamic stall aerodynamic formulation are also similar, but the shift of the unstable region towards higher angles of incidence is amplified for the 75% section model.

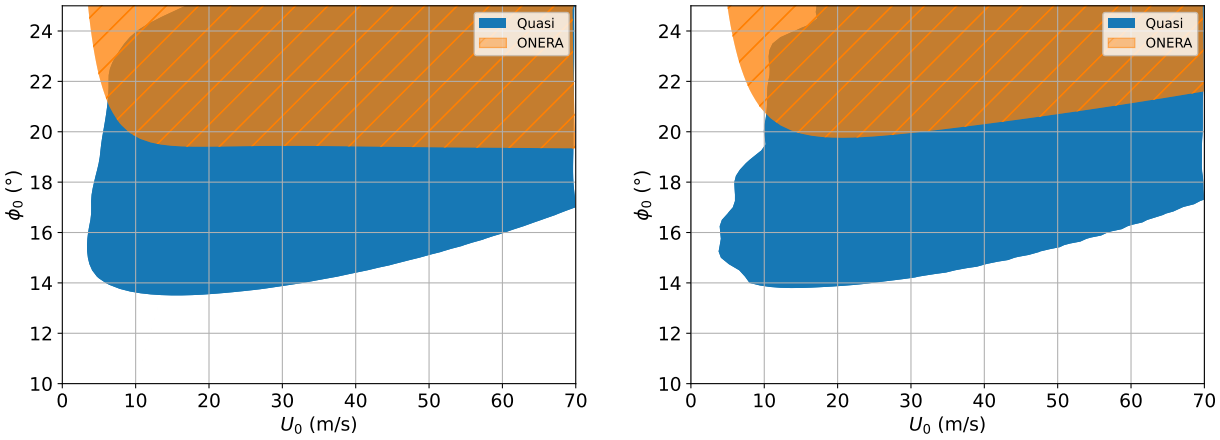

(a) Equivalent section

(b) Simple section at 75% of the blade

Figure 4.16: Comparison of the equivalent section model with a 75% section model; Stability maps using either quasi-steady aerodynamics or the ONERA dynamic stall model. The colored areas are unstable.

Between the 75% section model and the equivalent sectional model, the lift and drag coefficients polars are very close as shown in Figure 4.4. That's why, the instabilities arise for the same range of wind angle of incidence. The choice of sectional mass and chord for the 75% section model result in a slightly different mass ratio. It is 0.0706 for the equivalent section whereas the mass ratio is 0.061 for the 75% section model. It slightly reduces the aerodynamic damping and thus slightly increases the critical velocity for the 75% section model. One of the main differences between the two models comes from the chord value. The chord of the 75% section is 3m which is higher than the equivalent chord of 2.35m. By definition of the reduced velocity it leads to an overestimation of the critical wind speed for the 75% section model.

Effect of the torsion

The effect of the torsion on the stability can be investigated by removing the flexion-torsion coupling and the torsion angle from the equivalent section. The effective angle of attack simplifies as following:

$$\alpha_{\text{eff}}^{2D} = \alpha_{\text{twist}}^{2D} + \arctan\left(\frac{\sin(\phi_0 - \alpha_{\text{edgewise}}) - \frac{1}{U_R}\frac{\partial \tilde{y}}{\partial \tilde{t}}}{\cos(\phi_0 - \alpha_{\text{edgewise}}) - \frac{1}{U_R}\frac{\partial \tilde{x}}{\partial \tilde{t}}}\right) + \alpha_{\text{edgewise}} \tag{4.43}$$

The associated stability map is plotted in Figure 4.17b. Results obtained with the equivalent section model, considering torsional effects, are recalled in figure 4.17a. Neglecting the torsional effects, the unstable area does not changed much for low velocity ($U_0 < 30m/s$. But for $U_0 > 30m/s$ this simplified section model departs from the reference blade model and predicts a shift of the unstable zone towards lower angles of incidence, i.e. the opposite direction. Additional studies have also confirmed that within the terms added to model the static torsion, the one that modifies the most the stability map is $k_y\tilde{y}$.

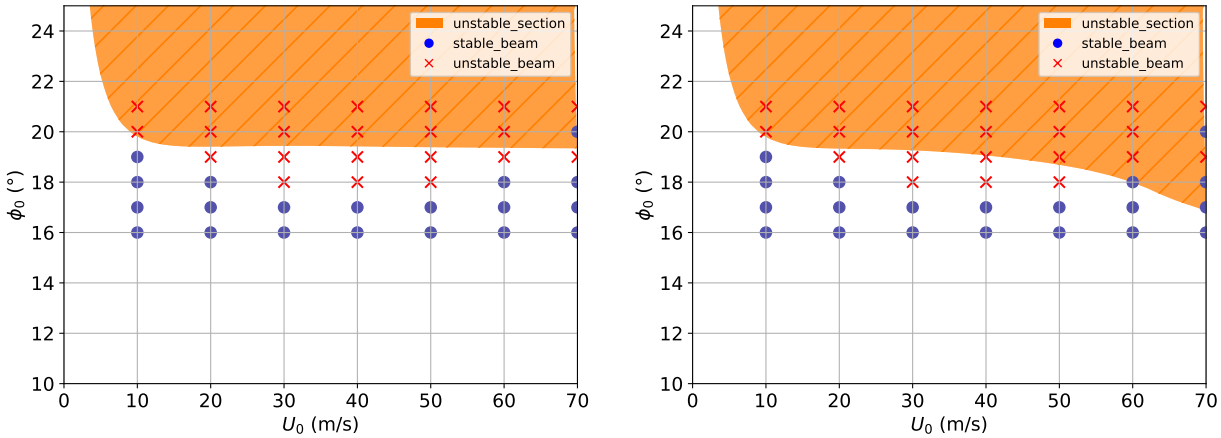

(a) Equivalent section

(b) Equivalent section without torsion

Figure 4.17: Comparison between the stability map of the beam and the equivalent section with and without the torsion.

4.4.4 Sensitivity to a parameter of the ONERA model

The mean slope of the dynamic stall loops is an important feature to assess the stability of the system. However, it is very sensitive to some of the parameters of the ONERA dynamic stall model. To illustrate this, parameter r_{0_l} which directly affects the intensity of the nonlinear forcing term ($r_l = \left(r_{0_l} + r_{2_l}\Delta c_l^2\right)^2$ in Equation 4.39b), has been changed from 0.13 to 0.2 and the same forced motions as in section 4.2.4 have been imposed to the equivalent section. As shown in Figure 4.18a the parameter r_{0_l} significantly modifies the dynamic stall loop for angle of attack below 20°.

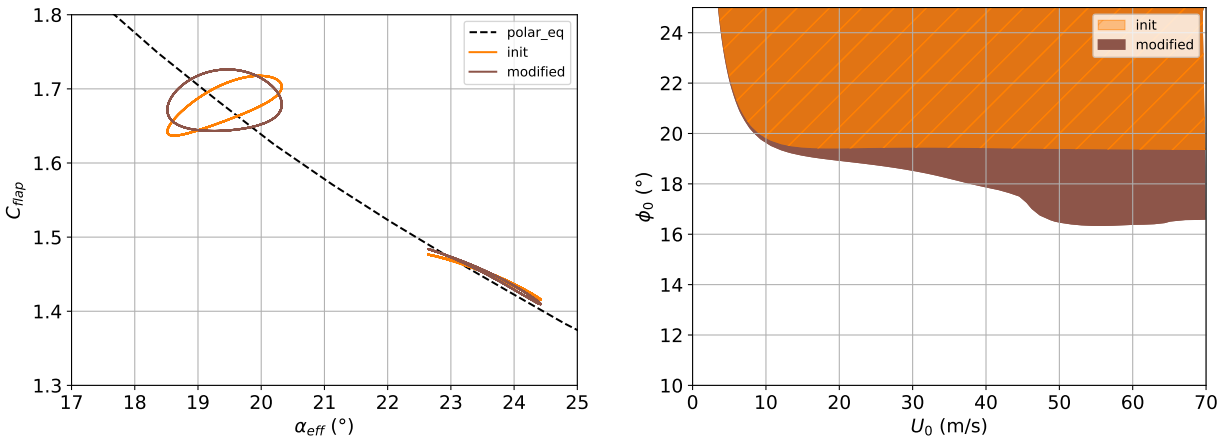

(a) Comparison of the dynamic stall loops of the load coefficient in the flapwise direction before and after the modification of parameter r_{0_l}. The wind speed is 40m/s ($\mathcal{U}_R = 5.3$).

(b) Stability map of the equivalent section before and after the modification of parameter r_{0_l}.

Figure 4.18: Effect of the modification of parameter r_{0_l} on the dynamic stall loops and on the stability map.

An increase (+50%) of the parameter r_{0_l} significantly changes the shape of the loop including its mean slope that is lower. This affects the stability map as depicted in Figure 4.18b. The main modification occurred for angle of attack below 20°. The unstable area has extended towards lower angle of attack because the mean slope of the loops decreases with increasing the parameter r_{0_l}. This highlights the difficulty to predict stability maps with semi-empirical dynamic stall models like the ONERA model. Special attention should be paid to the identification of the model parameters. To do that, experimental data base of dynamic stall loops with various mean angle of attack, reduced frequency and amplitude would be necessary.

4.5 Conclusion

The impact of several models of different fidelity has been investigated for the fluid as well as for the structure. First, efforts have been made to build an equivalent section model as close as possible to a blade model. It has led to define equivalent quantities describing synthetically the problem. Using this equivalent section, the effect of quasi-steady aerodynamics and of the ONERA dynamic stall model on the stability has been highlighted. The introduction of dynamic stall deeply modifies the dynamics of the system. Depending on the mean slope of the loop it can reverse the energy transfer. However, special caution need to be taken as this slope is very sensitive to the parameters of the dynamic stall model which highlight the difficulty to use such semi-empirical dynamic stall model for SIV predictions.

The ONERA model has also been coupled with a FEM blade model in order to compare its stability with the one of the equivalent section model. The main differences come from the simplification of the dynamic stall behavior of the blade into a unique dynamic as well as the additional torsion angle at the equilibrium due to geometric non-linearities. Both move the boundaries of stability.

The 3D effects of dynamic stall are not modeled yet. Experiments or high-fidelity simulations could allow to adapt the dynamic stall model for continuous blade approach.

Chapter 5

Study of stall-induced vibrations at standstill with high fidelity models

In the previous chapter, a linear study of the stall-induced vibrations has been conducted with a blade model and its equivalent section model coupled with the ONERA dynamic stall model. Thus, a stability map has been done in order to identify the unstable areas. Based on that kind of map, high-fidelity simulations coupling the FEM blade model with a CFD URANS solver can be chosen and realized. The goal is to take into account a better description of the flow and observe how it modifies the coupled system behavior compared to the lower fidelity model. The present investigation is progressive. First, the focus is put on the aeroelastic static equilibrium in order to understand how the increased complexity of the flow modeling affects the static loads. Then, the blade is forced to oscillate around these equilibrium states according to its flapwise mode, as it has been identified as the mode concerned by SIV. Emphasis has been put on the description of the phase shift between the loads and the flapwise velocity that directly affects the added aerodynamic damping. Finally, aeroelastic simulations have been performed for selected configurations, two stable and one unstable, according to low fidelity results. For each step of the study an estimation of the effects of both the angle of incidence ϕ_0 and wind speed U_0 is initiated. These preliminary high fidelity results will serve as a basis for recommendations to improve the modeling approach.

Contents

5.1 Cases description 116
5.1.1 The numerical setup 116
5.1.2 Choice of the cases to simulate 118
5.2 Study of the aeroelastic static equilibriums 119
5.2.1 Analysis of the $\phi_0 = 17°$ and $U_0 = 40$m/s case 119
5.2.2 Effect of the wind angle of incidence ϕ_0 123
5.2.3 Effect of the wind speed U_0 126
5.3 Study of the dynamic behavior of the aerodynamic loads induced by an imposed harmonic motion of the blade 128
5.3.1 Description of the imposed motions 128
5.3.2 Analysis of the $\phi_0 = 17°$ and $U_0 = 40$m/s case 130
5.3.3 Effect of the incidence ϕ_0 137
5.3.4 Effect of the wind speed U_0 139
5.4 Study of the aeroelastic dynamic behavior of the blade in stall conditions with a high-fidelity aeroelastic unsteady coupling 140
5.4.1 Description of the wind gust used to perturbed the blade 140
5.4.2 Analysis of the $\phi_0 = 17°$ and $U_0 = 40$m/s case 142
5.4.3 Effect of the incidence ϕ_0 143
5.4.4 Effect of the wind speed U_0 145

5.5 Conclusion 148

5.1 Cases description

This part describes how the numerical setup is built as well as how the conditions of incidence and wind speed of the high fidelity simulations have been chosen.

5.1.1 The numerical setup

As for the previous chapter, the study deals with a single isolated blade of a IEA15MW wind turbine at standstill position, positioned along the Z axis. The simulation mesh is constituted of two meshes, a first mesh describes the geometry of the blade (Figure 5.1) and is immersed in a background mesh that captures the wake (Figure 5.2).

The mesh of the blade has been recuperated on the IEA15MW github[1]. Usually the blade is fixed to a hub, however to simulate an isolated blade, the geometry has been closed by adding a spherical shape to the root. As a result, the close-blade mesh completely surrounds the blade. In the simulated cases, the wind speed will not exceed 50m/s which corresponds to a Reynolds number of $18 \cdot 10^6$ with respect to the maximum chord. The first cell size is $5\,\mu$m which gives an y+ of 0.55. As y+ is lower than one, this mesh is adapted for URANS simulations. The grid is constituted of 323 nodes all around the airfoils. The spanwise direction is discretized with 232 nodes. Finally, the surface mesh has been extended in the normal direction on approximately 7.5 m with 129 nodes, giving a 3D grid with a total of 9.1 million cells. A non-slip wall condition is placed on the skin while an overlap boundary condition, used for the chimera method, is set for the outer boundaries.

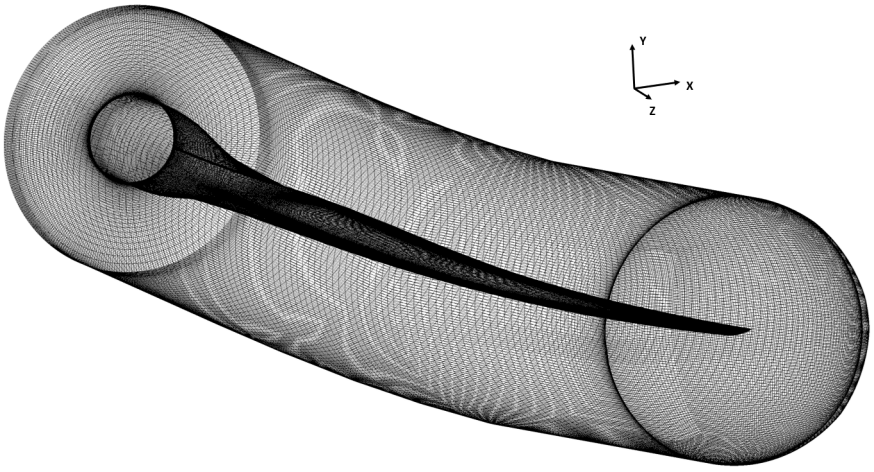

Figure 5.1: Close-blade mesh of the IEA15MW blade

The background mesh is composed of two areas, a cartesian core is surrounded by zones of mesh derefinement. For the chimera method to work properly, the close-blade mesh must stay within the core region. The size of this core grid should be chosen based on the expected amplitude of vibration of the blade. To be conservative, the amplitude of vibration was estimated using quasisteady aerodynamics. Based on the limit cycle oscillations observed around the deformed

[1] https://github.com/IEAWindTask37/IEA-15-240-RWT

state of the blade, an extending core toward the positive Y direction was set. The core is also extended in the negative X direction in order to capture the wake. With the pitch axis as reference, the core dimensions are $[-24\,\text{m}, 15\,\text{m}] \times [-15\,\text{m}, 27\,\text{m}] \times [-24\,\text{m}, 144\,\text{m}]$. In the Z direction, 20% of the blade length has been taken between the close-blade mesh and the core boundaries. Moreover, for the interpolation of the chimera method to be accurate the size of core cells need to be of equivalent size to that the outer cells of the close-blade mesh. As a consequence, the core grid contains $196 \times 211 \times 421 \approx 17 \cdot 10^6$ nodes. This core mesh is completed by zones with increasing cell size that reach a farfield of 300m. It raises the background mesh with 43.3 million additional cells. Thus, the total mesh contains $69.6 \cdot 10^6$ cells. A summary is given in the Table 5.1.

Table 5.1: Repartition of the mesh

Zone	Number of cell (M)	%
Total	69.6	100
Close-Blade	9.1	13.1
Cartesian core	17.2	24.7
Graded region	43.3	62.2

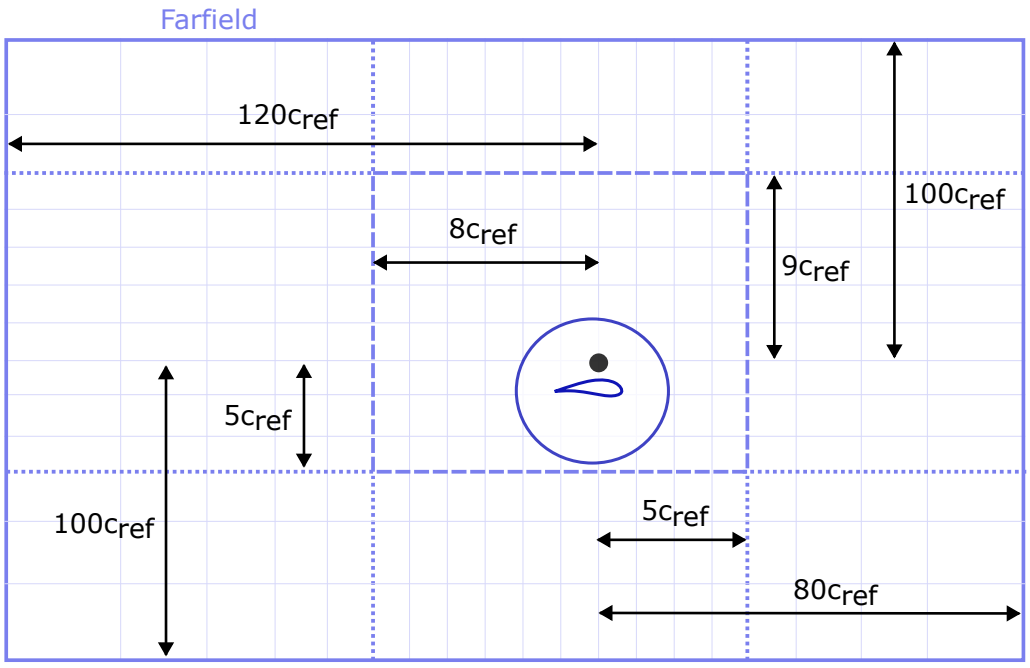

Figure 5.2: Scheme of the background mesh on the XY plan (not at scale). The black dot represents the pitch axis and the circle is the mesh of the blade. $c_{\text{ref}} = 3\,\text{m}$.

The reference state of the flow imposed at the farfield boundary condition, and as an initial state, is an uniform flow of velocity U_0 coming from the positive X with an angle of incidence ϕ and no inclination (no Z component). The atmospheric boundary layer is not modeled. The density ρ of the reference state is set to 1.225 kg/m^3, the kinematic viscosity ν to $1.56 \cdot 10^{-5} m^2/s$, the temperature T to $288.15K$, the pressure p to $101325Pa$ and the Spalart-Allmaras turbulent viscosity $\tilde{\nu}$ to $3.579 \cdot 10^{-6} m^2/s$. Based on the validation done in [29], this value of turbulent viscosity corresponds to a turbulent intensity of 4%.

Concerning the temporal discretization, the chosen time step is $\Delta t = \frac{c_{\text{ref}}}{200 U_0}$. For a wind speed of 40m/s, it corresponds to 8000 time steps per flapwise period. According to Figure 3.6, it is not enough to have completely converged dynamic stall loops but more time steps would have been computationally unaffordable for our purpose. In the literature, the number of time steps per period is about the thousands [7, 83] or the tens of thousands [30].

For the modeling of the blade, a finite element model with 100 corotated Euler-Bernoulli beam elements is used. The root is clamped while the tip is free.

5.1.2 Choice of the cases to simulate

In light of the numerical cost of aeroelastic unsteady simulations, the number of configurations that could be simulated was limited. Thus, each configuration needs to be carefully chosen. A demand of resources has been done to GENCI early in the thesis and a total of 4.2 millions hCPU have been obtained. With the previously presented mesh, an aeroelastic iteration takes 3.3 hCPU spread on 12x48 cores. The repartition of the computation cost between the CFD solver, the beam solver and the transfers is reported in table 5.2. It can be noticed that the majority of the computational cost is spend in the mesh deformation.

Table 5.2: Computation cost for one iteration

Step	Substep	hCPU	%
Total		3.33	100
CFD		1	30
CSM		0.03	0.8
Motion transfer		1.955	58.7
	Skin motion	0.1	2.29
	Mesh deformation	1.85	55
Load transfer		0.35	10.5

According to these performances and considering 8000 iterations per period ($T = 2\,\text{s}$) for $U_0 = 40\text{m/s}$ or 10000 iterations per period for $U_0 = 50\text{m/s}$, it was possible to perform 7 unsteady simulations of approximately 9 s that correspond to 4.5 periods of the flapwise mode (i.e. the lowest frequency mode).

Choice of the conditions (ϕ_0, U_0)

The choice of the ϕ_0, U_0 configurations to be simulated was made based on the stability map obtained with a FEM model of the blade coupled with the ONERA dynamic stall model, reported in Figure 5.3. The idea was to realize high-fidelity simulations within and outside the unstable area of the blade model. The conditions need also to be diverse in order to study the effect of the angle of incidence ϕ_0 and the wind speed U_0 on the stability. However, there is one constraint with the CFD. As shown in the Figure 3.7, there exists an angle of attack above which the URANS simulations are not valid anymore. Thus, the maximum angle of incidence used during this study should be limited. Based on the stability map (Figure 5.3) and the CFD constraint, a simulation plan has been set. It is given in the table 5.3. It is focused around the boundary of stability at $\phi_0 = 17°$ and $U_0 = 40\text{m/s}$.

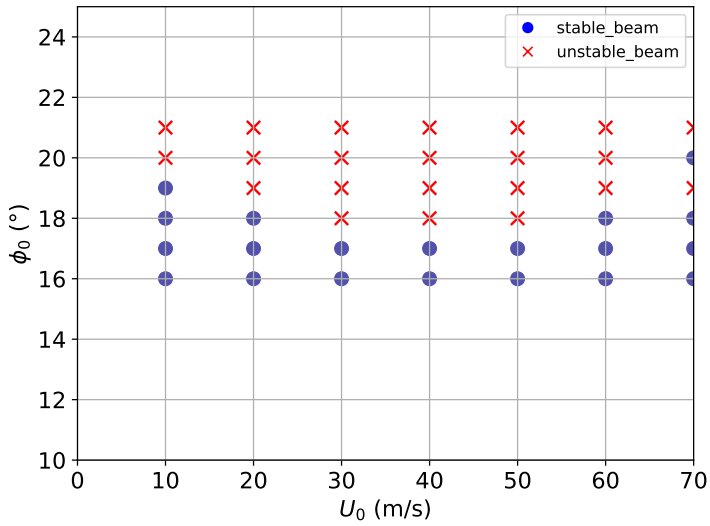

Figure 5.3: $\phi_0 - U_0$ stability map of the blade model coupled with the ONERA dynamic stall model.

Table 5.3: List of the simulations

Type	Conditions (ϕ_0, U_0)
Aeroelastic steady	(15,40), (16,40), (17,40), (18,40), (19,40), (17,50)
Imposed motion	(15,40), (17,40), (18,40), (17,50)
Aeroelastic unsteady	(17,40), (18,40), (17,50)

5.2 Study of the aeroelastic static equilibriums

Before looking at dynamic behaviors, the static aeroelastic equilibriums are analyzed. First, the focus is put on the $\phi_0 = 17°$ and $U_0 = 40$m/s case. Then, the effects of the incidence and the wind speed on the equilibrium state are investigated.

5.2.1 Analysis of the $\phi_0 = 17°$ and $U_0 = 40$m/s case

The IEA15MW blade is clamped at its root and immersed in an uniform wind flow of 40 m/s coming at an angle of incidence of 17°. The aerodynamic loads acting on the blade make it bend. The new state has modified the flow leading to new aerodynamic loads. After 20 iterations alternating between RANS simulations and static beam deformations, the static aeroelastic equilibrium is reached. The deformed state of the beam is reported in Figure 5.4 and the aerodynamic loads are plotted in Figure 5.5.

In Figure 5.4a and 5.4b, the deformation in directions x and y obtained with the CFD is compared to the deformation predicted with the aerodynamic strip theory. Strip theory (FastS) and Strip theory (IEA) refer to different sets of polars. The deformation labeled "Strip theory (IEA)" has been obtained using the polars of the github whereas "Strip theory (FastS)" used polars computed with FastS, see Appendix A. The blade has initially a prebend of 4m in the -Y direction (close to flapwise direction). Overall, the three models give similar flexion deformations. The tip of the blade moves by 7m in the Y direction and 1.2m in the X direction. The displacement in the

X direction is positive because the lift is stronger than the drag. Looking at the distribution of the aerodynamic force coefficient (Figure 5.5a), the small disparities between the deformed states can be explained. The strip theory model using the polar calculated with FastS reproduces well the general shape of the force coefficient distribution. But near the tip, the force coefficients along Y are a little underestimated compared to CFD, leading to a lower displacement in Y near the tip. For the strip theory model with IEA polars, the force coefficients are overestimated from the root to 70% of the blade. As a consequence, the deformed states is slightly overestimated beyond 40% of the blade radius.

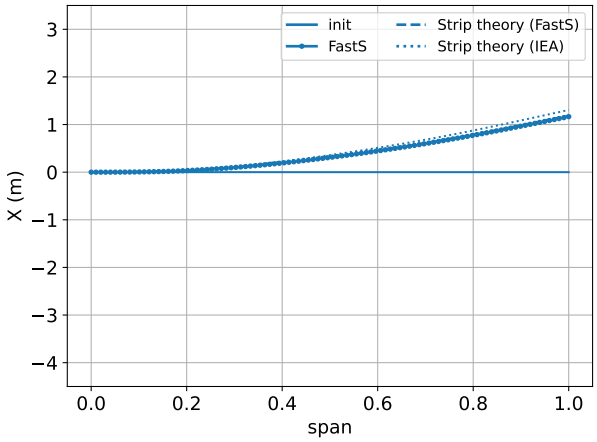

(a) Flexion in X

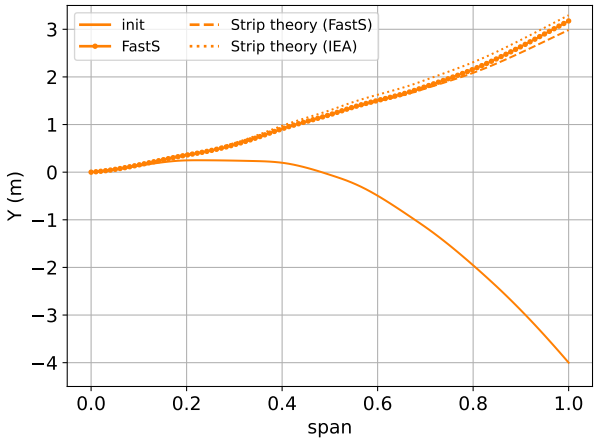

(b) Flexion in Y

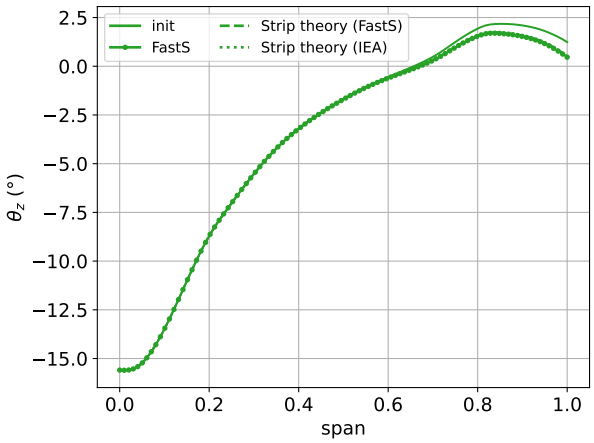

(c) Torsion

Figure 5.4: Deformation of the blade for $\phi_0 = 17°$ and $U_0 = 40$m/s; comparison of high-fidelity FEM-CFD results with predictions using aerodynamic strip theory.

Concerning the torsion plotted in Figure 5.4c, the solid line depicts the initial twist of the blade while the other curves represent the equilibrium twist angle. The difference between the initial twist and the current one is the torsion. It can be noted that all the models are superposed. All indicate that only the outer part rotates. It can be explained by the fact that the torsional stiffness decreases with the span (see Figure A.4).

Figure 5.5 also shows that the load coefficients computed with CFD present spanwise modulation. It is particularly visible on the force coefficient in Y. By looking more precisely at the distribution of wall pressure and streamlines of friction, indicating the flow direction near the wall, it appears that these fluctuations of sectional loads are caused by stall cells.

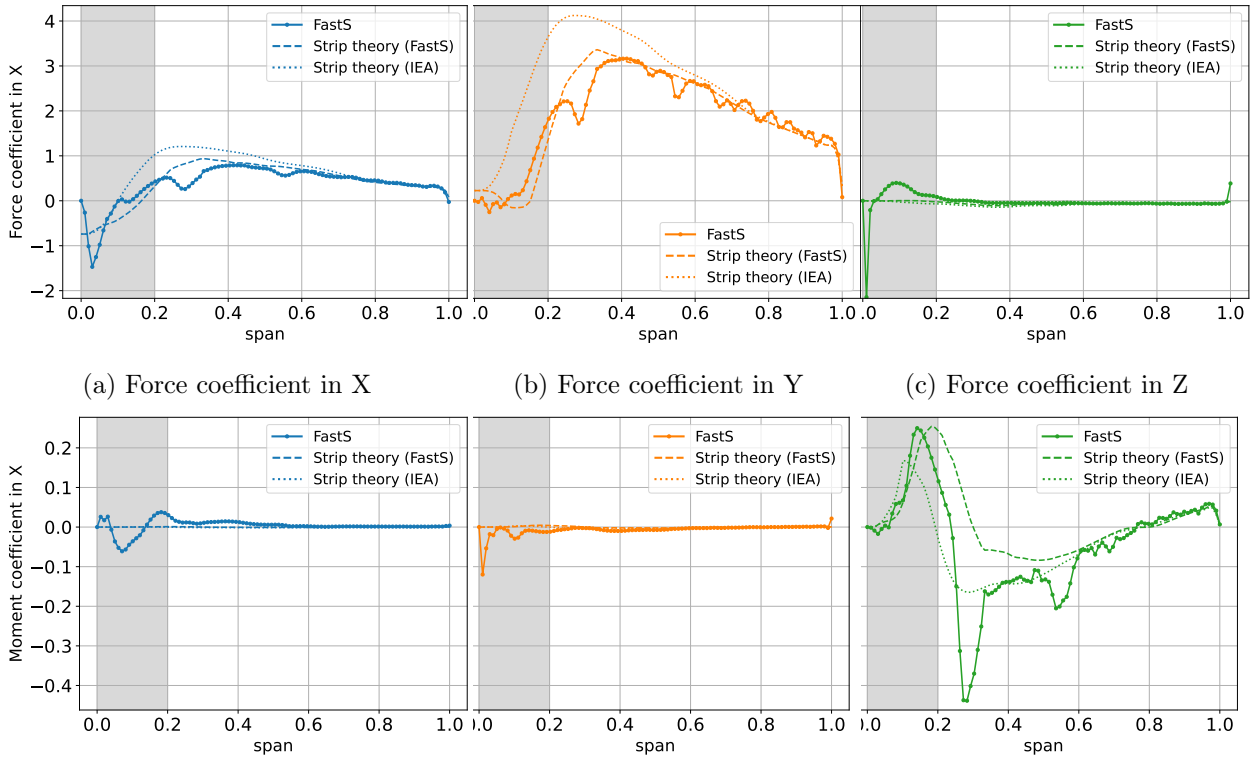

(a) Force coefficient in X (b) Force coefficient in Y (c) Force coefficient in Z

(d) Moment coefficient in X (e) Moment coefficient in Y (f) Moment coefficient in Z

Figure 5.5: Load coefficients on the blade for $\phi_0 = 17°$ and $U_0 = 40\text{m/s}$ (The forces have been nondimensionalized using the factor $\frac{1}{2}\rho c_{\text{eq}} U_0^2$ and the moments using $\frac{1}{2}\rho c_{\text{eq}}^2 U_0^2$). The shaded area corresponds to airfoils close to cylinder and where the loads are not well captured.

Figure 5.6 represents the distribution of pressure coefficient on the suction side of the blade. Only the last 30% of the blade are shown to better see the details. Streamlines of friction have been superposed on the pressure field in order to visualize the flow near the walls. The effect of the tip vortex is visible. The induced downwash velocity decreases locally the angle of attack, attaching the flow near the tip. The aspect ratio of the blade is high, making the influence area of the tip vortex small. Except for the tip, the blade is in a stall state, a separation line is present, indicating recirculation. Moreover, the Cp field and the separation line show spanwise modulation, provoking spanwise fluctuations in the sectional loads as visible in Figure 5.5.

The modulation of the separation line are accompanied by spanwise flow in the detached region, the streamlines curves around the most separated areas. This behavior is typical of stall cells as described by Dell'Orso et al. [36] (Figure 1.30) and others [91, 117]. Ragni and Ferreira [113] also observed similar pressure distribution due to stall cells. However, the stall cells observed here are much less periodic than the ones observed in the literature on simpler geometries. The present blade has varying chord, twist and even airfoil, breaking the periodicity.

In order to explore the 3D flow, an iso-surface of criterion $Q = 50$ colored by the velocity in Z is plotted for the last 30% of the blade in Figure 5.7. The tip vortex is clearly visible. It can also be noticed that other vortices are produced by the stall cells. It is difficult to be sure because the present stall cells are less pronounced but these vortices look like the one observed by Manolesos et al. [92] in Figure 1.31. Furthermore, closer to the stall cells, the flow is organized in two "layer". In the bottom layer, the velocity field in Z suggests that the flow converges toward the center of the cell. Whereas in the top layer, the flow gets away from the center.

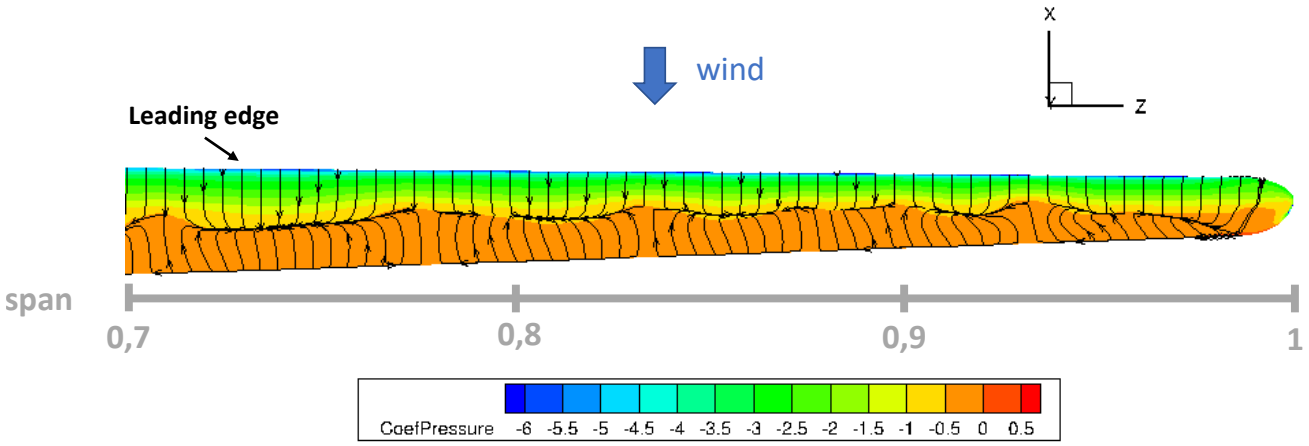

Figure 5.6: Pressure coefficient and streamlines of friction on the suction side of the blade

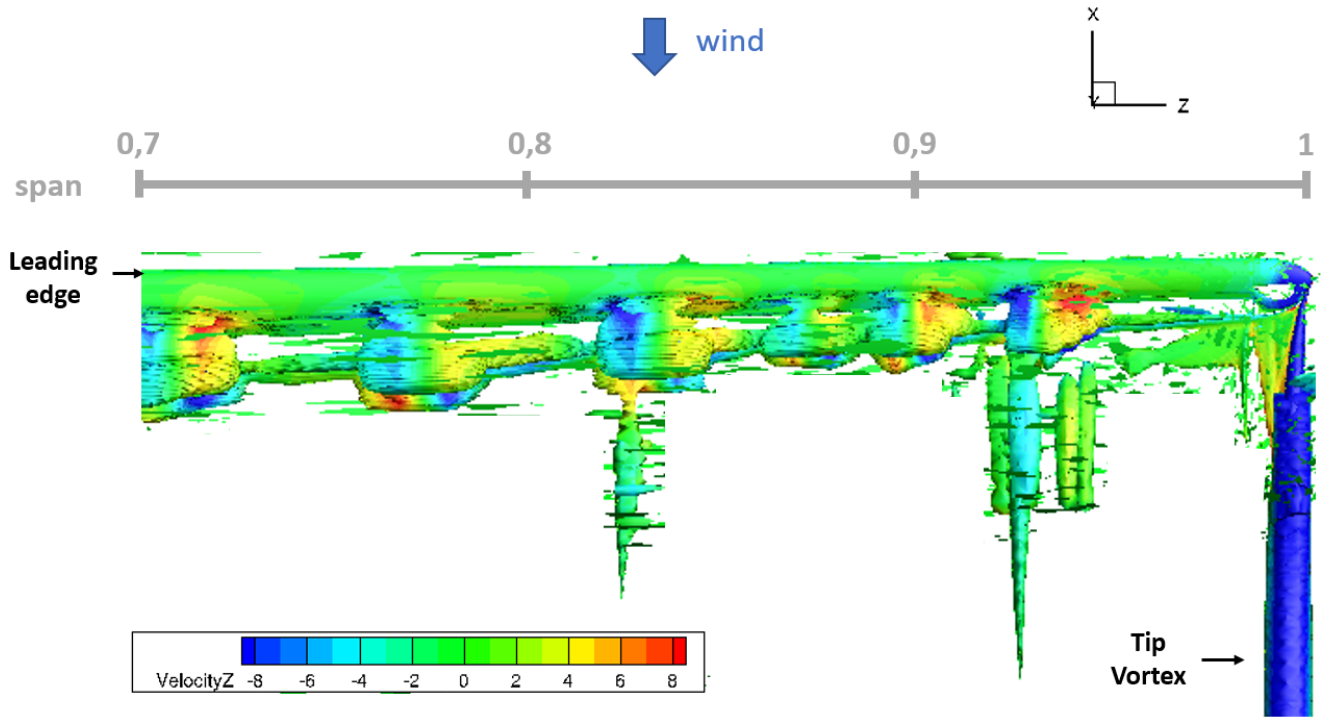

Figure 5.7: Criterion Q equal to 50 colored by the velocity in Z.

5.2.2 Effect of the wind angle of incidence ϕ_0

Now that the $\phi_0 = 17°$ and $U_0 = 40\text{m/s}$ configuration has been analyzed, let compare it to the equilibrium state of configurations with lower and higher wind angles of incidence.

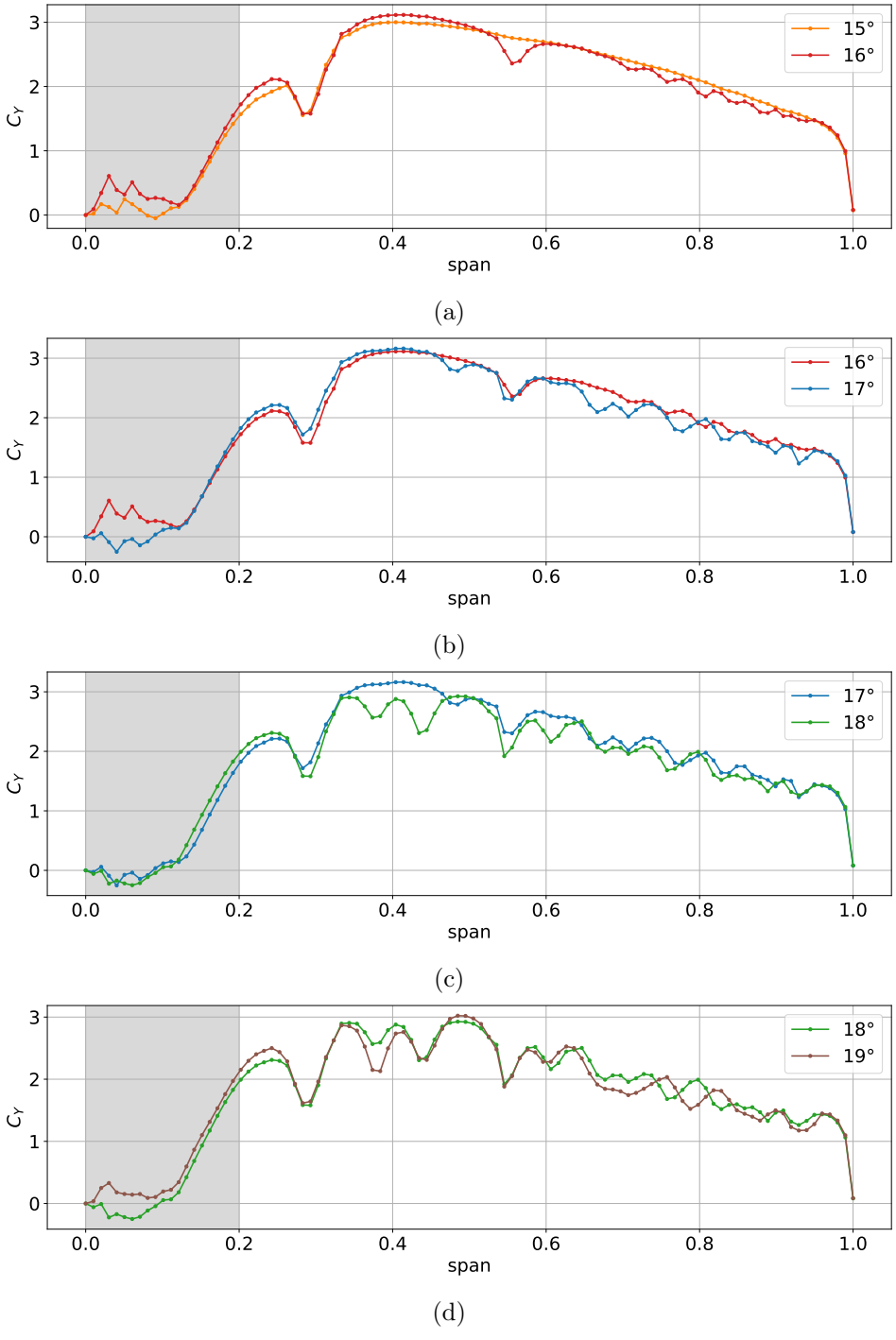

Figure 5.8: Comparison of the load coefficient in the Y axis for different angles of incidence ϕ_0 at $U_0 = 40\text{m/s}$. The forces have been nondimensionalized using the factor $\frac{1}{2}\rho c_{\text{eq}} U_0^2$.

The modification of the wind angle of incidence changes the aerodynamic loads and thus the aeroelastic state. For all the angles of incidence tested, the deformed shape in flexion varies but the torsion almost stays the same. That's why, this part focuses on the aerodynamic loads, and

particularly sectional forces in Y in order to study the evolution of the stall cells. The distributions of sectional forces along Y are compared two by two in Figure 5.8. The pressure fields and the streamlines of friction are also given for the various angles of incidence in Figure 5.9.

For an angle of incidence $\phi_0 = 15°$ (Figure 5.8a), there is no stall cell in the second half of the blade. By looking at Figure 5.9, it appears that the blade is stalled and a separation line is present. This one is smooth and there is no spanwise fluctuation. Even if the flow is separated, stall cells not always appear, as previously reported by Dell'Orso et al. [36]. By increasing a little the angle of incidence to 16°, stall cells appear in the last 30% of the blade and around 55%. By increasing again the angle of incidence to 17°, more stall cells with higher amplitude appear. And at 18°, stall cells even form from around 40% of the blade. The exact positions of the stall cells vary depending on the angle of incidence and are difficult to predict.

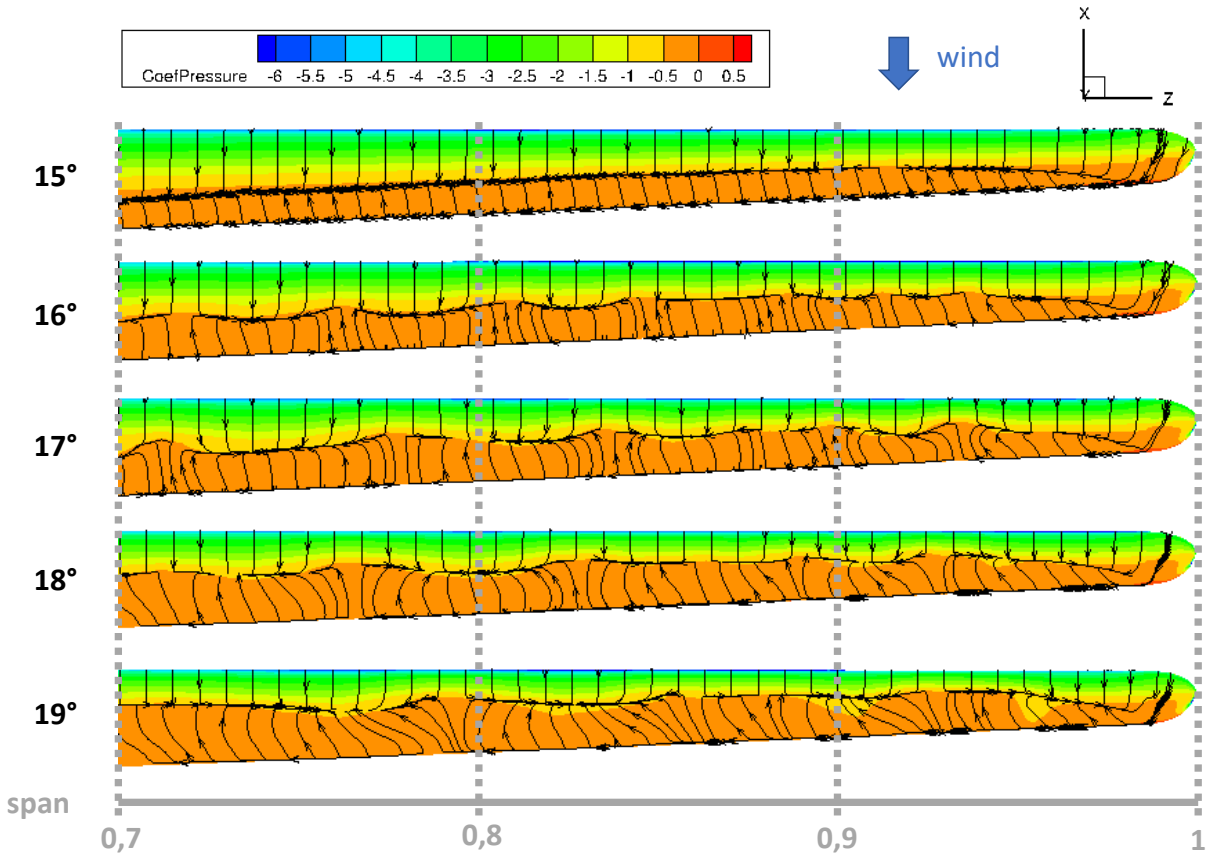

Figure 5.9: Coefficient of pressure on the skin suction side with streamline of friction for several angle of incidence ϕ_0 at $U_0 = 40\text{m/s}$

Figure 5.9 gives some details on the 3D flow behavior. As expected, the separation line moves toward the leading edge as the angle of incidence increases. Moreover, in average, the attached flow is oriented in the wind direction, but in the separated area, 3D spanwise flow is present.

The peaks of Figure 5.8 have been tracked in order to extract the size and amplitude of the stall cells (Figure 5.10). The size of a stall cell is defined here as the distance between two consecutive maxima or two consecutive minima.

$$Size_i = (s_{i+1} - s_{i-1})L_{blade} \tag{5.1}$$

where s_i is the span of the i-th peak.

As the fluctuations of C_Y due to the stall cells oscillate around a non-constant shape, the amplitude is defined by averaging two consecutive peak-to-peak amplitude of the coefficient C_Y.

$$A_i = \frac{|Y_i - Y_{i-1}| + |Y_{i+1} - Y_i|}{2} \frac{4}{Y_{i-1} + 2Y_i + Y_{i+1}} \tag{5.2}$$

where Y_i is the value of C_Y of the i-th peak.

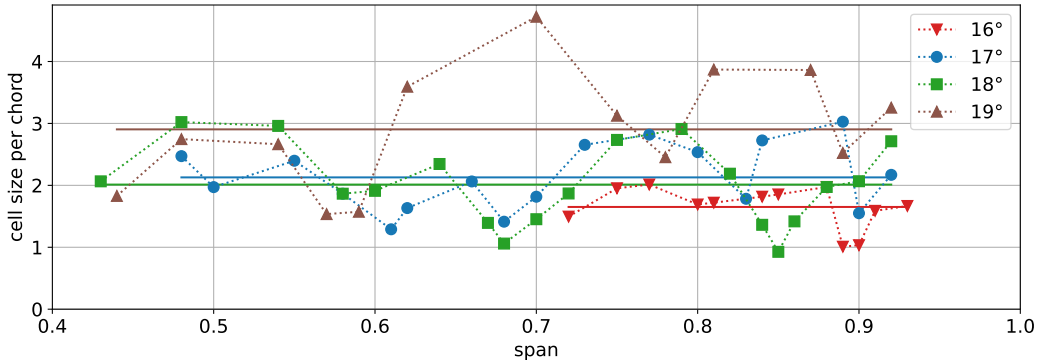

(a) Size of the stall cells divided by the local chord

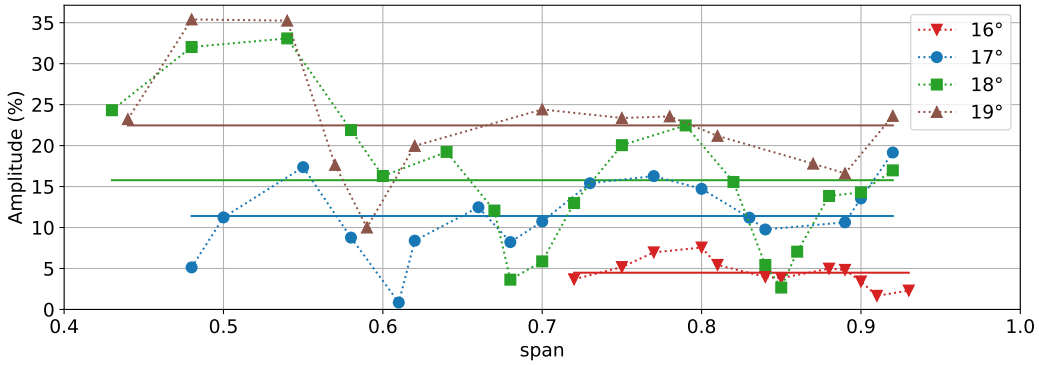

(b) Amplitude of C_Y of the stall cells compared to the local C_Y

Figure 5.10: Comparison of the size and amplitude of the stall cells for different angle of incidence ϕ_0 at $U_0 = 40$m/s. The solid lines indicate the mean value.

In Figure 5.10a, the size of the stall cells has been divided by the local chord so as to make the size of the cells dimensionless. The average size of the stall cells is about 1.5 to 3 local chord. As reported in Manolesos et al. [92], the size of the stall cells increases with the angle of attack, from 1.7 chord for $\phi_0 = 16°$ to 2.9 chord for $\phi_0 = 19°$. This is also coherent with the non-dimensional wavelength of stall cells obtained experimentally by Sarras et al. [120] (Figure 1) on a NACA4412: between 1.4 and 1.8 chord for angles of attack between 12° and 15°, and close to 2.3 chord for an angle of attack of 16°. However, if one can noticed some variations of stall cells size along the span (of the order of 1 to 2 local chord), no clear tendency appears along the blade for each angle of incidence.

The amplitude of the stall cells, measured by the amplitude of C_Y, is represented in Figure 5.10b. It can be noticed that the mean value of the amplitude rises with the angle of incidence. It means that for higher incidence the wall pressure coefficient has larger oscillations. The gap between the pressure coefficient within and outside the stall cell is wider. This observation can be linked to the stability analysis of Sarras et al. [120] (Figure 18), where the maximum growth rate of the unstable modes leading to stall cells are increased with the angle of attack.

5.2.3 Effect of the wind speed U_0

The wind speed can also affect the stall cells. As for the previous section, the force coefficients along Y and the streamlines of friction are compared for $U_0 = 40$ and 50m/s in the Figures 5.11 and 5.12 respectively.

It can first be noted that more stall cells are present for $U_0 = 50$m/s case, especially around the mid span. For the last 30% of the blade, the pattern of the stall cells is similar but with a little shift of the cells location.

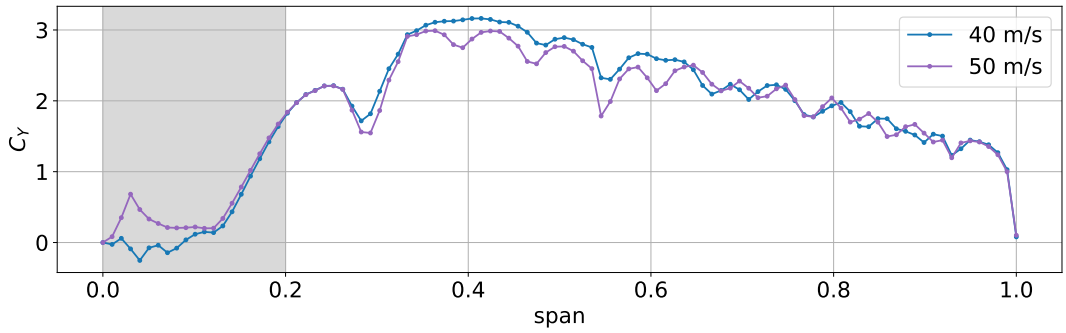

Figure 5.11: Comparison of the load coefficients in the Y axis for $U_0 = 40$m/s and 50m/s. The forces have been nondimensionalized using the factor $\frac{1}{2}\rho c_{\text{eq}} U_0^2$.

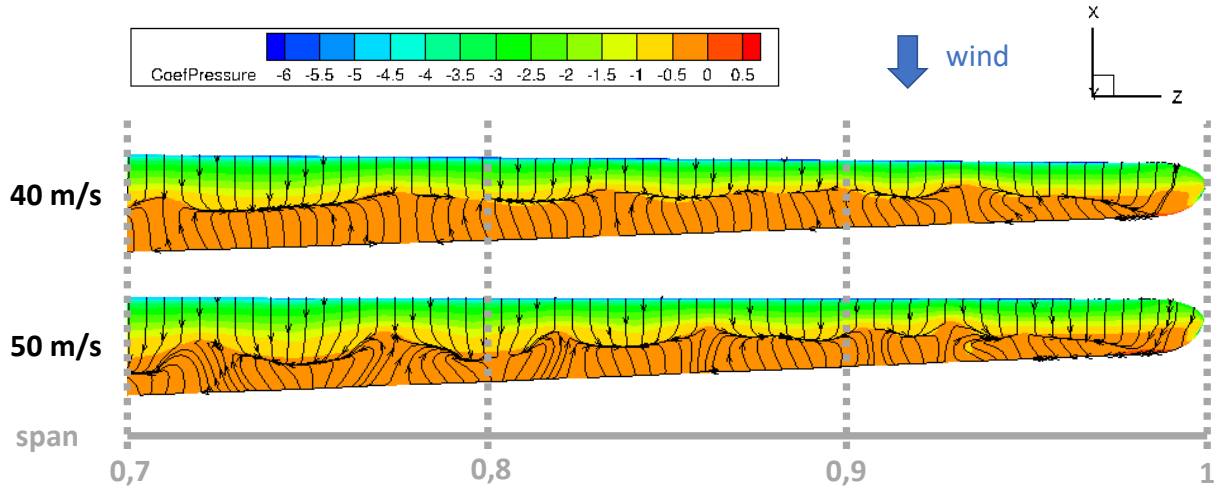

Figure 5.12: Coefficient of pressure on the skin suction side with streamline of friction for two wind speed at $\phi_0 = 17°$

Figure 5.12 also shows that the separation line modulation is larger for $U_0 = 50$m/s. Between the stall cells, the separation line moves toward the trailing edge increasing the wind velocity. It is confirmed looking at the pressure coefficient field since the -0.5 isoline is almost superposed to the separation line. The variation of the separation line and the pressure coefficient are correlated. This impact on the mean location of the separation line can be attributed to a Reynolds number effect. A higher Reynolds number delays the flow separation. Figures 5.11 and 5.12 also show that the Reynolds number impact the stall cells formation and amplification.

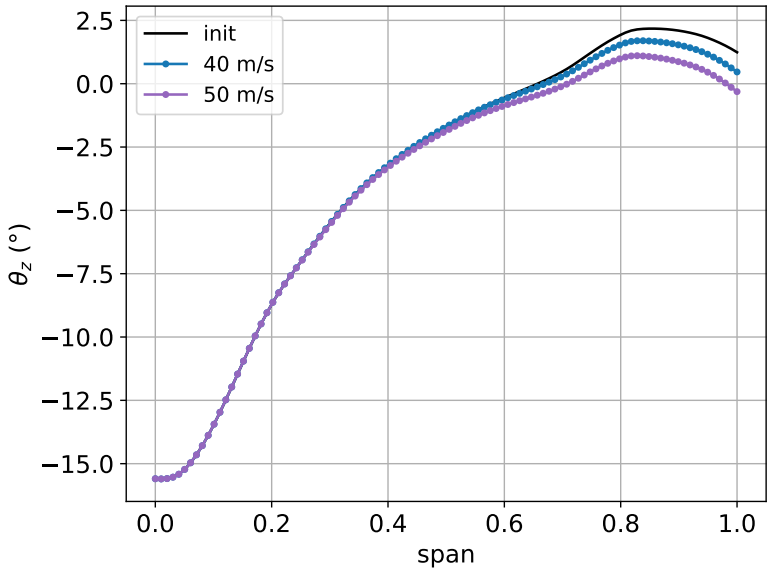

Figure 5.13: Deformation in torsion due to the wind speed U_0.

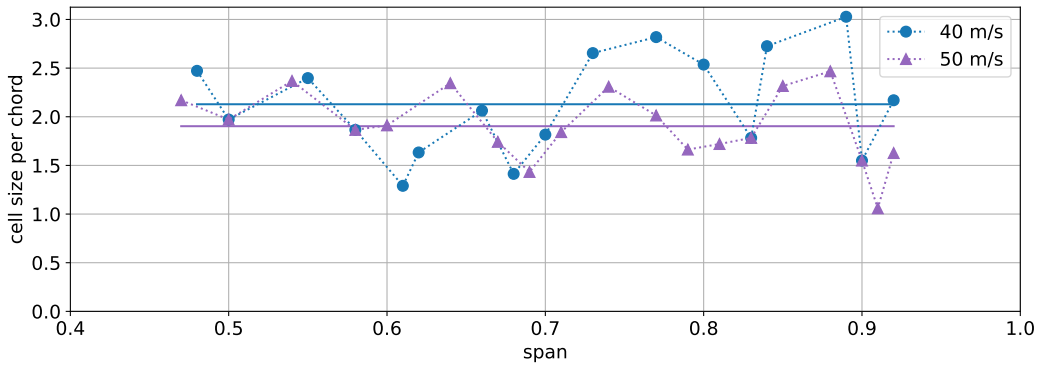

(a) Size of the stall cells divided by the local chord

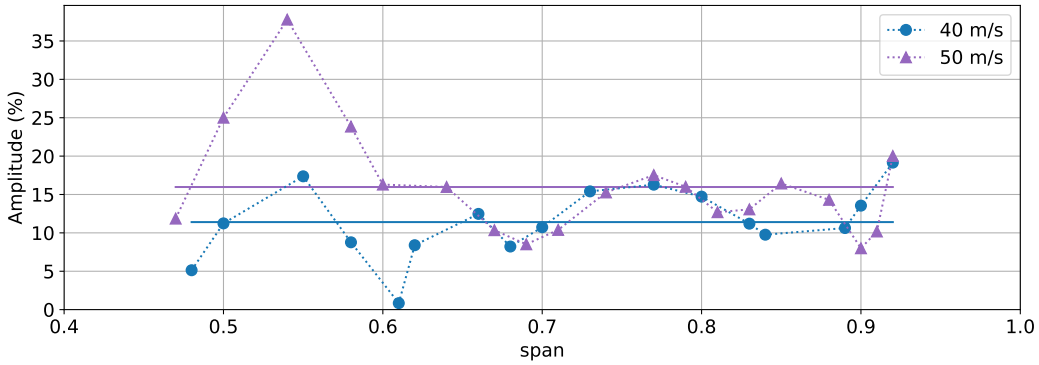

(b) Amplitude of C_Y of the stall cells compared to the local C_Y

Figure 5.14: Comparison of the size and amplitude of the stall cells for for two wind speeds at $\phi_0 = 17°$. The solid lines indicate the mean value.

It should also be noted that for $U_0 = 50$m/s, the aerodynamic loads are stronger, leading to a higher torsional blade deformation (see Figure 5.13) that can potentially have an impact on the

stall cells. Figure 5.13 compares the torsional deformation for $U_0 = 40$m/s and 50m/s. Until 60% of the blade, the angle of torsion of the blade is not significantly modified by the increasing wind speed due to a high torsional rigidity. But after 60%, the stiffness is lower leading to half a degree of difference on the angle of torsion at the tip between 40m/s and 50m/s. The torsional deformation should then be of negligible impact.

To go further on the topology of the stall cells, the cell size per chord and the amplitude of C_Y have been calculated in Figure 5.14 with the same method than the previous section. It appears that the shift in the stall cells positions, increasing the wind speeds, is due to a decrease of the cell size. Figure 5.14a shows that for the last 30% of the blade the average cell size per chord passes from 2.1 for 40m/s to 1.9 for 50m/s. Regarding the amplitude of the cells and even if the separation line showed stronger oscillations, Figure 5.14b shows that the amplitude of C_Y of the stall cell is the same for the last 30%. Around the mid span, the amplitude of the cells is however larger for 50m/s. It reflects the progressive appearance of stall cells in this area.

5.3 Study of the dynamic behavior of the aerodynamic loads induced by an imposed harmonic motion of the blade

In the previous section, the aeroelastic equilibrium states were investigated. The static deformation as well as the aerodynamics have been studied. It has been shown that the stall cells were dependent on the angle of incidence and on the wind speed. One way to assess the dynamic stability of the blade is to to study the motion-induced loads using prescribed oscillations of the blade along a structural mode. It is then possible to calculate the aerodynamic damping. If the aerodynamic damping is negative and higher than the structural damping, there is a risk of instability. In this section, the motion of the blade is imposed and the phase shift between the motion and the loads is analyzed as it drives the aerodynamic damping.

5.3.1 Description of the imposed motions

For all the cases, the structural modes are computed around the aeroelastic equilibrium state. Then, the blade is forced to move along the first structural mode corresponding to the first flapwise flexion mode. This mode has been chosen because it appeared to be the most unstable mode during the linear analysis of chapter 4 (§4.2) for the range of incidence under study. An illustration of the mode is given in Figure 5.15.

The frequency of the oscillations is given by the eigenvalue of the linear analysis. The exact temporal evolution of the imposed motion is given in Figure 5.16. It is a sinusoid of the first natural frequency that has been smoothed for the first period in order to have the displacement, velocity and acceleration equal to zero at the origin of time. A simple sinusoid with a non-zero velocity at the beginning would has caused a discontinuity of velocity compared to the equilibrium state.

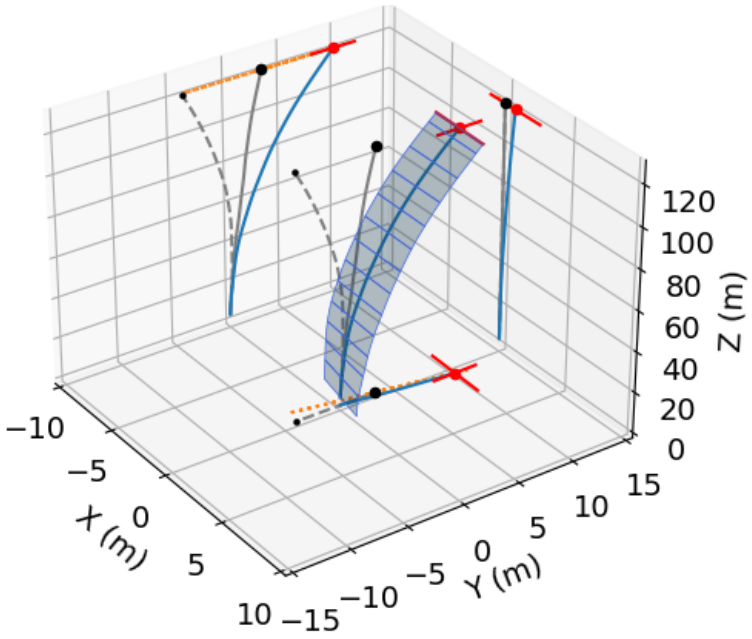

Figure 5.15: Illustration of the 1st flexion mode in flapwise around the aeroelastic equilibrium state (grey solid line) at $U_0 = 40\,\mathrm{m/s}$ and $\phi_0 = 17°$. The dashed line represents the initial configuration of the blade. The blade is projected on the three plans.

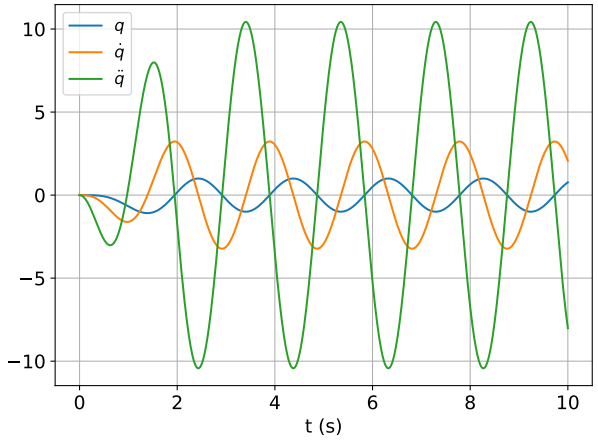

Figure 5.16: Modal coordinate of the imposed motion

The equations of the modal coordinate is the following.

$$q(t) = \begin{cases} 0, & t < 0, \\ q_0 \dfrac{1}{n}\left(\dfrac{t}{T}\sin(\omega t) + \dfrac{1}{\pi}\cos(\omega t) - \dfrac{1}{\pi}\right), & 0 \leq t < nT, \\ q_0 \sin(\omega t), & t \geq nT, \end{cases}$$

$$\dot{q}(t) = \begin{cases} 0, & t < 0, \\ -q_0 \dfrac{1}{nT} \left(\sin(\omega t) - t\omega \cos(\omega t)\right), & 0 \leq t < nT, \\ q_0 \omega \cos(\omega t), & t \geq nT, \end{cases}$$

$$\ddot{q}(t) = \begin{cases} 0, & t < 0, \\ -q_0 \omega^2 \sin(\omega t) \dfrac{t}{nT}, & 0 \leq t < nT, \\ -q_0 \omega^2 \sin(\omega t), & t \geq nT. \end{cases}$$

where q_0 is the amplitude, T is the period and ω is the pulsation of the first structural mode. Here, we have chosen $n = 1$.

The amplitude of the imposed motion is chosen so that the angle of attack around 80% of the blade has an amplitude of oscillation of 1°. This way, the dynamic stall loops are small to get closer to a linear analysis while being sufficiently large to discern the modification of the flow due to the motion.

5.3.2 Analysis of the $\phi_0 = 17°$ and $U_0 = 40$m/s case

First, let us focus again on the $\phi_0 = 17°$ and $U_0 = 40$m/s case (section 5.2.1) but this time with an imposed motion of the flapwise mode, which correspond to a reduced velocity $\mathcal{U}_R = 5.3$ or equivalently to a reduced frequency $k = \frac{1}{2\mathcal{U}_R} = 0.094$. In order to limit the impact of the transitional states, the first two periods of oscillations are ignored in the analysis. The mean sectional loads together with their minimal and maximal values are represented in Figure 5.17.

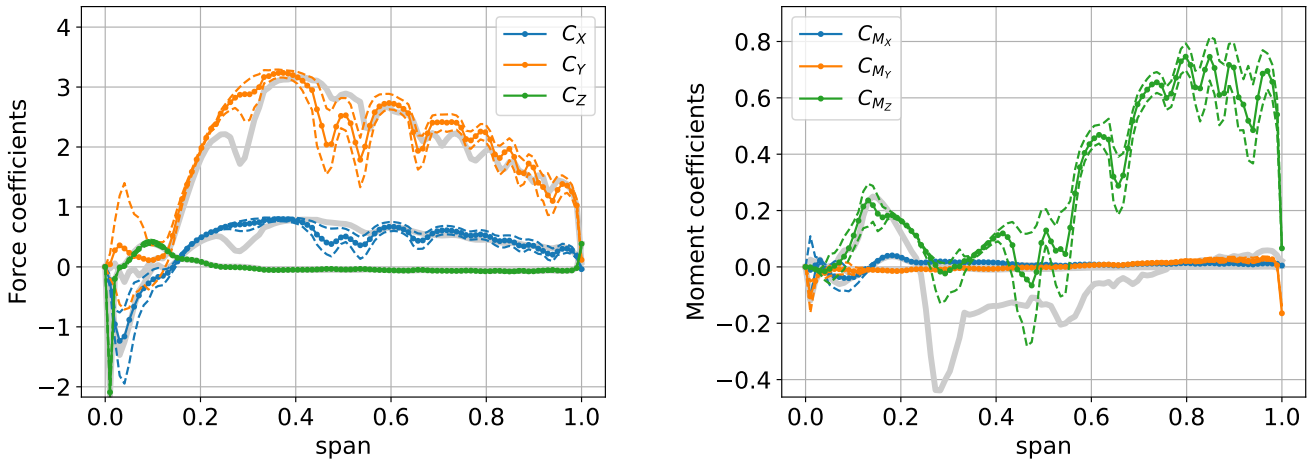

(a) Forces

(b) Moments

Figure 5.17: Load coefficients on the blade for $\phi_0 = 17°$ and $U_0 = 40$m/s. The solid lines are the mean loads while the dashed lines indicate the minimal and maximal values. The forces have been nondimensionalized using the factor $\frac{1}{2}\rho c_{\text{eq}} U_0^2$ and the moments using $\frac{1}{2}\rho c_{\text{eq}}^2 U_0^2$. Figure 5.5 is reported in grey.

By comparing the Figure 5.17 with the Figure 5.5, it can be noticed that the mean load coefficients obtained with the URANS simulations in imposed motion slightly differs from the one computed with the stationary RANS simulation. The amplitude of the stall cells also changed a

little and they have slightly moved (Figure 5.17a). This difference is due to the non linear nature of the dynamic stall. Further studies would be needed to assess whether a RANS simulation is appropriate to capture stall cells signatures.

The loading variation around its mean value is indicated by the minimal and maximal values reached during the cycles of imposed motion. The variations are small because the amplitude of the forced motion is also limited. The peaks of the envelope coincide with the peaks of the mean loads. It means that the stall cells barely move although the angle of attack varies. Knowing that the position of the stall cells should depend on the angle of incidence, it can be deduced that, at the imposed reduced frequency $k = 0.094$, the stall cells doesn't instantaneously adapt to the angle of attack. The coarse mesh in the spanwise direction could also be responsible for that.

Phase shift of the aerodynamic loads Let us now focus on the phase shift $\phi_{\dot{q}}$ of the aerodynamic loads with the blade velocity. It is defined such that the load coefficient of the imposed frequency is $C_Y \propto \cos(\omega t - \phi_{\dot{q}})$ when $\dot{q} \propto \cos(\omega t)$. A phase shift of zero means that the loads are in phase with the flapwise velocity while $\phi_{\dot{q}} = \pi/2$ means that the loads are in phase with the flapwise displacement. A load with a small positive phase shift $\delta\phi_{\dot{q}}$ is delayed compared to the flapwise velocity. This phase shift is an important feature since it is related to the aerodynamic damping. From Equation C.15, it can be shown (Appendix C) that the calculation of the work of the aerodynamic loads leads to an aerodynamic damping coefficient ξ^{aero} that is proportional to $-\cos(\phi_{\dot{q}})$. It can be deduced that a phase shift $\phi_{\dot{q}}$ between -90° and 90° induces a negative aerodynamic damping.

To estimate this phase shift, the natural method would have been to do a fast Fourier transform of the sectional loads but the signals are too short to use it. Thus, the method used here is based on cross-correlation with the local flapwise velocity, which is detailed in Appendix D. For each node of the beam, the sectional forces along Y are first filtered to extract only the signal at the imposed frequency. Then, it is cross-correlated with the flapwise velocity. The maximum of correlation gives the time lag that is expressed in term of phase shift. Note that a positive phase shift is here a phase delay, meaning that a maximum aerodynamic load will be delayed (with the phase angle $\phi_{\dot{q}}$) with a maximum flapwise velocity. This procedure is applied for the aerodynamic loads obtained with both the CFD model and the ONERA dynamic stall model. The calculated phase shifts are reported in Figure 5.18. Note that, as in stall condition the lift slope is negative the quasi-steady aerodynamic model is almost proportional to the flapwise velocity, which gives a phase shift at 0 for the quasi-steady aerodynamic model (also reported in Figure 5.18). The analysis is limited to the last 40% of the blade because the methodology is less robust closer to the root where the forces obtained with CFD are more chaotic.

Regarding the CFD results, the phases shift are between 120° and 180° along the blade, which means that the aerodynamic damping stays positive. On average, there is a slight decreasing tendency with the span until 95% of the blade length, indicating that the chord has an impact on the phase shift. Indeed, it is known that the dynamic stall loops depend on the reduced frequency. In the last 5% of the blade, the shift rises due to the influence of the tip vortex. A modulation of the phase shift can also be observed along the span. The shape of the sectional forces along Y is reported in dotted line in Figure 5.18) in order to locate the stall cells. It can be noted that within the stall cells, where the flow is more separated, the phase shift is lower, close to 120°, which produce a lower aerodynamic damping. Between the stall cells, where the flow is more attached, the phase shift is locally higher, close to 180°, which produce a higher aerodynamic damping.

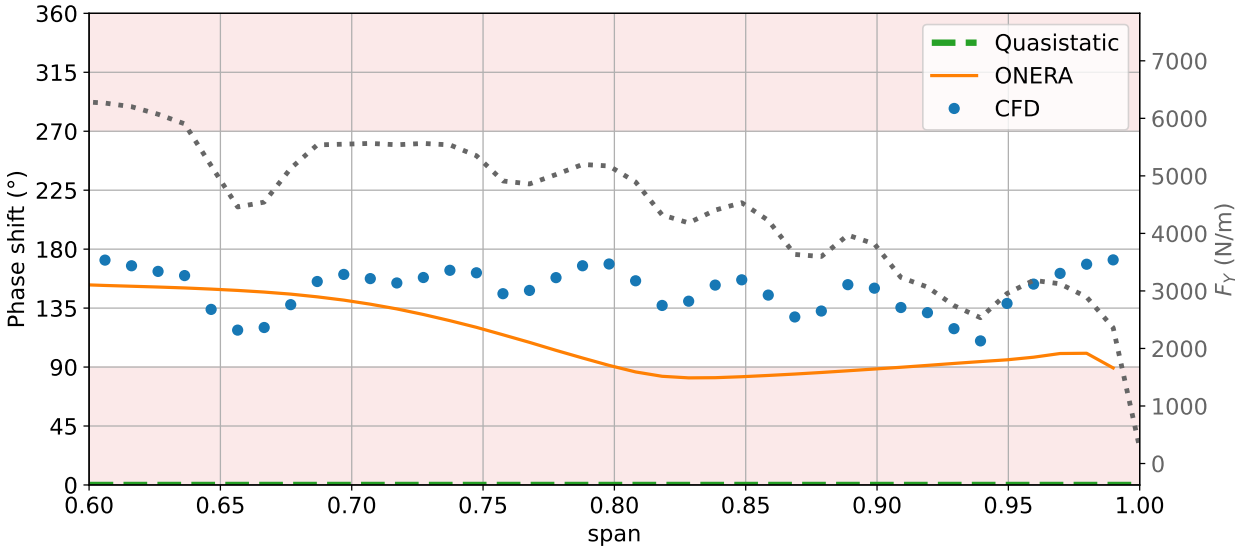

Figure 5.18: Phase shift between the sectional forces on Y and the flapwise velocity for the $\phi_0 = 17°$ and $U_0 = 40$m/s case. The red areas represents the areas of negative aerodynamic damping. The shape of F_Y is reported in dotted line.

For comparison, the phase shift obtained with the ONERA dynamic stall model is reported in Figure 5.18. Since the ONERA model is a sectional model, the variations due to the stall cells are not modeled. Still, a spanwise evolution is present due to the varying chord, twist and airfoil along the blade. The main effect comes from the augmentation of the reduced velocity due to the reduction of the chord with the span. The phase shift produced by the ONERA model is in accordance with the CFD results up to 70% of the span. Beyond that it decreases and crosses 90° at 80% which means that beyond that point and up to 90% of the span, the ONERA model produces a positive transfer of energy to the structure (i.e. a negative aerodynamic damping effect). Beyond 90% the phase shift remains slightly over 90°. According to those results, one can conclude that the overall aerodynamic damping predicted with the CFD is higher than the one produced with the ONERA dynamic stall model.

The flow behavior The aerodynamic loads analyzed before are the product of the flow behavior and especially the dynamic behavior of the stall cells. To observe their evolution, the pressure coefficient field along with the streamlines of friction, are reported over one period of oscillation in Figure 5.19. The period chosen begins at 8.2s when the blade displacement is at its maximum with no velocity. During half a period, the velocity along Y is negative inducing a higher apparent angle of attack. After that, the last two snapshots are during the upstroke, meaning that the instantaneous apparent angle of attack is lower. As deduced from the sectional loads, the stall cells stay at the same positions over the cycle. However, their shape changes. At T/5, the separation line has smooth spanwise oscillations but at 4T/5, the flow between the cells is more attached causing the formation of the vortices observed by Dell'Orso et al. [36] and Manolesos et al. [92] (see Figures 1.30 and 1.31). The center of the stall cells does not seem to move upstream or downstream whereas the separation line between two stall cells oscillates back and forth, stretching the cell and provoking the vortices. Between the cells, the separation line is closer to the leading edge when the angle of attack is high (T/5 and 2T/5) whereas it is closer to the trailing edge when the angle of attack is low (3T/5 and 4T/5). According to the previous section the loads are not in phase with the motion. It is however difficult to appreciate that with only the five snapshots

reported in Figure 5.19.

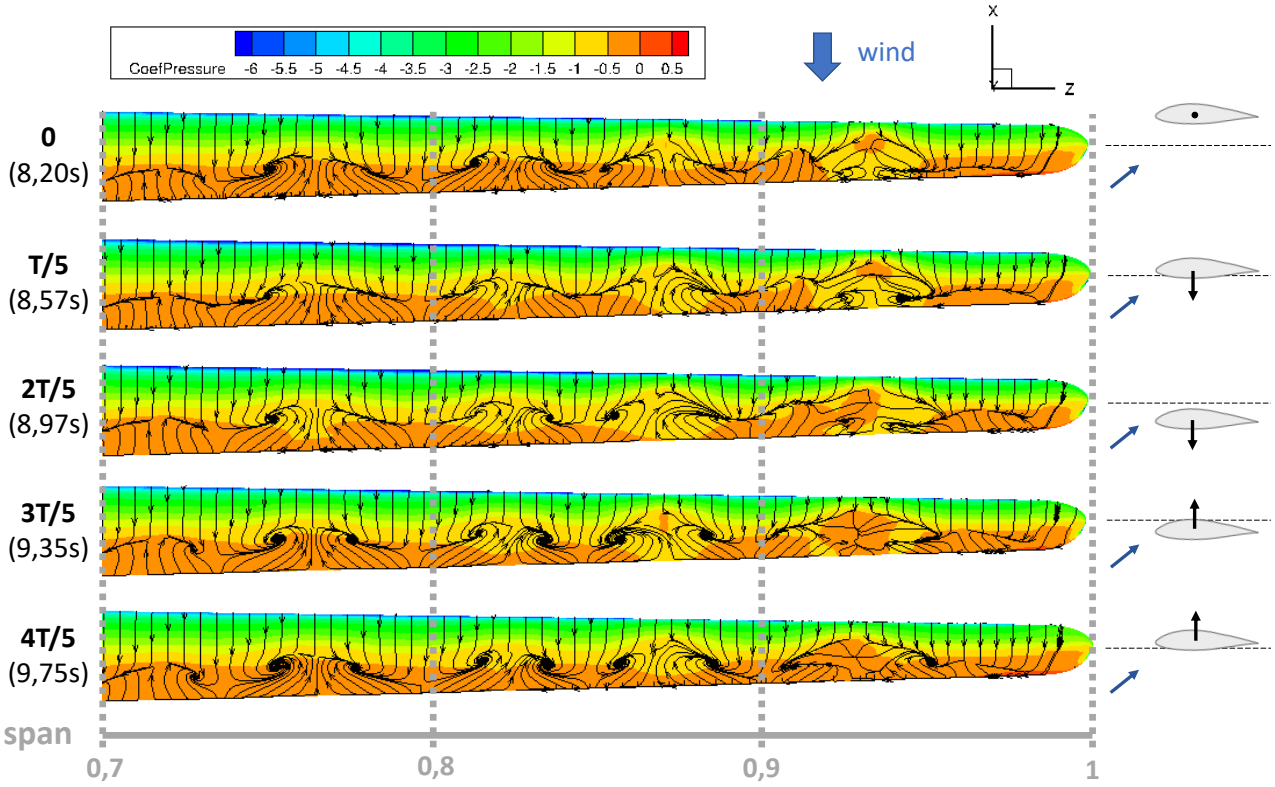

Figure 5.19: Pressure coefficient on the suction side along with streamline of friction for a wind angle of incidence $\phi_0 = 17°$ at $U_0 = 40$m/s over one period of flapwise oscillation. Some schemes indicate the motion of the blade.

The dynamic stall loops Another way to observe the evolution of the loads is to look directly at the dynamic stall loops as a function of the effective angle of attack. Two dynamic stall loops, one within a stall cell and the other one outside, are represented in Figure 5.20. Static polars have been added to indicate the stall angle and the values of the static loads. Their construction based on the static aeroelastic simulations is explained in Appendix A.

Both dynamic stall loops obtained with *FastS* have a positive mean slope like the one computed by Skrzypinski et al. [126] (Figure 6) with an extruded airfoil at the reduced frequency $k = 0.079$. As explained in chapter 4, it indicates that the aerodynamic damping is positive. At 80% span location (i.e. out of a stall cell) the phase shift with the local flapwise velocity is close to 170° which means that the aerodynamic force C_Y is almost proportional to the opposite of the flapwise velocity and thus to the effective angle of attack. The associated loop is then flat with a positive mean slope (i.e. positive aerodynamic damping). Within the stall cells (i.e. at 82% span location) the phase shift with the local flapwise velocity of the section is lower (close to 135°) producing a clockwise thicker loop and a smaller aerodynamic damping. By comparison, the ONERA dynamic stall loops are almost identical for both sections with a slope close to the horizontal because of a lower phase shift, close to 90° (Figure 5.18), indicating a very low aerodynamic damping. Moreover, It can be noticed that the two loops calculated with *FastS* have different mean value because of the stall cells, as seen in Figure 5.17. These mean values are higher than the static polars because the polars have been computed from stationary simulations, it has the same origin that the gap between Figure 5.5 and Figure 5.17. Regarding the ONERA dynamic stall model, it is based on

the IEA polars presented in Appendix A, making the ONERA loops at a lower position.

Let us also note that the higher frequency oscillations observed in the CFD loops comes from the vibration of the separated wake.

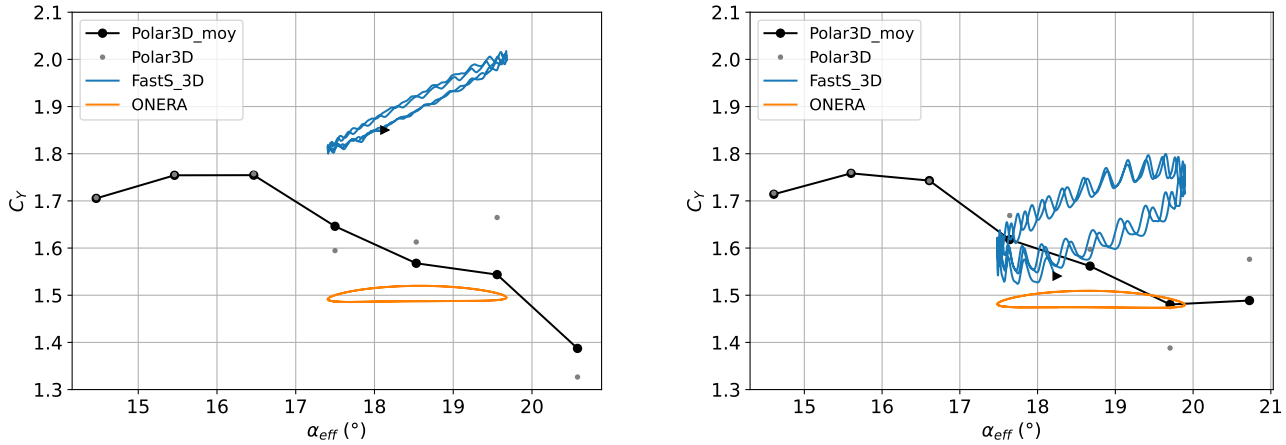

(a) span = 0.80 (b) span = 0.82

Figure 5.20: Dynamic stall loops as a function of the effective angle of attack between two stall cells (a) and within a stall cell (b) for a reduced frequency $k = 0.094$. All the loops are clockwise. The static polars in black are explained in the Appendix A.

The motion-induced pressure loading It is of interest to analyze the motion-induced pressure loading in order to better understand the motion-induced fluid mechanism and associated phase delay along the blade sections.

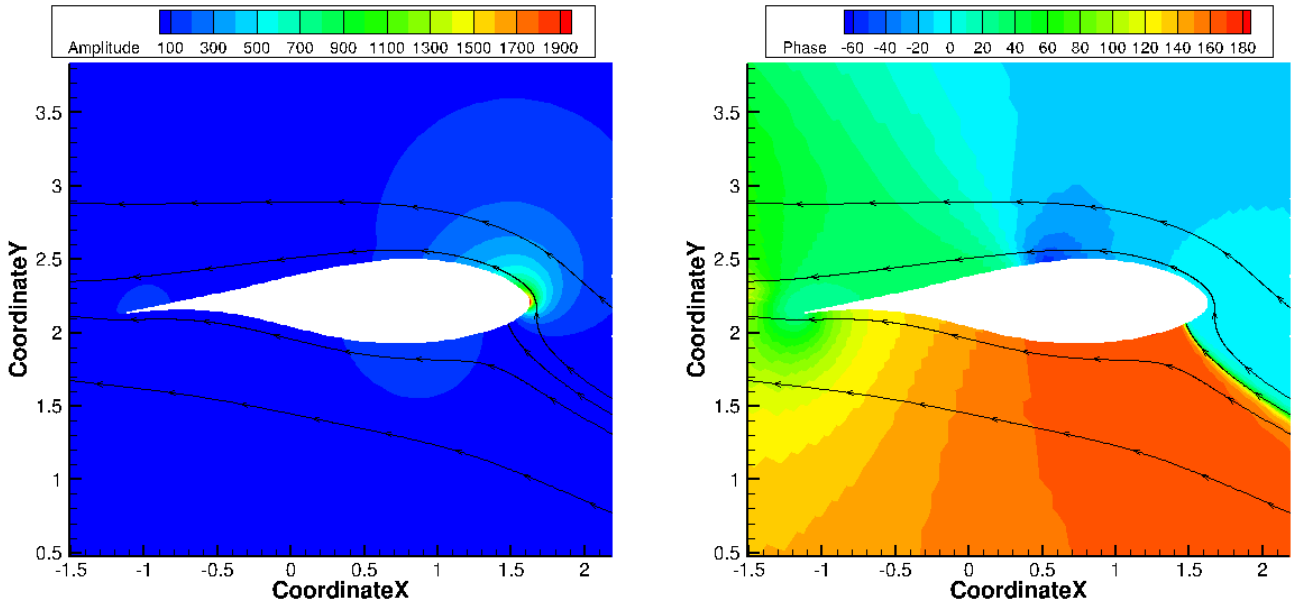

(a) Pressure amplitude in Pa (b) Phase field (°)

Figure 5.21: Amplitude and phase delay (with the flapwise velocity) of the motion-induced pressure for the blade section located at 80% of the span.

In the case of a flapwise motion, it is like the airfoils have an oscillating motion around the Y axis. This oscillating motion induces permanent adaptation of the flow. As a consequence, the neighbor pressure also follows an oscillating behavior. The amplitude and phase shift of these variations of pressure are reported for the whole field around the 80% section in the Figure 5.21. As for the force, the phase shift is here defined as the phase delay between the unsteady pressure and the flapwise velocity. As the effective angle of attack is almost proportional to the opposite of the flapwise velocity, the phase delay with the effective angle of attack can be defined as $\phi_\alpha = \phi_{\dot{q}} + 180°$. A phase shift $\phi_{\dot{q}} = 0°$ (i.e. $\phi_\alpha = 180°$) means that in the suction side, where the pressure coefficient decreases with the angle of attack, the flow adapts instantaneously to the effective angle of attack: an increase of the effective angle of attack produces an instantaneous decrease of the pressure at the suction side, out of the stalled area. In the pressure side, where the pressure coefficient globally increases with the angle of attack, a condition of quasi-steady behavior would rather be a phase shift $\phi_{\dot{y}} = 180°$ (i.e. $\phi_\alpha = 0°$).

In Figure 5.21a, it can be seen that the main variations of pressure are concentrated around the leading edge and in the first quarter chord of the suction side. It means that the main source of the phase shift of the loads is the phase shift of the pressure in this area. The pressure phase shift distribution is given in Figure 5.21b. Around the leading edge, the phase shift is close to zero, this means that when the effective angle of attack increases, the pressure decreases almost instantaneously. By going downstream in the suction side, the phase shift gradually decreases down to $-60°$ which means that the motion-induced pressure is in advance compared to the flapwise velocity. It can only happen if the acceleration of the motion plays a role as the acceleration is in advance compared to the angle of attack. In our case, it is the combination of the almost instantaneous change at the leading edge and the little advance in this area that gives the phase shift of the loads. Further downstream on the suction side, the pressure phase shift with the local flapwise velocity suddenly increases and becomes positive. This sudden rise of phase is somewhat linked to the degree of separation of the flow as it will be seen later. Finally, it can be noticed that passing the stagnation point provokes a 180° phase shift. On the pressure side, the pressure increases in phase with the rise of the angle of attack.

Let's now compare the pressure dynamics of two sections within and outside the stall cell. As seen in Figure 5.22 the main oscillations of pressure are concentrated in the first 30% of the chord in the suction side at 80% of the span (i.e. between two stall cells) and extend to 45% of the chord at 82% of the span (i.e. in a stall cell). In Figure 5.23, the wall pressure coefficient phase shift distribution along the chord are plotted for the two sections. For both sections, the phase shift at the leading edge is close to zero and decreases in the beginning of the suction side. The phase shift of the resulting force is mainly influenced by this part where the amplitude is high. The phase jump at the stagnation point can also be found at the same position for both sections. However, the rise of phase in the suction side is initiated at two different locations, around 40% chord for the 0.80 span section (i.e. between two stall cells) and around 45% chord for the 0.82 span section (i.e. within the stall cells). The rise of phase is much stiffer for the 0.82 span section for which the flow is more separated than the 0.8 span section.

Finally, the phase shift of the pressure can be linked to the phase shift of the sectional loads presented in Figure 5.18. As the sectional forces in Y are mainly due to the depression in the suction side, the phase shift of F_Y in the Figure 5.18 has been reported with a black line in Figure 5.23 with a subtraction of 180° in order to be compared with the phase shift of the pressure. It can be noticed that the integrated phase shift obtained from F_Y corresponds to the phase shift of the pressure on the first half of the suction side. It means that the shape of the dynamic stall loops (Figure 5.20) are mainly the produced by motion-induced fluid mechanisms on this first half of the suction side.

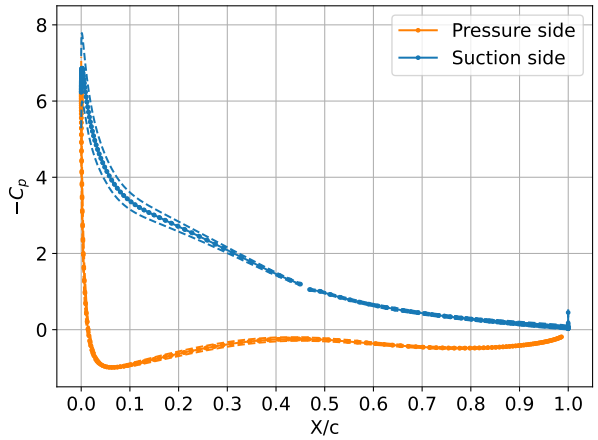

(a) span = 0.80

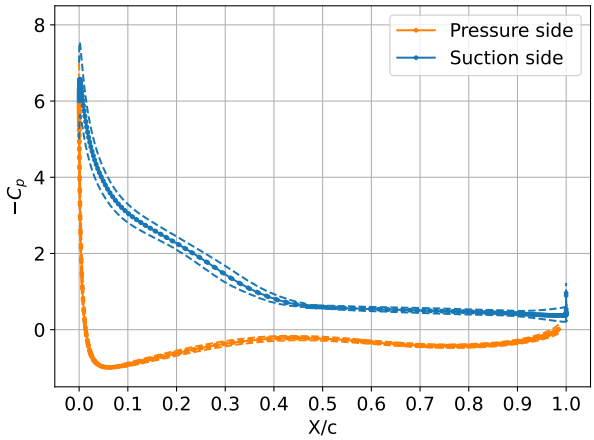

(b) span = 0.82

Figure 5.22: Variations of the pressure coefficient around its mean value induced by the imposed motion, for the two sections at 0.80 span (outside a stall cell) and at 0.82 span (within a stall cell). The solid lines are the mean loads while the dashed lines indicate the minimal and maximal values.

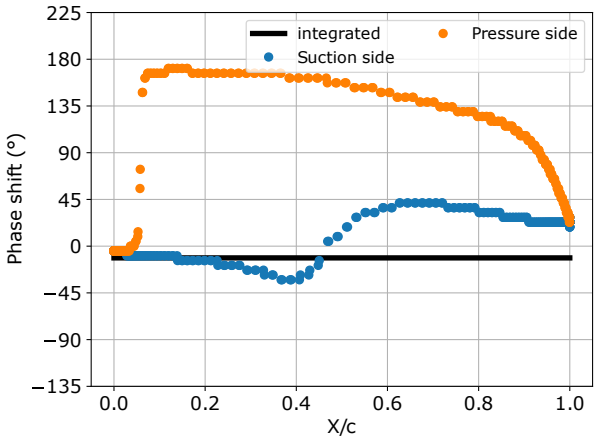

(a) span = 0.80

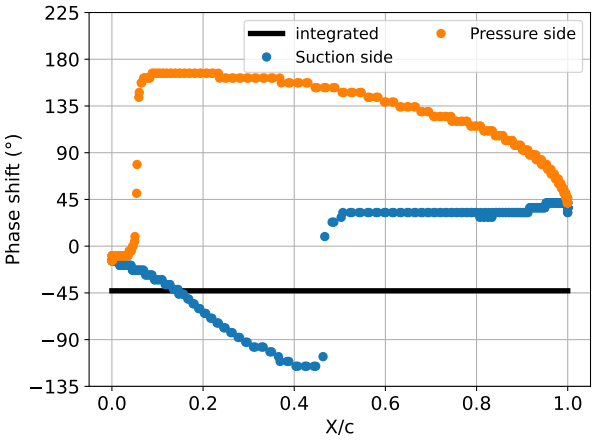

(b) span = 0.82

Figure 5.23: Phase shift of the pressure coefficient for the two sections at 0.80 span (outside a stall cell) and at 0.82 span (within a stall cell) span. The phase shift resulting from the integration of the pressure is added for comparison.

5.3.3 Effect of the incidence ϕ_0

The $\phi_0 = 17°$ and $U_0 = 40$m/s case has been studied in detail to understand the motion-induced fluid mechanism and motion-induced loadings for the blade submitted to a forced flapwise harmonic motion with low amplitude at a reduced frequency $k = 0.094$. Same imposed motion simulations have been conducted with other wind angles of incidence. The idea is to highlight the effect of the angle of incidence on the phase shift along the blade and its consequences on the aerodynamic damping and stiffness.

Impact on the phase shift

As for the $\phi_0 = 17°$ and $U_0 = 40$m/s case, the phase shift is calculated using the cross correlation between the filtered sectional forces on Y and the flapwise velocity. Results are plotted in Figure 5.24 for three wind angles of incidence. Phase shift computed with the ONERA dynamic stall model are also reported in Figure 5.24.

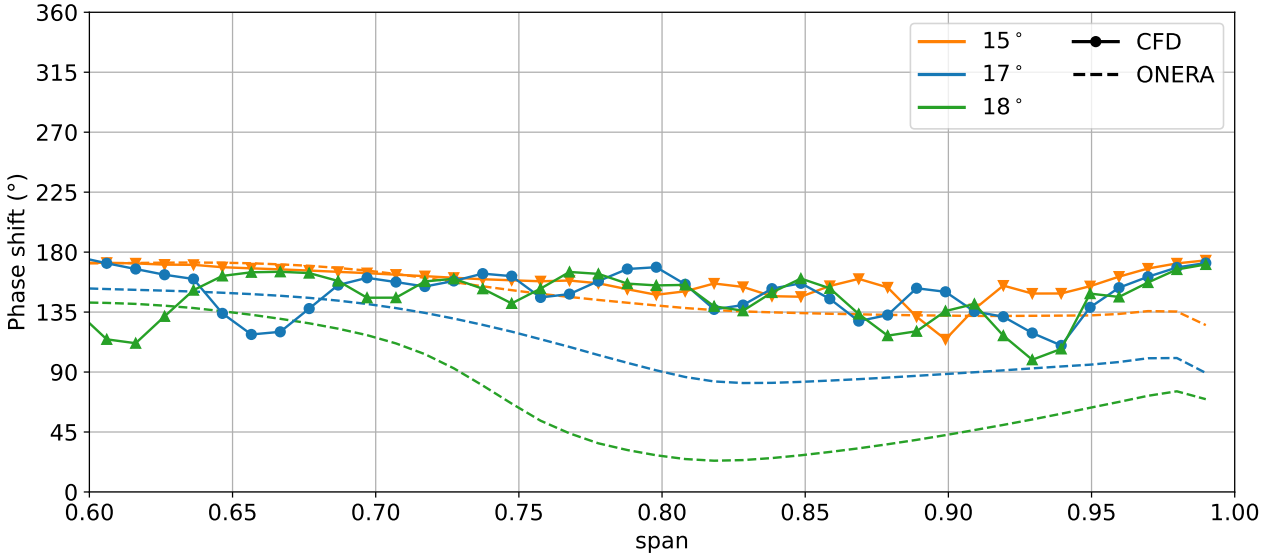

Figure 5.24: Phase shift between the sectional forces on Y and the flapwise velocity for the different wind angle of incidence ϕ_0 at $U_0 = 40$m/s.

With the ONERA dynamic stall, the phase shift globally decreases with the wind angle of incidence. At 80% of the span it goes from almost 140° for a wind angle of attack of 15° down to 30° for a wind angle of attack of 18°. Such a behavior is not observed with the URANS model. If the stall cells have extended along the blade and are more intense increasing the angle of attack, the mean evolution of the phase shift is similar for the three wind angles of attack. The phase shift obtained with the CFD and the ONERA dynamic stall model matches for 15° but not for higher incidences.

Impact on the aerodynamic damping

In order to assess if the blade risks an aeroelastic instability, the global aerodynamic damping ξ^{aero} of the mode needs to be computed. It is based on how much energy is transferred to the structure over a cycle of oscillation. If the forces are in phase with the velocity then the aerodynamic damping will be negative (see Appendix C). Another quantity of interest for an aeroelastic system is the added aerodynamic stiffness κ^{aero}. It can be useful to assess a risk of static aeroelastic instability and/or to estimate the evolution of the aeroelastic frequency using Equation C.9: $\frac{\omega^{AEL}}{\omega_0} = \sqrt{1 + \frac{\kappa^{aero}}{\kappa^{struct}}}$ with $\kappa^{struct} = 10.44$ N. The procedure to calculate these two quantities is given in Appendix C. The Figure 5.25 reports the aerodynamic damping, the aerodynamic stiffness and the expected aeroelastic frequency calculated from the simulations of the harmonic forced motion in flapwise, for various angles of incidence.

Model	ϕ_0 (°)	ξ^{aero} (%)	κ^{aero} (N)	ω^{AEL}/ω_0
CFD	15	**34,1** $\pm$ 1,0	**-1,0** $\pm$ 0,2	**0,95** $\pm$ 0,01
	17	**33,5** $\pm$ 2,5	**-1,8** $\pm$ 0,2	**0,91** $\pm$ 0,01
	18	**33,8** $\pm$ 5,0	**-2,2** $\pm$ 0,8	**0,89** $\pm$ 0,04
ONERA	15	**17,7** $\pm$ 0,5	**-1,65** $\pm$ 0,07	**0,918** $\pm$ 3e-3
	17	**4,5** $\pm$ 0,1	**-1,65** $\pm$ 0,02	**0,918** $\pm$ 1e-3
	18	**-1,7** $\pm$ 0,1	**-1,20** $\pm$ 0,01	**0,941** $\pm$ 6e-4

Figure 5.25: Aerodynamic damping and stiffness as well as the aeroelastic pulsation calculated from the forced motion simulations for various angle of incidence at $U_0 = 40\,\mathrm{m/s}$ and reduced frequency $k = 0.094$.

As expected by looking at Figure 5.3, the aerodynamic damping obtained with the ONERA dynamic stall model decreases with the angle of incidence and even becomes negative for $\phi_0 = 18°$. Nevertheless, it does not overcome the 3% of structural damping. Concerning the aerodynamic damping induced by the URANS model, even if the uncertainties are higher, one can note that the aerodynamic damping stays high around 35% and does not seem to diminish with the angle of incidence (Figure 5.25a). The differences between the aerodynamic damping obtained by the ONERA dynamic stall model and the CFD could be due to the turbulence intensity. Indeed, the ONERA model is based on experimental result with a turbulence intensity of 1%, however, the comparison between CFD and experimental data realized in [29] suggests that the turbulence intensity simulated with the present parametrisation of the Spalart turbulence model is about 4%, which induces different dynamic stall loops and thus the aerodynamic damping.

For the aerodynamic stiffness, both the ONERA dynamic stall model and the CFD predict values around -16% of the modal structural stiffness ($\kappa^{struct} = 10.44$ N) for a wind angle of attack equal to 17°. With the ONERA model the absolute value of the aerodynamic stiffness slightly decreases with the angle of incidence whereas it increase significantly with ϕ_0 with the CFD model. Nevertheless, both models agree in the fact that the aeroelastic frequency will be lower than the structural frequency, as shown in Figure 5.25.

5.3.4 Effect of the wind speed U_0

The wind speed is also an important parameter as it modifies the reduced frequency. In 2D, the reduced frequency changes the shape of the dynamic stall loops (Figure 3.9) and affects the energy transfer. In this section, fixing the wind angle of attack at 17°, two imposed motion simulations are compared in order to investigate the effect of the wind speed.

Impact on the phase lag

First, the phase lag between the sectional forces on Y and the flapwise velocity is examined for the last 40% of the blade (Figure 5.26).

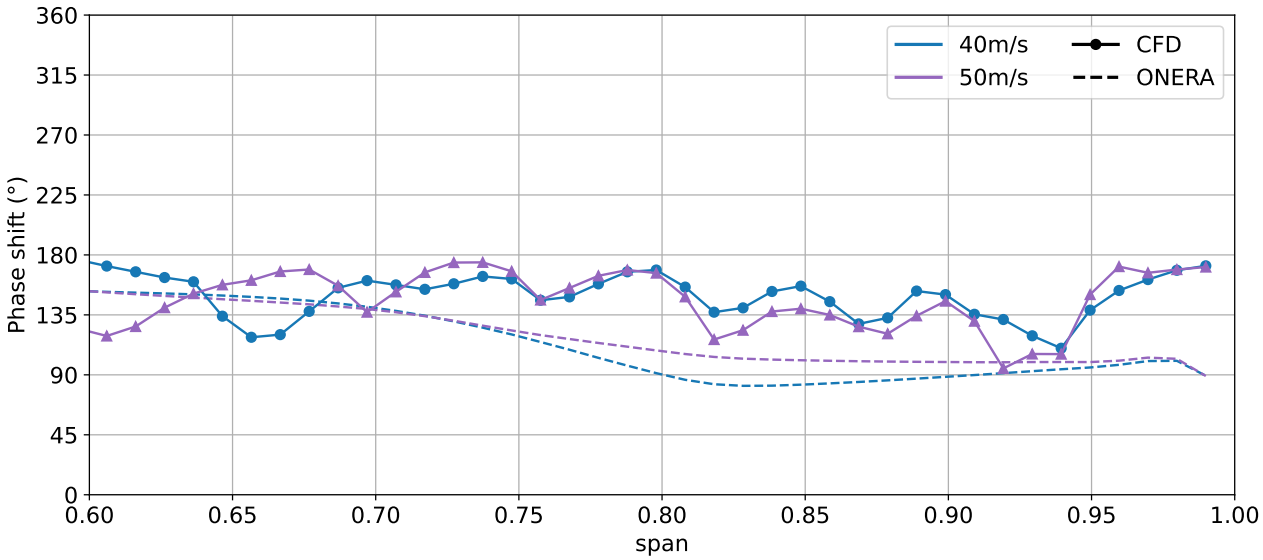

Figure 5.26: Phase shift between the force in Y and the flapwise velocity, for two wind speeds $U_0 = 40m/s$ and $50m/s$ (i.e. different reduced velocity $\mathcal{U}_R = 5.3$ and 6.61) at $\phi_0 = 17°$.

The phase shift of the loads obtained with the ONERA model increases with the wind speed beyond 75% of the span, leading to a higher positive aerodynamic damping (Figure 5.27a). Usually, the wind speed promotes the aeroelastic instabilities, but with these material properties of the blade, the static aeroelastic equilibrium has reduced the effective angle of attack and thus the risk of instability. It is visible in the stability map of the Figure 5.3.

On the contrary, it can be seen that the phase shift of the aerodynamic loads simulated with the URANS model slightly reduces between 80% and 94% of the span, increasing the wind speed (Figure 5.26). The change of angle of attack due to the static equilibrium does not offset the effect of the speed because it has low effect as seen in Figure 5.24.

Impact on the aerodynamic damping

Likewise, for the angle of incidence, the aerodynamic damping, the aerodynamic stiffness and the expected aeroelastic frequency are calculated from the simulations of the harmonic forced motion in flapwise are reported in Figure 5.27 for $U_0 = 40m/s$ and $50m/s$ (i.e. $\mathcal{U}_R = 5.3$ and 6.61).

Model	U_0 (m/s)	ξ^{aero} (%)	κ^{aero} (N)	ω^{AEL}/ω_0
CFD	40	**33,5** $\pm$ 2,5	**-1,8** $\pm$ 0,2	**0,91** $\pm$ 0,01
	50	**49,2** $\pm$ 10,0	**-5,1** $\pm$ 2,5	**0,72** $\pm$ 0,15
ONERA	40	**4,5** $\pm$ 0,1	**-1,65** $\pm$ 0,02	**0,918** $\pm$ 1e-3
	50	**9,6** $\pm$ 0,1	**-2,69** $\pm$ 0,03	**0,861** $\pm$ 2e-3

Figure 5.27: Aerodynamic damping and stiffness as well as the aeroelastic pulsation calculated from the forced motion simulations for two wind speeds $U_0 = 40m/s$ and $50m/s$ (i.e. two different reduced velocity $\mathcal{U}_R = 5.3$ and 6.61) at $\phi_0 = 17°$.

First, despite the large uncertainty on the aerodynamic damping computed with the CFD, it seems that the added aerodynamic damping increases significantly with the velocity from 33.5% for $U_0 = 40m/s$ to 49.2% for $U_0 = 50m/s$. With the ONERA dynamic stall model, the aerodynamic damping is much lower (4.5% at 40 m/s) but it also increases with the wind speed.

Regarding the aerodynamic stiffness, both the ONERA dynamic stall model and the CFD predict a reduction of the global stiffness due to the higher wind speed. The uncertainties are larger for the CFD but the results seem to converge toward the ONERA ones (Fig. C.2b). As a consequence, both models agree in the fact that the aeroelastic frequency will be lower than the structural frequency and continue to decrease with the velocity, as shown in Figure 5.27.

5.4 Study of the aeroelastic dynamic behavior of the blade in stall conditions with a high-fidelity aeroelastic unsteady coupling

The previous approach by imposed motion is important to understand the motion-induced fluid dynamics and associated load responses, but it has some limitations. The motion imposed could not be representative, in displacement and frequency, of the real aeroelastic motion. To overcome these limitations, coupled unsteady aeroelastic simulations are conducted. The temporal coupling strategy is a elementary loose coupling scheme as explained in chapter 2.

5.4.1 Description of the wind gust used to perturbed the blade

A dynamic aeroelastic instability is a motion-induced instability. An initial motion is needed to initiate de dynamics.

To perturb the blade it has been decided to use a wind gust. However, simulating a real gust in CFD is not that easy and takes some simulation time. So, the gust has only been modeled within the load transfer. It takes the form of a temporal function g_f that multiplies the loads given by the CFD before transferring it to the beam solver. As a consequence, the aeroelastic motion is not physical during the time duration of the gust. This part of the simulation has then not been used in the analysis.

The temporal function g_f used to model the gust simulate a temporary increased of the wind speed:

$$g_f = \left(\frac{U_0 + V_{\text{gust}}}{U_0}\right)^2 \tag{5.3}$$

where

$$V_{\text{gust}}(t) = \begin{cases} 0, & t < 0, \\ \frac{1}{2} V_{cg} \left(1 - \cos\left(\frac{2\pi t}{T}\right)\right), & 0 \leq t < T, \\ 0, & t \geq T, \end{cases} \tag{5.4}$$

with V_{cg} the maximum wind gust and T the time duration of the gust.

Realistic values are chosen for V_{cg} and T. According to Figure 3 of [63], the rise time and the amplitude are linked. The time duration of the gust is taken equal to the flapwise period (2s) in order to trigger the vibrations. As a consequence, the minimal value of the gust amplitude of a 50-year return gust is taken, namely 3m/s. It gives the gust plotted in Figure 5.28.

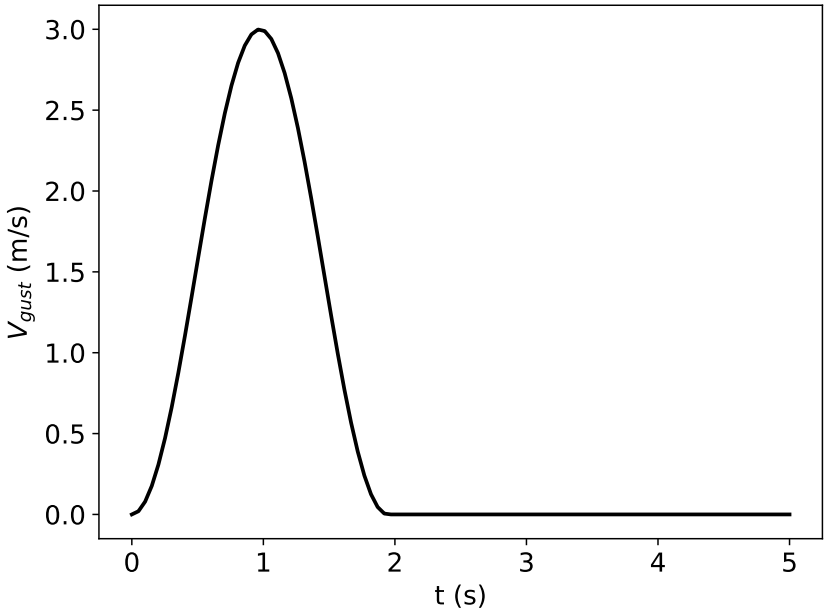

Figure 5.28: Evolution of V_{gust} with time

5.4.2 Analysis of the $\phi_0 = 17°$ and $U_0 = 40$m/s case

An unsteady aeroelastic simulation of approximately 9s has been performed for the $\phi_0 = 17°$ and $U_0 = 40$m/s ($\mathcal{U}_R = 5.3$) case. Tip position evolution with time is plotted in Figure 5.29.

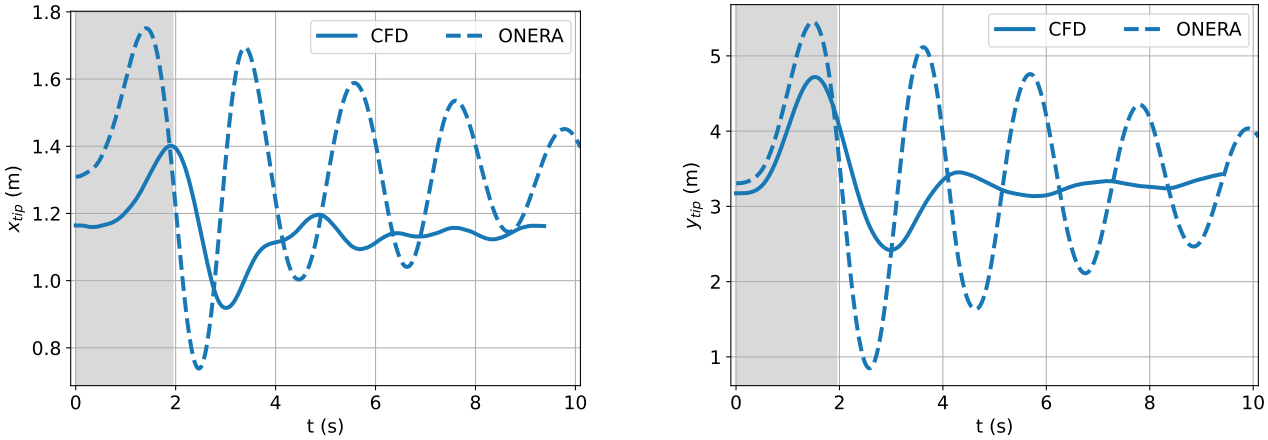

(a) x_{tip} (b) y_{tip}

Figure 5.29: Tip displacements in X (left) and Y (right) as a function of the time; Unsteady aeroelastic simulation for $\phi_0 = 17°$ and $U_0 = 40$m/s. The grey area gives the duration of the gust.

The blade is initially in its equilibrium state with no velocity. The wind gust perturbs the blade and makes it bend. This creates a first peak in displacement that occurs after the maximum velocity of the gust, because of inertia. After the gust is finished, the blade is free to oscillate from non-zero initial conditions in displacement and velocity generated by the gust. As the flapwise mode is more flexible and is more exposed to the lift force, the maximum displacement in the Y direction, which is close to the flapwise direction, is higher than for the X direction. Compared to the forced motion, where the amplitude of the tip displacement in Y was around 0.5m, the maximal tip displacement is here three times larger.

Figure 5.29 shows that the CFD responses in both X and Y are quickly damped. One can observe almost three periods of oscillation in the Y displacement signal. In the X direction, a higher frequency signature appears beyond 4s. It seems that the tip response in Y is dominated by the flapwise frequency. The latter first affects the tip response in X and the signature of an edgewise frequency only appears beyond 4s. By comparison, the ONERA responses are less damped than the CFD ones and the frequency of the signals are closer to the structural flapwise frequency (0.51 Hz).

In order to analyze further the dynamical response, frequency and damping informations are extracted from this damped short signal. A method would have been to fit damped sinusoid, but the signals don't seem to have a constant frequency and damping. That's why a method using the peaks has been employed. Instead of using the classical logarithmic decrement method, it has been used on half the difference between two successive peaks (maximum or minimum). Then, the damping can be computed with:

$$\delta = \ln\left(\frac{A_i}{A_{i+2}}\right) \qquad \& \qquad \xi = \frac{\delta}{\sqrt{4\pi^2 + \delta^2}} \tag{5.5}$$

with A_i is half the peak-to-peak amplitude between the peak i and peak i+1.

Moreover, the frequency is obtained by taking the inverse of time laps between two successive maximums or two successive minimums.

5.4.3 Effect of the incidence ϕ_0

Unsteady aeroelastic simulation has also been realized with a slightly higher angle of incidence for the same wind speed $U_0 = 40\text{m/s}$ ($\mathcal{U}_R = 5.3$). The history of their tip displacement is compared in Figure 5.30.

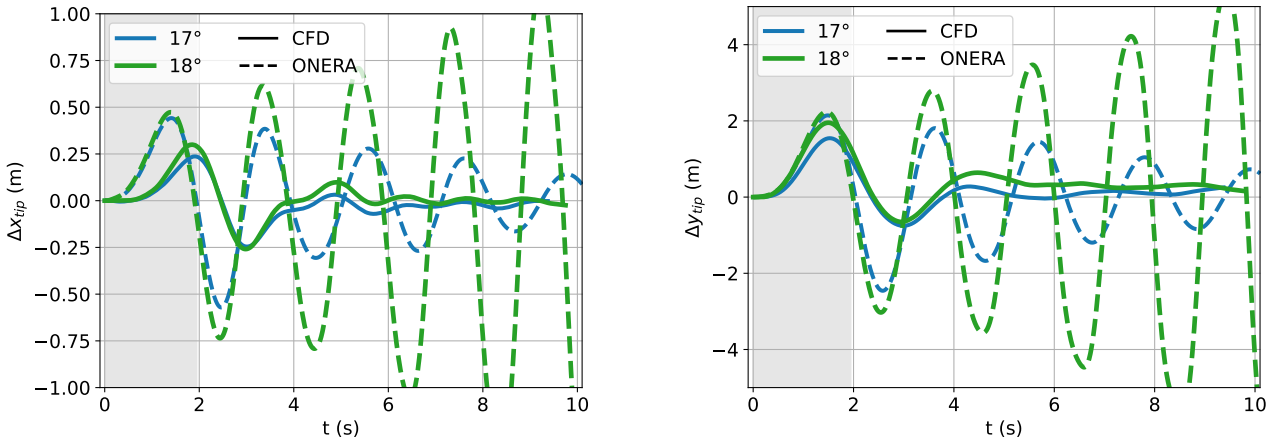

(a) ΔX_{tip} (b) ΔY_{tip}

Figure 5.30: Tip displacements in X (left) and Y (right) as a function of the time; Unsteady aeroelastic simulation for $U_0 = 40\text{m/s}$, $\phi_0 = 17°$ and 18°. The grey area gives the duration of the gust.

As it can be observed on the ONERA responses, the two simulations have been chosen so that one configuration is stable while the one of higher incidence is unstable. For the simulations with CFD, the wind gust has perturbed a little more the blade at an incidence of 18° than 17°. But the damped responses of the two CFD simulations are pretty similar. It is a completely different behavior than the simulations with the ONERA dynamic stall model.

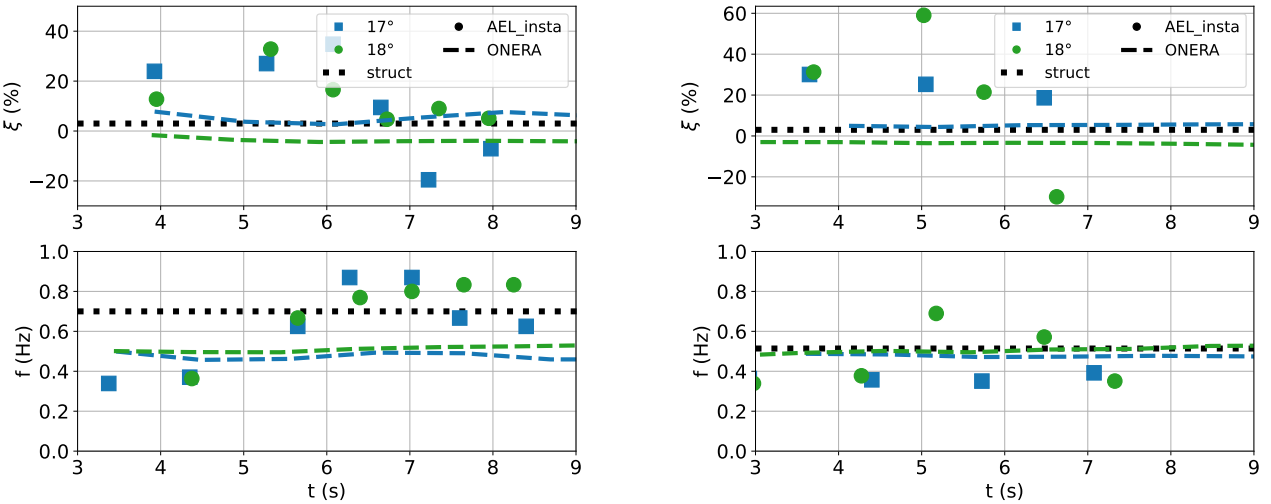

(a) ΔX_{tip} (b) ΔY_{tip}

Figure 5.31: Damping and frequency over time of the tip position history for two wind angles of incidence ($U_0 = 40\text{m/s}$). The dotted lines correspond to the frequencies of the (a) edgewise and (b) flapwise mode.

As it is known that dynamic stall is a non linear process that depends on the amplitude of oscillation, the damping and frequency can change with the amplitude of oscillation. That's why, the damping and frequency are computed over the time with the method introduced previously. The results are reported for the two simulations (17° and 18°) with CFD and ONERA dynamic stall model in Figure 5.31.

The signals are damped so quickly that only the one or two first values of the damping seem trustworthy. After 6s, the amplitudes are small which induces large variations in the measured damping. At the beginning, the damping is around 20% for the displacement in X and around 30% for the displacement in Y, which corresponds to what has been calculated previously harmonically forcing the flapwise motion.

In the X direction, both simulations have captured frequencies close to the frequency of the edgewise mode. For $\phi_0 = 18°$, the frequency ends at a higher level which supposes an added stiffness effect which has not been estimated for an edgewise motion. Before 4s, the effect of the flapwise mode can be observed in the motion in the X direction (Fig. 5.30a), which explains that the two first points in frequency of Figure 5.31 are close to 0.4 Hz. In the Y direction, the frequency measured is lower (0.4 Hz) than the flapwise structural frequency (0.51 Hz) as predicted by the imposed motion study, due to a negative added stiffness (see Figure 5.25).

No clear differences in terms of damping or frequency are observed between the CFD simulations with different angles of incidence.

Summary

To sum up the effect of the angle of incidence ϕ_0 on the stall induced vibrations, the previous results of damping and frequency of ΔY_{tip} are reproduced in the Figure 5.32 in function of the angle of incidence. To extend the range of incidence, additional simulations from Figure 5.3, coupling the corotated Euler Bernoulli beam model with the ONERA dynamic stall model, have been analysed.

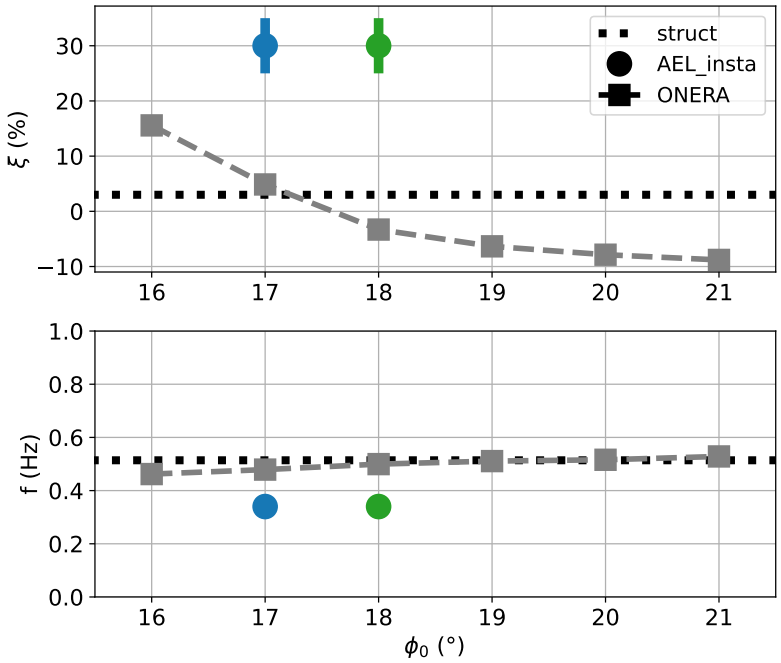

Figure 5.32: Damping and frequency towards the Y direction in function of the angle of incidence ϕ_0 at $U_0 = 40$m/s. The dotted lines correspond to the flapwise mode.

The damping calculated with the *pychrono/FastS* coupling is much higher than with the ONERA dynamic stall model. Moreover, the decrease of the damping with the incidence, present with the ONERA dynamic stall model, is not observed with the CFD. Concerning the frequency, the *pychrono/FastS* coupling exhibits a lower frequency with no observed influence of the incidence.

5.4.4 Effect of the wind speed U_0

The last simulation that has been performed is an aeroelastic unsteady simulation with a higher wind speed of 50m/s ($\mathcal{U}_R = 6.61$) while keeping the angle of incidence at 17°. The tip displacement and torsional angle are compared to those obtained at 40m/s ($\mathcal{U}_R = 5.3$) in Figure 5.33.

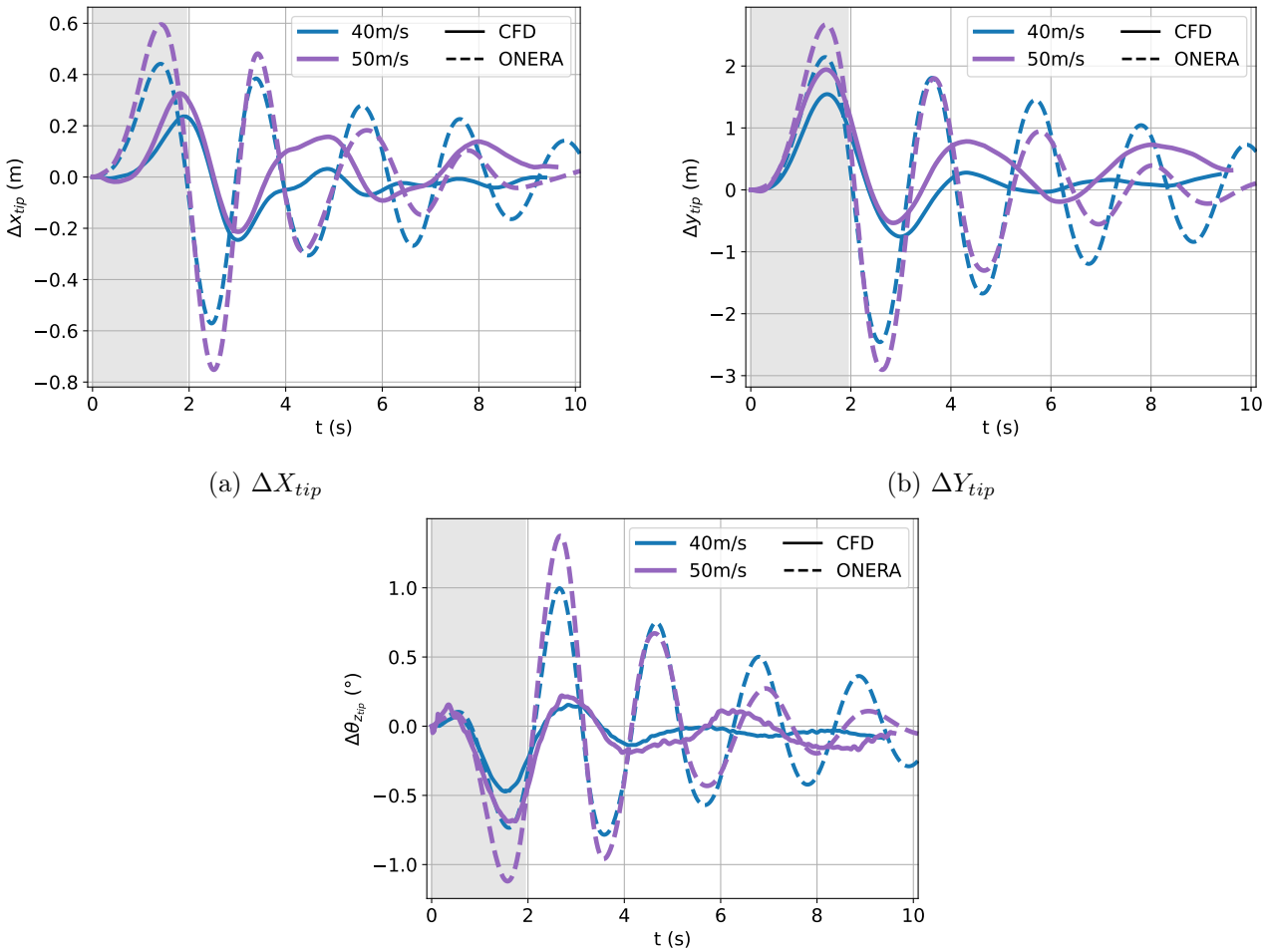

(a) ΔX_{tip}

(b) ΔY_{tip}

(c) $\Delta\theta_{Z_{tip}}$

Figure 5.33: Tip displacement history for two wind speeds, $U_0 = 40m/s$ and $50m/s$ (i.e. reduced velocity $\mathcal{U}_R = 5.3$ and 6.61) at $\phi_0 = 17°$. The grey area gives the duration of the gust.

At 50m/s, the wind gust has induced a higher maximal displacement as presumed by equation 5.3. For the displacement in X and Y, the 50m/s CFD response is still damped but much less than for 40m/s. This behavior is opposed to the one exposed by the simulations with the ONERA dynamic stall model where 50m/s response is more damped than the 40m/s response. Concerning the frequency, the edgewise mode frequency of the CFD response is no more visible in the X displacement for 50m/s because it is hidden by the X component of the flapwise mode, which has a larger period. It can also be noticed that the aeroelastic flapwise frequency has decreased with the

augmentation of the wind speed. This tendency is also present in the ONERA responses, however, the coupling with the ONERA dynamic stall model fails to correctly estimate the aeroelastic frequency. It underestimates the added aerodynamic stiffness.

The Figure 5.33c shows that the torsion is limited to less than 0.2° for the CFD, which suggests that the higher aerodynamic stiffness of the 50m/s response does not come from the torsion. For the ONERA responses, the torsion reaches 1° which can perhaps impact on the aerodynamic stiffness. The high frequency vibrations of torsion due to higher modes are negligible.

The details of the damping and frequency are given in Figure 5.34.

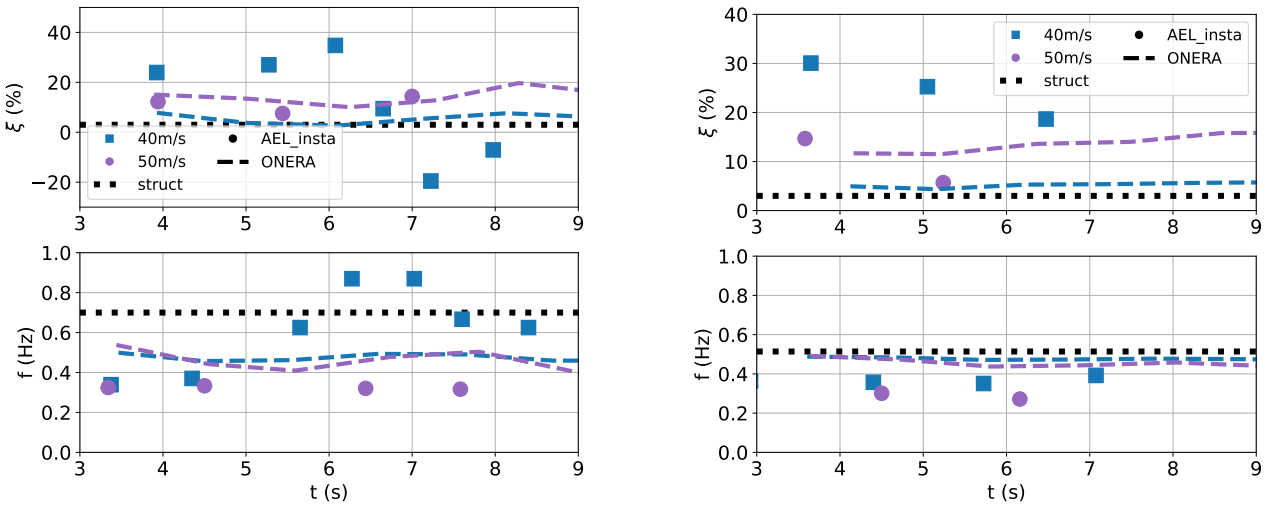

(a) ΔX_{tip} (b) ΔY_{tip}

Figure 5.34: Damping and frequency over time of the tip position history for two wind speeds, $U_0 = 40m/s$ and $50m/s$ at $\phi_0 = 17°$

The first thing to notice is that for 50m/s, the CFD values of damping and frequency present less variation in time because the response is less damped. Regarding the frequencies, results reported in Figure 5.34 confirm what had been observed in Figure 5.33. In the X direction the response at 50m/s is dominated by a lower frequency that is the one of an aeroelastic flapwise mode. Frequency results for the Y direction also show that at 40m/s, the flapwise frequency had fallen down from 0.51Hz to 0.34Hz. At 50m/s it falls to 0.28Hz. The frequency is here almost divided by two. This drop of frequency was partly predicted by the imposed motion simulations through the aerodynamic stiffness (Fig. 5.34).

Furthermore, it is clear that for 50m/s the CFD aeroelastic response is less damped than for 40m/s. It was 30% at 40m/s and it fall down to around 10% for 50m/s. This is in contradiction with the result obtained by the imposed motion. This large difference in damping with the imposed motion simulations probably comes from the large frequency drop of the flapwise aeroelastic frequency. Indeed, the reduced velocity used for the imposed motion simulations was set according the structural flapwise frequency. It was then more than twice as low as the one experienced by the blade at 50m/s. As the dynamic stall loops are greatly affected by the reduced velocity, it can have a large impact on the damping. The ONERA dynamic stall model has not been calibrated using dynamic stall loops of various frequency and thus is not able to predict this effect.

Following these results, it seems plausible that, for a blade with a lower flapwise frequency (more slender blade) or in higher wind speed, stall-induced vibrations emerge.

Summary

To sum up the effect of the wind speed U_0 on the stall induced vibrations, the previous results of damping and frequency of ΔY_{tip} are reproduced in the Figure 5.35 in function of the wind speed. To extend the range of velocity, additional simulations from Figure 5.3, coupling the corotated Euler Bernoulli beam model with the ONERA dynamic stall model, have been analysed.

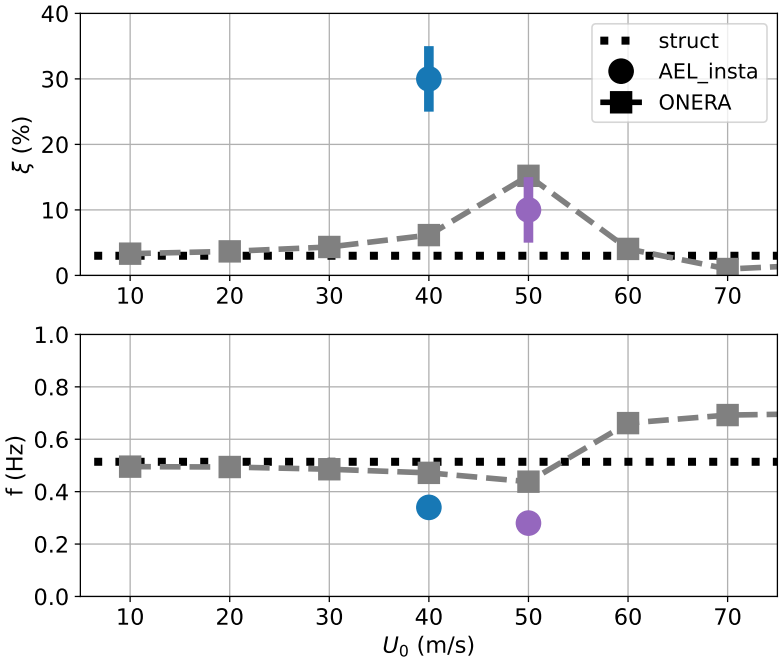

Figure 5.35: Damping and frequency towards the Y direction in function of the wind speed U_0 at $\phi_0 = 17°$. The dotted lines correspond to the flapwise mode.

With the ONERA dynamic stall model, for low wind speed, the damping and frequency are the ones of the structural flapwise flexion mode. As the velocity increases, the aerodynamic damping and stiffness get stronger, causing the global damping to increase and the aeroelastic frequency to decrease. At $\phi_0 = 17°$, the dynamic stall loops have a positive mean slope for a flapwise motion, justifying the positive aerodynamic damping. With the CFD model, the aeroelastic frequency is much lower and continue to decrease with the wind speed. It probably strongly modifies the dynamic stall loops, which as a result makes the damping to drop. This trend differs between the two models. At $U_0 = 50$m/s for the ONERA dynamic stall model, the damping starts to drop and the aeroelastic frequency rises towards the edgewise structural frequency. This modification of tendency may be explained by the torsion of the blade. As the wind speed increases, the angle of attack reduces and the edgewise mode becomes dominant. At low angle of attack, the damping of the edgewise mode is low but stays positive (Fig. 1.38).

5.5 Conclusion

In this chapter, an aeroelastic study of the blade of the IEA15MW, at standstill, and for potentially risky configurations regarding SIV, has been conducted gradually using a high fidelity CFD/CFM solver. First a static aeroelastic study has been performed for various wind conditions (angle of incidence and velocity). In addition to the analysis of the impact on the equilibrium state, the effect of both the wind incidence angle and velocity on the size and amplitude of the stall cells have been highlighted. Then, an extended investigation of the $\phi_0 = 17°$ and $U_0 = 40$m/s case in imposed motion on the flapwise mode has been realized. No spanwise translation of the stall cells has been observed but a periodic intensification has been noted. The phase shift of the loads leading to the aerodynamic damping and stiffness has also been studied. It appeared that the phase shift of the loads is different within or outside the stall cells, giving different dynamic stall loops. The distribution of the phase shift of the wall pressure is also affected by the position of the separation point. Results also showed that a little variation of the wind angle of incidence does not modify the phase shift of the loads, which is in contradiction to what is observed with ONERA dynamic stall model. Increasing the wind speed, the phase shift decreased with the URANS model whereas it rose with the dynamic stall model. For all the conditions that were simulated, a high level of aerodynamic damping of the order of 30% and a significant negative aerodynamic stiffness around -2 N leading to an aeroelastic frequency 10% lower than the structural one were obtained. Finally, unsteady aeroelastic simulations have confirmed that the aeroelastic frequency of the flapwise mode is strongly reduced (-35% for $U_0 = 40$m/s and -50% for $U_0 = 50$m/s) due to the aerodynamic stiffness. It also showed that the aerodynamic damping decreases with the wind velocity. The ONERA dynamic stall model was not able to predict these behavior. No instability was observed but with lower vibration frequency or higher wind speed, stall-induced vibrations could potentially occur.

This tendency was not observed by the imposed motion method as those simulations were performed for lower reduced velocity (computed with the structural flapwise frequency). These results therefore confirm, on the one hand, the importance of the reduced velocity parameters on the dynamic stall behavior and aerodynamic damping, and, on the other hand, the great interest to conduct free aeroelastic simulations.

These simulations constitute only a first look at the qualitative behavior of a blade before stall-induced vibrations. To obtain quantitative results, the mesh should be refined in the outer part of the blade in order to better capture the stall cells and their dynamics. Convergence studies are also needed to fix the quantitative values. Moreover, computation cost may be saved by not using the chimera method and choosing a cheaper mesh deformation method, perhaps less accurate. It will allow to obtain longer simulations with more periods of oscillations.

Conclusions and perspectives

Conclusions

This PhD work was conducted as part of a collaborative research project between the ONERA, the IFP Energies Nouvelles and the CNAM. The initial objective was to demonstrate the contribution of high-fidelity fluid-structure coupling to the modeling of new generation wind turbines. To achieve this, it was planned to couple a structure solver *DeepLines* developed at IFPEN with the CFD solver *FastS* developed at the ONERA. The structure solver *DeepLines* proved difficult to use in this context, and it was decided to choose the opensource structural solver of *Project Chrono*, developed at University of Parma, University of Wisconsin-Madison and members of its open source community, based on the finite element method and therefore entirely relevant to this project. The initial objective was also to first focus with standstill configurations which are concerned by three types of FSI problematics : coupled mode flutter, vortex induced vibrations (VIV) and stall induced vibrations (SIV). The literature review reported in Chapter 1 has permitted to identify the lack of study focusing on blade stall induced vibrations using a high fidelity approach and thus to define the new objectives of the thesis : study stall-induced vibrations on a reference wind turbine blade at standstill, using fluid-structure approaches of gradually increasing complexity, in order to highlight the effect of high-fidelity methods on the SIVs compared to lower fidelity methods. It was also decided to use the blade of the reference 15MW wind turbine, an open-source model free from confidentiality constraints, which is a standard model in the scientific community. This wind turbine model has been developed by academics and represents the best alternative to industrial wind turbines.

To answer this problematic, a modular python framework was built. It allows to switch easily between several levels of fluid-structure solver, from sectional model, using either a quasi-steady or nonlinear unsteady aerodynamic formulation, to high fidelity CFD/CSM. The latter required a particular investment. First, it was necessary to adopt and validate the *Chrono* solver for our study. Second, the *FastS* solver needed to be validated for dynamic stall configuration. Last it was necessary to develop appropriate transfer methods between the two solvers. As the interface between a beam model and a 3D CFD mesh is highly non-matching, the popular transfer methods were not adapted. Therefore, a kinematic motion transfer method has been implemented.

Using this modular framework, the stall-induced vibrations was investigated for the IEA15MW blade at standstill with increasing fidelity methods. The simplest approach to study stall-induced vibrations is to use a section model coupled with either a quasi-steady or dynamic stall aerodynamics formulation. However, a sectional model is far from a twisted and flexible blade. That's why an equivalent section model that is the closest possible to the IEA15MW full blade has been developed. This equivalent section model has two degrees of freedom in edgewise and flapwise for which the orientation is not fixed a priori, but takes into account the overall twist and material properties. It also considers the static torsional deformation along with the contribution in torsion of both the edgewise and flapwise deformations. Based on the idea of equalizing the aerodynamic damping of a sectional model to the one of a modal blade model, equivalent quantities including an equivalent chord, edgewise direction and aerodynamic polars have been identified. Using this equivalent section model, linear stability analysis had been performed with either a quasi-steady or ONERA dynamic stall aerodynamic formulation. It was shown that the aerodynamic formulation strongly affects the SIV stability map and that the most unstable mode is the flapwise mode. As a consequence, regarding the unsteady load in the flapwise direction (mainly the lift force) plotted

as a function of an effective angle of incidence, it was highlighted that instead of the surface and direction of rotation, the risk can be identified looking at the mean slope of the loop: a negative mean slope producing a positive energy transfer from the fluid to the structure. The equivalent section model has also proven its effectiveness in reproducing the SIV stability map of a FEM blade model coupled to the ONERA dynamic stall model under the strip theory hypothesis. The remaining differences in the stability map have however highlighted the difficulty to build an equivalent dynamic stall model describing the effect of all the dynamic stall loops of the blade into one loop. The impact of the geometric non linearities has also been observed at high wind speed where the unstable area has moved towards higher angle of incidence. Whether with the equivalent section or FEM model, results obtained using a semi-empirical dynamic stall model, such as the ONERA model, for SIV predictions, must be taken with caution as the loop characteristic that promotes the energy transfer can be very dependent on the parameters of the model. Special attention has then to be paid to the identification of the model parameters using experimental data bases of dynamic stall loops with various mean angle of attack, reduced frequency and amplitude.

Based on the stability map that has been drawn with "low-fidelity" approach, several wind conditions have been chosen to be simulated with the high-fidelity approach, coupling a FEM blade model with the URANS *FastS* solver. Compared to the dynamic stall model, the *FastS* solver allowed to simulate 3D effects. In aeroelastic stationary simulations, it has manifested through stall cells that generate an amplitude modulation of the lift distribution along the span. For each wind condition combining wind speed and wind angle of incidence, the positions of the stall cells are different and their sizes vary around 2 chords. It appeared that the angle of incidence increases the size of the stall cells while the wind speed reduces it.

The unsteady aeroelastic behavior of the blade, around its aeroelastic equilibrium state, has then been studied in two steps. First through the analysis of fluid and loading motion-induced responses to forced harmonic flapwise motions. Second, based on free aeroelastic responses to a discrete gust type excitation. Both, for wind conditions at the boundary of stability, according to the low-fidelity model predictions. For the imposed motions, the blade was forced to oscillate in its first flapwise structural mode shape and frequency, at low tip amplitude of 0.5m in Y, for different wind angles of incidence of 17° and 18°, and two wind speeds 40m/s ($\mathcal{U}_R = 5.3$) and 50m/s ($\mathcal{U}_R = 6.61$), around the calculated aeroelastic equilibrium state. For any of the low amplitude flapwise motions imposed to the blade no stall cell motion was detected, meaning that the stall cell time dynamic was probably higher than the one of the forced harmonic motion. However, these simulations have highlighted a difference of phase shift between the inside and the outside of the stall cells. Within the stall cells, where the flow is more separated, the aerodynamic loads have a lower phase shift than outside the stall cells. Moreover, these forced motion simulations have allowed to compute an aerodynamic damping and stiffness for several conditions. For all the simulations, a negative aerodynamic stiffness has been observed, for which the absolute value increased with the angle of incidence and the wind velocity. It leads to an aeroelastic frequency around 10% lower than the structural flapwise frequency. For the aerodynamic damping, low influence of the wind angle of incidence has been seen. It remains around 30% of aerodynamic damping for angle of incidence between 15° and 18°. The observed behavior was thus very different from the one obtained using the ONERA dynamic stall model for which the aerodynamic damping decreases and becomes negative with the rise of the wind angle of incidence.

Free aeroelastic simulations of the blade response to a discrete gust have confirmed that the aeroelastic flapwise mode frequency is strongly reduced (-35% for $U_0 = 40$m/s and -50% for $U_0 = 50$m/s) due to the aerodynamic stiffness. Increasing the wind speed from 40m/s to 50m/s has also led to less damped flapwise vibrations. This tendency was not observed by the imposed motion method as those simulations were performed for lower reduced velocity (computed with the

structural flapwise frequency). These results therefore confirm, on the one hand, the importance of the reduced velocity parameters on the dynamic stall behavior and aerodynamic damping, and, on the other hand, the great interest to conduct free aeroelastic high fidelity simulations.

Finally, no instability was observed but with lower vibration frequency or higher wind speed, stall induced vibrations could potentially occur and further investigations could then be conducted.

Discussion and perspectives

The vibrations observed and studied in this thesis were mainly in the flapwise direction, whereas in the literature, many studies on full wind turbines reported edgewise vibrations. Two possible explanations for this difference could be related to the angle of incidence and/or the angle of inclination. The present study is limited in the range of angle of incidence, but with linear analysis it is expected that for higher angles of incidence, the edgewise vibrations could be the most unstable. However, in such angles of incidence, URANS simulations are not adapted anymore because vortex shedding occurs which induces nonphysically large lift fluctuations. To overcome this limitation, DES simulations should be used to resolve sufficient turbulent fluctuations to break the large energy structures [14]. Another major difference difference between an isolated blade and a full rotor is the angle of inclination. In a full rotor, some blades experience large spanwise flow which may completely alter the behavior of the dynamic stall. That's why, it could be interesting to simulate isolated blades with an angle of inclination or a full rotor with several azimuth angles in order to investigate the effect on the stall cells and the dynamic stall loops. Nevertheless, no experimental study neither about the stall cells with spanwise flow nor during dynamic stall has been found. These kinds of studies are needed to further investigate the behavior of stall cells.

In the following, some perspectives are proposed, ranging from possible numerical improvements to new interesting investigations involving more slender blades or different inflow conditions.

Possible numerical improvements

First, it appeared that the simulated stall cells were discretized in the spanwise direction with only few cells. It is coarse and may hamper the motion of the stall cells during the blade oscillations. That's why, a finer mesh in the spanwise direction should be employed to better capture the dynamics of the stall cells.

Moreover, the present coupling between the finite element beam model and the CFD solver could be improved. Currently, the temporal coupling relies on a simple loose scheme in which the CFD and structural solvers are called only once per time step. Even without implementing a strong coupling where the aerodynamic loads and the internal forces are iteratively converged to equilibrium at each time step, which is computationally costly, a loose scheme with prediction-correction could be adopted to enhance accuracy while maintaining reasonable computational cost.

For the spatial coupling, the load transfer (Section 3.6) can also be improved. Between the slices, where the loads are linearly interpolated, information are lost. Instead of integrating the lineic loads, obtained from the slices and interpolated, with the shape function of the FEM model to compute the generalized loads, it would be preferable to integrate directly the wall pressure and shear stress. The beam shape function can be extrapolated to the blade wall based on kinematic assumptions and then used to integrate the wall pressure, allowing for a direct computation of the generalized loads. This approach would ensure that all wall loads are transferred without relying on spanwise interpolation. However, switching from line integrals to surface integrals may increase the computational cost.

Impact of the blade design

All the investigations in this thesis have been carried out on the IEA15MW wind turbine. But to assess the influence of the blade design, it would be interesting to perform similar studies on a larger blade, such as the IEA22MW, a new opensource reference wind turbine [149]. Compared to the 117m span of the IEA15MW blade, the IEA22MW blade reaches 137.8m. At the same time, the chord has also increased, resulting in a similar aspect ratio of 29.5 for both blades. However, in this new design, the mass density has increased more rapidly than the structural stiffness, leading to lower natural frequencies than those of the IEA15MW blade. The flapwise frequency passed from 0.51Hz to 0.38Hz and the edgewise decreased from 0.7Hz to 0.52 Hz.

To assess how the stability of the blade will evolve with this new design, a study similar to the one presented in this thesis should be conducted using the IEA22MW blade. However, a first estimation can be made by examining the evolution of the mass ratio $\mathcal{M}$ and the reduced velocity $\mathcal{U}_R$. For the mass ratio, defined as $\mathcal{M} = \frac{\rho c_{\text{eq}}^2}{m_{\text{eq}}}$, it is necessary to determine whether c_{eq}^2 or m_{eq} has increased the most. Based on the information provided in [149], the chord along the blade has increased by approximately 18% while the mass density along the blade is about 30% higher. It results in a mass ratio roughly 7% higher than the one of the IEA15MW blade. A larger mass ratio indicates a stronger fluid-structure coupling which amplifies the value of the aerodynamic damping. Consequently, a slower wind speed can trigger the instability, causing a shift of the unstable area (Fig. 4.8) towards the lower wind speeds. For the reduced velocity, defined as $\mathcal{U}_R = \frac{U_0}{c_{\text{eq}}\omega_{flap}}$, the rise of the chord length does not compensate the decrease of the flapwise frequency, leading to an increase of about 14% of the reduced velocity. On the stability map (Fig. 4.8), this corresponds to an approximate 12% reduction of the critical wind speeds $U_0^{crit} = \mathcal{U}_R^{crit} c_{\text{eq}}\omega_{flap}$.

This remains a preliminary estimation and many factors may influence this outcome. Nevertheless, it provides a first idea of the impact of increasing the blade size.

Impact of the inflow

In the present work, the inflow was assumed to be uniform, which is not realistic. Since turbulence is known to strongly affect the characteristics of dynamic stall loops [3], it would be more appropriate to use inflow conditions more representative of conditions experienced by wind turbines in terms of turbulence and atmospheric boundary layer. The wind conditions most likely to trigger stall-induced vibrations are those occurring during typhoon. The corresponding atmospheric boundary layer, the turbulence intensity and the length scale of the turbulence under typhoon conditions have been measured by Yi et al. [145] and Zhao et al. [151] and can be modeled by power laws with respect to height.

In wind tunnel experiments, turbulence can be generated installing grids but it remains very difficult to reproduce the large scales of turbulence encountered by wind turbines in the atmosphere. In contrast, numerical simulations allow the generation of such large scale turbulence, as demonstrated by Guma et al. [60] using a Mann box [84]. This approach consists in constructing a box in which the spatial spectral characteristics of the wind follow the Mann turbulence model. The resulting turbulent field is then convected through the simulation domain according to Taylor's frozen turbulence hypothesis. The difficulty is that the turbulence intensity decreases during the convection process.

Using this method, it would be interesting to investigate the effect of the turbulence and the atmospheric boundary layer on the stall cells and the stall-induced vibrations. Moreover, an evolution of the wind speed along the span due to the boundary layer is expected to modify the local reduced frequency and thus the global reduced frequency of the blade.

The emergency shutdown

Finally, in addition to the standstill configuration, the emergency shutdown represents another critical aeroelastic load case, as it can induce substantial loads on the turbine that must be carefully addressed. The emergency shutdown is triggered when the safety supervisor system estimates that the wind turbine may be in danger. The safety supervisor must quickly predict if the wind turbine will remain safe in the near future regardless of the causes [102]. For example, when an unexpected loss of the grid connection causes the generator torque to suddenly drop suddenly to zero, inducing an acceleration of the rotor speed rate. The activation of the emergency shutdown causes the blade to pitch toward 90° at their maximum pitch rate (8°/s for the NREL 5MW) in order stop the rotor as fast as possible. This rapid pitching causes the angle of attack of the blades to quickly decrease and become negative, producing a negative aerodynamic torque that decelerates the rotor. As the rotor speed drops, the module of the effective wind speed decreases as well. While avoiding danger it can lead to a severe structural response.

The emergency shutdown is expected to produce a challenging aeroelastic response due to rotational flow, the deceleration of the rotor and the dynamic stall. To investigate it, Heinz et al. [66] simulated the emergency shutdown of a full rotor of the NREL 5MW using a high-fidelity coupled CFD/CSM framework. The coupling methods between the CFD and the blade model are similar to those presented in this thesis, indicating that the tools developed here could also be applied to this scenario. During their simulation, Heinz et al. [66] observed a high level of fore-aft motion of the tower and an inversed flapwise blade deflection. They also simulated the same emergency shutdown using a Blade Element Momentum Theory (BEMT) model instead of the CFD. Even if the BEMT model is not adapted for such challenging conditions, the resulting aeroelastic responses were found to be similar. They concluded that the detailed modelling of the aerodynamic forces was not essential to predict the structural response.

However, compared to the NREL 5MW, the IEA15MW or the IEA22MW are significantly more flexible, resulting in a stronger fluid-structure coupling. It would therefore be interesting to investigate whether a Kramer like effect, that induces an overshoot of lift [148], has a significant impact on the aeroelastic response of these more flexible blades.

List of communications

Congress proceedings

- N. Cortes, X. Amandolese, J.-L. Pfister, F. Blondel, R. Boisard, J.-S. Schotté, Y. Mauffrey, *Numerical prediction of aerodynamic loads acting on a blade section-model oscillating in stall.*, In Journal of Physics: Conference Series (Vol. 2767, No. 2, p. 022014), June 2024, Florence, Italy.
- N. Cortes, J.-L. Pfister, X. Amandolese, J.-S. Schotté, R. Boisard, *Impact of fluid and structure models on Stall induced vibrations of a wind turbine blade at standstill.*, In Wind Energy Science Conference (WESC), June 2025, Nantes, France.

Journal articles

- N. Cortes, J.-L. Pfister, X. Amandolese, J.-S. Schotté, R. Boisard, *Impact of fluid and structure models on Stall induced vibrations of a wind turbine blade at standstill.*, (submitted)

Appendix

Appendix A

Presentation of the IEA15MW

The wind turbine chosen for our investigations is the 15MW of the International Energy Agency (IEA). It is an open-source model free from confidentiality constraints, which is a standard model in the scientific community. This wind turbine model has been developed by academics and represents the best alternative to industrial wind turbines.

A.1 General description

All the information about the IEA15MW, illustrated in Figure A.1, is available in [53]. A brief description is reported in this section.

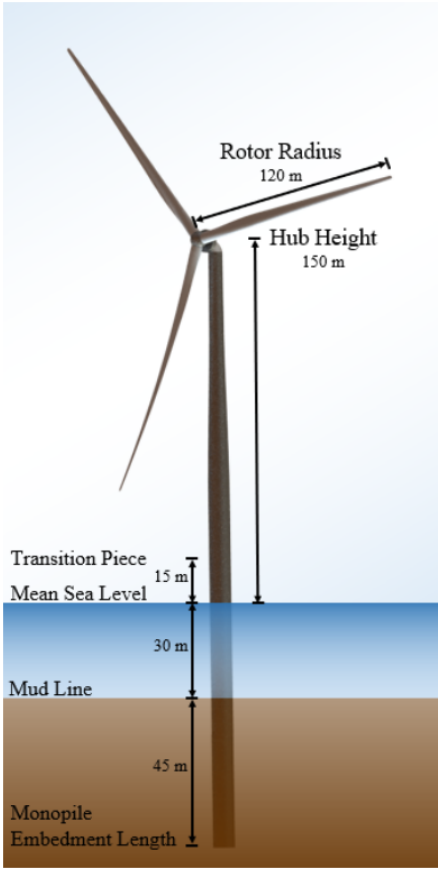

Figure A.1: The IEA Wind 15-MW reference wind turbine [53]

The IEA15MW is a large pitch regulated wind turbine with a rotor diameter of 240 meters and a hub height of 150 meters. The wind turbine starts with a wind speed of at least 3 m/s and needs to be stopped if the wind speed exceeds 25 m/s.

Blade properties

The IEA15MW blade length is 117 m long and its weight is around 65 metric tons. It is designed to achieve a power coefficient of 0.489. A picture of the blade is shown in Figure A.2.



Figure A.2: View from the suction side (top) and trailing edge (bottom) of the offshore wind turbine blade [53]

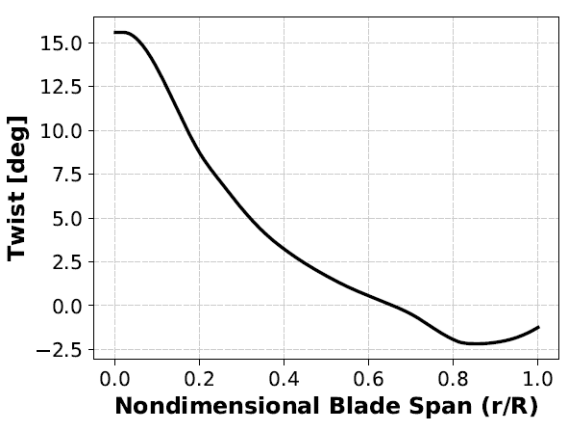

(a) Twist

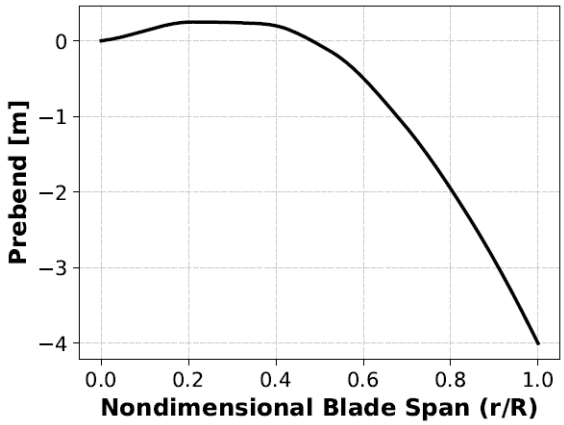

(b) Prebend

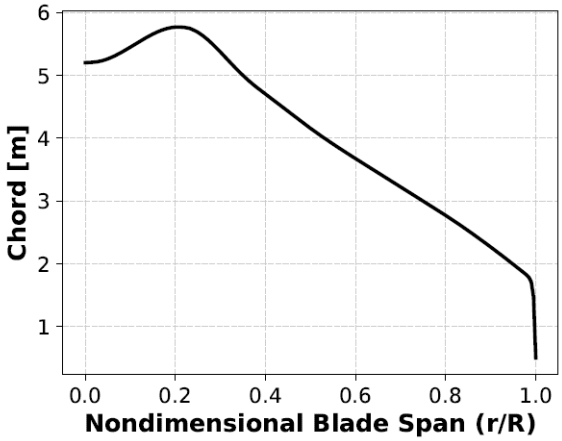

(c) Chord

Figure A.3: Blade planform spanwise quantities [53]

The blade spanwise quantities are reported in Figure A.3. The maximal chord is 5.77 m at 27.2 m of span (23.3%). The blade is twisted in order to place the airfoil at the right angle of attack during operation. Near the tip, the twist stops decreasing due to tip deflection constraints. Longer and slender blades are more flexible, leading to large tip deflection in operation. To avoid the blade hitting the tower, a prebend is added to the initial shape of the blade. However, the

molding process limits the maximum achievable prebend, which justifies the use of a constant twist near the tip. The blade is made of glass and carbon fiber leading to the structural properties of Figure A.4.

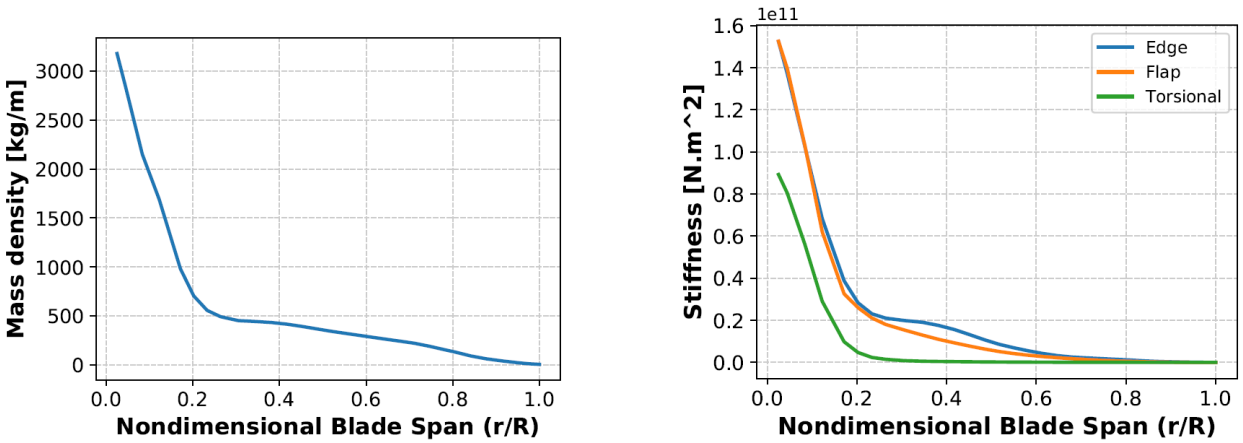

(a) Mass density

(b) Edgewise, flapwise, and torsional stiffness

Figure A.4: Blade beam structural properties [53]

A.2 The polars of the IEA15MW

The DTU FFA-W3 series of airfoils is used in the blade design and is shown in Figure A.5. The root has a cylindrical shape which progressively becomes a thick airfoil at 15% of span, the airfoils are then becoming thinner as they get closer to the tip.

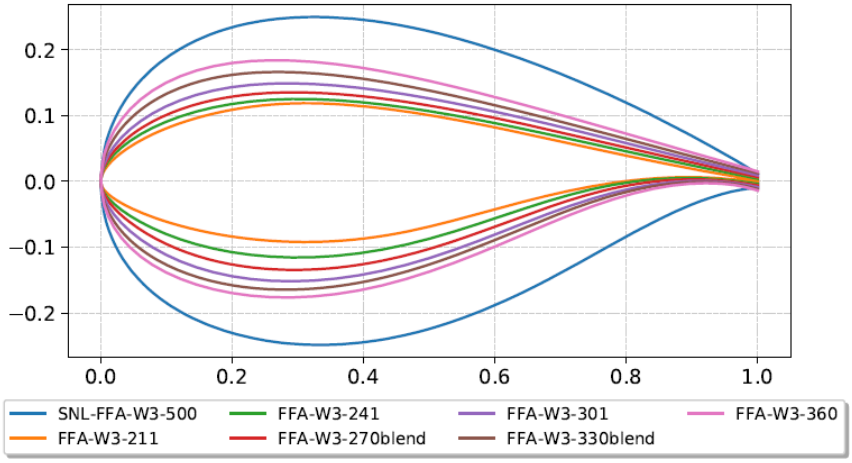

Figure A.5: DTU FFA-W3 airfoil family used in the IEA Wind 15-MW blade design [53]

A.2.1 2D polars

The polars of each airfoil are presented in Figures A.6, A.7, A.8, A.9, A.10, A.11 and A.12. For each airfoil, the polars have been calculated by 4 different solvers:

- The polars available in the github[1] are noted IEA. They have been computed with the 2D incompressible Navier-Stokes solver, EllipSys2D in fully turbulent with a transition model at Reynolds 10^7 [53]. A Du Selig 3D stall delay correction [42] has been applied.
- The polars computed with the compressible solver FastS, described in section 2.2, in 2D at Reynolds $5 \cdot 10^6$ using the Spalart-Allmaras turbulence model are named FastS2D. The flow is fully turbulent but no transition model has been used. For large angles of attack, vortex shedding occurs and leads to unsteady loads for which the minimum and maximum are indicated by dotted lines. This causes an overestimation of the lift. A common practice is to discard this part and extrapolate with the Viterna method [140], like the IEA polars.
- The polars calculated by IFP with SU2 in 2D using a $k-\omega$ SST turbulence model are quoted IFP [87].
- Bidadi et al. [15] used 3D Improved Delayed Detached Eddy Simulation to compute the polars at Reynolds 10^7.

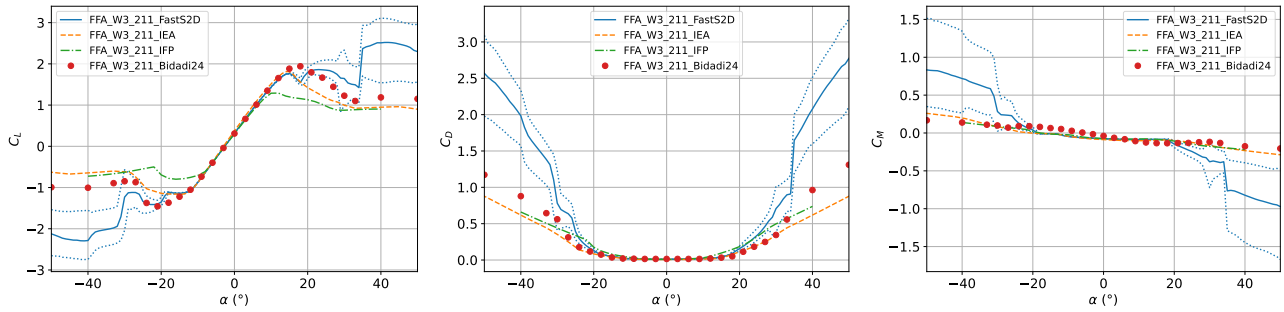

(a) C_L (b) C_D (c) C_M

Figure A.6: Static polars of the FFA-W3-211 (span>0.77) at $Re = 10^7$ for IEA and Bidadi, at $Re = 5 \cdot 10^6$ for FastS2D

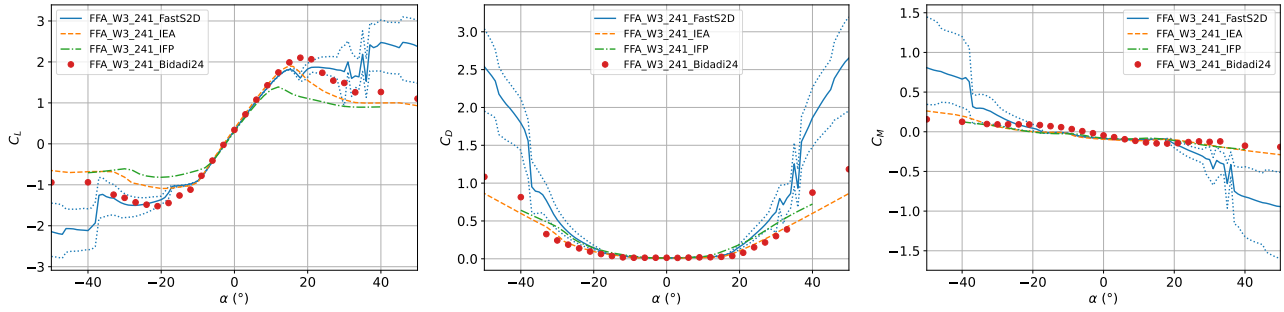

(a) C_L (b) C_D (c) C_M

Figure A.7: Static polars of the FFA-W3-241 (span=0.64) at $Re = 10^7$ for IEA and Bidadi, at $Re = 5 \cdot 10^6$ for FastS2D

[1] https://github.com/IEAWindTask37/IEA-15-240-RWT

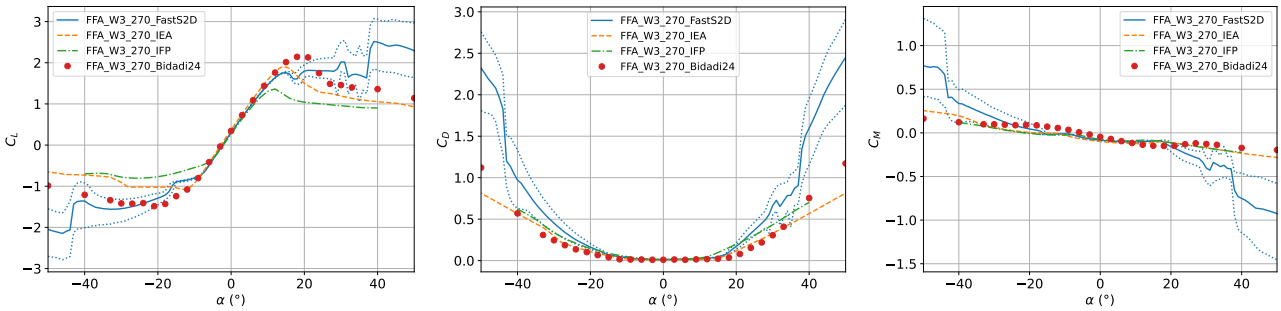

(a) C_L (b) C_D (c) C_M

Figure A.8: Static polars of the FFA-W3-270 (span=0.54) at $Re = 10^7$ for IEA and Bidadi, at $Re = 5 \cdot 10^6$ for FastS2D

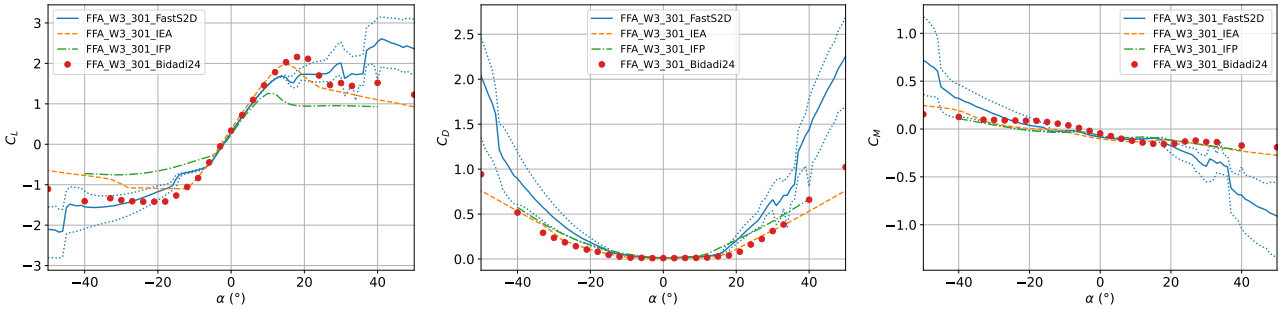

(a) C_L (b) C_D (c) C_M

Figure A.9: Static polars of the FFA-W3-301 (span=0.44) at $Re = 10^7$ for IEA and Bidadi, at $Re = 5 \cdot 10^6$ for FastS2D

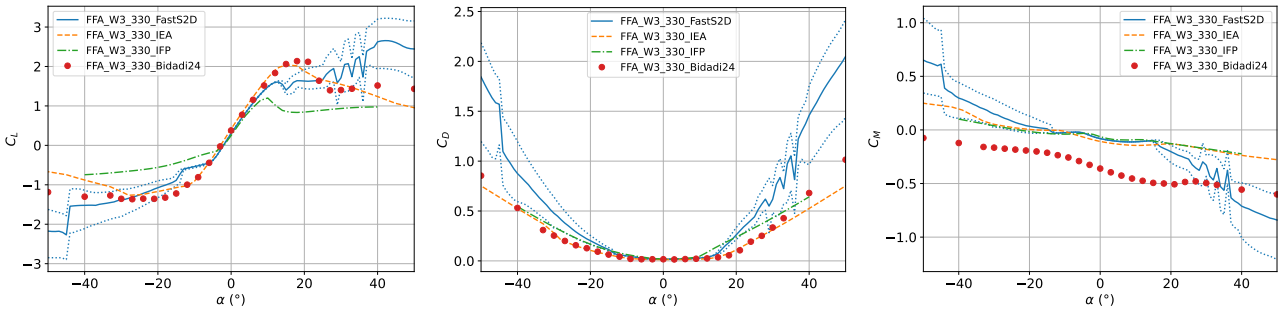

(a) C_L (b) C_D (c) C_M

Figure A.10: Static polars of the FFA-W3-330 (span=0.33) at $Re = 10^7$ for IEA and Bidadi, at $Re = 5 \cdot 10^6$ for FastS2D

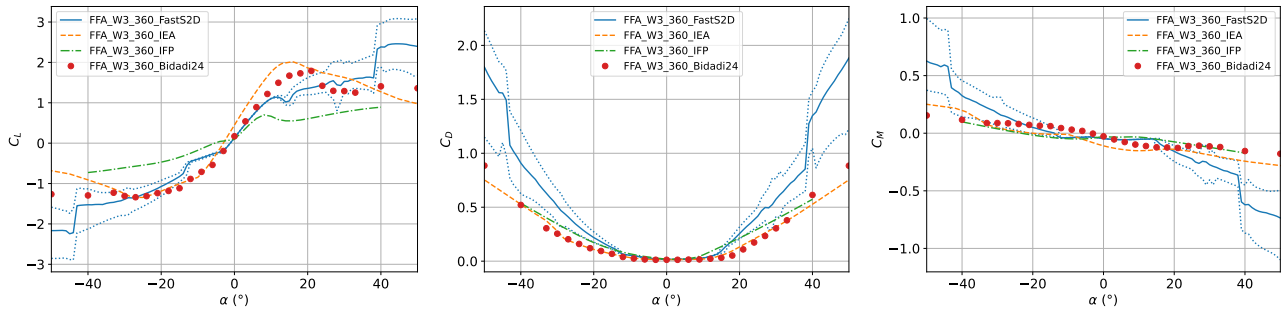

(a) C_L (b) C_D (c) C_M

Figure A.11: Static polars of the FFA-W3-360 (span=0.25) at $Re = 10^7$ for IEA and Bidadi, at $Re = 5 \cdot 10^6$ for FastS2D

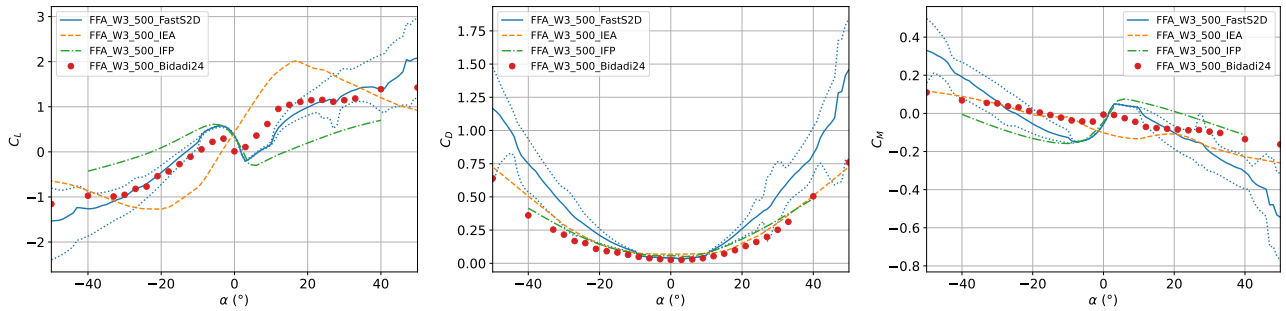

(a) C_L (b) C_D (c) C_M

Figure A.12: Static polars of the FFA-W3-500 (span=0.15) at $Re = 10^7$ for IEA and Bidadi, at $Re = 5 \cdot 10^6$ for FastS2D

It can be noticed that the polars of the outer airfoil (211, 241, 270 and 301) agree at low angle of attack. For thicker airfoils, separation arises even at low angle of attack, leading to significant variations in the aerodynamic polars. At higher angle of attack, the stall behavior of all airfoils differs depending on the solvers, since different turbulence modeling approaches yield different predictions of flow separation. This highlights the difficulty of computing aerodynamic polars in the stalled area, especially since the Reynolds number, the turbulence intensity and the surface roughness all have an influence.

A.2.2 Construction of 3D aeroelastic polars

The blade has a variable geometry along the span, leading to 3D effects that can modify the aerodynamics compared to the 2D behavior. To have a reference while analyzing the unsteady loads along the blade in Chapter 5, the idea has been to construct polars using the full blade in its aeroelastic equilibrium depending on the incidence. Thus, the loads have been extracted from the static simulations of section 5.2.2 and reported in blue dots in Figure A.13. Some variations can be attributed to the presence of stall cells, as a consequence, the loads have been averaged over 5% of the length in order to reduce the impact of the stall cells. This spatially averaged polars are represented in orange.

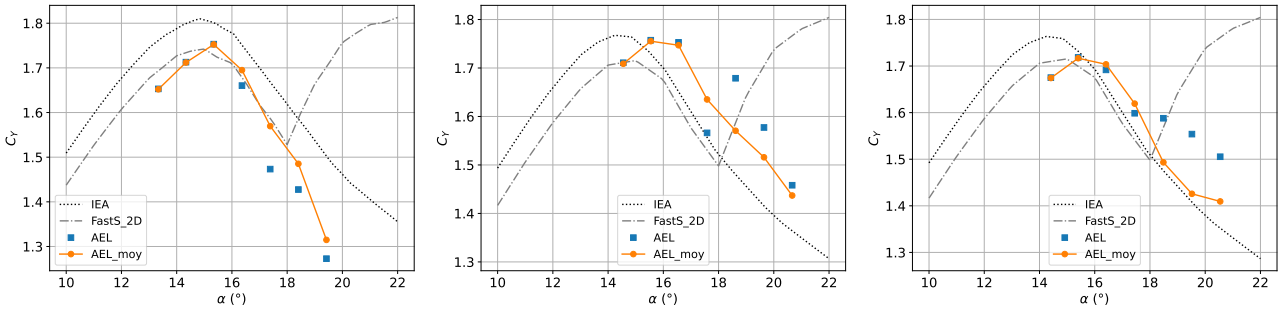

(a) span = 0.7 (b) span = 0.8 (c) span = 0.9

Figure A.13: Static polars along Y taking into account the 3D flow for three span coordinate. For AEL_moy, a mean over 5% of the blade is used to reduce the impact of the stall cells

First, it can be noticed that the AEL polars have a shift in incidence compared to the FastS2D polars. The twist and torsion of the blade are taken into account for the angle of attack in the AEL polars. It means that this shift is linked to 3D effect. The maximum load in Y is similar to the 2D calculation for span=0.7 and span=0.9 but the load is higher in 3D at span=0.8. Moreover, the AEL polars do not have the increasing loads at high angle of attack, due to vortex shedding, because the CFD step of the coupling is a stationary simulation. In the 2D polars the simulations were unsteady.

Appendix B

Calculation of the A, B and C matrix of the equivalent polar equation

The matrices A, B and C come from the conservation of the aerodynamic dampings of the flapwise and edgewise modes between the equivalent section and the beam model.

$\alpha_{\text{twist}}^{2D}$ is a parameter that only moves the polar horizontally. It is taken equal to zero during the resolution and will be identified afterwards in order to position the linear part on the one of the FFA-W3-241 polar.

For the flapwise mode, the equality is:

$$\begin{pmatrix} -\sin(\alpha_{\text{edgewise}}) \\ \cos(\alpha_{\text{edgewise}}) \end{pmatrix} \cdot \left[\frac{\partial}{\partial \dot{\tilde{y}}} \left(\tilde{U}^2_{\text{eff}_{2D}} \right) \mathbf{R}_{\boldsymbol{\phi_0}} \begin{pmatrix} C_D^{2D}(\phi_0) \\ C_L^{2D}(\phi_0) \end{pmatrix} + \frac{\partial \alpha_{\text{eff}}^{2D}}{\partial \dot{\tilde{y}}} \left(\mathbf{R}_{\boldsymbol{\phi_0}} \begin{pmatrix} \frac{\partial C_D^{2D}}{\partial \alpha_{\text{eff}}^{2D}}(\phi_0) \\ \frac{\partial C_L^{2D}}{\partial \alpha_{\text{eff}}^{2D}}(\phi_0) \end{pmatrix} + \left. \frac{\partial \mathbf{R}_{\boldsymbol{\phi}}}{\partial \alpha_{\text{eff}}^{2D}} \right|_0 \begin{pmatrix} C_D^{2D}(\phi_0) \\ C_L^{2D}(\phi_0) \end{pmatrix} \right) \right]$$
$$= \int_0^1 \tilde{c}(s) \frac{\boldsymbol{\phi_{X,flap}}}{c_{\text{eq}} \|\boldsymbol{\phi_{flap}}\|} \cdot \left[\frac{\partial}{\partial \dot{q}_{flap}} \left(\tilde{U}^2_{\text{eff}} \right) \mathbf{R_0}^T \mathbf{R}_{\boldsymbol{\alpha_t}} \mathbf{R}_{\boldsymbol{\phi_0}} \begin{pmatrix} C_D(\phi_0 + \alpha_{\text{twist}}) \\ C_L(\phi_0 + \alpha_{\text{twist}}) \\ 0 \end{pmatrix} \right.$$
$$\left. + \frac{\partial \alpha_{\text{eff}}}{\partial \dot{q}_{flap}} \mathbf{R_0}^T \mathbf{R}_{\boldsymbol{\alpha_t}} \left(\mathbf{R}_{\boldsymbol{\phi_0}} \begin{pmatrix} \frac{\partial C_D}{\partial \alpha_{\text{eff}}}(\phi_0 + \alpha_{\text{twist}}) \\ \frac{\partial C_L}{\partial \alpha_{\text{eff}}}(\phi_0 + \alpha_{\text{twist}}) \\ 0 \end{pmatrix} + \left. \frac{\partial \mathbf{R}_{\boldsymbol{\phi}}}{\partial \alpha_{\text{eff}}} \right|_0 \begin{pmatrix} C_D(\phi_0 + \alpha_{\text{twist}}) \\ C_L(\phi_0 + \alpha_{\text{twist}}) \\ 0 \end{pmatrix} \right) \right] ds \tag{B.1}$$

For the edgewise direction, the equation is:

$$\begin{pmatrix} \cos(\alpha_{\text{edgewise}}) \\ \sin(\alpha_{\text{edgewise}}) \end{pmatrix} \cdot \left[\frac{\partial}{\partial \dot{\tilde{x}}} \left(\tilde{U}^2_{\text{eff}_{2D}} \right) \mathbf{R}_{\boldsymbol{\phi_0}} \begin{pmatrix} C_D^{2D}(\phi_0) \\ C_L^{2D}(\phi_0) \end{pmatrix} + \frac{\partial \alpha_{\text{eff}}^{2D}}{\partial \dot{\tilde{x}}} \left(\mathbf{R}_{\boldsymbol{\phi_0}} \begin{pmatrix} \frac{\partial C_D^{2D}}{\partial \alpha_{\text{eff}}^{2D}}(\phi_0) \\ \frac{\partial C_L^{2D}}{\partial \alpha_{\text{eff}}^{2D}}(\phi_0) \end{pmatrix} + \left. \frac{\partial \mathbf{R}_{\boldsymbol{\phi}}}{\partial \alpha_{\text{eff}}^{2D}} \right|_0 \begin{pmatrix} C_D^{2D}(\phi_0) \\ C_L^{2D}(\phi_0) \end{pmatrix} \right) \right]$$
$$= \int_0^1 \tilde{c}(s) \frac{\phi_{X_{edge}}}{c_{\text{eq}} \|\phi\|} \cdot \left[\frac{\partial}{\partial \dot{q}_{edge}} \left(\tilde{U}^2_{\text{eff}} \right) \mathbf{R_0}^T \mathbf{R}_{\boldsymbol{\alpha_t}} \mathbf{R}_{\boldsymbol{\phi_0}} \begin{pmatrix} C_D(\phi_0 + \alpha_{\text{twist}}) \\ C_L(\phi_0 + \alpha_{\text{twist}}) \\ 0 \end{pmatrix} \right.$$
$$\left. + \frac{\partial \alpha_{\text{eff}}}{\partial \dot{q}_{edge}} \mathbf{R_0}^T \mathbf{R}_{\boldsymbol{\alpha_t}} \left(\mathbf{R}_{\boldsymbol{\phi_0}} \begin{pmatrix} \frac{\partial C_D}{\partial \alpha_{\text{eff}}}(\phi_0 + \alpha_{\text{twist}}) \\ \frac{\partial C_L}{\partial \alpha_{\text{eff}}}(\phi_0 + \alpha_{\text{twist}}) \\ 0 \end{pmatrix} + \left. \frac{\partial \mathbf{R}_{\boldsymbol{\phi}}}{\partial \alpha_{\text{eff}}} \right|_0 \begin{pmatrix} C_D(\phi_0 + \alpha_{\text{twist}}) \\ C_L(\phi_0 + \alpha_{\text{twist}}) \\ 0 \end{pmatrix} \right) \right] ds \tag{B.2}$$

with $\mathbf{R}_{\boldsymbol{\alpha_t}} = \begin{pmatrix} \cos(\alpha_{\text{twist}}) & -\sin(\alpha_{\text{twist}}) & 0 \\ \sin(\alpha_{\text{twist}}) & \cos(\alpha_{\text{twist}}) & 0 \\ 0 & 0 & 1 \end{pmatrix}$

These two equations can be regrouped into the following system:

$$A(\alpha) \frac{d}{d\alpha} \begin{pmatrix} C_D^{2D} \\ C_L^{2D} \end{pmatrix} + B(\alpha) \begin{pmatrix} C_D^{2D} \\ C_L^{2D} \end{pmatrix} = C(\alpha) \tag{B.3}$$

with

$$A = \begin{pmatrix} -\frac{\partial \alpha_{\text{eff}}^{2D}}{\partial \dot{\tilde{y}}} \sin(\alpha_{\text{edgewise}}) & \frac{\partial \alpha_{\text{eff}}^{2D}}{\partial \dot{\tilde{y}}} \cos(\alpha_{\text{edgewise}}) \\ \frac{\partial \alpha_{\text{eff}}^{2D}}{\partial \dot{\tilde{x}}} \cos(\alpha_{\text{edgewise}}) & \frac{\partial \alpha_{\text{eff}}^{2D}}{\partial \dot{\tilde{x}}} \sin(\alpha_{\text{edgewise}}) \end{pmatrix} \mathbf{R}_{\boldsymbol{\phi_0}}$$

and

$$B = \begin{pmatrix} -\frac{\partial}{\partial \dot{\tilde{y}}} \left(\tilde{U}_{\text{eff}_{2D}}^2 \right) \sin(\alpha_{\text{edgewise}}) & \frac{\partial}{\partial \dot{\tilde{y}}} \left(\tilde{U}_{\text{eff}_{2D}}^2 \right) \cos(\alpha_{\text{edgewise}}) \\ \frac{\partial}{\partial \dot{\tilde{x}}} \left(\tilde{U}_{\text{eff}_{2D}}^2 \right) \cos(\alpha_{\text{edgewise}}) & \frac{\partial}{\partial \dot{\tilde{x}}} \left(\tilde{U}_{\text{eff}_{2D}}^2 \right) \sin(\alpha_{\text{edgewise}}) \end{pmatrix} \mathbf{R}_{\boldsymbol{\phi_0}} + \begin{pmatrix} -\frac{\partial \alpha_{\text{eff}}^{2D}}{\partial \dot{\tilde{y}}} \sin(\alpha_{\text{edgewise}}) & \frac{\partial \alpha_{\text{eff}}^{2D}}{\partial \dot{\tilde{y}}} \cos(\alpha_{\text{edgewise}}) \\ \frac{\partial \alpha_{\text{eff}}^{2D}}{\partial \dot{\tilde{x}}} \cos(\alpha_{\text{edgewise}}) & \frac{\partial \alpha_{\text{eff}}^{2D}}{\partial \dot{\tilde{x}}} \sin(\alpha_{\text{edgewise}}) \end{pmatrix}$$

Then, by developing the expression, A and B becomes:

$$A = \begin{pmatrix} -\cos(\alpha - \alpha_{\text{edgewise}}) \sin(\alpha - \alpha_{\text{edgewise}}) & -\cos^2(\alpha - \alpha_{\text{edgewise}}) \\ \cos(\alpha - \alpha_{\text{edgewise}}) \sin(\alpha - \alpha_{\text{edgewise}}) & -\sin^2(\alpha - \alpha_{\text{edgewise}}) \end{pmatrix}$$

and

$$B = \frac{1}{2} \begin{pmatrix} \cos(2\alpha - 2\alpha_{\text{edgewise}}) - 3 & -\sin(2\alpha - 2\alpha_{\text{edgewise}}) \\ -\cos(2\alpha - 2\alpha_{\text{edgewise}}) - 3 & \sin(2\alpha - 2\alpha_{\text{edgewise}}) \end{pmatrix}$$

Finally, C is a vector that regroup the second member of Equation B.1 and Equation B.2.

Appendix C

Calculation of the aerodynamic damping and stiffness

With simulations in which modal oscillations are prescribed to the structure, it becomes possible to evaluate the aerodynamic damping and stiffness associated with the forced motion. This appendix details the procedure to compute them.

First, we start from the dynamic equation of the structure:

$$\mathbf{M}\ddot{\boldsymbol{x}} + \mathbf{D}\dot{\boldsymbol{x}} + \mathbf{K}\boldsymbol{x} = \boldsymbol{F^{aero}} + \boldsymbol{R} \tag{C.1}$$

where $\mathbf{M}$, $\mathbf{D}$ and $\mathbf{K}$ are the mass, damping and stiffness operators of the structure. $\boldsymbol{F^{aero}}$ represents the aerodynamic loads while $\boldsymbol{R}$ corresponds to the reaction forces at the support.

The imposed motion is expressed as:

$$\boldsymbol{x} = q_0 \boldsymbol{\phi} \sin(\omega_0 t) \tag{C.2}$$

where $\boldsymbol{\phi}$ is the structural mode, ω_0 is the pulsation of the mode and q_0 is the chosen amplitude.

Injecting this expression into the dynamic equation leads to:

$$q_0 \left[\omega_0 \mathbf{D}\boldsymbol{\phi} \cos(\omega_0 t) + \left(\mathbf{K} - \omega_0^2 \mathbf{M}\right) \boldsymbol{\phi} \sin(\omega_0 t)\right] = \boldsymbol{F^{aero}} + \boldsymbol{R} \tag{C.3}$$

Projecting the dynamic equation on the mode ϕ makes the generalized forces $g^{aero} = \boldsymbol{\phi}^T \boldsymbol{F^{aero}}$ appear.

$$q_0 \left[\omega_0 \delta \cos(\omega_0 t) + \left(\kappa - \omega_0^2 \mu\right) \sin(\omega_0 t)\right] = g^{aero} + r \tag{C.4}$$

where μ, δ and κ are, respectively, the modal mass, damping and stiffness.

C.1 Aerodynamic stiffness

To evaluate aerodynamic stiffness, we need to look at the forces that are in phase with displacement by multiplying equation C.4 by $\sin(\omega_0 t)$. It is equivalent of doing a first harmonic analysis.

$$q_0(\kappa - \omega_0^2 \mu) \sin^2(\omega_0 t) + q_0 \omega_0 \delta \cos(\omega_0 t) \sin(\omega_0 t) - g^{aero} sin(\omega_0 t) = r \sin(\omega_0 t) \tag{C.5}$$

Then the equation is averaged on one period:

$$\frac{q_0}{2}(\kappa - \omega_0^2 \mu) - \frac{1}{T} \int_0^T g^{aero} \sin(\omega_0 t) dt = -\frac{1}{T} \int_0^T r \sin(\omega_0 t) dt \tag{C.6}$$

The averaged loads in phase with displacement can be seen as an aerodynamic stiffness that modifies the total stiffness of the system.

$$\kappa^{aero} = -\frac{2}{q_0} \frac{1}{T} \int_0^T g^{aero} \sin(\omega_0 t) dt \tag{C.7}$$

The effect of this additional stiffness is to modify the pulsation of the system. The estimated aeroelastic pulsation is thus:

$$\omega^{AEL} = \sqrt{\frac{\kappa + \kappa^{aero}}{\mu}} \tag{C.8}$$

It can be compared to the structural frequency with the following factor:

$$\frac{\omega^{AEL}}{\omega_0} = \sqrt{1 + \frac{\kappa^{aero}}{\kappa}} \tag{C.9}$$

C.2 Aerodynamic damping

This time, to evaluate aerodynamic damping, we need to look at the forces that are in phase with the velocity by multiplying equation C.4 by $\cos(\omega_0 t)$.

$$q_0\omega_0\delta\cos^2(\omega_0 t) + q_0(\kappa - \omega_0^2\mu)\cos(\omega_0 t)\sin(\omega_0 t) - g^{aero}\cos(\omega_0 t) = r\cos(\omega_0 t) \tag{C.10}$$

Then the equation is averaged on one period:

$$\frac{q_0}{2}\omega_0\delta - \frac{1}{T}\int_0^T g^{aero}\cos(\omega_0 t)dt = \frac{1}{T}\int_0^T r\cos(\omega_0 t)dt \tag{C.11}$$

The averaged loads in phase with the velocity can be seen as an aerodynamic damping that modifies the total damping of the system.

$$\delta^{aero} = -\frac{2}{q_0\omega_0}\frac{1}{T}\int_0^T g^{aero}\cos(\omega_0 t)dt \tag{C.12}$$

Thus, the aerodynamic damping coefficient can be obtained:

$$\xi^{aero} = \frac{\omega_0}{2\kappa}\delta^{aero} \tag{C.13}$$

C.2.1 Alternative calculation

If the total power of the aerodynamic forces is available, another way of calculating the aerodynamic damping is possible.

As power is aerodynamic loads times velocity $\dot{\boldsymbol{x}} \cdot \boldsymbol{F^{aero}}$, using the imposed motion, the power can be computed from the generalized forces.

$$P = q_0\boldsymbol{\phi}^T\omega_0\cos(\omega_0 t) \cdot \boldsymbol{F^{aero}} = q_0\omega_0 g^{aero}\cos(\omega_0 t) \tag{C.14}$$

Thus,

$$\delta^{aero} = -\frac{2}{q_0^2\omega_0^2}\frac{1}{T}\int_0^T P(t)dt \tag{C.15}$$

And finally, $\int_0^T P(t)dt$ is the work of the aerodynamic W^{aero} loads over one period.

$$\delta^{aero} = -\frac{1}{q_0^2\pi\omega_0}W^{aero} \tag{C.16}$$

C.2.2 Link with the phase shift

In chapter 5, the aerodynamic damping is discussed based on phase shift results. The link between the phase shift and the aerodynamic damping is presented here. Let's suppose that the aerodynamic load is harmonic with a phase shift $\phi_{\dot{q}}$ with the velocity: $\boldsymbol{F^{aero}} = \boldsymbol{F_0}\cos(\omega_0 t + \phi_{\dot{q}})$. From Equation C.15, the aerodynamic damping becomes:

$$\delta^{aero} = -\frac{2}{q_0\omega_0}\frac{1}{T}\int_0^T \boldsymbol{\phi}^T \cos(\omega_0 t)\cdot \boldsymbol{F_0}\cos(\omega_0 t + \phi_{\dot{q}})dt \tag{C.17}$$

$$\delta^{aero} = -\frac{g_0^{aero}}{q_0\omega_0}\cos(\phi_{\dot{q}}) \tag{C.18}$$

Thus,

$$\xi^{aero} = -\frac{g_0^{aero}}{2q_0\kappa}\cos(\phi_{\dot{q}}) \tag{C.19}$$

C.3 Application to the blade of the IEA15MW

The detailed methodology has been applied to high fidelity imposed flapwise motion simulations presented in 5.3.3 and 5.3.4.

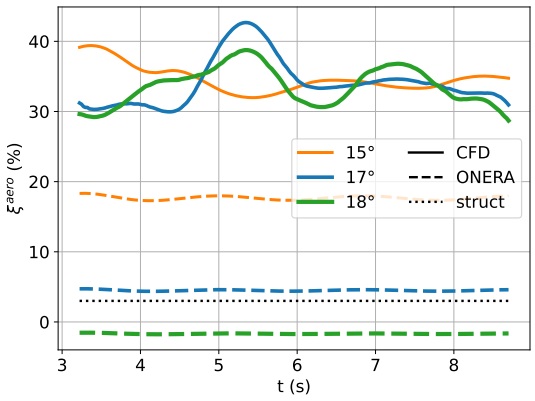

(a) ξ^{aero}

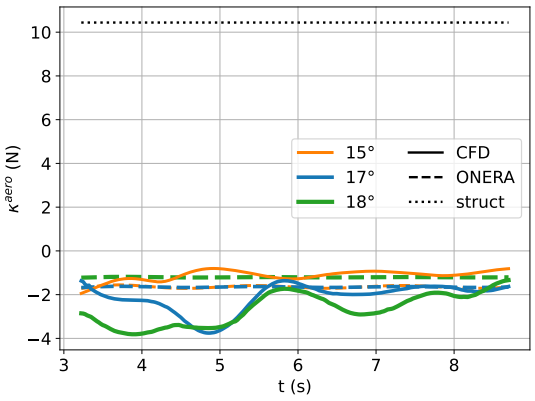

(b) κ^{aero}

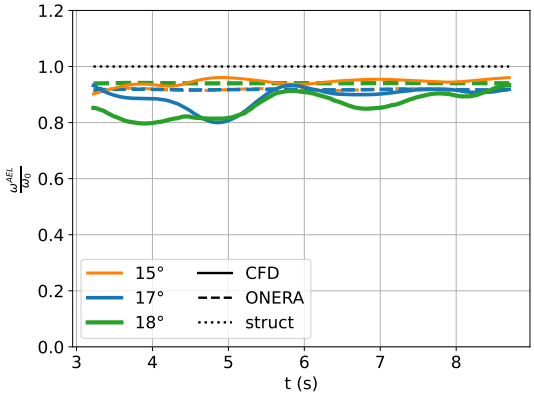

(c) ω^{AEL}/ω_0

Figure C.1: Evolution of (a) the aerodynamic damping and (b) stiffness as well as (c) the aeroelastic pulsation during the forced motion simulations for various angle of incidence at $U_0 = 40\,\mathrm{m/s}$ and reduced frequency $k = 0.094$.

The Figures C.1 and C.2 show the evolution of both the aerodynamic damping and stiffness, obtained with a sliding window, during the simulations of the harmonic forced motion in flapwise, for various angles of incidence and wind speeds. In theory, the values of aerodynamic damping and stiffness should not depend of the window, but if the simulation has not fully converged yet or if there is an additional behavior of the flow independent of the motion, the values of aerodynamic damping and stiffness can fluctuate. The Figures C.1 and C.2 are thus used to estimate a mean aerodynamic damping and stiffness and evaluate the uncertainty caused by these fluctuations. The results presented in Figures 5.25 and 5.27 are the mean more or less the maximum difference from the mean of the last period (2s).

For example, during the URANS simulations of the 50m/s case, the aerodynamic damping was first under the one of the 40m/s case, then it has escalated quickly and exceeded the damping of the 40m/s case, see Figure C.2. This is certainly due to a lack of convergence of the simulation, especially in the 40% to 60% region of the blade. More periods of oscillation would have been necessary to converge.

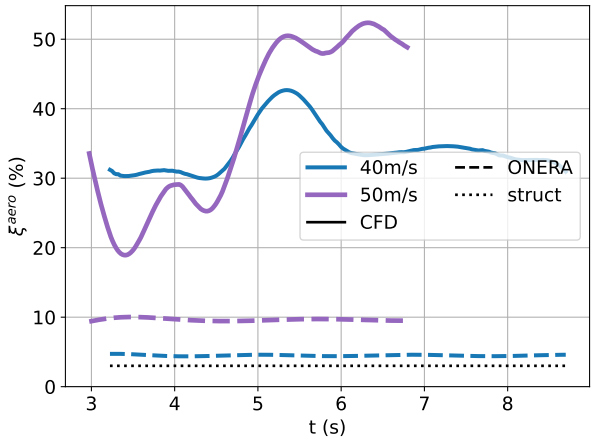

(a) ξ^{aero}

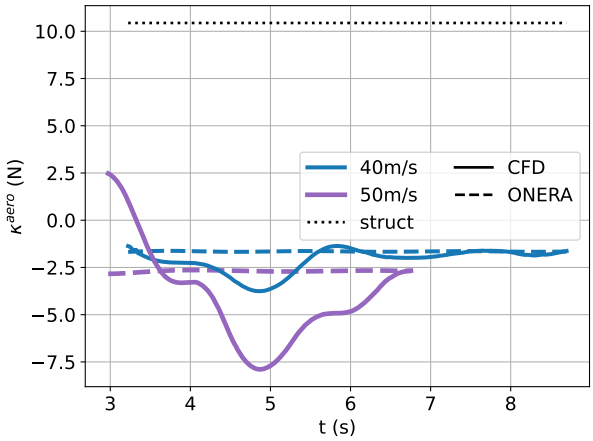

(b) κ^{aero}

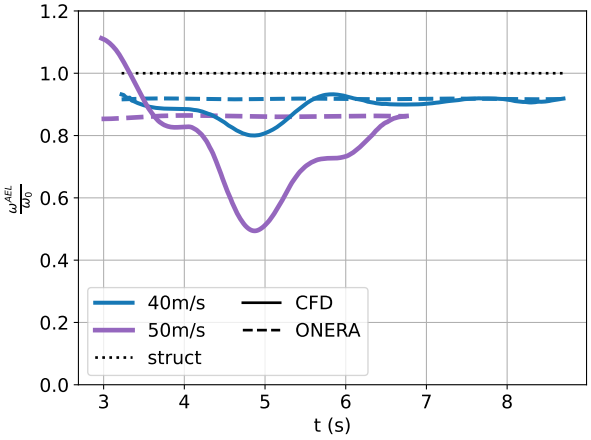

(c) ω^{AEL}/ω_0

Figure C.2: Evolution of (a) the aerodynamic damping and (b) stiffness as well as (c) the aeroelastic pulsation during the forced motion simulations for two wind speeds $U_0 = 40m/s$ and $50m/s$ (i.e. two different reduced velocity $\mathcal{U}_R = 5.3$ and 6.61) at $\phi_0 = 17°$.

Appendix D

Calculation of the phase shift with the blade velocity

This appendix introduces the method used on chapter 5 to calculate the phase shift of the lineic forces or the pressure with the blade velocity. It is based on the cross-correlation between the lineic forces or pressure and the blade velocity. To illustrate the method, the example of the lineic force coefficient along Y at 80/% span is taken for the configuration at the wind speed $U_0 = 40\text{m/s}$ and the wind angle of incidence $\phi_0 = 17°$.

First, the force coefficient C_Y and the velocity on Y at 80% of the blade are represented in Figure D.1.

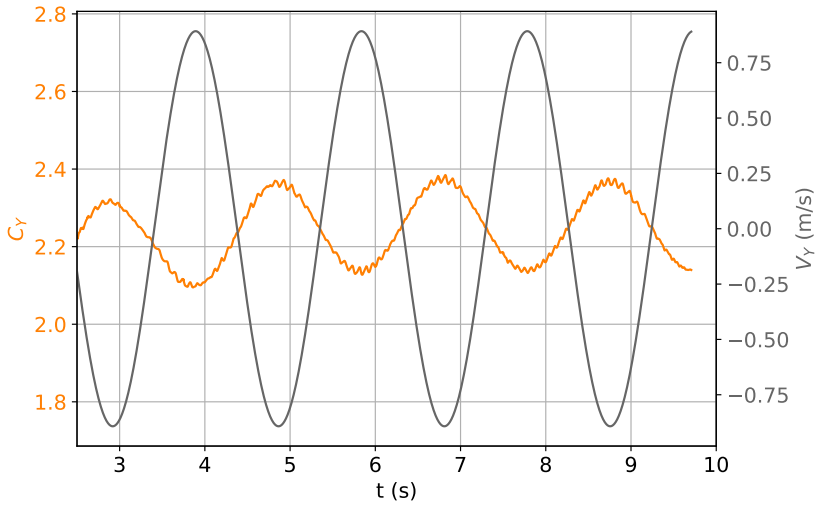

Figure D.1: Force coefficient C_Y and velocity V_Y with time at span=0.80 for the configuration with a wind speed of 40m/s and an angle of incidence of 17°.

The force coefficient signal contains higher frequencies that will be filtered in order to smooth out the following cross correlation. A mask is applied to the fast Fourier transform of the signal to keep only the frequencies between $0.2f_{flap}$ and $1.8f_{flap}$ with f_{flap} being the frequency of the forced motion. The filtered signal is rebuilt with an inverse Fourier transform and show in Figure D.2. The amplitudes of variation have changed but as long as the peaks are at the same time that the unfiltered signal, it can be used to calculate the phase shift.

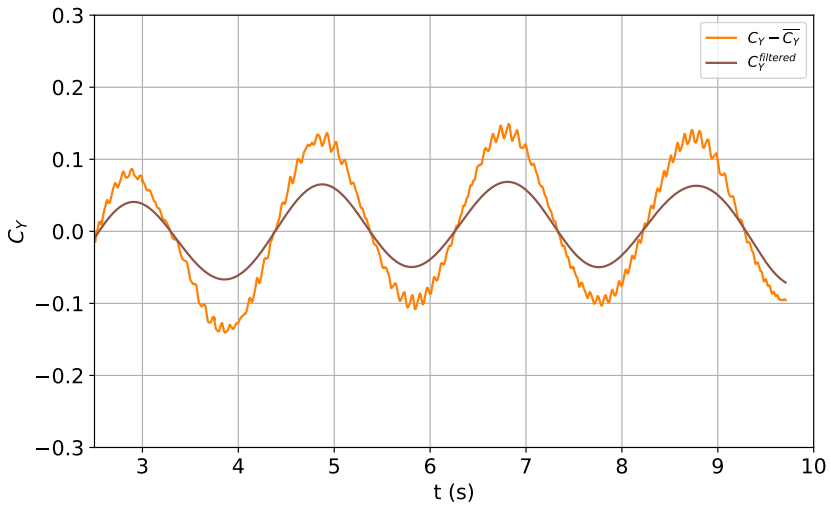

Figure D.2: Force coefficient $C_Y - \overline{C_Y}$ before and after being filtered with time at span=0.80 for the configuration with a wind speed of 40m/s and an angle of incidence of 17°.

Then, the cross correlation is realized between the filtered C_Y signal and blade velocity using the following formula:

$$\text{Corr}[k] = \sum_{l=0}^{N-1} C_Y^{filtered}[l] V_Y[l-k] \tag{D.1}$$

The Correlation is plotted in Figure D.3 as a function of the phase found from the sampling frequency. The phase shift $\phi_{\dot{q}}$ is given by the phase of the maximum correlation. Here, $\phi_{\dot{q}}$ is equal to 169°.

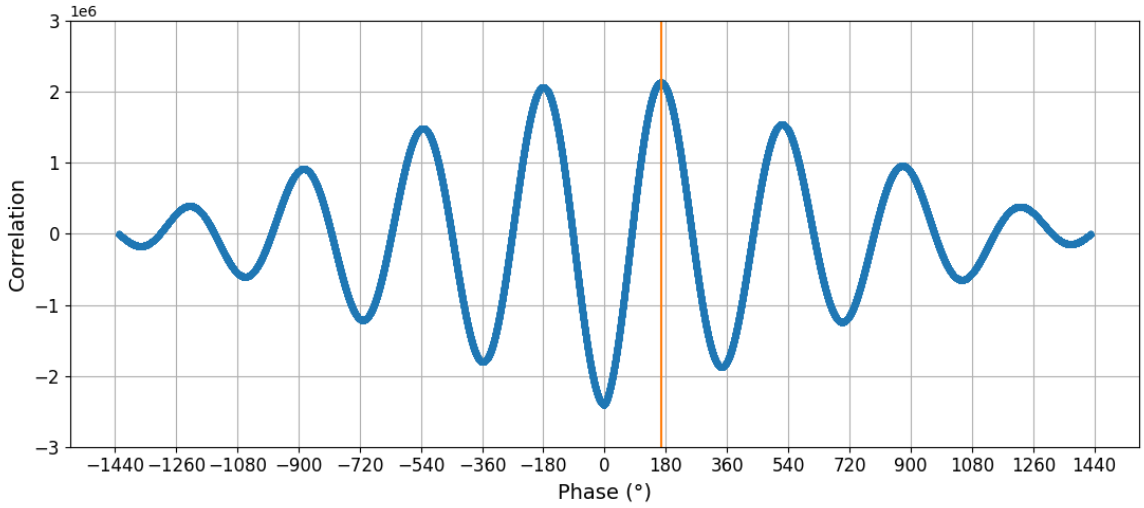

Figure D.3: Cross correlation of the filtered force coefficient C_Y with the velocity V_Y.

Bibliography

[1] https://www.epfl.ch/labs/lfmi/projects/viv-porous-objects. (Cited pages xi and 13.)

[2] Xavier Amandolese. Low speed flutter and post-critical behaviour of flat plate and naca0018 section models in a wind tunnel. In First International Symposium on Flutter and Its Application, IFSA2016, IFSA-4R19, Japan Aerospace Exploration Agency Paper JAXA-SP-16-008E, Tokyo, Japan, pages 447–455, 2016. (Cited page 37.)

[3] Xavier Amandolese and Edmond Széchényi. Experimental study of the effect of turbulence on a section model blade oscillating in stall. Wind Energy: An International Journal for Progress and Applications in Wind Power Conversion Technology, 7(4):267–282, 2004. (Cited pages xii, xiii, 24, 28, 29, 65, 67, 68, 69, 152 and 207.)

[4] Xavier Amandolese, Pascal Hémon, and Shehryar Manzoor. The transient temporal response of a flexible bridge deck subjected to a single gust. Journal of Computational and Applied Mathematics, 246:153–160, 2013. (Cited page 37.)

[5] C Anderson, H Heerkes, and R Yemm. The use of blade-mounted dampers to eliminate edgewise stall vibration. In EWEC-CONFERENCE-, pages 207–211, 1999. (Cited page 37.)

[6] Ekaterina Antimirova, Jiyoung Jung, Zilan Zhang, Aaron Machuca, and Grace X Gu. Overview of computational methods to predict flutter in aircraft. Journal of Applied Mechanics, 91(5):050801, 2024. (Cited pages xi and 10.)

[7] Galih Bangga. Numerical studies on dynamic stall characteristics of a wind turbine airfoil. Journal of Mechanical Science and Technology, 33:1257–1262, 2019. (Cited pages 24, 38, 48, 118 and 193.)

[8] Galih Bangga, Thorsten Lutz, and Matthias Arnold. An improved second-order dynamic stall model for wind turbine airfoils. Wind Energy Science, 5(3):1037–1058, 2020. (Cited page 30.)

[9] Galih Bangga, Surya Hutani, and Henidya Heramarwan. The effects of airfoil thickness on dynamic stall characteristics of high-solidity vertical axis wind turbines. Advanced Theory and Simulations, 4(6):2000204, 2021. (Cited page 27.)

[10] Galih Bangga, Marina Carrion, William Collier, and Steven Parkinson. Technical modeling challenges for large idling wind turbines. Journal of Physics: Conference Series, 2626(1): 012026, oct 2023. doi: 10.1088/1742-6596/2626/1/012026. URL https://dx.doi.org/10.1088/1742-6596/2626/1/012026. (Cited page 42.)

[11] Olivier A Bauchau. Dymore user's manual. Georgia Institute of Technology, Atlanta, 2007. (Cited page 51.)

[12] Bridget M Benner, Daniel W Carlson, Banafsheh Seyed-Aghazadeh, and Yahya Modarres-Sadeghi. Vortex-induced vibration of symmetric airfoils used in vertical-axis wind turbines. Journal of Fluids and Structures, 91:102577, 2019. (Cited pages xi and 16.)

[13] SI Benton and MR Visbal. The onset of dynamic stall at a high, transitional reynolds number. Journal of Fluid Mechanics, 861:860–885, 2019. (Cited pages xi, 24, 25 and 26.)

[14] Shreyas Bidadi, Ganesh Vijayakumar, Ashesh Sharma, and Michael A Sprague. Mesh and model requirements for capturing deep-stall aerodynamics in low-mach-number flows. Journal of Turbulence, 24(8):393–418, 2023. (Cited pages 48 and 151.)

[15] Shreyas Bidadi, Ganesh Vijayakumar, Georgios Deskos, and Michael Sprague. Three-dimensional aerodynamics and vortex-shedding characteristics of wind turbine airfoils over 360-degree angles of attack. Energies, 17(17):4328, 2024. (Cited page 162.)

[16] Gunjit Bir and Jason Jonkman. Aeroelastic instabilities of large offshore and onshore wind turbines. In Journal of Physics: Conference Series, volume 75, page 012069. IOP Publishing, 2007. (Cited pages 42 and 44.)

[17] RL Bisplinghoff and H Ashley. Principles of Aeroelasticity. John Wiley, New York, 1962. (Cited page 10.)

[18] R. D. Blevins. Flow-induced vibration. 1977. (Cited pages xi, 4, 14, 15 and 68.)

[19] Pieter Boersma, Bridget Benner, Todd Currier, and Yahya Modarres-Sadeghi. Experimental evidence of coupled-mode flutter in a two-meter-long non-rotating wind turbine blade. Journal of Fluids and Structures, 112:103611, 2022. (Cited pages xi, 4, 11, 12, 43, 44 and 188.)

[20] E Branlard, J Jonkman, JH Porter, G Vijayakumar, B Jonkman, M Singh, E Mayda, and K Dixon. A generalized wind turbine cross section as a reduced-order model to gain insights in blade aeroelastic challenges. In Journal of Physics: Conference Series, volume 2767, page 022005. IOP Publishing, 2024. (Cited pages 85 and 86.)

[21] Andy P Broeren and Michael B Bragg. Spanwise variation in the unsteady stalling flowfields of two-dimensional airfoil models. AIAA journal, 39(9):1641–1651, 2001. (Cited page 33.)

[22] S Brown. Displacement extrapolations for cfd+ csm aeroelastic analysis. In 38th Structures, Structural Dynamics, and Materials Conference, page 1090, 1997. (Cited pages xii and 54.)

[23] Lawrence W Carr, Kenneth W McAlister, and William J McCroskey. Analysis of the development of dynamic stall based on oscillating airfoil experiments. Technical report, National Aeronautics and Space Administration, 1977. (Cited pages xi, xii, 23 and 38.)

[24] Paola Causin, Jean-Frédéric Gerbeau, and Fabio Nobile. Added-mass effect in the design of partitioned algorithms for fluid–structure problems. Computer methods in applied mechanics and engineering, 194(42-44):4506–4527, 2005. (Cited page 57.)

[25] PK Chaviaropoulos. Flap/lead–lag aeroelastic stability of wind turbine blade sections. Wind Energy: An International Journal for Progress and Applications in Wind Power Conversion Technology, 2(2):99–112, 1999. (Cited page 41.)

[26] PK Chaviaropoulos. Flap/lead–lag aeroelastic stability of wind turbine blades. Wind Energy: An International Journal for Progress and Applications in Wind Power Conversion Technology, 4(4):183–200, 2001. (Cited page 41.)

[27] PK Chaviaropoulos, NN Soerensen, Martin Otto Laver Hansen, IG Nikolaou, KA Aggelis, J Johansen, Mac Gaunaa, T Hambraus, Heiko Frhr von Geyr, Ch Hirsch, et al. Viscous and aeroelastic effects on wind turbine blades. the viscel project. part ii: Aeroelastic stability investigations. Wind Energy: An International Journal for Progress and Applications in Wind Power Conversion Technology, 6(4):387–403, 2003. (Cited page 41.)

[28] Chuan Chen, Jing-wei Zhou, Fengming Li, and Endi Zhai. Stall-induced vibrations analysis and mitigation of a wind turbine rotor at idling state: Theory and experiment. Renewable Energy, 187:710–727, 2022. (Cited page 42.)

[29] N Cortes, X Amandolese, JL Pfister, F Blondel, R Boisard, JS Schotté, and Y Mauffrey. Numerical prediction of aerodynamic loads acting on a blade section-model oscillating in stall. In Journal of Physics: Conference Series, volume 2767, page 022014. IOP Publishing, 2024. (Cited pages 65, 117 and 138.)

[30] M Costes, F Richez, A Le Pape, and R Gavériaux. Numerical investigation of three-dimensional effects during dynamic stall. Aerospace Science and Technology, 47:216–237, 2015. (Cited page 118.)

[31] Luca Damiola, Muhammad Faheem Siddiqui, Mark Charles Runacres, and Tim De Troyer. Influence of free-stream turbulence intensity on static and dynamic stall of a naca 0018 aerofoil. Journal of Wind Engineering and Industrial Aerodynamics, 232:105270, 2023. (Cited pages 24 and 29.)

[32] Frédéric Daude. Méthode d'intégration temporelle implicite pour la simulation des grandes échelles: application à la réduction du bruit de cavité. PhD thesis, Université de Poitiers, 2007. (Cited page 48.)

[33] Augustina De Boer. Computational fluid-structure interaction: spatial coupling, coupling shell and mesh deformation. PhD thesis, 2008. (Cited pages 51 and 52.)

[34] Aukje de Boer, Alexander H van Zuijlen, and Hester Bijl. Review of coupling methods for non-matching meshes. Computer methods in applied mechanics and engineering, 196(8): 1515–1525, 2007. (Cited page 53.)

[35] Emmanuel De Langre. Frequency lock-in is caused by coupled-mode flutter. Journal of fluids and structures, 22(6-7):783–791, 2006. (Cited page 15.)

[36] Haley Dell'Orso, Burak A Tuna, and Michael Amitay. Measurement of three-dimensional stall cells on a two-dimensional naca0015 airfoil. AIAA Journal, 54(12):3872–3883, 2016. (Cited pages xii, 33, 34, 121, 124 and 132.)

[37] Grigorios Dimitriadis. Introduction to nonlinear aeroelasticity. John Wiley & Sons, 2017. (Cited pages xii, 30, 31, 61, 63 and 102.)

[38] Grigorios Dimitriadis and Jing Li. Bifurcation behavior of airfoil undergoing stall flutter oscillations in low-speed wind tunnel. AIAA journal, 47(11):2577–2596, 2009. (Cited page 37.)

[39] Donnard. Contribution à l'étude du comportement aérodynamique d'un rotor d'éolienne. Master's thesis, ENSEM-INPL, 2002. (Cited pages xii, 31, 32 and 33.)

[40] B Dose, H Rahimi, I Herráez, B Stoevesandt, and J Peinke. Fluid-structure coupled computations of the nrel 5mw wind turbine blade during standstill. In Journal of Physics: Conference Series, volume 753, page 022034. IOP Publishing, 2016. (Cited pages xi, 17 and 44.)

[41] Earl H Dowell, RH Scanlan, F Sisto, HC Curtiss Jr, and H Saunders. A modern course in aeroelasticity. 1981. (Cited page 87.)

[42] Zhaohui Du and Michael Selig. A 3-d stall-delay model for horizontal axis wind turbine performance prediction. In 1998 ASME Wind Energy Symposium, page 21, 1998. (Cited page 162.)

[43] Jack R Edwards and Meng-Sing Liou. Low-diffusion flux-splitting methods for flows at all speeds. AIAA journal, 36(9):1610–1617, 1998. (Cited page 47.)

[44] David M Eggleston and Forrest Stoddard. Wind turbine engineering design. 1987. (Cited page 37.)

[45] Alejandra S Escalera Mendoza, Ipsita Mishra, and D Todd Griffith. An open-source numad model for the iea 15 mw blade with baseline structural analysis. In AIAA SCITECH 2023 Forum, page 2093, 2023. (Cited page 44.)

[46] C Farhat and M Lesoinne. On the accuracy, stability, and performance of the solution of three-dimensional nonlinear transient aeroelastic problems by partitioned procedures. In 37th Structure, Structural Dynamics and Materials Conference, page 1388, 1996. (Cited page 106.)

[47] Charbel Farhat, Michael Lesoinne, and Patrick Le Tallec. Load and motion transfer algorithms for fluid/structure interaction problems with non-matching discrete interfaces: Momentum and energy conservation, optimal discretization and application to aeroelasticity. Computer methods in applied mechanics and engineering, 157(1-2):95–114, 1998. (Cited pages 52 and 53.)

[48] Charbel Farhat, Kristoffer G Van der Zee, and Philippe Geuzaine. Provably second-order time-accurate loosely-coupled solution algorithms for transient nonlinear computational aeroelasticity. Computer methods in applied mechanics and engineering, 195(17-18): 1973–2001, 2006. (Cited pages 55 and 56.)

[49] Carlos A Felippa, KC Park, and MR Ross. A classification of interface treatments for fsi. In Fluid Structure Interaction II: Modelling, Simulation, Optimization, pages 27–51. Springer, 2010. (Cited pages xii and 50.)

[50] Théo Flament. Modèle d'ordre réduit de structures non-linéaires pour l'aéroélasticité des turbomachines. PhD thesis, HESAM Université, 2023. (Cited page 49.)

[51] Peter Fuglsang, Ioannis Antoniou, Kristian S Dahl, and Helge Aa Madsen. Wind tunnel test of the ffa-w3-241, ffa-w3-301 and naca 63-430 airfoils. 1998. (Cited pages xiii, 63, 64 and 105.)

[52] Yuan Cheng Fung. An introduction to the theory of aeroelasticity. Courier Dover Publications, 2008. (Cited page 10.)

[53] Evan Gaertner, Jennifer Rinker, Latha Sethuraman, Frederik Zahle, Benjamin Anderson, Garrett Barter, Nikhar Abbas, Fanzhong Meng, Pietro Bortolotti, Witold Skrzypinski, et al. Definition of the iea 15-megawatt offshore reference wind turbine. 2020. (Cited pages xvi, 89, 159, 160, 161 and 162.)

[54] Rongzhen Gao, Junwei Yang, Hua Yang, and Xiangjun Wang. Wind-tunnel experimental study on aeroelastic response of flexible wind turbine blades under different wind conditions. Renewable Energy, 219:119539, 2023. (Cited page 42.)

[55] C. William Gear. The automatic integration of ordinary differential equations. Communications of the ACM, 14(3):176–179, 1971. (Cited page 48.)

[56] Charles William Gear. The numerical integration of ordinary differential equations. Mathematics of Computation, 21(98):146–156, 1967. (Cited page 48.)

[57] N Gregory, VG Quincey, CL O'Reilly, and DJ Hall. Progress report on observations of three-dimensional flow patterns obtained during stall development on aerofoils, and on the problem of measuring two-dimensional characteristics. Citeseer, 1971. (Cited page 33.)

[58] D Todd Griffith and Mayank Chetan. Assessment of flutter prediction and trends in the design of large-scale wind turbine rotor blades. In Journal of Physics: Conference Series, volume 1037, page 042008. IOP Publishing, 2018. (Cited pages 11 and 44.)

[59] Christian Grinderslev, Niels Nørmark Sørensen, Georg Raimund Pirrung, and Sergio González Horcas. Multiple limit cycle amplitudes in high-fidelity predictions of standstill wind turbine blade vibrations. Wind Energy Science, 7(6):2201–2213, 2022. (Cited page 19.)

[60] Giorgia Guma, Galih Bangga, Thorsten Lutz, and Ewald Krämer. Aeroelastic analysis of wind turbines under turbulent inflow conditions. Wind Energy Science, 6(1):93–110, 2021. (Cited page 152.)

[61] Patrick R Hammer, Daniel J Garmann, and Miguel R Visbal. Effect of aspect ratio on finite-wing dynamic stall. AIAA Journal, 60(12):6581–6593, 2022. (Cited pages xii, 35 and 36.)

[62] Patrick R Hammer, Daniel J Garmann, and Miguel R Visbal. Effect of aspect ratio on swept-wing dynamic stall. AIAA Journal, 61(10):4367–4377, 2023. (Cited pages xii and 36.)

[63] Ásta Hannesdóttir, David Robert Verelst, and Albert Meseguer Urbán. Extreme coherent gusts with direction change–probabilistic model, yaw control and wind turbine loads. Wind Energy Science Discussions, 2022:1–22, 2022. (Cited page 141.)

[64] Morten H Hansen. Aeroelastic instability problems for wind turbines. Wind Energy: An International Journal for Progress and Applications in Wind Power Conversion Technology, 10(6):551–577, 2007. (Cited pages xii, 3, 9, 39, 40, 44 and 103.)

[65] Morten Hartvig Hansen, Mac Gaunaa, and Helge Aagaard Madsen. A Beddoes-Leishman type dynamic stall model in state-space and indicial formulations. 2004. (Cited page 61.)

[66] Joachim C Heinz, Niels N Sørensen, and Frederik Zahle. Fluid–structure interaction computations for geometrically resolved rotor simulations using cfd. Wind Energy, 19(12):2205–2221, 2016. (Cited pages 71, 73, 74, 76 and 153.)

[67] Joachim C Heinz, Niels N Sørensen, Frederik Zahle, and Witold Skrzypiński. Vortex-induced vibrations on a modern wind turbine blade. Wind Energy, 19(11):2041–2051, 2016. (Cited pages 17 and 44.)

[68] Joachim Christian Heinz, Niels N Sørensen, and Frederik Zahle. Partitioned fluid-structure interaction for full rotor computations using CFD. PhD thesis, 2013. (Cited pages xii, xiii, 45, 46, 53, 54, 55, 56, 57 and 192.)

[69] JG Holierhoek. An overview of possible aeroelastic instabilities for wind turbine blades. Wind Engineering, 37(4):421–440, 2013. (Cited pages 9 and 37.)

[70] SG Horcas, T Barlas, F Zahle, and NN Sørensen. Vortex induced vibrations of wind turbine blades: Influence of the tip geometry. Physics of Fluids, 32(6):065104, 2020. (Cited page 17.)

[71] SG Horcas, NN Sørensen, F Zahle, GR Pirrung, and T Barlas. Vibrations of wind turbine blades in standstill: Mapping the influence of the inflow angles. Physics of Fluids, 34(5): 054105, 2022. (Cited pages xi, 4, 17, 18, 19, 44, 189 and 190.)

[72] Xugang Hua, Qingshen Meng, Bei Chen, and Zili Zhang. Structural damping sensitivity affecting the flutter performance of a 10-mw offshore wind turbine. Advances in Structural Engineering, 23(14):3037–3047, 2020. (Cited page 44.)

[73] X Huang, M Albers, PS Meysonnat, M Meinke, and W Schröder. Analysis of the effect of freestream turbulence on dynamic stall of wind turbine blades. International Journal of Heat and Fluid Flow, 85:108668, 2020. (Cited page 29.)

[74] Christopher Lee Kelley and Joshua Paquette. Investigation of flutter for large, highly flexible wind turbine blades. In Journal of Physics: Conference Series, volume 1618, page 052078. IOP Publishing, 2020. (Cited page 12.)

[75] Janik Kiefer, Claudia E Brunner, Martin OL Hansen, and Marcus Hultmark. Dynamic stall at high reynolds numbers induced by ramp-type pitching motions. Journal of Fluid Mechanics, 938:A10, 2022. (Cited pages xii, 27 and 28.)

[76] Yusik Kim and Zheng-Tong Xie. Modelling the effect of freestream turbulence on dynamic stall of wind turbine blades. Computers & Fluids, 129:53–66, 2016. (Cited page 29.)

[77] Jesper Winther Larsen, Søren RK Nielsen, and Steen Krenk. Dynamic stall model for wind turbine airfoils. Journal of Fluids and Structures, 23(7):959–982, 2007. (Cited page 30.)

[78] Célia Laurent. Étude d'écoulements transitionnels et hors équilibre par des approches DNS et RANS. PhD thesis, Ecole nationale supérieure d'arts et métiers-ENSAM, 2012. (Cited pages 46 and 193.)

[79] Gordon J Leishman. Principles of helicopter aerodynamics. Cambridge university press, 2006. (Cited page 5.)

[80] J Gordon Leishman. Introduction to aerospace flight vehicles. Embry-Riddle Aeronautical University, 2023. (Cited pages xi and 22.)

[81] J Gordon Leishman and TS Beddoes. A semi-empirical model for dynamic stall. Journal of the American Helicopter society, 34(3):3–17, 1989. (Cited page 29.)

[82] Bei Li, De Tian, Xiaoxuan Wu, Huiwen Meng, and Yi Su. The impact of bend–twist coupling on structural characteristics and flutter limit of ultra-long flexible wind turbine composite blades. Energies, 16(15):5829, 2023. (Cited page 44.)

[83] Cédric Liauzun. Assessment of CFD techniques for wind turbine aeroelasticity. In ASME Pressure Vessels and Piping Conference, volume 47888, pages 341–350, 2006. (Cited pages 38 and 118.)

[84] Jaime Liew, Riccardo Riva, and Tuhfe Göçmen. Efficient mann turbulence generation for offshore wind farms with applications in fatigue load surrogate modelling. In Journal of Physics: Conference Series, volume 2626, page 012050. IOP Publishing, 2023. (Cited page 152.)

[85] Dajun Liu and Takafumi Nishino. Numerical analysis on the oscillation of stall cells over a naca 0012 aerofoil. Computers & Fluids, 175:246–259, 2018. (Cited page 34.)

[86] Don W Lobitz. Aeroelastic stability predictions for a mw-sized blade. Wind Energy: An International Journal for Progress and Applications in Wind Power Conversion Technology, 7(3):211–224, 2004. (Cited page 11.)

[87] J Loubeyres, J-L Pfister, F Blondel, and N Guy. Stall flutter instabilities on the iea-15 reference wind turbine in idling conditions: code-to-code comparisons and physical analyses. In Journal of Physics: Conference Series, volume 2265, page 032019. IOP Publishing, 2022. (Cited pages xiii, 42, 44, 63, 162 and 195.)

[88] Chao Lu and Tong-guang Wang. Modeling three-dimensional dynamic stall. Applied Mathematics and Mechanics, 32(4):393–400, 2011. (Cited page 30.)

[89] Per Lundsager, H Petersen, and S Frandsen. The Dynamic Behaviour of the Stall-regulated Nibe a Wind Turbine: Measurements and a Model for Stall-induced Vibrations. Risø National Laboratory, 1981. (Cited page 37.)

[90] N Maman and Charbel Farhat. Matching fluid and structure meshes for aeroelastic computations: a parallel approach. Computers & Structures, 54(4):779–785, 1995. (Cited page 53.)

[91] Marinos Manolesos and Spyros G Voutsinas. Study of a stall cell using stereo particle image velocimetry. Physics of Fluids, 26(4), 2014. (Cited pages 34 and 121.)

[92] Marinos Manolesos, Georgios Papadakis, and Spyros G Voutsinas. Experimental and computational analysis of stall cells on rectangular wings. Wind Energy, 17(6):939–955, 2014. (Cited pages xii, 33, 34, 121, 125 and 132.)

[93] Daigo Maruyama, Didier Bailly, and Gérald Carrier. High-quality mesh deformation using quaternions for orthogonality preservation. AIAA journal, 52(12):2712–2729, 2014. (Cited page 50.)

[94] Ivan Mary, Pierre Sagaut, and Michel Deville. An algorithm for unsteady viscous flows at all speeds. International journal for numerical methods in fluids, 34(5):371–401, 2000. (Cited page 47.)

[95] William J McCroskey, Kenneth W McAlister, Laurence W Carr, and SL Pucci. An experimental study of dynamic stall on advanced airfoil sections. volume 1: Summary of the experiment. Technical report, 1982. (Cited page 37.)

[96] Baptiste Meral. Validation d'une méthode haute fidélité de simulation des rotors d'hélicoptères, 2022. (Cited pages xii and 49.)

[97] Sanjay Mittal and Saurav Singh. Vortex-induced vibrations at subcritical re. Journal of Fluid Mechanics, 534:185–194, 2005. (Cited page 18.)

[98] T Moeller. Blade cracks signal new stress problem. WindPower Monthly, 25, 1997. (Cited page 41.)

[99] Hans Mueller-Vahl, Christoph Strangfeld, Christian Navid Nayeri, Christian Oliver Paschereit, and David Greenblatt. Thick airfoil deep dynamic stall. In Wind Energy-Impact of Turbulence, pages 35–40. Springer, 2014. (Cited pages xi, 25 and 26.)

[100] ourworldindata. Electricity mix. Technical report, ourworldindata, 2024. URL https://ourworldindata.org/electricity-mix. (Cited page 1.)

[101] Michael P Païdoussis, Stuart J Price, and Emmanuel De Langre. Fluid-structure interactions: cross-flow-induced instabilities. Cambridge University Press, 2010. (Cited page 102.)

[102] Andreas Søndergaard Pedersen and Christian Sigge Steiniche. Safe operation and emergency shutdown of wind turbines. Aalborg University, 2012. (Cited page 153.)

[103] Alberto Pellegrino and Craig Meskell. Vortex shedding from a wind turbine blade section at high angles of attack. Journal of Wind Engineering and Industrial Aerodynamics, 121: 131–137, 2013. (Cited pages 15, 16 and 189.)

[104] Didier Petot. Differential equation modeling of dynamic stall. La Recherche Aerospatiale(English Edition), (5):59–72, 1989. (Cited pages 29 and 30.)

[105] Jean-Lou Pfister. Instabilities and optimization of elastic structures interacting with laminar flows. PhD thesis, UNIVERSITE PARIS-SACLAY, 2019. (Cited page 49.)

[106] Serge Piperno and Charbel Farhat. Partitioned procedures for the transient solution of coupled aeroelastic problems - part ii: energy transfer analysis and three-dimensional applications. Computer methods in applied mechanics and engineering, 190(24-25):3147–3170, 2001. (Cited page 55.)

[107] Serge Piperno, Charbel Farhat, and Bernard Larrouturou. Partitioned procedures for the transient solution of coupled aroelastic problems - part i: Model problem, theory and two-dimensional application. Computer methods in applied mechanics and engineering, 124(1-2): 79–112, 1995. (Cited pages 45, 55 and 192.)

[108] Georg Raimund Pirrung, Christian Grinderslev, Niels Nørmark Sørensen, and Riccardo Riva. Vortex-induced vibrations of wind turbines: From single blade to full rotor simulations. Renewable Energy, 226:120381, 2024. (Cited pages 19 and 189.)

[109] ES Politis, IG Nikolaou, PK Chaviaropoulos, F Bertagnolio, Niels N Soerensen, and Jeppe Johansen. Know-blade task-4 report. navier-stokes aeroelasticity. 2005. (Cited page 41.)

[110] ES Politis, PK Chaviaropoulos, VA Riziotis, SG Voutsinas, and Ignacio Romero-Sanz. Stability analysis of parked wind turbine blades. In Proceedings of the EWEC, pages 16–19. Scientific Track, Marseille, 2009. (Cited pages 31 and 42.)

[111] Pariya Pourazarm, Yahya Modarres-Sadeghi, and Matthew Lackner. A parametric study of coupled-mode flutter for mw-size wind turbine blades. Wind Energy, 19(3):497–514, 2016. (Cited pages 11, 43 and 44.)

[112] Sara C Pryor and Rebecca J Barthelmie. A global assessment of extreme wind speeds for wind energy applications. Nature Energy, 6(3):268–276, 2021. (Cited page 4.)

[113] Daniele Ragni and Carlos Ferreira. Effect of 3d stall-cells on the pressure distribution of a laminar naca64-418 wing. Experiments in Fluids, 57(8):127, 2016. (Cited page 121.)

[114] Norizham Abdul Razak, Thomas Andrianne, and Grigorios Dimitriadis. Flutter and stall flutter of a rectangular wing in a wind tunnel. AIAA journal, 49(10):2258–2271, 2011. (Cited pages 37 and 38.)

[115] Antonio Recuero and Dan Negrut. Co-rotational formulation in chrono. ProjectCHRONO, Technical documentation, Università di Parma, Parma, Italy, accessed Feb, 19(2018):2, 2016. (Cited pages 50 and 193.)

[116] Roald Rietema. On the aeroelasticity of an extreme scale wind turbine: Using an FSI framework in NLR's in-house code ENSOLV. PhD thesis, 2019. (Cited pages 44, 45, 46, 52 and 192.)

[117] Daniel Rodríguez and Vassilis Theofilis. On the birth of stall cells on airfoils. Theoretical and Computational Fluid Dynamics, 25:105–117, 2011. (Cited page 121.)

[118] RTE. Futurs énergétiques 2050. Technical report, Réseau de Transport d'Électricité, 2021. URL https://www.rte-france.com/analyses-tendances-et-prospectives/bilan-previsionnel-2050-futurs-energetiques#Lesresultatsdeletude. (Cited pages 1 and 187.)

[119] S Sarkar and H Bijl. Nonlinear aeroelastic behavior of an oscillating airfoil during stall-induced vibration. Journal of Fluids and Structures, 24(6):757–777, 2008. (Cited page 41.)

[120] Konstantinos Sarras, Cynthia Tayeh, Vincent Mons, and Olivier Marquet. Linear stability analysis of turbulent mean flows based on a data-consistent reynolds-averaged navier–stokes model: prediction of three-dimensional stall cells around an airfoil. Journal of Fluid Mechanics, 1001:A41, 2024. (Cited pages 33 and 125.)

[121] W R Sears and B O Sparks. On the reaction of an elastic wing to vertical gusts. Journal of the Aeronautical Sciences, 9(2):64–81, 1941. (Cited page 10.)

[122] Anupam Sharma and Miguel Visbal. Numerical investigation of the effect of airfoil thickness on onset of dynamic stall. Journal of Fluid Mechanics, 870:870–900, 2019. (Cited pages xii and 27.)

[123] Juan Carlos Simo and Loc Vu-Quoc. On the dynamics in space of rods undergoing large motions—a geometrically exact approach. Computer methods in applied mechanics and engineering, 66(2):125–161, 1988. (Cited pages 63 and 195.)

[124] Witold Skrzypiński and Mac Gaunaa. Wind turbine blade vibration at standstill conditions—the effect of imposing lag on the aerodynamic response of an elastically mounted airfoil. Wind Energy, 18(3):515–527, 2015. (Cited page 42.)

[125] Witold Skrzypiński, Mac Gaunaa, Niels Sørensen, Frederik Zahle, and Joachim Heinz. Vortex-induced vibrations of a du96-w-180 airfoil at 90° angle of attack. Wind Energy, 17(10):1495–1514, 2014. (Cited page 16.)

[126] Witold Robert Skrzypinski, Mac Gaunaa, Niels N Sørensen, and Frederik Zahle. Modelling of unsteady airfoil aerodynamics for the prediction of blade standstill vibrations. In EWEC 2012-European Wind Energy Conference & Exhibition. European Wind Energy Association (EWEA), 2012. (Cited page 133.)

[127] Witold Robert Skrzypiński, Mac Gaunaa, Niels Sørensen, Frederik Zahle, and Joachim Heinz. Self-induced vibrations of a du96-w-180 airfoil in stall. Wind Energy, 17(4):641–655, 2014. (Cited pages 5, 42 and 191.)

[128] Niels N Sørensen and Scott Schreck. Computation of the national renewable energy laboratory phase-vi rotor in pitch motion during standstill. Wind Energy, 15(3):425–442, 2012. (Cited page 37.)

[129] Philippe Spalart and Steven Allmaras. A one-equation turbulence model for aerodynamic flows. In 30th aerospace sciences meeting and exhibit, page 439, 1992. (Cited pages 48 and 193.)

[130] Tyler Stehly, Patrick Duffy, and Daniel Mulas Hernando. Cost of wind energy review: 2024 edition. Technical report, National Renewable Energy Laboratory (NREL), Golden, CO (United States), 2024. (Cited page 1.)

[131] H Stiesdal. Extreme wind loads on stall regulated wind turbines. 1995. (Cited page 37.)

[132] Alexandre Suss. Couplage des methodes Navier-Stokes et Lattice Boltzmann pour les simulations aerodynamiques instationnaires. PhD thesis, HESAM Université, 2023. (Cited page 48.)

[133] DM Tang and EH Dowell. Comments on the onera stall aerodynamic model and its impact on aeroelastic stability. Journal of fluids and structures, 10(4):353–366, 1996. (Cited page 104.)

[134] Theodore Theodorsen. General theory of aerodynamic instability and the mechanism of flutter. Technical report, National Advisory Committee for Aeronautics. Langley Aeronautical Lab., 1949. (Cited page 10.)

[135] J Thirstrup Petersen, H Aagaard Madsen, A Björck, P Enevoldsen, S Øye, H Ganander, and D Winkelaar. Prediction of dynamic loads and induced vibrations in stall. Technical report, Riso National Laboratory, 1998. (Cited page 39.)

[136] CT Tran and D Petot. Semi-empirical model for the dynamic stall of airfoils in view of the application to the calculation of responses of a helicopter blade in forward flight. 1980. (Cited page 29.)

[137] Paul Veers, Katherine Dykes, Eric Lantz, Stephan Barth, Carlo L Bottasso, Ola Carlson, Andrew Clifton, Johney Green, Peter Green, Hannele Holttinen, et al. Grand challenges in the science of wind energy. Science, 366(6464):eaau2027, 2019. (Cited pages xi, 1 and 2.)

[138] Paul Veers, Carlo L Bottasso, Lance Manuel, Jonathan Naughton, Lucy Pao, Joshua Paquette, Amy Robertson, Michael Robinson, Shreyas Ananthan, Thanasis Barlas, et al. Grand challenges in the design, manufacture, and operation of future wind turbine systems. Wind Energy Science, 8(7):1071–1131, 2023. (Cited pages xi, 2 and 3.)

[139] Miguel R Visbal and Daniel J Garmann. Analysis of dynamic stall on a pitching airfoil using high-fidelity large-eddy simulations. AIAA Journal, 56(1):46–63, 2018. (Cited page 24.)

[140] Larry A Viterna and David C Janetzke. Theoretical and experimental power from large horizontal-axis wind turbines. Technical report, 1982. (Cited page 162.)

[141] Kai Wang, Vasilis A Riziotis, and Spyros G Voutsinas. Aeroelastic stability of idling wind turbines. Wind Energy Science, 2(2):415–437, 2017. (Cited pages 5, 42, 44 and 191.)

[142] Qi Wang, Michael A Sprague, Jason Jonkman, Nick Johnson, and Bonnie Jonkman. Beamdyn: A high-fidelity wind turbine blade solver in the fast modular framework. Wind Energy, 20(8):1439–1462, 2017. (Cited pages 63 and 195.)

[143] Xiangjun Wang, Lifeng Jiang, Ali Amjad, Hua Yang, and Junwei Yang. Experimental investigation on aeroelastic response of long flexible blades in turbulent flow. Applied Energy, 375:124109, 2024. (Cited page 43.)

[144] AE Winkelmann. On the occurrence of mushroom shaped stall cells in separated flow. In 16th Fluid and Plasmadynamics Conference, page 1734, 1983. (Cited page 35.)

[145] Guixiang Yi, Jingjing Pan, Lin Zhao, Lili Song, Genshen Fang, Wei Cui, and Yaojun Ge. Profiles of mean wind and turbulence intensity during strong typhoon landfall. Journal of Wind Engineering and Industrial Aerodynamics, 228:105106, 2022. (Cited pages 152 and 207.)

[146] Steven A Yon and Joseph Katz. Study of the unsteady flow features on a stalled wing. AIAA journal, 36(3):305–312, 1998. (Cited page 34.)

[147] GH Yu, XC Zhu, and ZH Du. Numerical simulation of a wind turbine airfoil: dynamic stall and comparison with experiments. Proceedings of the Institution of Mechanical Engineers, Part A: Journal of Power and Energy, 224(5):657–677, 2010. (Cited pages 24 and 38.)

[148] Yuelong Yu, Xavier Amandolese, Chengwei Fan, and Yingzheng Liu. Experimental study and modelling of unsteady aerodynamic forces and moment on flat plate in high amplitude pitch ramp motion. Journal of Fluid Mechanics, 846:82–120, 2018. (Cited page 153.)

[149] Frederik Zahle, Athanasios Barlas, Kenneth Lønbæk, Pietro Bortolotti, Daniel Zalkind, Lu Wang, Casper Labuschagne, Latha Sethuraman, and Garrett Barter. Definition of the iea wind 22-megawatt offshore reference wind turbine. 2024. (Cited pages 152 and 207.)

[150] Tatiana Zarutskaya and Rimon Arieli. On vortical flow structures at wing stall and beyond. In 35th AIAA Fluid Dynamics Conference and Exhibit, page 4913, 2005. (Cited page 35.)

[151] Lin Zhao, Wei Cui, and Yaojun Ge. Measurement, modeling and simulation of wind turbulence in typhoon outer region. Journal of Wind Engineering and Industrial Aerodynamics, 195:104021, 2019. (Cited pages 152 and 207.)

Résumé du mémoire

Introduction

Pour faire face au changement climatique, il est nécessaire de réduire l'utilisation des énergies fossiles. Avec l'énergie solaire, l'énergie éolienne est un substitut prometteur pour nous aider à réduire nos émissions de carbone. Dans son rapport « Futurs énergétiques 2050 » [118], le gestionnaire du réseau de transport d'électricité en France (RTE) présente des scénarios permettant à la France d'atteindre la neutralité carbone en 2050. Chaque scénario repose sur une réduction drastique des combustibles fossiles, compensée en partie par l'augmentation des énergies renouvelables, notamment l'énergie éolienne terrestre et offshore. Par exemple, dans les scénarios qui ne reposent pas sur l'énergie nucléaire mais uniquement sur les énergies renouvelables, la puissance installée des éoliennes terrestres doit passer de 18 GW à 74 GW en 2050, soit une multiplication par 4. De plus, 60 GW d'éoliennes offshore doivent être installés. Pour répondre à cette demande croissante, des améliorations technologiques sont nécessaires afin de continuer à réduire le coût de l'énergie éolienne.

Cela passe par l'agrandissement des éoliennes, rendant les pales plus légères, plus élancées et donc plus flexibles. Cette évolution les rend donc plus sensibles aux instabilités aéroélastiques, en particulier à l'arrêt, lorsque des vents forts peuvent provenir de n'importe quelle direction. De telles conditions peuvent se produire lors de l'installation des éoliennes, pendant leur maintenance ou en cas de défaillance du système d'alignement avec le vent. Les angles d'attaque aérodynamiques peuvent alors être très éloignés du fonctionnement normal de la machine, mettant la pale dans un état de décrochage. Ces cas d'éolienne à l'arrêt font l'objet du cas de charge (DLC) 6 de la certification CEI 61400-1.

Dans cette position, plusieurs phénomènes aéroélastiques sont susceptible d'apparaître, à savoir les vibrations induitent par vortex (VIV), les vibrations induitent par décrochage (SIV) et le flottement par couplage de mode. Ces phénomènes aéroélastiques résultent de l'interaction entre les forces aérodynamiques et la déformation de la structure. Lorsque la structure bouge, elle modifie l'écoulement de l'air. Ainsi, les forces aérodynamiques appliquées à la structure changent et en retour, impactent le mouvement de la structure. Les instabilités dynamiques se produisent lorsque ce couplage entraîne un transfert d'énergie de l'écoulement vers la structure. Parmi les instabilités susceptibles d'apparaître sur une pale à l'arrêt, cette thèse se concentre sur les vibrations induites par décrochage (Stall Induced Vibrations, SIV), où un processus de décrochage dynamique non linéaire peut conduire à un transfert d'énergie défavorable du fluide vers la structure. Alors que les approches numériques couplant des codes de simulations "haute-fidélité" fluide et structure (CFD/CSM) sont courantes en aéronautique, elles demeurent rares dans le domaine éolien.

L'objectif principal de cette thèse est donc de développer un outil de simulation CFD/CSM couplé et de l'utiliser, conjointement à des approches plus simples, pour étudier le comportement aéroélastique des vibrations induites par décrochage d'une grande pale d'éolienne de 15MW à l'arrêt.

Chapitre 1 : Les phénomènes aéroélastique d'une éolienne à l'arrêt

Afin de choisir le phénomène aéroélastique a étudier durant cette thèse, une revue de la littérature sur les différents phénomènes aéroélastiques pouvant affecter une éolienne à l'arrêt soumise à des vents forts a été réalisée. Trois principaux phénomènes ont été détaillés : le flottement par couplage de mode, les vibrations induites par vortex et les vibrations induites par décrochage.

Le flottement par couplage de mode

Le flottement par couplage de mode est une instabilité aéroélastique grave pouvant entraîner la rupture. Il se caractérise par le couplage de deux modes de structure ou plus à travers l'écoulement. Il a été observé pour la première fois sur les ailes d'avions pendant la Première Guerre mondiale et concerne principalement le couplage flexion-torsion. Il affecte les ailes ou les pales à faible angle d'attaque. Une illustration est proposée à la Figure R.1. La plupart du temps, l'angle de torsion oriente la force de portance dans la même direction que la vitesse, induisant une puissance positive du fluide vers la structure.

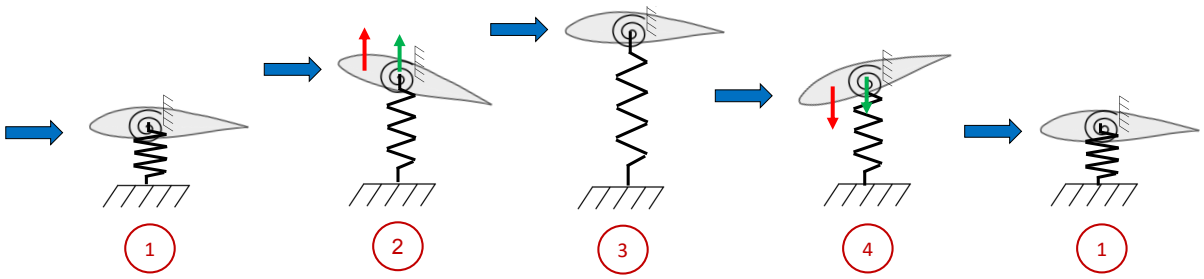

Figure R.1: Schéma d'un mode instable issu du flottement

Les conditions favorables au flottement par couplage de mode, à savoir un écoulement attaché de vitesse élevée, sont potentiellement réunies lorsque l'éolienne est en opération. Cela suggère que le risque de flottement par couplage de mode est plus élevé en fonctionnement. C'est pourquoi la plupart des études portent sur les éoliennes en fonctionnement. Néanmoins, celles-ci ont montré que la vitesse de rotation critique était supérieure à la vitesse de fonctionnement.

Bien que la vitesse de l'air soit plus faible à l'arrêt, l'écoulement est très différent entre une pale à l'arrêt et une pale en rotation. Pour étudier spécifiquement le cas à l'arrêt, Boersma et al. [19] ont mené des expériences sur une pale d'éolienne NREL 5 MW à l'échelle 30:1 placée dans une soufflerie. En remettant à l'échelle la vitesse de vent mesurée en soufflerie, ils ont trouvé une vitesse de vent critique d'environ 230 m/s pour une pale de taille réelle. Celle-ci est bien supérieure à la vitesse de vent rencontrée par une éolienne à l'arrêt. Il est donc peut probable que ce phénomène se produise sur une éolienne réelle.

Les vibrations induites par vortex

Les vibrations induites par vortex (VIV) sont une instabilité aéroélastique qui affecte les corps non profilés et qui a d'abord été étudiée par les ingénieurs civils pour les cheminées. En tant que corps non profilé, la tour de l'éolienne est sujette au VIV, mais à des angles d'attaque très élevés, les pales agissent également comme des corps non profilés pouvant ainsi subir le VIV. Cette instabilité est déclenchée par la formation de tourbillons qui génèrent des forces périodiques sur la structure. Si la fréquence des efforts aérodynamiques est proche d'une fréquence naturelle de la structure,

l'écoulement peut se coupler à la structure par un processus de *lock-in* qui produit des vibrations auto-limitées en amplitude.

Il a été observé expérimentalement que, pour une forme et un nombre de Reynolds donnés, la fréquence sans dimension du détachement tourbillonnaire est constante. Ce nombre sans dimension a été nommé nombre de Strouhal :

$$St = \frac{D f_s}{U_0}$$

où U_0 est la vitesse de l'écoulement, D une distance caractéristique et f_s la fréquence du détachement tourbillonnaire.

Pellegrino and Meskell [103] ont détaillé la variation du nombre de Strouhal du profil NREL S809 en fonction de l'angle d'attaque. Les résultats ont été obtenus à partir de simulations CFD d'une section fixe. La valeur minimale de St est d'environ 0,13 à un angle d'attaque de 90° et augmente lorsque l'angle d'attaque s'éloigne de 90°, pour atteindre environ 0,19 à 50° et 130°.

Concernant les pales complètes, l'impact de l'angle de pitch et de l'angle d'inclinaison de l'écoulement a été analysé par Horcas et al. [71] sur une pale de l'IEA 10MW pour un vent de 18m/s. Une carte de l'amplitude crête à crête selon la direction de la corde a ainsi été établie. Il a été observé que seules certaines combinaisons d'angles de pitch et d'inclinaison conduisent à des vibrations induites par vortex. On peut remarquer un régime à forte inclinaison en forme de C, entre 40° et 60°, et un régime à faible inclinaison sans forme claire, autour de 30°. Les deux régimes concernent un angle de pitch compris entre 80° et 105°, ce qui est plus étroit que la plage d'angles pour un profil aérodynamique 2D.

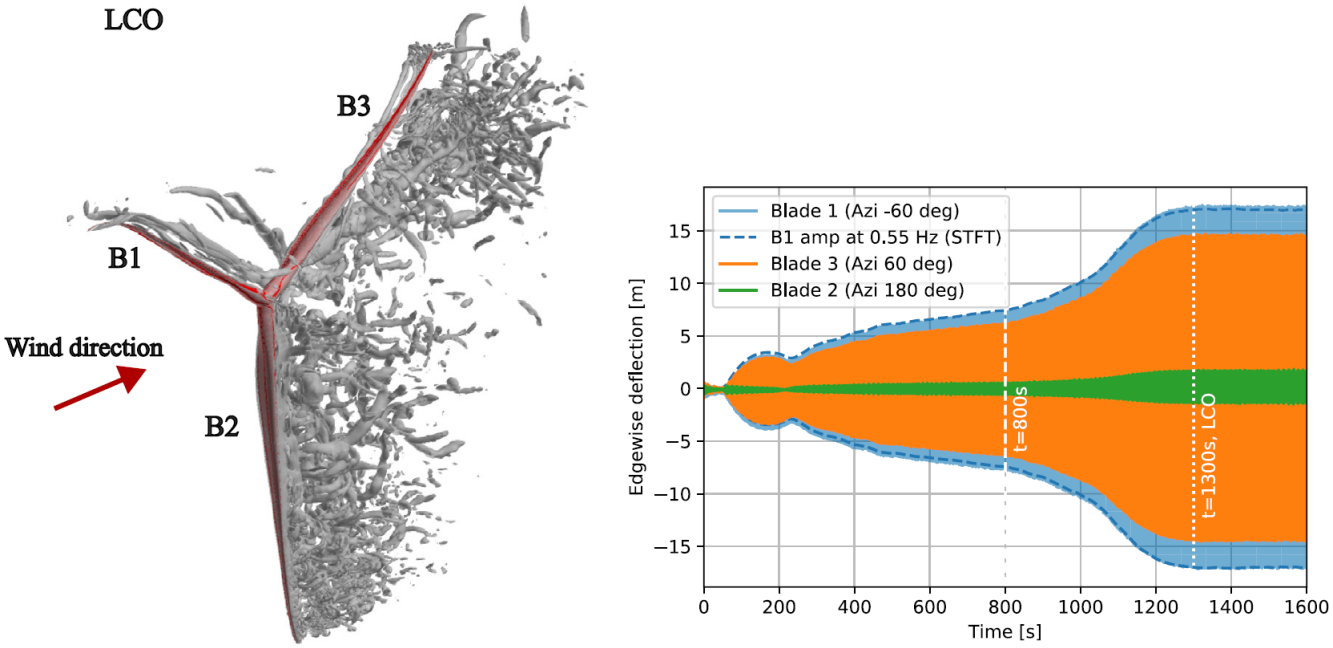

(a) Émissions de tourbillons représentés à l'aide d'iso-surfaces du critère Q de 5 pendant le LCO à 1600 s. [108]

(b) Démarrage des vibrations selon la corde pour les trois pales [108]

Figure R.2

Pirrung et al. [108] ont étendu l'étude à une simulation CFD/CSM complète du rotor. Certaines simulations ont été choisies sur la base de la cartographie de Horcas et al. [71] et celle qui a conduit aux vibrations les plus importantes a été détaillée. Elle correspond à un rotor placé dans

un écoulement uniforme de 18 m/s avec un angle de lacet de 90°. Toutes les pales sont tournées à 80°. La position azimutale est telle que la pale 1 a un angle d'inclinaison de 60°. Dans cette configuration, la simulation de pale isolée de Horcas et al. [71] a conduit à des vibrations selon la corde d'une amplitude à l'extrémité de 0,6 m. Cependant, comme on peut le constater sur la Figure R.2b, les vibrations ont atteint une amplitude crête à crête d'environ 30 m pour une pale de 96 m de long. Ce qui est supérieur à toutes les vibrations obtenues avec une pale isolée. Une visualisation de l'écoulement pendant le cycle limite (Figure R.2a) montre que le détachement de tourbillons de la pale 1 est bien corrélé. Le sillage de la pale 3 est composé de tourbillons orientés selon l'envergure provoqué par les mouvements importants de la structure, superposé à un fond de tourbillons sans corrélation. Aucune corrélation selon l'envergure n'est visible dans le sillage de la pale 2.

De telles conditions de vent ont une probabilité d'occurrence relativement élevée et constituent un sujet de préoccupation en termes de fatigue des pales. Cela est particulièrement vrai au regard du niveau élevé de vibrations obtenu lors des simulations avec rotor complet.

Les vibrations induites par décrochage

Les vibrations induites par décrochage (SIV) sont une instabilité aéroélastique principalement rencontrée dans le génie civil. Cependant, elles peuvent également apparaître pour les profils aérodynamiques en régime décroché. Contrairement au flottement classique, le SIV peut apparaître même si le mouvement de la structure n'est décrit que par un seul degré de liberté en flexion ou en torsion. Il se caractérise par un amortissement aérodynamique négatif. La vitesse de vibration de la pale induit des efforts aérodynamiques qui, en retour, favorisent le mouvement. Les oscillations sont amplifiées jusqu'à ce que le système atteigne un cycle limite (LCO) à cause des non-linéarités. Même si le SIV est similaire en génie civil et en aéronautique, les méthodes pour l'étudier diffèrent selon le domaine. Avec des corps profilés, l'écoulement peut n'être que partiellement séparé, ce qui justifie l'utilisation de modèles de décrochage dynamique. Au contraire, les corps non profilés sont généralement complètement décrochés et la vitesse critique est principalement estimée à l'aide d'une aérodynamique quasi-stationnaire.

Dans le cadre des vibrations induites par décrochage, les instabilités sont de deux types. Le premier type regroupe le flottement de décrochage et le galop de torsion, qui font référence aux vibrations de torsion. Le terme "stall flutter" est utilisé en aéronautique, où les corps sont profilés, tandis que le terme "galop" est utilisé en génie civil, où les corps sont non profilés. Le pont de Tacoma est un exemple célèbre de galop de torsion en génie civil. Le deuxième type de SIV correspond au galop de flexion, qui fait référence aux vibrations en flexion. Il affecte principalement les corps dont le coefficient de portance ou le coefficient aérodynamique transversal a une pente négative. Par exemple, les éoliennes régulées par décrochage étaient sujettes à des vibrations selon la corde pendant leur fonctionnement. Pour limiter la survitesse en fonctionnement, les pales entraient en régime décroché lorsque la vitesse du vent dépassait une valeur spécifique. De plus, avec le tilt, les pales subissaient un angle d'attaque variant dans le temps, ce qui entraînait un décrochage dynamique. Cependant, ce type d'éolienne n'est plus utilisé. L'autre type d'éolienne, l'éolienne régulée activement par pitch, n'entre pas en décrochage pendant son fonctionnement car le pitch est contrôlé pour limiter la vitesse du rotor et ne nécessite pas la saturation passive du régime décroché. Ainsi, elles ne sont pas susceptibles de subir un SIV pendant leur fonctionnement. Cependant, les pales des éoliennes régulées par pitch peuvent subir un angle d'attaque (AoA) élevé lorsque l'éolienne est à l'arrêt ou en mode de fonctionnement ralenti si le vent provient du côté. Cela signifie que, dans de telles conditions, les pales peuvent décrocher et être potentiellement soumises au SIV.

Les vibrations induites par décrochage sont différentes des vibrations induites par vortex, car le SIV est induit par le mouvement tandis que le VIV est provoqué par une instabilité de l'écoulement. Cela signifie que le SIV nécessite une perturbation initiale (par exemple la turbulence) pour démarrer, tandis que le VIV est déclenché par la formation de tourbillons, un phénomène purement fluidique. Par conséquent, les vitesses réduites qui déclenchent les VIV ou les SIV sont différentes. Pour le VIV, la vitesse réduite doit être proche de l'inverse du nombre de Strouhal afin que le détachement des tourbillons soit synchronisé avec la structure, tandis que pour le SIV, l'amortissement aérodynamique diminue et devient négatif lorsque la vitesse réduite augmente, de sorte que l'instabilité apparaît lorsque la vitesse réduite atteint une valeur spécifique correspondant au moment où l'amortissement aérodynamique négatif l'emporte sur l'amortissement structurel. De plus, la plage d'angles d'attaque des instabilités diffère également. Le VIV concerne les angles d'attaque compris entre 80° et 105°, tandis que le SIV peut se produire pour tous les angles d'attaque satisfaisant les conditions de portance, de traînée et de moment. En général, il se produit lorsque la pente de portance est négative, ce qui signifie qu'il peut se produire juste après l'angle de décrochage, lorsque l'écoulement autour de l'aile est encore partiellement séparé, ou à des angles d'attaque beaucoup plus élevés.

Dans ce contexte, plusieurs études ont examiné le SIV sur les éoliennes. Wang et al. [141] a simulé une éolienne complète de 10 MW au ralenti avec lacet. Le modèle était constitué d'éléments de poutre aéroélastiques couplés au modèle de décrochage dynamique de l'ONERA. Il a permis d'effectuer des simulations temporelles et une analyse aux valeurs propres du système couplé. Les fortes vibrations selon la corde observées dans les simulations temporelles ont été confirmées par l'analyse des valeurs propres, où les modes orientés selon la corde étaient instables pour tous les angles azimutaux. Les modes de flap étaient également instables, mais uniquement pour une plage limitée d'angles azimutaux autour de 0°. Cependant, les simulations basées sur le modèle de décrochage dynamique ne sont pas capables de capturer le comportement 3D de l'écoulement qui peut être important dans l'apparition de l'instabilité. Skrzypiński et al. [127] a examiné la possibilité de SIV et VIV sur un profil aérodynamique extrudé à l'aide de simulations URANS. Le profil aérodynamique a été placé dans un écoulement uniforme à un angle d'attaque de 24°, ce qui correspond à l'angle le plus instable donné par une analyse pseudo-statique. Le profil a été forcée d'osciller d'avant en arrière dans le sens de la corde. Il semble que lorsque la fréquence des oscillations est proche de la fréquence de détachement des tourbillons, la puissance des efforts aérodynamiques est positive, ce qui indique un possible VIV. En diminuant la fréquence d'oscillation, la puissance diminue d'abord, puis redevient positive, ce qui indique un possible SIV. La vitesse de vent nécessaire pour déclencher le SIV était cependant très élevée pour cette configuration. De plus, il s'agissait uniquement de simulations de profils aérodynamiques extrudés avec des mouvements harmoniques imposés. Des investigations supplémentaires pourraient donc être nécessaires.

Choix du phénomène aéroélastique

Un résumé des conditions de vent déclenchant le flottement par couplage de mode (flutter), les vibrations induites par vortex (VIV) et les vibrations induites par décrochage (SIV) est présenté Figure R.3.

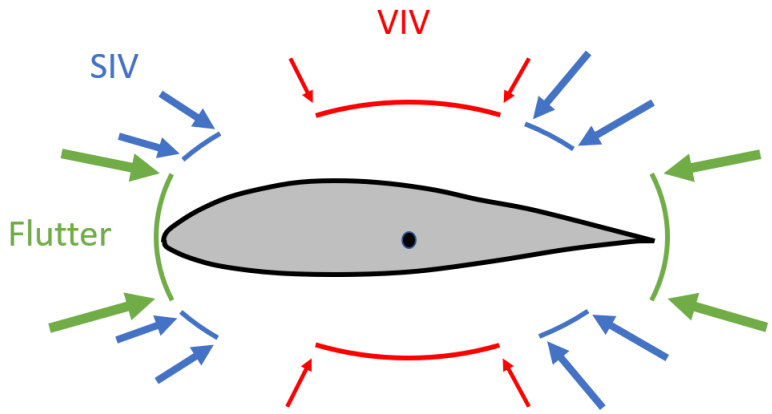

Figure R.3: Représentation schématique montrant la direction du vent susceptible de déclencher des instabilités aéroélastiques. L'épaisseur de la flèche donne une idée de la vitesse critique.

Sur la base de cette revue de la littérature, il a été établi que parmi les phénomènes de flottement par couplage de modes, VIV et SIV, celui qui était le moins bien compris et qui ne bénéficiait pas de simulation haute fidélité CFD/CSM était le SIV. C'est pourquoi il a été décidé de se concentrer sur les vibrations induites par décrochage dans le cadre de cette thèse.

Chapitre 2 : Les méthodes numériques pour les simulations aéroélastique hautes fidélités

En aéroélasticité, la dynamique des fluides et celle des structures interagissent. Il est donc nécessaire de simuler les deux phénomènes physiques, en utilisant l'un comme conditions aux limites pour l'autre. Il existe deux approches principales pour traiter les problèmes multi-domaines impliquant différentes physiques. L'approche de couplage monolithique regroupe les différentes physiques dans un seul système et les résout toutes ensemble. À l'inverse, l'approche de couplage partitionné résout les différentes physiques séparément et l'interaction est réalisée en échangeant les données nécessaires via une interface commune [68, 116].

L'approche monolithique est généralement utilisée pour des problèmes de couplage spécifiques. Le système complet d'équations est assez rigide, ce qui rend cette approche difficile à calculer et ingérable sur le plan logiciel pour les applications industrielles [107]. Elle est principalement utilisée dans un contexte universitaire afin de permettre une analyse mathématique détaillée [68].

D'un point de vue numérique, l'approche partitionnée présente plusieurs avantages par rapport à l'approche monolithique. Les sous-systèmes étant traités indépendamment, il est possible d'utiliser des solveurs spécialisés pour chaque domaine du système global. Cette approche est très flexible et permet une modularité logicielle. En aéroélasticité, le solveur fluide calcule le comportement de l'écoulement et fournit les efforts fluide (c'est-à-dire la pression sur la paroi et la contrainte de cisaillement). Ensuite, un module de transfert des efforts transforme ces efforts fluide en un format d'efforts accepté par le solveur structurel. Ce dernier déforme la structure en fonction de son chargement. Enfin, un module de transfert de mouvement déplace les interfaces fluides en

fonction de la position de la structure. Avec la CFD, les conditions aux limites sont déplacées et le maillage est déformé. Un schéma de cette procédure est présenté dans la Figure R.4.

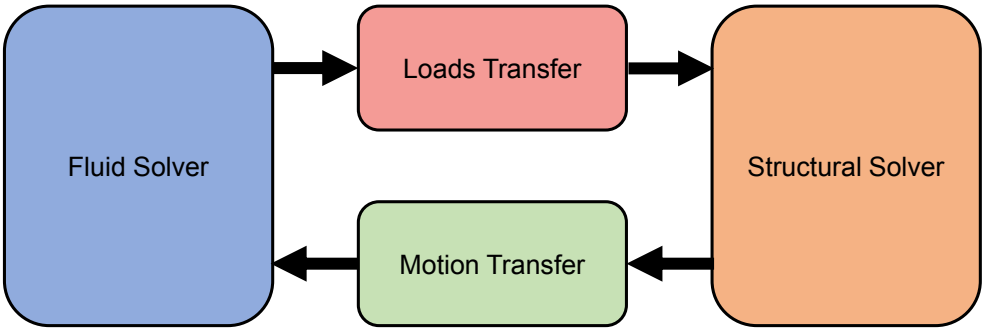

Figure R.4: Schéma du couplage partitionné

Dans cette thèse, une approche monolithique est utilisée au chapitre 4 avec le modèle sectionnel équivalent. Mais les simulations haute fidélité utilisent une approche partitionnée.

Les outils choisis pour les simulations haute fidélité

Le solveur CFD utilisé dans la présente étude pour simuler la dynamique des fluides est le solveur *FastS* développé à l'ONERA [78]. Il s'agit d'un solveur de recherche optimisé pour les maillages structurés qui permet de réaliser des simulations (Unsteady) Reynolds-Averaged Navier–Stokes (URANS). Les équations compressibles de Navier-Stockes sont résolues à l'aide d'une technique de discrétisation par volumes finis. Elle consiste à subdiviser l'espace à l'aide d'un maillage et à résoudre la forme conservatrice des équations de Navier-Stockes dans chaque volume. La valeur moyenne des quantités de l'écoulement dans un volume est ensuite obtenue en additionnant tous les flux à chacune de ses faces au fil du temps. Dans *FastS*, la turbulence est modélisée à l'aide du modèle de Spalart-Allmaras [129]. Il suppose que le tenseur de contrainte de Reynolds suit l'hypothèse de Boussinesq, ce qui introduit une viscosité turbulente. Le modèle de Spalart-Allmaras est un modèle à une équation qui donne l'évolution temporelle et spatiale de cette viscosité turbulente. Les simulations URANS avec le modèle Spalart-Allmaras sont efficaces pour simuler des écoulements attachés ou légèrement détachés autour des ailes et des pales [7].

Concernant la structure, un modèle de poutre semble approprié pour une pale d'éolienne. Le solveur de poutre corotationnelle d'Euler-Bernoulli inclus dans *projectChrono* [115] a été choisi. La formulation corotationnelle consiste à décomposer le mouvement de chaque élément en un mouvement rigide et un mouvement de déformation. Le mouvement rigide est décrit par le mouvement d'un repère corotationnel attaché à l'élément, ce qui permet d'obtenir une rotation aussi grande que l'on souhaite. La déformation est ensuite résolue dans le repère corotationnel. De cette manière, l'hypothèse des petites déformations peut être prise dans ce repère local.

Un outil de déformation de maillage est également utilisé pour que le déplacement de la structure puisse être pris en compte dans le solver fluide. Ici, la déformation de maillage est réalisée par *Quantum*, un outil développé à l'ONERA. Celui-ci est fondé sur une méthode de pondération inverse par la distance (IDW) avec des quaternions. L'avantage de *Quantum* est qu'il permet d'importantes déformations tout en conservant l'orthogonalité du maillage près des parois.

Chapitre 3 : Implémentation et validation d'un environnement de couplage modulaire pour les simulations couplant fluide et structure

Pour simuler numériquement les phénomènes aéroélastiques, une approche modulaire basée sur un couplage partitionné entre différents solveurs fluide et structure a été choisie. Elle permet de passer facilement d'un niveau de fidélité à l'autre pour le calcul du fluide et/ou de la structure. Pour fonctionner ensemble, ces deux solveurs doivent échanger des informations. Le couplage entre plusieurs solveurs a été implémenté, mais le développement principal concerne le couplage entre *Chrono* et *FastS*. Les idées générales sont les suivantes. *Chrono* a besoin des efforts aérodynamiques sur chaque nœud de la poutre. Ces efforts sont issus de l'intégration de la pression aux parois CFD et de la contrainte de cisaillement pour chaque section liée à un nœud structurel. Le solveur structurel déforme la pale en fonction des forces aérodynamiques. Ensuite, le solveur CFD *FastS* a besoin d'un maillage de la nouvelle configuration de la pale. Pour ce faire, les parois du maillage doivent être déformées en fonction du déplacement de la poutre. Comme le maillage fluide et le maillage de la poutre ne concordent pas à l'interface, une méthode cinématique fondée sur l'hypothèse de sections rigides doit être employée. *Quantum* permet la propagation de la déformation dans le volume du maillage. Ce chapitre traite de l'implémentation et de la validation de toutes ces étapes.

L'objectif du présent framework Python développé dans le cadre de cette thèse est d'interagir avec les différents solveurs fluides et structures, et de regrouper les méthodes de transfert. Le framework s'articule autour d'un fichier principal qui appelle les différentes classes. Celui-ci commence par lire les paramètres et initialiser les solveurs correspondants. Ensuite deux fonctions sont possibles: une fonction de couplage statique permet de calculer l'équilibre aéroélastique et une fonction de couplage aéroélastique dynamique dans laquelle la boucle temporelle est implémentée. Les principales catégories de classes sont les classes fluides, les classes structures et les classes de transfert. Un diagramme UML est présenté à la figure R.5.

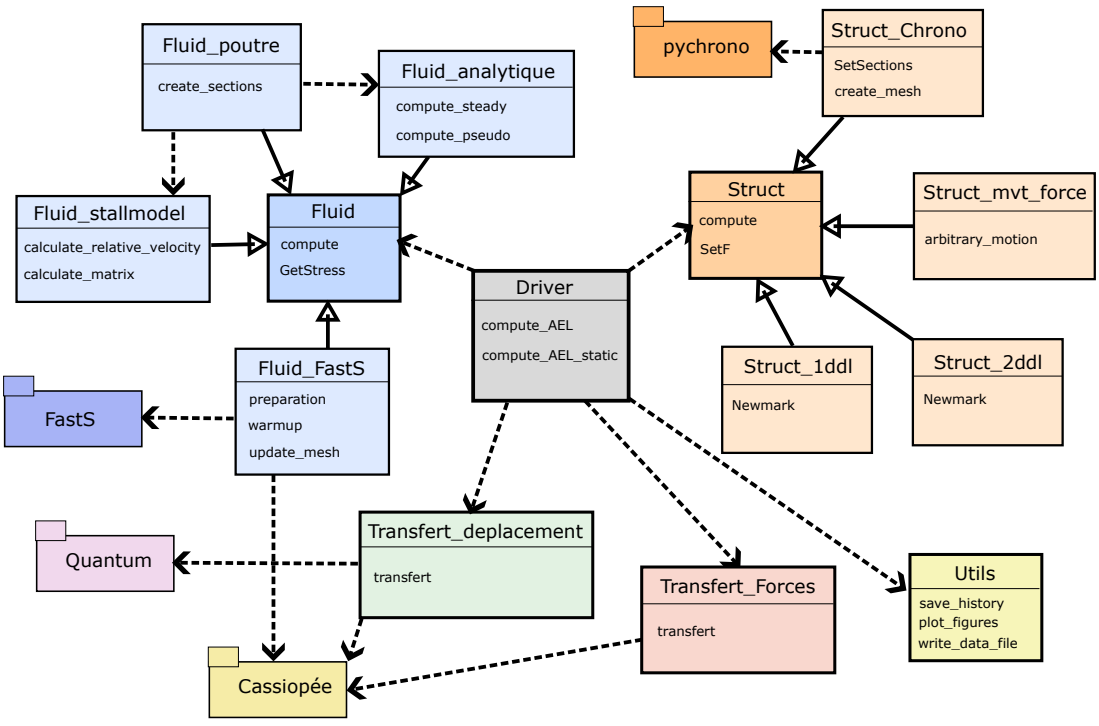

Figure R.5: Diagramme UML du framework python

Validation des solveurs fluide et structure

L'objectif de cette section a été de valider la capacité du solveur CFD *FastS* à capturer le processus de décrochage dynamique d'une section de profil aérodynamique épais, représentative d'une pale d'éolienne, forcée à osciller en pitch. Les résultats de *FastS* ont été comparés à des expériences réalisées sur un profil aérodynamique NACA 63_4421 et aux résultats obtenus avec le modèle de décrochage dynamique de l'ONERA. Les essais ont consisté à simuler un profil oscillant à l'aide du solveur CFD *FastS* pour $\bar{\alpha} = 13,5°$, $\tilde{\alpha} = 8°$ et trois fréquences réduites différentes $k_1 = 0,0183$ (oscillation lente), $k_2 = 0,0785$ et $k_3 = 0,183$ (oscillation rapide). Le profil aérodynamique est forcé à osciller en pitch autour de son quart de corde selon l'expression :

$$\alpha = \bar{\alpha} + \tilde{\alpha}\sin(2\pi f t)$$

où la fréquence f est choisie de manière à correspondre à la fréquence réduite prescrite. En ce qui concerne les résultats dynamiques du coefficient de portance, le solveur *FastS* et le modèle de décrochage dynamique reproduisent correctement les boucles expérimentales pour $k_1 = 0,0183$ et $k_2 = 0,0785$. Pour la fréquence réduite la plus élevée ($k_3 = 0,183$), le solveur CFD sous-estime légèrement le dépassement de portance au-delà de 17°, tandis que le modèle de décrochage dynamique ONERA produit une boucle pour laquelle le coefficient de portance est considérablement sous-estimé pendant le processus de rattachement.

La mise en données structure de la pale de l'IEA 15MW dans *Chrono* a également été validée en se confrontant aux résultats de Loubeyres et al. [87]. Ces essais consistent à mesurer les déplacements de l'extrémité de la pale pour des forces axiales, dans le plan ou hors du plan, d'intensité variable. Ces résultats ont été obtenus à l'aide de deux solveurs basés sur des modèles géométriquement exacts de la théorie des poutres permettant des déplacements et des rotations importants : *DeepLines* et *BeamDyn*. Le premier, *DeepLines*, utilise une formulation similaire à celle développée par Simo and Vu-Quoc [123], tandis que *BeamDyn* s'appuie sur une méthode spectrale [142]. Les résultats obtenus avec *Chrono* concordent bien avec ceux obtenus avec les solveurs *BeamDyn* et *DeepLines*. Des différences significatives sont néanmoins observées pour le déplacement de l'extrémité dans le plan rotor suite à une charge pure dans le plan rotor. Il semble que notre modèle éléments finis soit plus rigide dans le plan rotor que les deux autres modèles. Sinon, tous les couplages flexion-torsion et flexion-flexion sont correctement reproduits.

Implémentation et vérification des transferts

Les méthodes de transferts ont ensuite été implémentées et vérifiées.

Pour le transfert du mouvement, à chaque pas de temps, la pale se déplace. Il faut donc calculer les nouvelles coordonnées de chaque point du maillage de la peau fluide à chaque itération. Les coordonnées d'un point P_i du maillage fluide peuvent être décomposées en coordonnées du point projeté sur la ligne moyenne de la poutre et en position du point dans la section associée:

$$\boldsymbol{X}^{(i)} = \boldsymbol{X_C}\left(s^{(i)}\right) + \mathbf{R}\left(s^{(i)}\right)\boldsymbol{X_l}\left(s^{(i)}\right) \tag{5.2}$$

où $\boldsymbol{X}^{(i)}$ est la coordonnée dans le repère global du point P_i, $s^{(i)}$ est l'abscisse curviligne du point projeté sur la ligne moyenne de la poutre, $\boldsymbol{X_C}\left(s^{(i)}\right)$ est la coordonnée du point de la ligne moyenne, $\mathbf{R}\left(s^{(i)}\right)$ est la matrice de rotation du point de la ligne moyenne et $\boldsymbol{X_l}\left(s^{(i)}\right)$ est la position du point P_i dans la section de poutre par rapport au repère de section $\mathcal{R}_s$.

Pour vérifier la méthode et son implémentation, les efforts obtenues à l'aide d'une simulation CFD rigide à $U_0 = 40m/s$ et $\alpha_0 = 3°$ sont imposées au modèle de poutre. Une simulation structurelle statique est effectuée pour calculer l'état déformé. Ce nouvel état est utilisé pour calculer la

nouvelle géométrie du maillage de la peau comme expliqué précédemment. Les géométries initiale et déformée du maillage de la peau sont comparées aux états initial et déformé de la poutre dans la Figure R.6.

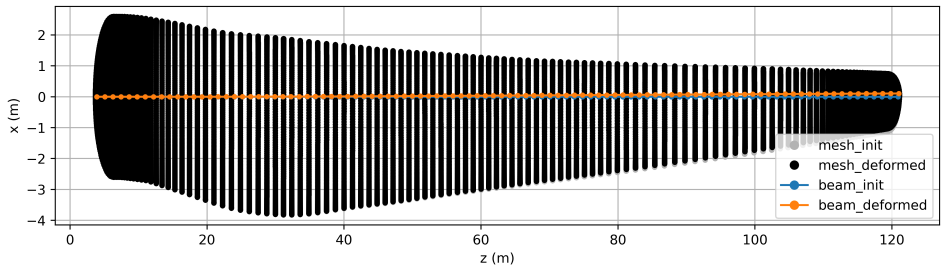

(a) Direction X

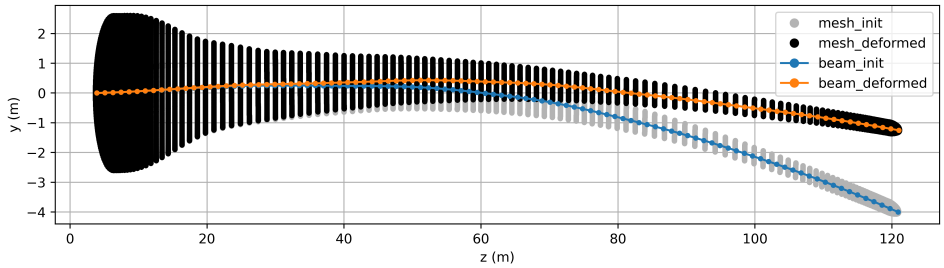

(b) Direction Y

Figure R.6: Déformation du maillage de peau

La ligne moyenne non déformée de la pale en bleu a été initialement placée dans le maillage initial de la paroi en gris. Ensuite, la poutre a été déformée pour prendre la forme orange. Ainsi, chaque point de la paroi en noir a correctement suivi la déformation et se trouve autour de l'état déformé de la poutre.

La deuxième méthode de transfert à implémenter est le transfert des forces aérodynamiques. Étant donné que le maillage structurel et le maillage fluide sont très différents, il a été choisi d'utiliser des coupes du maillage de peau le long de la pale. L'orientation des coupes est déterminée par l'orientation des sections de la structure. Pour les poutres d'Euler-Bernoulli, les sections sont perpendiculaires à la direction locale de la pale. Ensuite, la pression et la contrainte de cisaillement aux parois sont intégrées le long des contours définis par l'intersections des coupes et de la paroi, ce qui donne les forces linéiques. Un schéma est présenté dans la Figure R.7.

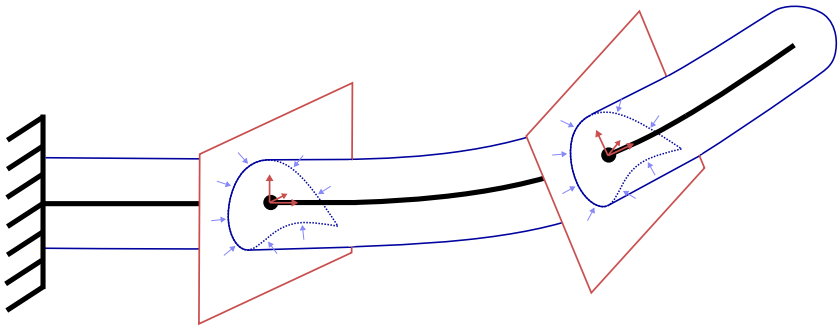

Figure R.7: Schéma des coupes. Les repères rouges sont les repères locaux des sections $\mathcal{R}_s$.

Chapitre 4 : Étude des vibrations induites par décrochage en utilisant des méthodes basse fidélité

Des études antérieures ont mis en évidence que les grandes pales d'éoliennes pouvaient potentiellement être sujettes à des vibrations induites par décrochage (SIV) à l'arrêt. L'évaluation des risques nécessite des calculs FSI pour différentes conditions de vent (direction et vitesse), ce qui peut s'avérer prohibitif avec une approche haute fidélité. De nombreuses études sur les vibrations induites par décrochage ont été réalisées à l'aide d'approches sectionnelles. Plus simples et moins coûteuses en termes de calcul, ces approches permettent d'étudier facilement différentes conditions de vent mais peuvent être remises en question pour les pales vrillées à section variable. Dans ce contexte, comment choisir la section la plus pertinente d'une pale spécifique ? Est-il possible de définir une section équivalente ? Des questions se posent également concernant le modèle aérodynamique. Des approches quasi-statiques sont souvent utilisées, mais des études supplémentaires s'intéressant aux instabilités liées au processus de décrochage dynamique sont nécessaires. En effet, comme pour le flottement de décrochage, les boucles de décrochage dynamique devraient également avoir un impact sur l'amortissement aérodynamique. Cependant, les modèles de décrochage dynamique dépendent fortement des profils de section, de l'angle d'attaque moyen et de la fréquence réduite (qui est proportionnelle à la corde), ce qui soulève à nouveau la question du choix de la meilleure section le long de la pale ou de l'identification d'une section équivalente. Dans ce contexte, l'objectif de ce chapitre est d'évaluer le potentiel des approches par modèle de section pour étudier les vibrations induites par décrochage à l'arrêt. Notre objectif est de construire un modèle de section équivalent qui soit le plus proche possible d'une pale complète spécifique, la pale de l'IEA15MW. Pour ce faire, un modèle de section équivalent à 2 degrés de liberté (*flapwise* et *edgewise*), couplé avec un modèle d'aérodynamique quasi-stationnaire ou avec le modèle de décrochage dynamique de l'ONERA, sera comparé à une approche continue. Enfin, cette étude vise également à préparer des simulations haute fidélité en identifiant quelques configurations de SIV pertinentes.

Développement d'un modèle de section équivalente

Le modèle développé est une section équivalente, non liée à une section spécifique de la pale. Il possède deux degrés de liberté, *edgewise* dans la direction x et *flapwise* dans la direction y. La direction x est définie par α_{edgewise} selon une direction de référence utilisée dans le github de l'IEA15MW. Comme la pale est vrillée, la corde de la section équivalente n'est pas nécessairement alignée avec la direction *edgewise*. Un angle $\alpha^{2D}_{\text{twist}}$ est alors introduit dans la Figure R.8. Dans la mesure où le moment aérodynamique de torsion peut déformer la pale, une équation d'équilibre en torsion est également prise en compte, ainsi que la contribution des couplages flexion-torsion. Tous les paramètres de la section équivalente sont choisis afin de modéliser la dynamique de l'IEA15MW aussi fidèlement que possible. L'idée générale consiste à comparer les équations du mouvement de la section équivalente avec les équations modales de la pale, en ne tenant compte que des modes *flapwise* et *edgewise*, afin d'identifier les meilleurs paramètres de section. Ce processus d'identification est réalisé en tenant compte d'un modèle aérodynamique quasi-stationnaire introduisant une vitesse effective et un angle d'attaque effectif qui dépendront du mouvement.

La procédure comprend cinq étapes. La première étape consiste à écrire l'équation linéarisée sans dimension du modèle de section à 2 degrés de libertés. Dans la deuxième étape, le même traitement est effectué pour les équations modales de la pale. Ensuite, dans une troisième étape, les termes d'amortissement aérodynamique dominants selon le *flapwise* des deux modèles sont mis en regard. Des hypothèses simplificatrices négligeant le vrillage, le *prebend* (pré-déformation) et les couplages flexion-torsion permettent l'identification d'une corde et d'un angle équivalents α_{edgewise}.

Dans la quatrième étape, les hypothèses sont relaxées tout en gardant la corde équivalente. La comparaison des deux amortissements aérodynamiques permet alors de définir une polaire équivalente calculable numériquement. Enfin, les coefficients de couplage flexion-torsion sont identifiés dans une cinquième étape en comparant les raideurs aérodynamiques des deux modèles.

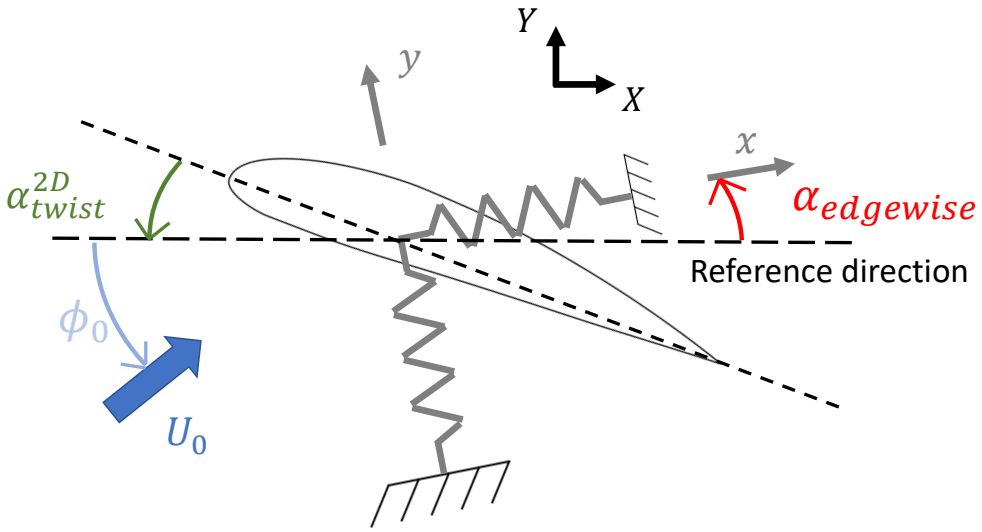

Figure R.8: Schéma de la section équivalente

Le modèle de section équivalente a été validé via une confrontation avec un modèle modal linéarisé de pale, constitué des 7 premiers modes structurels, couplé à un modèle aérodynamique quasi-stationnaire. Une analyse de stabilité présentée dans la Figure R.9 montrent que le modèle de section et le modèle modal de pale prédisent des zones instables identiques à l'exception d'un léger décalage dû à la rigidité aérodynamique non équivalente.

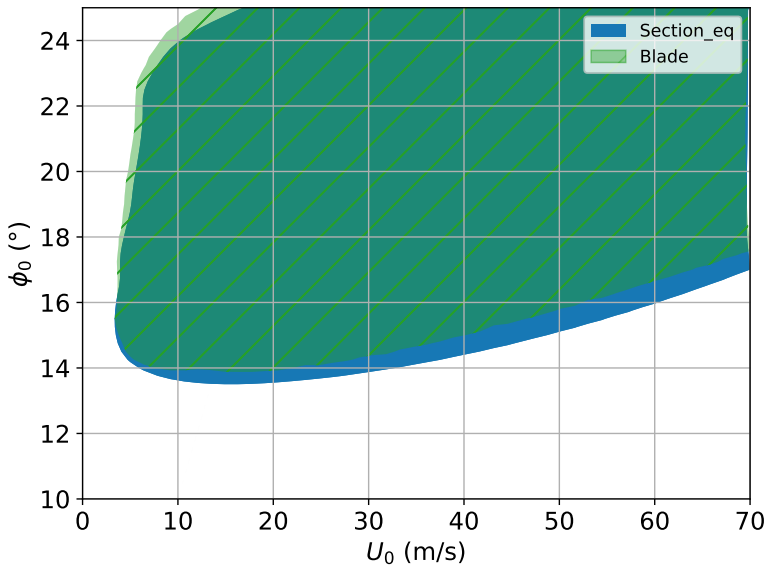

Figure R.9: Cartes de stabilité de la section équivalente et du modèle modal linéarisé de pale (avec les 7 premiers modes) utilisant une aérodynamique quasi-stationnaire. Les zones colorées sont instables.

Effet du modèle de décrochage dynamique

Les effets du modèle de décrochage dynamique de l'ONERA sur le comportement aéroélastique de la section équivalente est étudié. Lorsqu'il s'agit d'un décrochage dynamique, la forme de la boucle aérodynamique instable est très importante pour évaluer le risque d'instabilité. À titre d'exemple, un mouvement sinusoïdal dans le sens *flapwise* (perpendiculaire à la corde) est imposé à la section équivalente avec une amplitude de $0,085c_{\text{eq}}$ pour les angles d'incidence 18° et 22° et un vent de 40 m/s. Le lien entre la pente de la boucle de décrochage dynamique représentée en fonction de l'angle d'attaque effectif (Fig R.10a) et le sens de rotation dans un graphique de Lissajous (Fig R.10b) peut être compris en suivant un cycle de mouvement harmonique (étapes 1 à 4 de la Figure R.10). L'étape 1 correspond à un maximum de q_{flap} où $\dot{q}_{flap} = 0$. L'angle d'attaque effectif est égal à l'angle d'incidence. De l'étape 1 à l'étape 3, $\dot{q}_{flap}$ est négatif. L'angle d'attaque effectif augmente jusqu'au point 2, puis diminue pour atteindre le point 3 où q_{flap} est minimal et $\dot{q}_{flap} = 0$. De l'étape 3 à l'étape 1, $\dot{q}_{flap}$ est positif. L'angle d'attaque effectif diminue pour atteindre son minimum au point 4, puis il augmente à nouveau jusqu'au point 1. La comparaison de la hauteur relative des points 2 et 4 donne la direction de rotation de la boucle sur le graphique de Lissajous. Lorsque 2 est supérieur à 4, comme pour la boucle autour de 19.5°, la rotation est antihoraire dans une représentation de Lissajous (c'est-à-dire qu'il n'y a pas de risque d'instabilité). Mais lorsque 2 est inférieur à 4, comme pour la boucle autour de $23,5°$, la rotation est horaire dans une représentation de Lissajous (c'est-à-dire qu'il y a un risque d'instabilité).

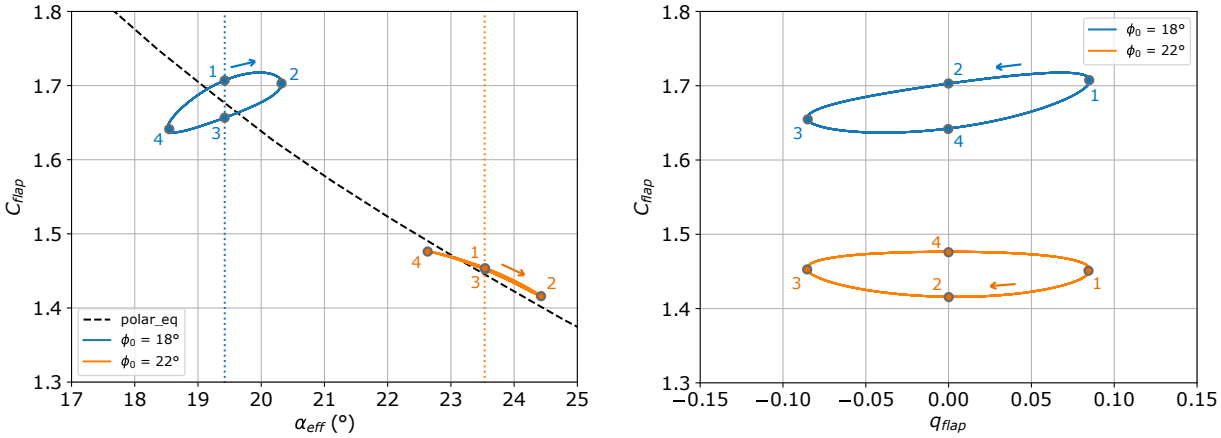

(a) Boucles de décrochage dynamique

(b) Graphique de Lissajous

Figure R.10: Évolution des coefficients de forces en fonction de (a) l'angle d'attaque effectif et (b) de la coordonnée *flapwise*.

Analyse de stabilité avec un modèle éléments finis de la pale

Dans cette section, le modèle de section équivalente est comparé à un modèle éléments finis de la pale complète qui utilise des éléments de poutre Euler-Bernoulli *corotated* tenant compte des non-linéarités géométriques. La comparaison des zones d'instabilité (Fig R.11) permet d'évaluer la représentativité et les limites du modèle de section équivalente.

Les résultats sont globalement cohérents entre les deux modèles. Cependant, près de la ligne neutre, certaines croix (c'est-à-dire des résultats instables pour le modèle de pale FEM) se trouvent en dehors de la zone instable du modèle de section équivalente. Cela provient probablement de l'effet combiné du décrochage dynamique de chaque section le long de la poutre qui n'est pas pris en compte par le modèle de section équivalente. L'effet de l'angle de torsion de l'état d'équilibre

qui déplace la zone instable est visible à partir de 60 m/s pour le modèle éléments finis. Cet effet est compensé par les boucles de décrochage dynamique dans le modèle de section équivalente.

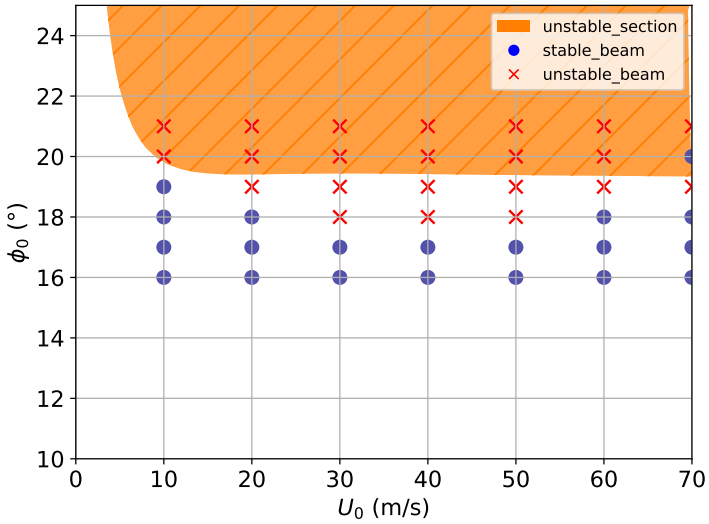

Figure R.11: Carte de stabilité $\phi_0 - U_0$ comparant le modèle de section equivalente et le modèle élément finis.

Discussions

Ces points de divergence entre les deux modèles sont ensuite discutés.

Contrairement à l'aérodynamique quasi-stationnaire, le décrochage dynamique a sa propre dynamique. Chaque section ayant une corde différente, le retard introduit par le décrochage dynamique est propre à chaque section. Lors du calcul de la force généralisée sur la pale, le comportement de chaque section doit donc être combiné. Or dans le modèle de section équivalente, le comportement aérodynamique est modélisé par un simple modèle de décrochage dynamique de l'ONERA, ce qui n'est pas équivalent à la dynamique combiné de toutes les sections de la pale. Cette simplification est évaluée et rend compte d'une limite d'un modèle de section équivalente.

Un autre point investigué est l'impact des polaires équivalentes sur l'équilibre aéroélastique. Comme ni la force généralisée moyenne, ni la raideur aérodynamique ajoutée, ne sont conservées entre la section équivalente et le modèle de pale, un écart dans l'état d'équilibre est observé. Cela se traduit par un déplacement des zones instables.

A part ces points de divergence entre modèles, certains points de modélisation de la section équivalente sont aussi discutés. La section équivalente proposée est comparée à un modèle de section plus simple afin d'identifier les propriétés les plus importantes. Il ressort que les plus grands changements proviennent d'une modification de la vitesse réduite pour une même vitesse de vent dû à la corde ainsi que de la modélisation de la torsion via le couplage flexion-torsion.

Enfin, l'impact d'un paramètre du modèle de décrochage dynamique de l'ONERA sur la stabilité de la section équivalente est évalué. La principale modification concerne les angles d'incidence inférieur à 20°. La zone instable s'est étendue vers des angles d'attaque plus faibles, car la pente moyenne des boucles diminue avec l'augmentation du paramètre r_{0_l}. Cela souligne la difficulté de prédire les cartes de stabilité avec des modèles de décrochage dynamique semi-empiriques comme le modèle ONERA. Une attention particulière doit être accordée à l'identification des paramètres du modèle. Pour ce faire, une base de données expérimentales des boucles de décrochage dynamique avec différents angles d'attaque moyens, fréquences et amplitudes réduites serait nécessaire.

Chapitre 5 : Étude des vibrations induites par décrochage en utilisant des méthodes haute fidélité

La carte de stabilité précédemment réalisée a permit d'identifier les zones à priori instables et de choisir les simulations intéressantes à effectuer en haute fidélité couplant le modèle de pale FEM avec un solveur CFD URANS. L'objectif est de prendre en compte une meilleure description de l'écoulement et d'observer comment cela modifie le comportement du système couplé par rapport au modèle de décrochage dynamique de l'ONERA.

L'étude porte sur une pale isolée de l'IEA15MW en position d'arrêt et positionnée le long de l'axe Z. Le maillage de simulation est un maillage chimère constitué de deux maillages, un premier maillage décrit la géométrie de la pale et est immergé dans un second maillage d'arrière-plan qui capture le sillage.

Étude de l'équilibre aéroélastique

Avant d'examiner les comportements dynamiques, les équilibres aéroélastiques statiques sont analysés. La pale IEA15MW est fixée à sa base et immergée dans un écoulement uniforme de 40 m/s arrivant avec un angle d'incidence de 17°. Les efforts aérodynamiques agissant sur la pale la font fléchir. Le nouvel état modifie l'écoulement, entraînant de nouvelles forces aérodynamiques.

Dans l'ensemble, le modèle basse fidélité, basé sur la théorie des bandes, donne des déformations en flexion et torsion similaires au modèle haute fidélité. En effet, les forces et moments prédits par les deux modèles sont également proches. Cependant, les coefficients de force calculés avec la CFD présentent une modulation selon l'envergure. Cela est particulièrement visible sur le coefficient de force en Y. En examinant plus précisément la distribution de la pression sur la paroi et les lignes de de frottement, qui indiquent la direction de l'écoulement près de la paroi, il apparaît que ces fluctuations des forces sectionnelles sont causées par des cellules de décrochage (Fig R.12). Cela induit un écoulement 3D complexe que l'on peut observer grâce à une iso-surface de critère Q (Fig R.13).

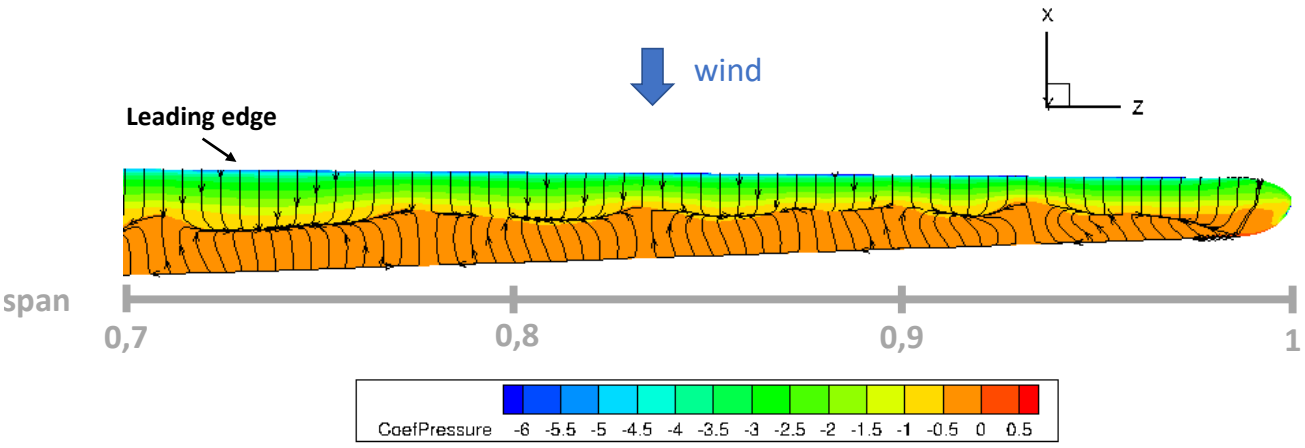

Figure R.12: Coefficient de pression et lignes de friction sur l'extrado de la pale

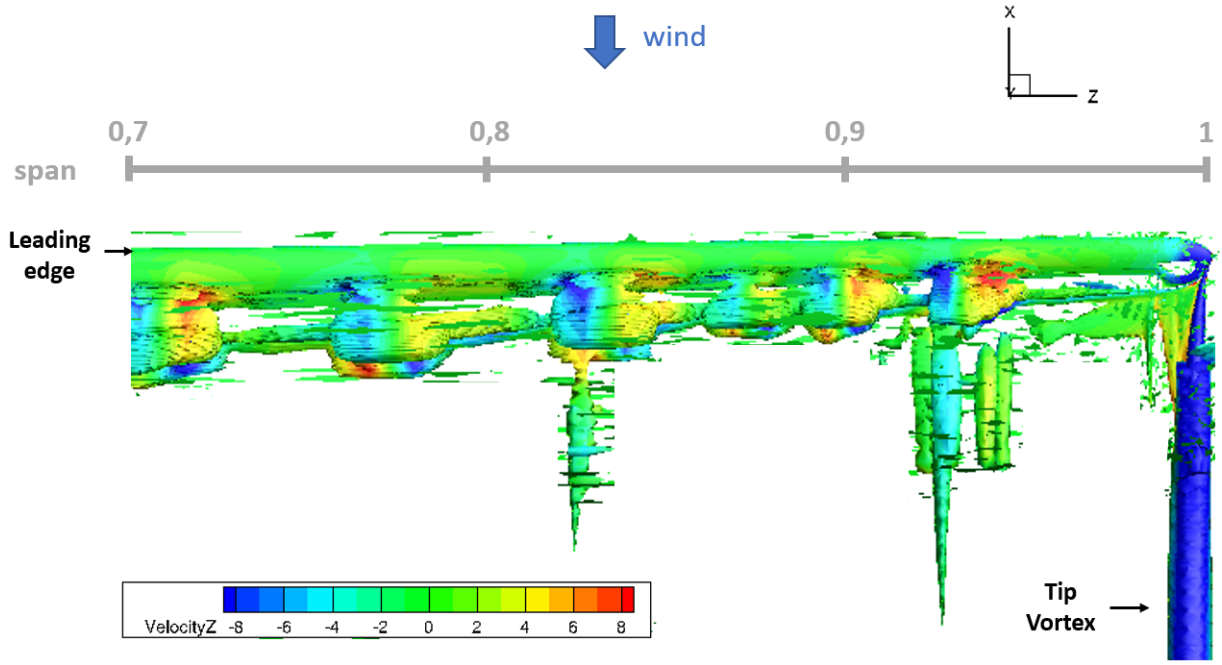

Figure R.13: Iso-surface de critère Q de valeur 50 colorisée par la vitesse selon Z

En faisant varier l'angle d'incidence, on remarque que les cellules de décrochage ne sont pas toujours présentes. Pour la pale de l'IEA15MW, celles-ci apparaissent à partir de $\phi_0 = 16°$, puis entraînent des variations de portance augmentant avec l'incidence. Leurs positions le long de la pale dépendent également de l'incidence. La taille moyenne des cellule de décrochage est comprise entre 1,5 et 3 cordes. Concernant l'effet de la vitesse du vent, on note que la taille des cellules de décrochage a légèrement diminué avec l'augmentation de vitesse. Bien que les cellules de décrochage soient plus marquées, avec de plus grandes oscillations de la ligne de séparation, les variations de portance ne sont que peu affectées.

Étude du comportement aérodynamique induit par un mouvement forcé harmonique

Dans la section précédente, les équilibres aéroélastique ont été étudiés. Une façon d'évaluer la stabilité dynamique de la pale consiste à étudier les forces induites par un mouvement harmonique d'un mode structurel de pale autour d'un état d'équilibre. Il est alors possible de calculer l'amortissement aérodynamique ajouté. Si l'amortissement aérodynamique est négatif et supérieur à l'amortissement structurel, il existe alors un risque d'instabilité. Comme montré précédemment, le mode *flapwise* est le plus risqué dans nos conditions de vents, c'est donc ce mode qui est imposé à la structure.

L'aspect le plus important pour comprendre l'amortissement aérodynamique ajouté est le déphasage des forces aérodynamiques par rapport à la vitesse de la structure. Un déphasage $\phi_{\dot{q}}$ compris entre -90° et 90° induit un amortissement aérodynamique négatif.

En regardant les déphasages des forces obtenus avec la CFD (Figure R.14), ceux-ci sont compris entre 120° et 180° le long de la pale, ce qui signifie que l'amortissement aérodynamique reste positif. En moyenne, on observe une légère baisse le long de la pale jusqu'à 95%, ce qui indique que la corde a un impact sur le déphasage. En effet, on sait que les boucles de décrochage dynamique dépendent de la fréquence réduite. Dans les derniers 5%, le déphasage augmente en raison de l'influence du tourbillon de bout de pale. Une modulation du déphasage peut également être observée le long

de la pale. Les forces sectionnelles selon Y sont représentées en pointillés dans la Figure R.14 afin de localiser les cellules de décrochage. On peut noter que dans les cellules de décrochage, où l'écoulement est plus séparé, le déphasage est plus faible, proche de 120°, ce qui produit un amortissement aérodynamique plus faible. Entre les cellules de décrochage, où l'écoulement est plus attaché, le déphasage est localement plus élevé, proche de 180°, ce qui produit un amortissement aérodynamique plus élevé.

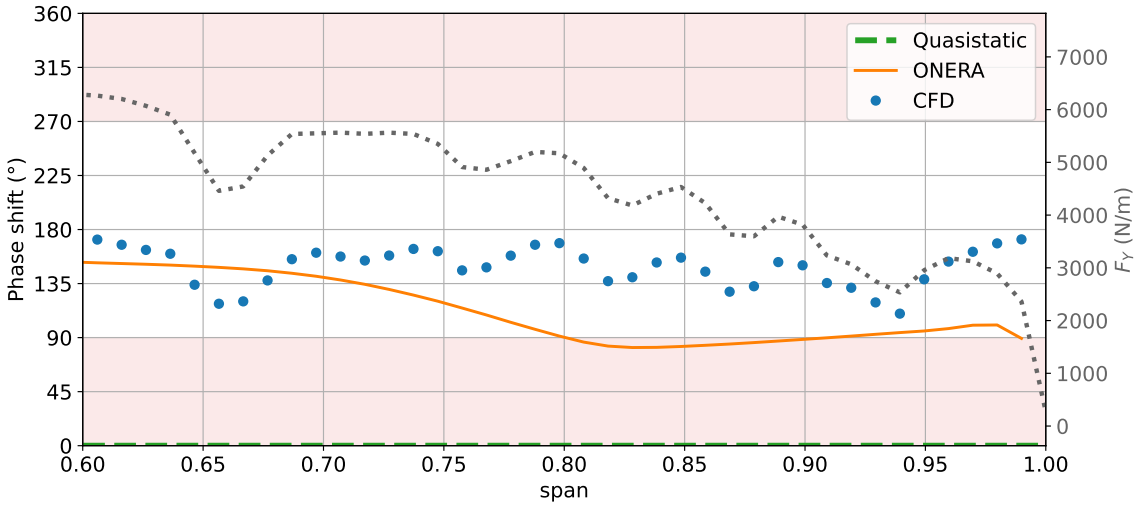

Figure R.14: Déphasage entre les forces sectionnelles selon Y et la vitesse pour le cas $\phi_0 = 17°$ et $U_0 = 40\text{m/s}$. Les zones rouges représentent les zones d'amortissement aérodynamique négatif. F_Y est représentée par une ligne pointillée.

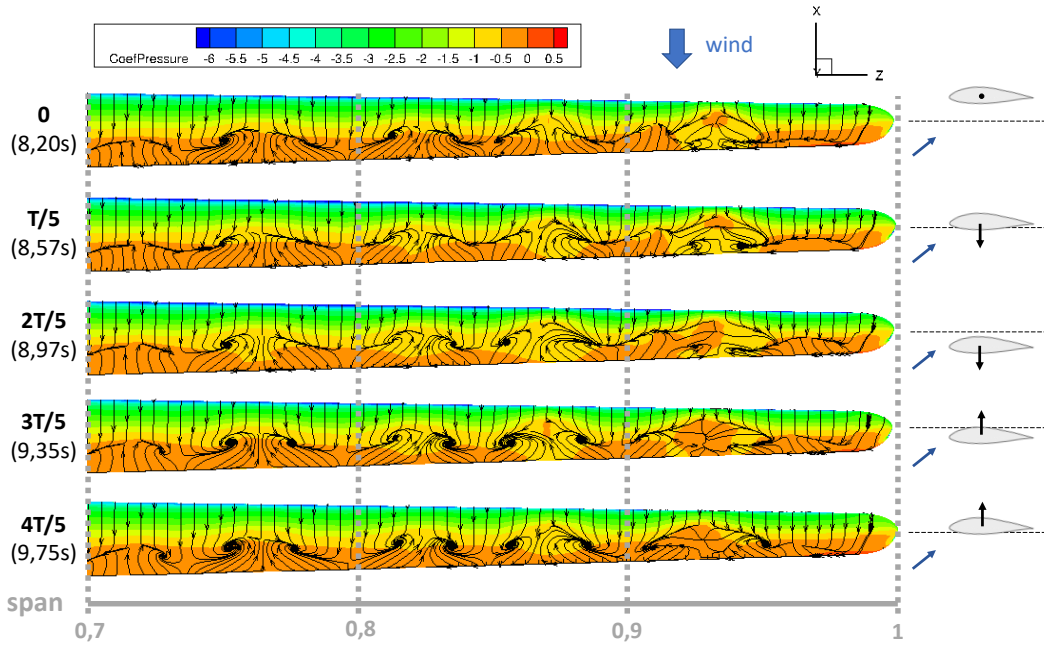

Figure R.15: Coefficient de pression à l'extrado et ligne de courant pour un angle d'incidence $\phi_0 = 17°$ et $U_0 = 40\text{m/s}$ sur une période d'oscillation.

Les forces aérodynamiques sont le résultat du comportement de l'écoulement et en particulier

du comportement dynamique des cellules de décrochage (Figure R.15). Comme on peut le déduire des forces sectionnelles, les cellules de décrochage restent aux mêmes positions tout au long du cycle. Cependant, leur forme change. Le centre des cellules de décrochage ne semble pas se déplacer vers l'amont ou l'aval, alors que la ligne de séparation située entre deux cellules oscille d'avant en arrière, étirant la cellule et provoquant des tourbillons.

En faisant varier l'angle d'incidence de 15° à 18°, on observe que celui-ci n'a que peu d'influence sur l'amortissement ajouté et la fréquence aéroélastique. L'amortissement aérodynamique reste élevé, de l'ordre de 35% et la fréquence aéroélastique est réduite de 10% par rapport à la fréquence de la structure seule. Concernant l'effet de la vitesse du vent, il semble que l'amortissement aérodynamique ajouté augmente considérablement avec la vitesse, passant de 30% pour $U_0 = 40m/s$ à 50% pour $U_0 = 50m/s$. De plus, la fréquence aéroélastique diminue encore davantage avec l'augmentation de la vitesse.

Étude du comportement aéroélastique dynamique d'une pale en décrochage

L'approche précédente par mouvement imposé est importante pour comprendre les réponses du fluide induites par le mouvement, mais elle présente certaines limitations. Le mouvement imposé n'est pas représentatif, en termes de déplacement et de fréquence, du mouvement aéroélastique réel. Pour surmonter ces limites, des simulations aéroélastiques couplées instationnaires sont réalisées. Pour perturber la pale, il a été décidé d'utiliser une rafale de vent.

Pour estimer l'effet de l'incidence, deux simulations à incidence 17° et 18° avec une vitesse de vents de 40 m/s ont été réalisées (Figure R.16).

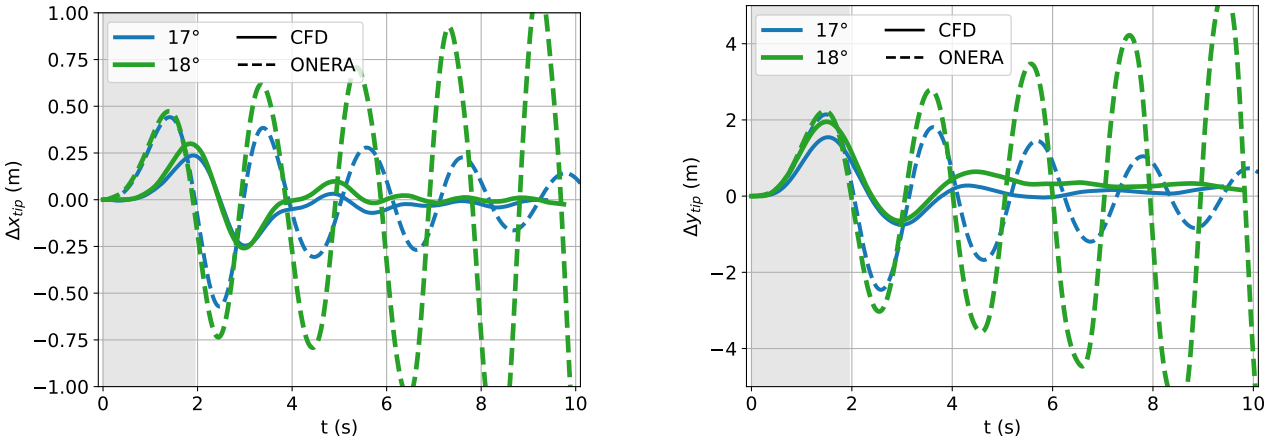

(a) Δx_{tip} (b) Δy_{tip}

Figure R.16: Déplacements du bout de pale selon X (à gauche) et selon Y (à droite) en fonction du temps pour $U_0 = 40$m/s, $\phi_0 = 17°$ et 18°. La zone grise indique la durée de la rafale.

Dans la direction Y, la fréquence mesurée est inférieure (0,4 Hz) à la fréquence structurelle *flapwise* (0,51 Hz) en raison d'une rigidité supplémentaire négative, comme cela a été prédit par l'étude du mouvement imposé. Cependant, aucune différence notable en termes d'amortissement ou de fréquence n'est observée entre les simulations avec différents angles d'incidence.

Une simulation supplémentaire à une incidence de 17° et une vitesse de vent de 50 m/s a été réalisée pour observer l'effet de la vitesse du vent (Figure R.17).

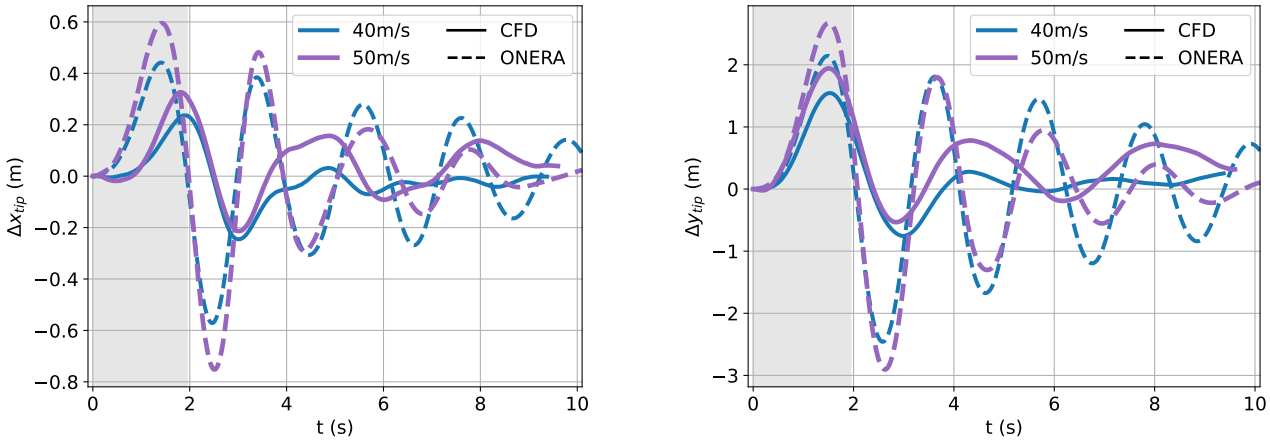

(a) Δx_{tip} (b) Δy_{tip}

Figure R.17: Déplacement du bout de pale pour deux vitesses de vent, $U_0 = 40m/s$ et $50m/s$ (c'est-à-dire une vitesse réduite $\mathcal{U}_R = 5,3$ et 6,61) à $\phi_0 = 17°$. La zone grise indique la durée de la rafale.

Il est clair que pour 50 m/s, la réponse aéroélastique est moins amortie que pour 40 m/s. L'amortissement est de 20% à 40 m/s et tombe à environ 10% pour 50 m/s. Ceci est en contradiction avec les résultat obtenus par le mouvement imposé. Cette grande différence d'amortissement avec les simulations de mouvement imposé provient probablement de la forte baisse de fréquence de la fréquence aéroélastique *flapwise*. En effet, pour 40 m/s, la fréquence *flapwise* est passée de 0,51 Hz à 0,34 Hz. Et pour 50 m/s, elle tombe à 0,28 Hz. La fréquence est ici presque divisée par deux. Au vu de ces résultats, il semble plausible que, pour une pale ayant une fréquence *flapwise* plus faible (pale plus effilée) ou dans des conditions de vent plus fort, des vibrations induites par décrochage puissent potentiellement apparaître.

Conclusion

L'objectif initial était de se concentrer dans un premier temps sur les configurations d'éoliennes à l'arrêt concernées par trois types d'instabilités aéroélastiques : le flottement par couplage de modes, les vibrations induites par vortex (VIV) et les vibrations induites par décrochage (SIV). La revue de la littérature présentée au chapitre 1 a permis d'identifier le manque d'études axées sur les vibrations induites par décrochage des pales à l'aide d'approche haute fidélité et ainsi de définir les nouveaux objectifs de la thèse : étudier les vibrations induites par décrochage sur une pale d'éolienne de référence à l'arrêt, en utilisant des approches fluide-structure de complexité croissante, afin de mettre en évidence l'apport des méthodes haute fidélité sur les SIV par rapport aux méthodes de fidélité moindre. Il a également été décidé d'utiliser la pale de l'éolienne de référence de l'IEA 15MW, un modèle open source libre de toute contrainte de confidentialité, qui est un modèle standard dans la communauté scientifique. Ce modèle d'éolienne a été développé par des universitaires et représente la meilleure alternative aux éoliennes industrielles.

Pour répondre à cette problématique, un framework Python modulaire a été développé. Il permet de passer facilement d'un niveau de solveur fluide-structure à l'autre, allant du modèle sectionnel, utilisant soit une formulation aérodynamique quasi-stationnaire, soit un modèle de décrochage dynamique, jusqu'au couplage CFD/CSM haute fidélité. Ce dernier a nécessité un investissement particulier. Tout d'abord, le solveur *FastS* a dû être validé pour la configuration

de décrochage dynamique. Ensuite, il a fallu développer des méthodes de transfert appropriées entre les deux solveurs. L'interface entre un modèle de poutre et un maillage CFD 3D étant très différente, les méthodes de transfert courantes n'étaient pas adaptées. Une méthode de transfert cinématique a donc été mise en œuvre.

L'approche la plus simple pour étudier les vibrations induites par décrochage consiste à utiliser un modèle de section couplé à une formulation aérodynamique de décrochage quasi-stationnaire ou dynamique. Cependant, un modèle de section est géométriquement éloigné d'une pale vrillée et flexible. C'est pourquoi un modèle de section équivalente aussi proche que possible de la pale complète IEA15MW a été développé. Ce modèle de section équivalent possède deux degrés de liberté *flapwise* et *edgewise*, en tenant compte du vrillage et des propriétés matériaux. Sur la base de l'idée d'égaliser l'amortissement aérodynamique d'un modèle sectionnel avec celui d'un modèle de pale modal, des quantités équivalentes, notamment une corde équivalente, une direction *edgewise* et des polaires aérodynamiques équivalentes, ont été identifiées.

Le modèle de section équivalente a prouvé son efficacité dans la reproduction de la carte de stabilité SIV d'un modèle de pale FEM couplé au modèle de décrochage dynamique de l'ONERA sous l'hypothèse de la théorie des bandes. Les différences restantes dans la carte de stabilité ont toutefois mis en évidence la difficulté de construire un modèle de décrochage dynamique équivalent décrivant l'effet de toutes les boucles de décrochage dynamique de la pale en une seule boucle. Que ce soit avec la section équivalente ou le modèle FEM, les résultats obtenus à l'aide d'un modèle de décrochage dynamique semi-empirique, tel que le modèle ONERA, pour les prévisions SIV, doivent être considérés avec prudence, car la caractéristique des boucles qui favorise le transfert d'énergie peut être très dépendante des paramètres du modèle.

Sur la base de la carte de stabilité établie à l'aide d'une approche « basse fidélité », plusieurs conditions de vent ont été sélectionnées pour être simulées à l'aide d'une approche haute fidélité, en couplant un modèle de pale FEM avec le solveur URANS *FastS*. Comparé au modèle de décrochage dynamique, le solveur *FastS* a permis de simuler des effets 3D. Dans les simulations aéroélastiques stationnaires, cela s'est manifesté par des cellules de décrochage qui génèrent une modulation d'amplitude de la distribution de portance le long de l'envergure. Le comportement aéroélastique instationnaire de la pale autour de son état d'équilibre aéroélastique a ensuite été étudié en deux étapes. Tout d'abord, à travers l'analyse des forces aérodynamique induites par un mouvement harmonique forcé selon le mode de flexion *flapwise*. Ensuite, sur la base des réponses aéroélastiques libres provoquées par une excitation de type rafale discrète. Pour l'ensemble des mouvements de faible amplitude imposés à la pale, aucun mouvement de cellule de décrochage n'a été détecté, ce qui signifie que la dynamique des cellules de décrochage était probablement plus lente que celle du mouvement harmonique forcé. Cependant, ces simulations ont mis en évidence une différence de déphasage entre l'intérieur et l'extérieur des cellules de décrochage. À l'intérieur des cellules de décrochage, où l'écoulement est plus séparé, les forces aérodynamiques ont un déphasage plus faible qu'à l'extérieur des cellules de décrochage. Pour l'amortissement aérodynamique, seul une très faible influence de l'angle d'incidence du vent a été observée. l'amortissement reste autour de 30% pour les angles d'incidence compris entre 15° et 18°. Le comportement mis en évidence était donc très différent de celui obtenu à l'aide du modèle de décrochage dynamique de l'ONERA, pour lequel l'amortissement aérodynamique diminue et devient négatif avec l'augmentation de l'angle d'incidence du vent. Des simulations aéroélastiques de la pale suite à une rafale discrète ont confirmé que la fréquence du mode aéroélastique *flapwise* est fortement réduite (-35% pour $U_0 = 40$m/s et -50% pour $U_0 = 50$m/s) en raison de la raideur aérodynamique. L'augmentation de la vitesse du vent de 40 m/s à 50 m/s a également entraîné une diminution de l'amortissement des vibrations *flapwise*. Ce comportement n'a pas pus être capturé avec le modèle de l'ONERA. Finalement, aucune instabilité aéroélastique n'a été observée dans les conditions simulées.

Perspectives

Toutes les recherches présentées dans cette thèse ont été menées sur l'éolienne IEA15MW. Cependant, afin d'évaluer l'influence de la conception des pales, il serait intéressant de mener des études similaires sur une pale plus grande, telle que l'IEA22MW [149]. Cependant, une première estimation peut être faite en examinant l'évolution du rapport de masse $\mathcal{M}$ et de la vitesse réduite $\mathcal{U}_R$. Un rapport de masse supérieur d'environ 7% à celui de la pale IEA15MW indique un couplage fluide-structure plus fort qui amplifie la valeur de l'amortissement aérodynamique. Par conséquent, une vitesse de vent plus faible peut déclencher l'instabilité. L'augmentation de la corde ne compense pas la diminution de la fréquence de flexion *flapwise*, ce qui entraîne une augmentation d'environ 14% de la vitesse réduite. Sur la carte de stabilité, cela correspond à une réduction d'environ 12% des vitesses critiques du vent.

De plus, dans le présent travail, l'écoulement a été supposé uniforme, ce qui n'est pas réaliste. Étant donné que la turbulence a une forte influence sur les caractéristiques des boucles de décrochage dynamique [3], il serait plus approprié d'utiliser des conditions d'écoulement entrant plus représentatives des conditions rencontrées par les éoliennes en termes de turbulence et de couche limite atmosphérique. Les conditions de vent les plus susceptibles de déclencher des vibrations induites par décrochage sont celles qui se produisent pendant les typhons. Dans, la couche limite atmosphérique correspondante, l'intensité de la turbulence et l'échelle de longueur de la turbulence dans des conditions de typhon ont été mesurées par Yi et al. [145] et Zhao et al. [151] et peuvent être modélisées par des lois de puissance en fonction de la hauteur.